Investigation and Control of Unsteady Flow Conditions on Airfoils

Kissing, Johannes Maximillian Emanuel

(2020)

DOI (TUprints): https://doi.org/10.25534/tuprints-00014201

Publikationstyp: Dissertation

Fachbereich: 16 Fachbereich Maschinenbau

Quelle des Originals: https://tuprints.ulb.tu-darmstadt.de/14201

Investigation and Control of Unsteady Flow Conditions on Airfoils

Am Fachbereich Maschinenbau
der Technischen Universität Darmstadt
zur
Erlangung des Grades eines Doktor-Ingenieurs (Dr.-Ing.)
genehmigte

Dissertation

vorgelegt von

Johannes Maximillian Emanuel Kissing, M.Sc.

aus Neuss

Berichterstatter:	Prof. Dr.-Ing. C. Tropea
Mitberichterstatter:	Prof. Dr.-Ing. L. David
Tag der Einreichung:	11.08.2020
Tag der mündlichen Prüfung:	06.10.2020

Darmstadt 2020

D 17

Johannes Maximillian Emanuel Kissing:
Investigation and Control of Unsteady Flow Conditions on Airfoils

Darmstadt, Technische Universität Darmstadt
Jahr der Veröffentlichung der Dissertation auf TUprints: 2020
Tag der mündlichen Prüfung: 06.10.2020

Bitte zitieren Sie dieses Dokument als:
URN: urn:nbn:de:tuda-tuprints-142017
URL: https://tuprints.ulb.tu-darmstadt.de/id/eprint/14201

For Hannah and
for Karoline and Hans-Jürgen

Abstract

In this thesis, efficiency enhancement approaches for two unsteady aerodynamic scenarios are considered to provide the basis for future improvements.

The first scenario addresses transient inflow conditions on a stationary airfoil, representative of gust loads on wind turbine blades or bridge decks. It aims at the experimental validation of aerodynamic transfer functions, known as the Sears and Atassi formulations, which allow for a prediction of unsteady loads. Both functions are found to be capable of load prediction if inflow assumptions are carefully reproduced. It is also shown that no fundamental difference between both functions exists, if they are normalized appropriately. In order to simplify the generation of periodic inflow conditions in a wind tunnel, a gust generation approach utilizing a single pitching and plunging airfoil is derived and experimentally validated. It is demonstrated that high frequency and amplitude gusts can be generated with the aid of optimized airfoil kinematics, derived from the Theodorsen theory, using a single airfoil.

The second scenario considers steady inflow conditions on a pitching and plunging airfoil in the deep dynamic stall regime where a leading edge vortex (LEV) occurs, representative for beating wings of Micro Air Vehicles (MAVs). The detachment process of the vortex is investigated to provide the basis for consecutive flow control efforts. A model that allows for the prediction of the occurrence of secondary structures, which can initiate the vortex detachment, is derived and validated using facilities with complementary parameter spaces due to different working media. In order to prolong the LEV growth phase on the airfoil and attain higher overall lift, a DBD plasma actuator is used to manipulate the flow field at topologically critical locations on different airfoils. The growth phase of the vortex is prolonged, which indicates an enhancement of the induced lift. Considerations regarding the control authority of the actuator are used to derive and test the minimum effective actuation period, which is sought to demonstrate the potential for future enhancements of the control concept.

Kurzfassung

Diese Arbeit befasst sich mit Ansätzen zur Effizienzsteigerung in zwei instationären aerodynamischen Szenarien.

Fluktuierende Anströmbedingungen an einem stationären Flügelprofil stellen das erste untersuchte Szenario dar, welches repräsentativ für Böenlasten an Windturbinenblättern oder Brückenkörpern ist. Hierbei besteht das Ziel in der Validierung aerodynamischer Übertragungsfunktionen nach Sears und Atassi, welche die Vorhersage instationärer, aerodynamischer Lasten erlauben. Es wird gezeigt, dass beide Funktionen unter der Berücksichtung und sorgsamen Reproduktion der vorhergesehenen Einströmbedingungen in der Lage sind, instationäre, aerodynamische Lasten vorherzusagen. Zudem kann nachgewiesen werden, dass unter Einbezug einer Normalisierung keine fundamentalen Unterschiede zwischen beiden Formulierungen existieren. Um die Generation von fluktuierenden Einströmbedingungen in einem Windkanal zu simplifizieren wird ein Ansatz, basierend auf der Verwendung eines einzelnen Flügelprofils, hergeleitet und experimentell validiert. Dabei kommen optimierte Bewegungsprofile zum Einsatz, welche aus der Theodorsen-Theorie hergeleitet werden. Im Vergleich zu anderen Böengeneratoren ermöglicht der vorgestellte Ansatz Böen großer Amplitude und Frequenz unter Verwendung eines einzelnen Flügelprofils zu produzieren.

Das zweite aerodynamische Szenario befasst sich mit der Strömung um Flügelprofile, welche kombinierte Hub- und Nickbewegungen in stationärer Anströmung ausführen. Diese Betrachtung erfolgt im Bereich des tiefen dynamischen Strömungsabrisses indem ein Vorderkantenwirbel das Strömungsfeld dominiert. Die gewählten Bedingungen sind beispielsweise repräsentativ für schlagende Flügel eines Mikro-Luftfahrzeugs. Zunächst wird das Ablöseverhalten des Vorderkantenwirbels untersucht, um die Grundlage für spätere Strömungsbeeinflussungen zur Verfügung zu stellen. Ein Modell zur Vorhersage des Aufkommens von Sekundärstrukturen, welche das Ablösen des Wirbels initiieren können, wird mit Hilfe zweier Versuchseinrichtungen unterschiedlicher Arbeitsmedien hergeleitet und validiert. Um die Wachstumsphase des Vorderkantenwirbels und damit die Phase erhöhten Auftriebs zu verlängern, werden dielektrische Barriereentladungs-Plasma-Aktuatoren zur Manipulation des Strömungsfeldes an topologisch kritischen Stellen auf verschiedenen Flügelprofilen eingesetzt. Die Wachstumsphase des Vorderkantenwirbels wird signifikant verlängert, was auf einen erhöhten Auftrieb am Flügelprofil schließen lässt. Untersuchungen der Wirkreichweite des Plasma-Aktuators werden genutzt, um die minimale effektive Aktuierungsperiode herzuleiten und zu testen. Dieses Vorgehen dient der Demonstration des Potentials zukünftiger Anstrengungen zur Effizienzsteigerung.

Acknowledgments

First of all I would like to thank *Prof. Dr.-Ing. Cameron Tropea* for giving me the opportunity to pursue my research at the Institute for Fluid Dynamics and Aerodynamics (SLA) at the Technische Universität Darmstadt. The granted freedom, his confidence, his open ear and carefully placed, crucial questions contributed to this thesis as much as the facilities at the wind tunnel in Griesheim. I would also like to thank *Prof. Dr.-Ing. Laurant David* for refereeing my thesis. For the continuation of the support of my research, gratitude is owed to *Prof. Dr.-Ing. Jeanette Hussong.* Beyond numerical aspects of the project, *Apl. Prof. Dr.-Ing. Suad Jakirlic* was always an open-minded and valuable point of contact.

Deep gratitude is owed to *Jochen Kriegseis* for all the inspirations and fruitful discussions at any time, day or night. The exchange of ideas and their critical assessment contributed significantly to the scientific level of this thesis. Deep gratitude is also owed to *Nathaniel Wei*, whos genius and hard work was essential to the first considered scenario, but contributed to the thesis in many other aspects as well. Numerical considerations of both scenarios, the intercontinental collaboration and the experiments in Oldenburg would neither have been possible nor as fruitful without the encouragement of *Sebastian Wegt*, *Zhenyao Li* and *Tom Wester.* It is a great pleasure to work and socialize with all of you!

The financial support from the *Sino-German Center* and the *Deutsche Forschungsgemeinschaft* through the projects TR 194/55-1 and GZ-1280 are gratefully acknowledged. During my project I was allowed to interact with many people around the world, who inspired me a lot.

The help of students was the indispensable basis of my research. Many thanks for your commitment and your passion: *Mesut Albayrak, Lauritz Beck, Viktor Berchtenbreiter, Jonas Bergner, Kian Büchel, Jannick Erhard, Julian Hofmann, Mark Keenan, Alexander Kiefer, Alexander Kohlstetter, Jan Schäfer, Bastian Stumpf, Maximillian Stumpp* and *Stefan Triess.*

The creative, cooperative and pleasant working atmosphere at the wind tunnel facilities in Griesheim was essential for managing experimental challenges but also provided valuable changes of perspective on professional and private aspects. For this, I would like to thank *Andreas Bauer, Alexander Beck, Jan Breitenbach, Philipp Brockmann, Johannes Feldmann, Mark Gloerfeld, Amandine Guissart, Till Kaupe, Max Kuhnhenn, Lingxi Li, Max Luh, Klaus Schiffmann, Benedikt Schmidt* and *Fabian Tenzer.* The outcome and quality of multiple experimental realizations was made possible by the workshop under the guidance of *Ilona Kaufhold. Stephanie Lath, Birgit Neuthe* and *Monika Medina-Espana* supported the project in all the administrative aspects, but also made seemingly hopeless bureaucratic issues possible.

The commitment to discuss issues of others and the corresponding change of perspective is something that should not be taken for granted. Therefore, and for proof-reading this thesis, I would like to express my gratitude to *Bernd Hauk* and *Philipp Brockmann.*

Finally, my deepest gratitude is owed to my fiancee *Hannah Hauk* and to my parents, *Karoline* and *Hans-Jürgen Kissing.* The encouragement of my parents, their support during my studies and their confidence allowed me to get to this point. *Hannah*, I would like to thank you for your patience, support and the tranquility you gave me during the last years. Without you on my side and your love, all of this would not have been possible.

Thank you.

Johannes

Contents

1 Introduction

This introductory chapter provides a motivation for investigation of the transient aerodynamic scenarios considered in this thesis in section 1.1 and reviews some fundamentals of unsteady aerodynamics along with relevant literature in section 1.2. In section 1.3 the objectives of the thesis and an outline of how these were achieved are summarized. Parts of this chapter have been published in Wei et al. (2019a,b) and Kissing et al. (2020a,b,c).

1.1 Motivation

In real-world applications, aerodynamically loaded profiles like wings of passenger airplanes, bridge decks or blades of wind turbines experience transient inflow conditions. These can arise through gust encounter, flight maneuvers or misalignment of components and can lead to significant load fluctuations. Novel propulsion concepts of micro air vehicles (MAVs) employing flapping wings also inherently involve unsteady flow conditions. These, as with flapping wings of insects or birds, make use of beneficial unsteady lift effects. Transient or unsteady aerodynamics deals with dynamic flow conditions and the resulting, fluctuating aerodynamic loads. The demand for efficiency enhancements and the reduction of the environmental impact of applications related to unsteady aerodynamics require not only a deeper understanding of underlying physics, but also require approaches to best exploit such knowledge. This represents the broader topic of the present thesis.

Unsteady aerodynamics is usually classified according to the reduced frequency k (Leishman, 2017). To compute it, the frequency of a moving airfoil or the wavelength of an inflow perturbation are typically considered in respect to the convectively covered distance of the mean flow. For higher k the unsteadiness of the phenomena increases. In k, neither the amplitude of the unsteadiness nor the perturbation wavelength with respect to the chord of the airfoil are taken into account.

In this thesis two alternative aspects to k will be used for classification of unsteady scenarios. The first concerns the boundary conditions, for instance a change of inflow conditions or a moving lifting surface. The second classifies the situation according to the induced flow field, typically light or deep stall. These two variants are pictured in Fig. 1.1 and will be briefly elaborated below.

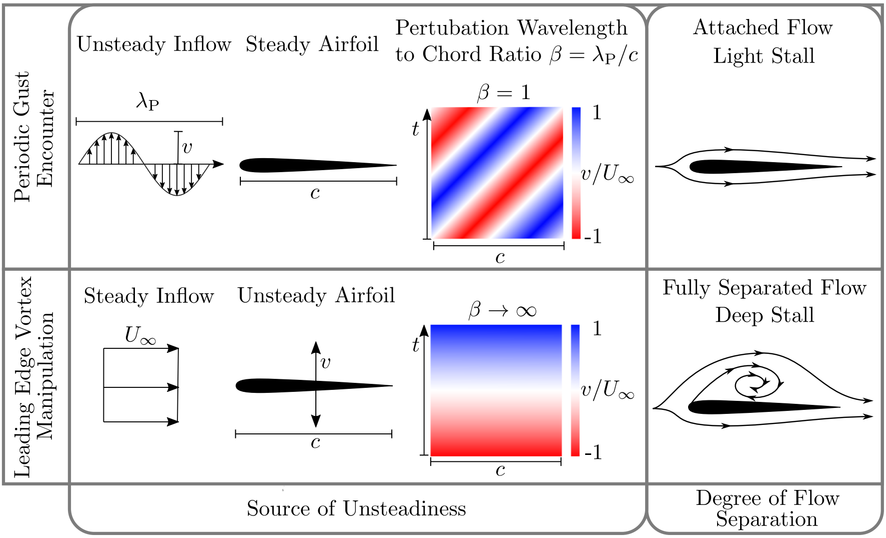

Figure 1.1: Classification of unsteady aerodynamic scenarios investigated in this thesis. Unsteady boundary conditions or degree of flow separation can be used to classify unsteadiness.

The first criterion involves unsteady inflow conditions and a fixed lifting surface, steady inflow and a moving lifting surface, or a combination of both. The unsteadiness is described by the ratio of the inflow perturbation wavelength in the mean flow direction λ_P to the airfoil chord c, denoted as β. In contrast to the reduced frequency k, for β only the inflow perturbation is considered and not the airfoil motion. For large ratios ($\beta \gg 1$), the airfoil experiences an inflow fluctuation simultaneously over its entire chord, more characteristic of a steady inflow and a moving airfoil. In contrast, periodic gust encounter of a stationary airfoils are described by $\beta \leq 1$. These two limiting cases are pictured in Fig 1.1.

The degree of flow separation in terms of an attached or fully separated flow over the airfoil, also denoted as light and deep stall, is used as an alternative classification criterion and is also depicted in Fig 1.1.

Middle sections of wind turbine blades and bridge decks in gusty inflow conditions are examples of steady airfoils in unsteady inflow with an attached flow and with a correspondingly low value of β. Note, that this does not hold true for wind turbine blade sections close to the root or tip or if they are misaligned and not operating at their design set-point. On the other hand, the beating wings of birds and MAVs are exemplary for unsteady airfoils in steady inflow, where severe flow separation occurs due to excessive effective inflow angle excursions. For these applications, unsteady loads can be beneficial in terms of increased lift, as exploited by insects or birds and used to improve flight characteristics of MAVs (Ho et al., 2003). However, these unsteady loads can also be detrimental and endanger the structural integrity and durability of wind turbine blades or bridge decks due to high fluctuating loads (Spinato et al., 2009; Billah & Scanlan, 1991).

To what extent performance improvement or higher efficiency can be achieved when unsteady aerodynamics is involved depends strongly on application. Fluctuating loads may necessitate larger safety margins, or they may be inherently useful, as in the enhanced lift characteristics mentioned above. For instance, a better understanding of transient loads on wind turbine blades, which are exemplary for a periodic gust encounter, would allow reduced design safety margins needed to guarantee structural integrity; thus potentially reducing blade weight or prolonging blade lifetime (Veers & Butterfield, 2001). This would also allow increased rotor diameter, which is an established approach to increase efficiency via reduced cost of energy (CoE) (Johnson et al., 2010). To generically investigate these possibilities of performance enhancement, the two scenarios illustrated in the upper and lower rows of Fig 1.1 will be addressed in this thesis.

Transient loads during periodic gust encounters are analytically described by aerodynamic transfer functions, sometimes termed admittance functions (in the car industry). In order to allow for a better understanding of the prescribed loads and enable future efficiency and performance enhancements, one of the central aims of this thesis is to theoretically evaluate and experimentally validate certain aerodynamic transfer functions. Additionally, the experimental simplification of periodic gust generation, necessary to investigate airfoil response, is another objective in this context.

Novel propulsion concepts of MAVs adapt biological flight to realize unrivaled manoeuvrability and lift at very low flight speeds and corresponding Reynolds numbers Re (Eldredge & Jones, 2019). These characteristics are attributed to the leading edge vortex (LEV) growing over a rapidly translating and rotating wing. As long as the LEV accumulates circulation on an airfoil, it induces additional lift, which drops when the vortex detaches. Animals keep the vortex attached longer to their wings by adapting their wing shape (Ristroph et al., 2010) or kinematics to attain higher lift and thus increase their performance. When aiming for an efficiency or performance enhancement of MAV propulsion concepts based on flapping wings, keeping the LEV attached to an airfoil is a promising approach (Ho et al., 2003). The second central aim of the present thesis is the development and validation of an experimental flow control approach to prolong the LEV growth phase on a pitching and plunging airfoil. This is accomplished with the aid of a dielectric barrier discharge plasma actuator (DBD-PA) as a flow manipulation device. By prolonging the vortex growth phase and/or delaying the vortex detachment, higher overall lift can be attained, enabling performance and efficiency enhancements.

1.2 Unsteady Aerodynamic Scenarios

This section briefly addresses fundamentals of unsteady aerodynamics and provides a literature review for both aerodynamic scenarios in subsections 1.2.1 and 1.2.2.

Scenarios considered in this thesis are encountered on an airfoil when it experiences unsteady effective inflow conditions. In this context, effective inflow conditions are those experienced by the airfoil. These conditions are determined by the combination of the effective inflow angle evolution on an airfoil $\alpha_{\text{eff}}(t)$ and the effective inflow velocity evolution $U_{\text{eff}}(t)$. Fluctuations of both quantities can arise from an unsteady inflow or a motion of the airfoil (cf. Fig. 1.1). Despite this difference in the source of unsteadiness, both cases can lead to dynamic stall phenomena and stall regimes, as discussed below.

Dynamic Stall

The effect of dynamic changes of α_{eff} on aerodynamic forces encountered by an airfoil and the flow field is explained by the dynamic stall phenomena. This was first observed by Kramer (1932), who discovered that the lift on an airfoil can be augmented beyond the static stall angle by a dynamic change of α_{eff}. The overshoot of lift is possible because the inviscid pressure field about the airfoil adjusts to the instantaneous flow with the speed of sound while viscous effects lag behind (cf. Cebeci et al., 2005). After reaching an overshoot peak, the unsteady lift evolution drops below the steady case, forming a hysteresis, which is exemplary depicted for a pitching airfoil in Fig. 1.2. Here, the aerodynamic force acting in normal direction on an airfoil F_{N} is shown over the variation of α_{eff}. F_{N}, which is directly indicative for lift, is compared between a steady change of α_{eff} (dashed line) and a dynamic change of α_{eff} (solid line).

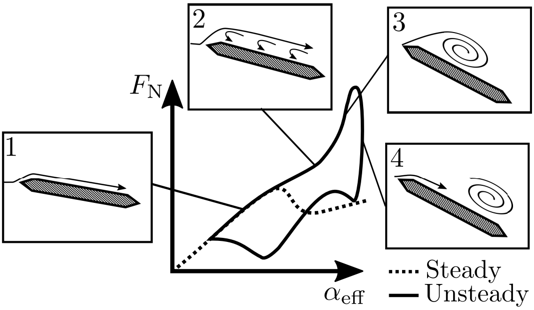

Figure 1.2: Dynamic stall phenomena encountered by airfoils if their effective inflow angle α_{eff} changes dynamically. The normal force F_{N} acting on a pitching airfoil is depicted schematically for a steady change of the effective inflow angle α_{eff} (dashed line) and for an unsteady change (solid line). Different stages of the flow field are linked to the force hysteresis with the aid of pictographs. Adapted from Carr (1988).

Different stages of the lift hysteresis were linked to the flow field around a pitching airfoil via the pressure distribution by McCroskey et al. (1976). For low α_{eff}, unsteady and steady lift evolve concurrently. The flow around the airfoil is attached in both cases (cf. pictograph 1 in Fig. 1.2). In contrast to the steady lift, the unsteady lift continues to increase when the static stall angle is reached. In the steady case, flow reversal over the airfoil causes an increase of the pressure on the suction side of the airfoil, leading to the breakdown of lift – and F_{N}. Although flow reversal occurs in the boundary layer for both cases, the flow remains globally attached to the airfoil in the unsteady case. This second stage is illustrated in pictograph 2. When α_{eff} is further dynamically changed, a leading edge vortex (LEV) forms by the roll-up of the separated shear layer at the leading edge of the airfoil in stage 3. As long as the LEV grows on the airfoil, the unsteady lift continues increasing, while it drops once the vortex stops accumulating circulation and starts to convect downstream (stage 4).

Scenarios considered in this thesis occur for different amplitudes of the effective inflow angle $\hat{\alpha}_{\text{eff}}$ and frequencies of the perturbation. For gust encounters, stages 1 and 2 are considered, while the leading edge vortex occurs in stages 3 and 4 for higher excursions of $\hat{\alpha}_{\text{eff}}$. Nevertheless, the flow fields above airfoils in both cases are described by the dynamic stall phenomena. Further classification of scenarios is possible with the aid of the stall regime, descriptive for the degree of flow separation over the airfoil and discussed below.

Stall Regimes

The key parameters determining the degree of flow separation and peak forces during dynamic stall are the reduced frequency k and the effective angle of attack amplitude $\hat{\alpha}_{\text{eff}}$, as discussed by McCroskey (1982). The reduced frequency k, which is defined according to Leishman (2017) as

$$k = \frac{\pi f c}{U_\infty}, \tag{1.1}$$

where f is the oscillation frequency of the airfoil motion, c the chord length and U_∞ the free stream velocity, represents the ratio of the time for a fluid element to convect across the airfoil in relation to the period of oscillation.

Dependent on the combination of k and $\hat{\alpha}_{\mathrm{eff}}$, different stall regimes can be observed on an airfoil. Two of them are depicted in Fig. 1.3 for a purely pitching airfoil. The first regimes, where no flow separation occurs or the separation region does not exceed the thickness of the airfoil, are denoted as stall onset and light stall respectively (McCroskey, 1982). Separation, which starts from the trailing edge, occurs only over parts of the airfoil and does not reach the leading edge in the light stall regime. In these regimes, the maximum unsteady lift for the lowest drag penalty can be achieved. This assumption is supported by findings of Ol et al. (2009), Baik et al. (2012) and Manar & Jones (2019), who found that potential flow models can account for the flow and resulting forces in both regimes, even if light separation occurs.

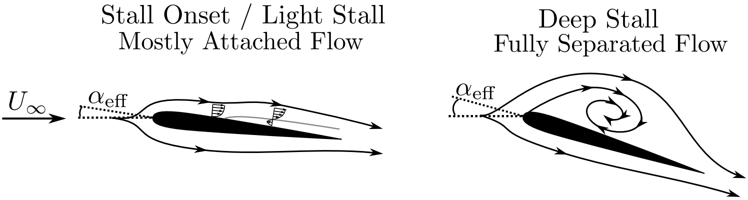

Figure 1.3: Schematic representation of stall regimes on a pitching airfoil. The inflow is from the left. Illustration adapted from McCroskey (1982)

If $\hat{\alpha}_{\mathrm{eff}}$ is further increased, the deep stall regime occurs, which is dominated by vortices occurring at the leading edge of the airfoil. This regime is characterized by severe flow separation over the entire airfoil, where the separation zone extends about one chord length into the free stream. For further details on dynamic stall, the reader is referred to Carr (1988) and Leishman (2017).

1.2.1 Periodic Gust Encounter

In this section, an introduction and literature review for aerodynamic transfer functions and for gust generation approaches will be given. The focus of this section will be on inflow conditions, crucial to meet assumptions conforming with transfer function formulation and to allow an experimental validation of them.

Aerodynamic Transfer Functions

In order to better understand and capture the dynamics of gust-airfoil interactions, Sears (1938) modeled the problem using the principles of thin airfoil theory. By approximating the airfoil as a series of point vortices distributed along its camber line, potential flow analysis can be applied. When a periodic gust normal to the airfoil is supplied as an inflow condition, the effects on the vorticity profile on and in the wake of the airfoil can be computed. Integrating the vorticity profile on the airfoil yields what Sears called the lift contribution of the apparent mass (cf. von Karman, 1938; Sears, 1941), whereas integrating the vorticity profile in the wake provides the forces due to unsteady effects in the wake itself. The latter component of the lift force involves a function $C(k)$ developed by Theodorsen (1934), which depends only on the reduced frequency k. A transfer function for the unsteady lift on an airfoil in a periodic gust can thus be constructed by combining the apparent mass and wake effect lift components with the quasi-steady lift derived from the Kutta-Joukowski theorem. This transfer function is known as the Sears function.

Fig. 1.4 depicts inflow conditions in accordance with the assumptions of the Sears formulation. These include a fluctuation of the vertical inflow velocity $\hat{v}$, normal to the airfoil with the reduced frequency k_1. In contrast to Theodorsen's formulation, where the motion frequency of the airfoil is used to

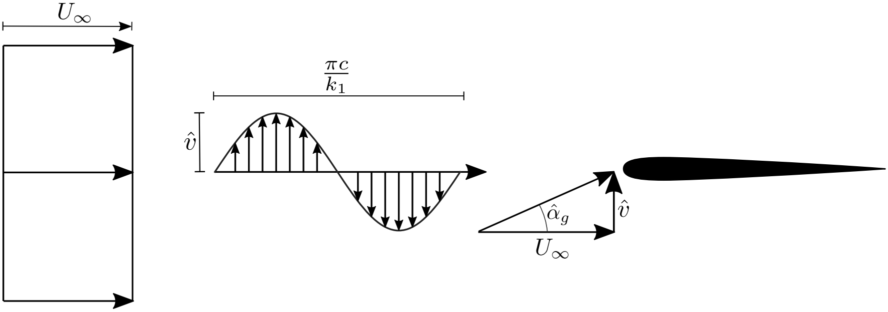

Figure 1.4: Inflow conditions according to Sears. Fluctuations in the normal velocity component $\hat{v}$ with reduced frequency k_1 impinge on the airfoil. The resulting angle of attack variations are represented by $\hat{\alpha}_g$. (Reprinted from Wei et al. (2019a), with permission of Cambridge University Press. © 2019 Cambridge University Press.)

compute k, the wavelength of the inflow perturbation is used to compute k_1. The superposition of the vertical perturbation with the free stream velocity U_∞ produces a fluctuation of the effective inflow angle on the airfoil, which is denoted as gust angle amplitude $\hat{\alpha}_g$ for gust encounter scenarios. This is illustrated by the inflow velocities shown as vectors on the leading edge of the airfoil in Fig. 1.4.

While the Sears function is restricted by its derivation to flows in which the assumptions of thin airfoil theory and potential flow hold, it is nevertheless attractive because of its simplicity: it only depends on the reduced frequency of the incoming gust and is mathematically straightforward. In addition to being widely used to predict unsteady loads in gust-response problems, the Sears function has also enjoyed broader applicability across research areas ranging from active flow control (e.g. Zhao et al., 2016) to aeroacoustics (e.g. Wang & Gursul, 2017).

The Sears function was extended by Goldstein & Atassi (1976) and Atassi (1984) using second-order models to account for the distortion of the gust and flow field due to the presence of the airfoil. This allowed the effects of airfoil camber and mean angle of attack to be incorporated. In the process, the possibility of accounting for fluctuations in the streamwise as well as in the flow-normal velocity was introduced.

The additional fluctuation in the streamwise direction $\hat{u}$, with the reduced frequency k_2 is illustrated in Fig. 1.5. Here, $\hat{u}$ is added to U_∞ and determines $\hat{\alpha}_g$ in conjunction with $\hat{v}$, which is illustrated by the inflow conditions on the leading edge of the airfoil. The additional streamwise velocity fluctuation is coupled to the vertical fluctuation in the Atassi function, which will be further evaluated below.

The second-order model introduced by Goldstein & Atassi (1976) and Atassi (1984) will be referred to as the Atassi function. Greenberg (1947) also developed a model involving fluctuations in the streamwise velocity as well as harmonic oscillations of the airfoil, in which the free stream velocity pulsated in a sinusoidal manner. These streamwise fluctuations are different from those imposed by Atassi, and are particularly relevant to rotorcraft (cf. Leishman, 2017). Lysak et al. (2013) developed a correction for the Sears function that takes effect at high reduced frequencies ($k > 1$), and Massaro &

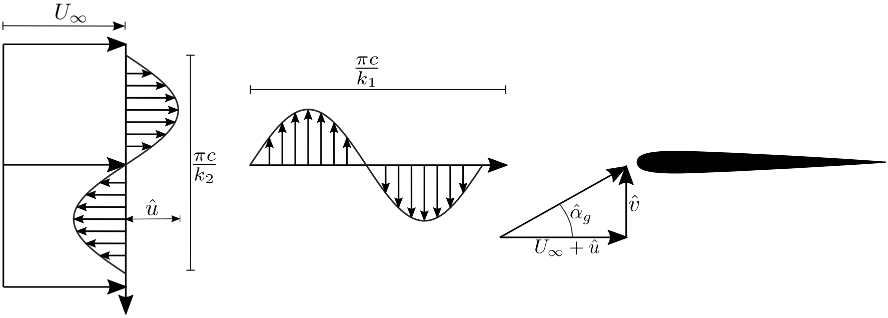

Figure 1.5: Inflow conditions according to Atassi. In addition to the normal-velocity fluctuations from the Sears problem, streamwise-velocity fluctuations with amplitude $\hat{u}$ and reduced frequency k_2 are also present. This extra gust profile is mathematically coupled with the Sears-problem gust. (Reprinted from Wei et al. (2019a), with permission of Cambridge University Press. © 2019 Cambridge University Press.)

Graham (2015) derived an additional correction for three-dimensional effects as a function of aspect ratio. It is worth noting that these analytical extensions do not deviate from the Sears function itself under its original assumptions and flow conditions.

Despite its age, applicability and adaptability, the Sears function has not been extensively validated in experiments, due in part to the difficulty of creating repeatable sinusoidal gusts in the vertical velocity component only. Early attempts, such as that of Hakkinen & Richardson (1957), proved inconclusive because of limitations in measurement technology. Commerford & Carta (1974) tested the function on a thin plate at only a single reduced frequency ($k = 3.9$), and found significant deviation from the Sears prediction. In contrast, Jancauskas & Melbourne (1986) used two controlled-circulation airfoils to produce single frequency sinusoidal gusts over a range of reduced frequencies up to $k = 0.37$, and found excellent agreement with the Sears function when a NACA 0006 airfoil was used as the test profile. Until recently, this was the only study reported in literature to use single frequency sinusoidal gusts to test the Sears function experimentally. Sankaran & Jancauskas (1992) showed that the Sears function could also be reproduced using a spectral decomposition of the force signal to isolate various reduced frequencies within multimodal gusts, such as those occurring in the flow behind a turbulence-generating screen. This spectral approach was used by Larose (1999) and Hatanaka & Tanaka (2002), who both observed significant deviation from the Sears function when cross-sectional profiles of various bridge decks were employed as the test profile. The latter study reproduced the general trend of the Sears function in experiments with a NACA 0012 airfoil. More recently, Lysak et al. (2016) were able to verify their thickness correction model for a range of airfoils using the same kind of measurement technique.

The Sears function has its roots in potential flow theory and therefore the use of turbulent wind tunnel flows to verify the theory creates ambiguities when comparing the inflow conditions to the original conditions of the theory. These ambiguities affect the applicability of the Sears function: Jancauskas & Melbourne (1983) showed that increasing the background turbulence of the incoming gust flow could improve experimental correspondence with the Sears function on bridge-deck profiles that deviated significantly from theory under more laminar conditions. To clarify this, Cordes et al. (2017) returned to the generation of single frequency sinusoidal gusts in order to test whether the Sears function would hold for a Clark-Y airfoil. In contrast with what one might expect from the results of Lysak et al. (2016), a trend opposite to that of Sears was found, which matched instead the trend of the Atassi function. This difference was attributed to the distortion of the flow field due to airfoil angle of attack and camber that is modeled by Atassi but not by Sears. However, numerical simulations of the experimental apparatus by Wegt (2017) showed that the active grid used to generate sinusoidal gusts for the experiments produced highly three-dimensional flows and that the relative strength of the gusts were not constant over the range of tested reduced frequencies. This has been subsequently confirmed in experiments by Traphan et al. (2018). Thus, while the results of Cordes et al. (2017) show that there are differences between the Sears and Atassi functions that delineate where each can be applied, these differences remain ambiguous as to whether they stem from the choice of airfoil or the inflow conditions themselves.

In order to determine more precisely the conditions under which these analytical transfer functions can be applied in real-world flow situations, it is necessary to disentangle the differences between the Sears and Atassi functions, both in their formulation and in their correspondence with experimental data.

Periodic Gust Generation

The generation of well-defined periodic flow disturbances in a laboratory environment is a critical requirement for experiments involving unsteady aerodynamics, aircraft control, gust disturbances, unsteady sensor calibration, and many other applications. For investigations concerned with aerodynamic transfer functions, the generation of distinct inflow fluctuations is elementary for the validity, significance and applicability of findings in respect to inflow conditions prescribed by the respective analytical function. Modeling a periodic disturbance in simulations is comparatively easy: one must only specify a fluctuating velocity as an inflow condition, and the effects of the resulting flow can be studied directly, assuming that the correct boundary conditions for the outlet of the domain and for the surface of the test object are imposed. These can be treated in various ways, depending on the type of solver employed and the nature of the problem being studied (e.g. Ekaterinaris & Platzer, 1998; Visbal, 2011). However, in experiments, generating the desired inflow conditions can be significantly more difficult. For example, gust disturbances of uniform character can be created from the turbulent fluctuations shed behind a passive grid (e.g. Lysak et al., 2016). Also, active grids have demonstrated the ability to control the intensity and structure of turbulence in experimental settings (cf. Makita, 1991; Cekli & van de Water, 2010; Knebel et al., 2011; Griffin et al., 2019, etc.) These methods generate gust disturbances over a continuous spectrum. In many cases however, it is desirable to produce disturbances at a single frequency. For example, a number of methods exist for generating vortical structures at a given frequency. Vortex shedding behind large cylinders or pylons yields periodic fluctuations in velocity that can be used in experiments (cf. Larose, 1999), though a precise determination of the shedding frequency can be difficult. The vortices shed by an impulsively plunging plate can also be used to represent gust disturbances (Hufstedler & McKeon, 2019).

Nevertheless, for numerous applications, a sinusoidal gust is required. Sinusoidal gusts are also useful for tests of aircraft dynamics and controls, in which a series of well-defined, single frequency disturbance input allows the frequency response of the system to be established (Bennett & Gilman, 1966). The calibration of pressure transducers for unsteady conditions may also be achieved using a smooth, sinusoidal velocity signal.

The usefulness of sinusoidal gust disturbances in experimental investigations has led to the development of several methods of generating them. One of the earliest and simplest generators, constructed by Hakkinen & Richardson (1957), involved a plunging plate in a wind tunnel. The apparatus was used in an attempt to experimentally validate the Sears function, but proved unsatisfactory due to sensor noise. Subsequent gust generation systems, possibly inferring that a single actuated plate was not sufficient for producing well-defined gusts, became increasingly complex. Bennett & Gilman (1966) used four plates, mounted in pairs on the walls of a wind tunnel and actuated together by a series of linkages, to produce sinusoidal gusts for experiments with scale models of aircraft. Ham et al. (1974) and Jancauskas & Melbourne (1986) generated gusts using a pair of controlled-circulation airfoils. The concept was extended by Tang et al. (1996) in an array of four such airfoils. Approaches using arrays of six or more vanes (e.g. Saddington et al., 2015; Cordes et al., 2017; Wei et al., 2019a) have been tested, though the wakes of the vanes tend to introduce turbulent fluctuations into the downstream flow conditions. Simpler generation mechanisms involving two pitching plates (e.g. Lancelot et al., 2015; Wood et al., 2017) avoid wake effects by construction, but tend to be limited in both the amplitude of the gusts produced and reduced frequency they can achieve. However, this design has been proven to be effective in transonic wind tunnels (Brion et al., 2015). Notably, in none of the aforementioned studies is the precise character of the gust disturbance analyzed or controlled; a periodically fluctuating velocity component with alternating peaks and troughs is typically deemed sufficiently sinusoidal. Alternatively, a single pitching airfoil has been demonstrated in many contexts to be sufficient for generating vortical gust disturbances, where smooth, sinusoidal disturbances are not required and wake effects do not need to be controlled (Klein et al., 2014, 2017).

The question of generating well-defined gusts using a single oscillating plate or foil should not be resolved by mere convention or consensus, especially since there are several advantages to such an apparatus for experiments. A single foil produces far less blockage in a wind tunnel than more complicated gust generation devices. The actuation is also far simpler and less costly, and facilitates operation, maintenance and removal. Lastly, the simple actuation mechanism of the airfoil means that the parameter space that must be traversed in order to characterize the gust generator is significantly smaller than that of multi-vane devices or active grids, for example.

1.2.2 Leading Edge Vortex Characteristics & Manipulation

The second unsteady aerodynamic scenario considered in this thesis is the manipulation of the leading edge vortex (LEV) with a dielectric barrier discharge plasma actuator (DBD-PA). Here, LEVs on unsteady airfoils are examined, although they can also arise on airfoils during gust encounter. The LEV emerges when the effective inflow angle on the airfoil α_{eff} changes rapidly and significantly, according to the dynamic stall phenomena and the deep stall regime. Inflow conditions experienced on a pitching and plunging airfoil are illustrated in Fig. 1.6. The superposition of the plunging velocity of the airfoil $\dot{h}$ and the free stream velocity U_∞ determine the effective inflow velocity U_{eff} on the airfoil. The geometric angle of attack, denoted in Fig. 1.6 as α, and the induced angle of attack due to the plunging motion, determine the effective inflow angle α_{eff} experienced by the airfoil. Despite similar

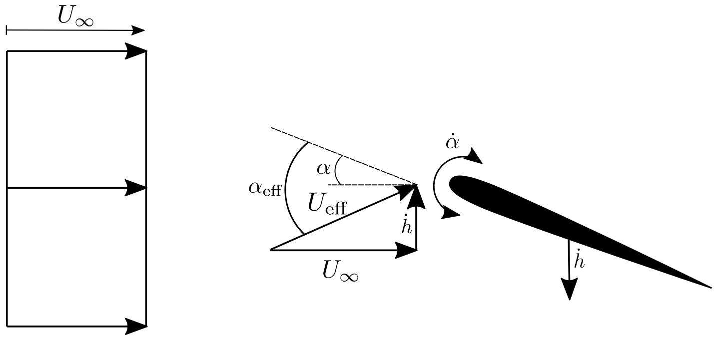

Figure 1.6: Inflow conditions on a pitching and plunging airfoil. The inflow is from the left with U_∞. The airfoil plunges with the velocity $\dot{h}$ and pitches with the angular velocity $\dot{\alpha}$. The superposition of all inflow contributions yields the effective inflow velocity U_{eff} under the effective inflow angle α_{eff}.

effective inflow conditions on the airfoil with respect to a gust encounter, the airfoil experiences the same inflow changes over its entire chord line. Transfer functions for gust encounters do not account for such simultaneous changes.

The following paragraphs will address the occurrence and effects of LEVs in biological flight before LEV detachment mechanisms, known from literature, will be introduced. Based on these fundamentals a literature review of experimental and numerical flow control studies targeting dynamic stall scenarios with LEVs will be given. A brief introduction of DBD-PAs as flow control devices will conclude this section.

Leading Edge Vortices in Biological Flight

Biological propulsion based on flapping wings offers unique advantages in lift and manoeuvrability at low flight Reynolds numbers *Re*. Both features are essential to increase the performance and efficiency of micro-air vehicles (MAV) and energy harvesting devices or to enhance their gust tolerance. Flapping flight aerodynamics are dominated by the leading edge vortex (LEV), which grows on a wing when the effective inflow angle changes rapidly and significantly. The LEV forms by a roll-up of the separated leading edge shear layer, caused by an adverse pressure gradient at the leading edge. The emergence of the LEV and its effects on aerodynamic forces on the airfoil constitute the dynamic stall phenomena, as discussed by Carr (1988). Formation and subsequent growth of the LEV induces increased transient lift. This induced lift drops when the vortex detaches, which is accompanied by a large nose-down pitching moment. The increased overall lift during LEV growth and the lift drop during its detachment can be explained considering finite-domain impulse theory, which allows to disentangle lift force contributions on an unsteady airfoil. Based on a lift formulation derived from this theory, Siala & Liburdy (2019) were able to identify the center convection rate of the LEV and its circulation accumulation rate as governing contributors to the overall measured lift on a pitching and plunging flat plate in deep dynamic stall. Similarly, Kriegseis & Rival (2014) and Wang et al. (2013) found that a positive circulation accumulation rate of the LEV contributed favorably to the overall lift, while an increased center convection rate reduced lift. It is known that insects gain higher transient lift at low Reynolds numbers with an attached LEV (cf. Dickinson et al., 1999; Ellington et al., 1996) and that this higher lift is prolonged with the aid of active feedback control to keep the vortex attached to their wings (Ristroph et al., 2010).

In terms of dimensionless parameters, hovering insects and birds in cruise flight were found to execute wing kinematics at a chord based Reynolds number

$$Re = \frac{U_\infty c}{\nu} \tag{1.2}$$

of the order of $10^3 - 10^4$, where U_∞ is the free-stream velocity, c the airfoil chord and ν is the kinematic viscosity (cf. Ellington, 1984). The Strouhal number

$$St = \frac{2fh_0}{U_\infty}, \tag{1.3}$$

where f is the plunging frequency and h_0 the plunging amplitude, varies between 0.2 and 0.4 for efficient propulsion, while the reduced frequency k is optimized according to the respective St and the wing planform area (cf. Triantafyllou et al., 1993; Nudds et al., 2004, etc.) MAVs are designed for a wide range of Re from 0 up to 60,000, a higher k between 0.146 and 1.2 and lower St up to 0.07, compared to biological flapping flight, due to the high inertial loads of moving wings (cf. Jones & Babinsky, 2010; Jones & Platzer, 2001; de Croon et al., 2015).

Leading Edge Vortex Detachment

When aiming at higher overall lift on flapping wings by delaying the LEV detachment with flow control, the vortex detachment process has to first be sufficiently understood.

Rival et al. (2014) found the chord length c to be the characteristic length scale for vortex detachment on a plunging flat plate with different leading edge geometries and a NACA 0012 airfoil. By consideration of the flow topology, following concepts introduced by Foss (2004), they found that the LEV induced lift on the airfoil drops when fluid begins to recirculate around the trailing edge. An early stage of the flow topology during the LEV growth phase on an unsteady flat plate is depicted in Fig. 1.7. Here, the LEV is

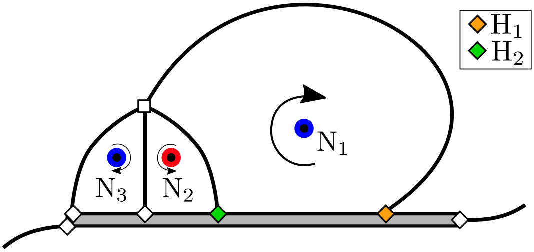

Figure 1.7: Topological sketch of the flow field around a pitching and plunging flat plate with a leading edge vortex (LEV), denoted as node N_1, growing on the airfoil. Nodes are indicated by circles, a full-saddle by a square and half-saddles by diamonds. Secondary vortices, also termed secondary structures, are highlighted as nodes N_2 and N_3. (Reprinted from Kissing et al. (2020c). © 2020 by American Physical Society.)

denoted as node N_1. Recirculation is initiated when the rear stagnation point behind the LEV on the airfoil surface, denoted as H_1 and marked by a orange diamond in Fig. 1.7, travels beyond the trailing edge. The recirculated fluid is entrained between the vortex and airfoil, and finally feeds secondary vortices (nodes N_2 and N_3) ahead of the main vortex, which grow and interrupt the LEV from its feeding shear layer.

Nevertheless, Sattari et al. (2012) found in a generic experiment that a two-dimensional starting vortex produced by a DBD-PA on the rear edge of a plate detaches from its feeding shear layer in absence of any geometric length scale. This suggests that vortex detachment can occur independent of any length scale. Likewise, Widmann & Tropea (2015) found that for a pitching and plunging flat plate at intermediate Re and a higher k, in combination with a large effective angle of attack amplitude $\hat{\alpha}_{\mathrm{eff}}$, the LEV stops accumulating circulation before the rear stagnation point behind the vortex reaches the trailing edge. They conclude that c is not the defining length scale for the investigated experimental parameters.

Instead, a viscous response of the boundary layer between the LEV and the airfoil is identified to cause an abrupt eruption of surface fluid that initiates the growth of secondary vortices ahead of the main vortex. In this detachment scenario, secondary vortices, also referred to as secondary structures, grow and cut off the LEV from its feeding shear layer. From a topological point of view, growing secondary structures (nodes N_2 and N_3 in Fig. 1.7) cause their rear confining stagnation point H_2, marked as a green diamond in in Fig. 1.7, to travel downstream. When secondary vortices N_2 and N_3 grow, vorticity carrying fluid from the leading edge shear layer is redirected into N_3 and does no reach the main LEV N_1 anymore. This, in turn, causes the main LEV to detach. They term this locally initiated detachment mechanism 'boundary-layer eruption', which adopts the terminology used by Doligalski et al. (1994). To distinguish between both detachment mechanisms, Widmann & Tropea (2015) develop the so-called covering ratio κ:

$$\kappa \approx \sqrt{2.4 \cdot 2} c^{-0.5} k^{-0.5} \nu^{0.25} a_0^{-0.25} U_\infty^{-0.25}, \tag{1.4}$$

where a_0 represents a shape parameter describing the curvature of the leading edge shear layer. Based on empirical observation of the transition between detachment mechanisms a threshold for the transition between mechanisms, termed κ_{trans} , is also given. The 'boundary-layer eruption' detachment, which takes place without recirculation of fluid around the trailing edge, was also observed by Wojcik & Buchholz (2014) and Akkala & Buchholz (2017) for a LEV on a plunging flat plate at high k between 1 and 2.

To date there are no analytical models available which describe the temporal or spatial occurrence of either detachment mechanisms. To determine actuation location and timing for future flow control approaches, both aspects have to be addressed for an effective and efficient manipulation.

Leading Edge Vortex Manipulation

To exploit beneficial LEV lift effects further for MAVs or energy harvesting devices, manipulation of the LEV is a frequently considered approach (cf. Eldredge & Jones, 2019). Numerous studies attempt to trap vortices on steady airfoils with the aid of passive or active flow manipulation. Potential flow analysis of a trapped vortex on a steady airfoil using a leading edge flap and suction by Rossow (1978) indicated an order of magnitude higher lift potential (also denoted as super lift). The experimental feasibility of this approach was demonstrated by Riddle et al. (1999). A comprehensive review for flow control on steady delta wings, where similar lift enhancements can be achieved with various flow control devices, is given by Gursul et al. (2007).

Until the majority of flow control studies on unsteady airfoils, which use a plasma actuator for manipulation, aimed at a fast reattachment of the leading edge shear layer. However, considering other actuator principles, it was demonstrated that a pulsed combustion actuator can be used to alter the LEV characteristics and thus the lift evolution on a pitching NACA 4413 airfoil (cf. Woo & Glezer, 2010). By a combination of oscillatory suction and blowing on the leading edge of a pitching NACA 0015 profile and a trailing edge flap, an increase of the net lift was achieved while simultaneously reducing the nose-down pitching moment during LEV detachment (cf. Greenblatt & Wygnanski, 2001; Greenblatt et al., 2001). Permanent separation control, which aims at reattaching the leading edge shear layer, inevitably suppresses the LEV formation and thus high transient lift, which is reasonable if the vortex induced effects are intended to be mitigated to maintain structural integrity.

A multitude of flow control actuators have been used successfully for separation control. Examples include synthetic jets in Taylor & Amitay (2015), suction and blowing devices by Greenblatt & Wygnanski (2001) and plasma actuators by Post & Corke (2006). Plasma actuators have the advantage of being fast acting and very lightweight due to the absence of moving parts (cf. Cattafesta & Sheplak, 2011). Both features are especially important when considering highly dynamic wing motion and resulting inertial forces.

The objectives of plasma flow control to achieve favourable aerodynamic effects have been quite varied. Moreau (2007) distinguishes among the manipulation of the separation, the laminar-to-turbulent transition, and the turbulence manipulation. A review of separation control is given by Corke et al. (2010). Kriegseis et al. (2016) discuss the applicability and fluid mechanic efficiency of DBD plasma actuators for in-flight applications via consideration of the control authority of plasma actuators. They conclude that an efficient flow manipulation can be achieved more likely by targeting laminar-to-turbulent transition instead of separation control, due to the low momentum transfer of the actuator.

Closed-loop separation control with a plasma actuator at the leading edge of a pitching NACA 0012 airfoil was first tested by Lombardi et al. (2013). By adding momentum to the leading edge shear layer they achieved a faster reattachment of the shear layer during pitch up. The highest net lift increase was achieved when separation control was temporally disabled, such that a LEV could form. With the aid of pulsed plasma actuators on the leading edges of vertical axis wind turbine (VAWT) blades, Ben-Harav & Greenblatt (2016) and Greenblatt et al. (2014) were able to increase the turbine net power by ten percent. They conclude that this is also achieved by reattaching the leading edge shear layer more rapidly, and additionally, by an LEV that is closer to the blade surface.

So far flow control attempts of the leading edge vortex on unsteady airfoils were designed by implementing separation control from the leading edge. This approach inevitably suppresses the formation of the LEV, as demonstrated numerically by Visbal (1991), and does not target an exploitation of its beneficial effects in terms of transient lift, as observed in biological flight.

1.3 Objectives and Outline of the Thesis

The overall scope of this thesis is to provide the basis for future performance and efficiency enhancements of applications dominated by unsteady aerodynamics. Periodic gust encounter of airfoils and the manipulation of the leading edge vortex growth on a pitching and plunging airfoil with the aid of plasma actuators are chosen to demonstrate the development of different performance enhancement approaches. Consequently, objectives and the structure of this thesis are differentiated according to which scenario is considered. The structure of this thesis is depicted in Fig. 1.8.

Facilities used to obtain experimental results and data processing strategies will be introduced and evaluated in **Chapter 2**.

Periodic Gust Encounter
Analytical formulations, which allow the prediction of unsteady loads, are provided by transfer functions. The first part of this thesis is devoted to the theoretical and experimental validation of aerodynamic transfer functions, addressed in **Chapter 3**.

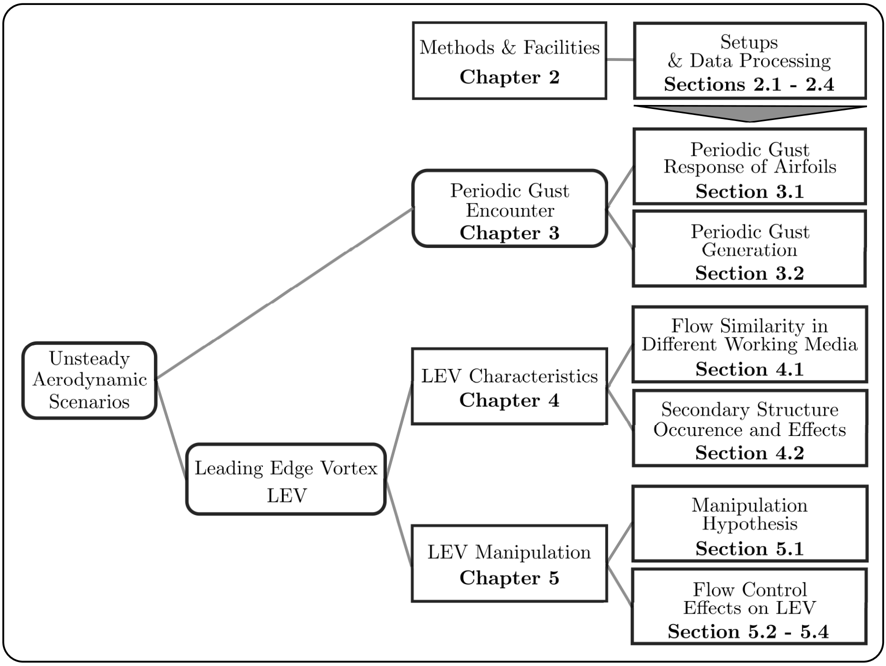

Figure 1.8: Outline of the thesis with the two considered unsteady aerodynamic scenarios (rounded boxes) and corresponding investigations.

Previously encountered deviations of measurement results from the Sears function and an agreement with the Atassi formulation (Cordes et al., 2017) will be further examined in **section 3.1**. Here, both transfer functions are experimentally validated in a wind tunnel at the University of Oldenburg, which is equipped with an active grid for gust generation. Based on a careful consideration of inflow assumptions of the respective formulations, these conditions are reproduced with the aid of the active grid to finally validate transfer functions. Theoretical considerations and experimental validation results are also elucidated in Wei et al. (2019a).

Insights gained from the evaluation of transfer functions regarding the influence of inflow conditions and encountered challenges in the production of the desired conditions motivated the development of a simple method for gust generation, presented in **section 3.2**. This method uses a single airfoil with kinematics optimized using another transfer function introduced by Theodorsen (1934). Respective considerations and results are also published in Wei et al. (2019b).

Leading Edge Vortex Characteristics and Manipulation

The introduction of a flow control approach to exploit beneficial lift effects of the LEV more extensively is the overall scope of the second part of this thesis, addressed in **Chapters 4 and 5**. A prolongation of the LEV growth period and increased net lift is expected to be achieved by delaying the vortex detachment process. The manipulation hypothesis introduced in this thesis focuses on the suppression of the boundary-layer eruption detachment mechanism (c.f. section 1.2.2), where secondary structures ahead of the main LEV cause its detachment. As a prelude to flow control, the occurrence of secondary structures is studied in **Chapter 4** to enable a precise design of flow control timing and location. Corresponding investigations make use of two facilities, a wind tunnel at TU Darmstadt (Germany) and a water tunnel at the Beihang University (China) to extend the attainable parameter range. To allow results from each facility to be compared, an approach to establish comparability will be presented in **section 4.1**. The occurrence of secondary structures and their effect on the LEV detachment is investigated by a combination of Eulerian and Lagrangian methods, presented in **section 4.2**. Comparability aspects and insights into the occurrence and effects of secondary structures are also discussed in Kissing et al. (2020a) an Kissing et al. (2020b).

Lessons learned from the in-depth study of secondary structures are then used to develop and parameterize a manipulation hypothesis in **Chapter 5**, which is also experimentally validated. The developed approach adapts the biological principle of an enhanced LEV induced lift instead of suppressing the vortex by separation control, and was first proposed by Kütemeier et al. (2019). The body force induced by a dielectric barrier discharge plasma actuator (DBD-PA) applied at topological critical locations will be utilized to achieve a prolonged LEV growth phase, which is discussed in **section 5.1**. After a validation of the feasibility and effectiveness of the manipulation hypothesis on a pitching and plunging flat plate in **section 5.2**, its robustness is also tested in **section 5.3**. Therefore, different motions kinematics of the flat plate and complementary tests on a NACA 0012 airfoil are evaluated. In order to enhance the efficiency of plasma flow control, temporal and spatial aspects of the actuators control authority are utilized to derive and test the minimum effective actuation period in **section 5.4**. The development of the manipulation hypothesis and its validation is also presented in Kissing et al. (2020c).

In **Chapter 6** conclusions regarding the potential efficiency enhancement approaches will be drawn for both scenarios and an outlook for future research will be given.

2 Methods and Facilities

In this chapter experimental facilities, measurement systems, numerical setups and data processing strategies utilized to obtain results for the two considered aerodynamic scenarios will be introduced. The experimental and numerical setups established for the investigations of periodic gust response of airfoils are introduced in section 2.1. The wind tunnel, airfoil motion apparatus and PIV measurement setup, along with the relevant post-processing considerations used for the optimization of gust generation at TU Darmstadt are introduced in section 2.2. Investigations of LEV characteristics, associated with the second aerodynamic scenario, were conducted at TU Darmstadt with the same facilities used for gust generation optimization. Preliminary studies for these investigations are presented in section 2.3. They address the two-dimensionality of the flow field around pitching and plunging airfoils and additional data processing approaches related to the determination of LEV circulation and size and Lagrangian coherent structures. Finally, the extension of the setup for LEV manipulation by a DBD plasma actuator is introduced in section 2.4. This encloses a brief recap of the plasma actuator working principle and structure as well as its integration into the experimental facility. Parts of this chapter have been published in Wei et al. (2019a,b) and Kissing et al. (2020a,b,c)

2.1 Periodic Gust Response Setup

Investigations of lift response of airfoils encountering periodic inflow conditions in section 3.1 of Chapter 3 use a wind tunnel equipped with an active grid at the University of Oldenburg, which will be introduced below. Hot-wire and PIV measurement systems, used to characterise transient inflow conditions on the airfoil, will be presented along with the force measurement system for transient lift determination. Finally, the setup for complementary numerical investigations using an Unsteady Reynolds-Averaged Navier-Stokes (RANS) framework will be introduced.

Wind Tunnel and Active Grid

The experiments were carried out in a closed-circuit wind tunnel at the University of Oldenburg, details of which are given in Knebel et al. (2011). The test section had a cross-section of 1.00 × 0.80 m. An active grid was installed in the tunnel at the front of the test section, 1.1 m upstream from the quarter-chord point of the airfoil. It comprised nine 3D-printed vanes, each with a NACA 0016 airfoil with $c_1 = 71$ mm chord and 0.8 m span. The turbulence intensity in the middle of the tunnel, measured using a hot-wire anemometer, was less than 0.3 %. The vanes were pitched about their quarter-chord point with a sinusoidal signal. Details of the motion protocols employed in this study are given below in section 3.1.2. A schematic of the wind tunnel and active grid is shown in Fig. 2.1.

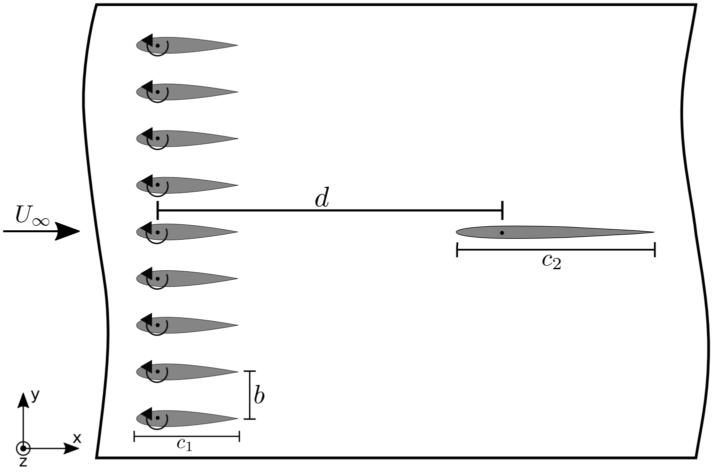

Figure 2.1: Schematic showing the setup of the wind tunnel and active grid (not to scale). The distance between the grid and the quarter-chord point of the test airfoil is $d = 1.1\,\mathrm{m}$. The vanes of the active grid have a chord length of $c_1 = 71\,\mathrm{mm}$. (Reprinted from Wei et al. (2019a), with permission of Cambridge University Press. © 2019 Cambridge University Press.)

A NACA 0006 airfoil with a chord of $c_2 = 202$ mm and 800 mm span was constructed at the TU Darmstadt and served as a test airfoil. It was composed of two carbon-fiber shells attached to an aluminum spine, such that the airfoil was both smooth and rigid against torsion. This profile was selected to conform to the thin airfoil assumption of Sears, based on predictions from the XFOIL software (cf. Drela, 1989) for the range of angles of attack the airfoil could encounter without incurring flow separation. A thin strip of fluorescent foil at the location of the laser sheet reduced surface reflections when PIV measurements were performed.

Hot-Wire Measurements

To obtain empirical relations between the grid amplitude $\hat{\theta}$ and gust-angle amplitude $\hat{\alpha}_\mathrm{g}$ over the range of experimental flow conditions, as well as estimates for the Atassi gust parameters ϵ and k_2, a large parameter space of grid amplitudes and reduced frequencies was tested for two distinct grid configurations (detailed in section 3.1.2). Data were collected using a CTA (Constant Temperature Anemometer) system from *DANTEC DYNAMICS*, consisting of a *Stream Line Automatic Calibrator* for X-wire calibration, a *StreamLine* frame with two CTA modules, a 6 mm short support of type *55H24* and an X-wire of type *55P51*.

During the characterization of the inflow the calibrated X-wire was placed at the centerline of the empty wind tunnel at the intended leading edge position of the airfoil, 1 m downstream of the active grid. For each frequency and amplitude 40,000 values were taken at a sampling frequency of 20 kHz resulting in a duration of 2 s per grid protocol.

To cover the broad range of possible reduced frequencies and gust amplitudes, the grid was characterized for frequencies from 1 Hz to 10 Hz with grid amplitudes from 2.5 ° up to 20 ° for free stream velocities between 15 m/s and 25 m/s.

Force Measurements

A pair of K3D120 3-axis force balances and a TS110 moment sensor from *ME-Messsysteme* allowed forces and moments to be measured at the airfoil quarter-chord point. Thirty seconds of force data were collected for each measurement. All measurements, including measurements with the PIV system, were started simultaneously via a trigger provided two seconds after the active-grid protocol was started.

Particle Image Velocimetry (PIV) Setup

To investigate the spatial and temporal structures occurring in the flow, PIV measurements were performed. The PIV setup was a stereoscopic configuration from *LaVision*, composed of two *Phantom Miro 320S* high-speed cameras operated at a frame rate of 500 Hz. This reduced temporal resolution and a RAM size of the cameras of 12 GB enabled a total measurement time of 5.5 s. The cameras were mounted above and below the test section. A *Litron LDY-303HE* Nd:YLF dual-cavity high-speed pulsed laser illuminated the suction side of the airfoil from the rear of the tunnel. Images were recorded and evaluated with *LaVision's DaVis 8.4* software with 16×16 pixel interrogation areas, 50 % overlap, and outlier interpolation.

Numerical Setup

Numerical simulations of the flow field in the wind tunnel were performed with the aim of complementing the experimental measurements. Two configurations were studied, corresponding to two different inflow conditions. The first configuration corresponded to conditions specified by Sears (see Fig. 1.4) and simulated the flow past a NACA 0006 airfoil with chord length $c_2 = 0.2\,\mathrm{m}$. The second simulation involved only the nine oscillatory vanes without an airfoil model and intended to reproduce the tunnel unsteadiness as encountered in the experiments (see Fig. 1.5).

The computations were performed within the Unsteady RANS (Reynolds-Averaged Navier-Stokes) computational framework employing the baseline and eddy-resolving versions of the near-wall Reynolds-stress-model, RSM, by Jakirlic & Hanjalic (2002). The model is capable of asymptotically capturing both the strengthened viscosity effects and the kinematic wall blocking. The latter model property is expressed in terms of both Reynolds-stress and stress-dissipation anisotropy coping with correct asymptotic behavior of all turbulence quantities when approaching the wall. Unlike the baseline model, its eddy-resolving formulation (denoted by Improved Instability-Sensitive

RSM - IISRSM) is capable of resolving the fluctuating turbulence. This model feature, created in line with the Scale-Adaptive Simulation (SAS) methodology proposed originally by Menter & Egorov (2010) and in conjunction with their $k-\omega$ SST eddy-viscosity model of turbulence, is achieved by suppressing the modelled turbulence towards a corresponding sub-scale level. The characteristic size of the unresolved sub-scale turbulent eddies is proportional to the von Karman length scale (comprising the second derivative of the velocity field: $\nabla^2 U$), which mimics, analogous to the grid-spacing Δ in LES (Large-Eddy Simulation), the relevant length-scale of the SAS-related residual turbulence. The turbulence suppression in the SAS modelling framework is achieved by introducing an additional production term (P_{SAS}) into the scale-supplying equation governing the ω-quantity (with $\omega \propto \varepsilon/k$ representing inverse turbulent time scale). Herewith, an appropriate enhancement of the turbulence activity originating from the resolved motion, especially within the shear layer regions, is ensured; interested readers are referred to Jakirlić & Maduta (2015) and Maduta et al. (2017) for more details.

The model equations are implemented into the open source toolbox OpenFOAM®, used for all simulations. The code employs a finite-volume discretisation method based on the integral form of the general conservation law applied in conjunction with block-structured grid arrangements. The flow domains considered are meshed by the OpenFOAM® relevant utility denoted as "blockMesh". The temporal resolution adopted guarantees a Courant number smaller than one in the entire solution domain. The discretisation of the convection terms is achieved using a blended central differencing scheme implemented in the differed-correction approach manner. This methodology is considered adequate in view with regard to the fine grid used in the regions with high gradients.

The first computational setup is concerned with the flow past a NACA 0006 airfoil. The inflow cross-section is positioned immediately downstream of the active grid. The incoming gusty flow conditions are represented by a time-dependent sinusoidal velocity condition at the inlet (compare with Fig. 1.4). The two-dimensional solution domain (not shown here) with the inflow plane located at 1.1 m upstream of the test airfoil quarter-chord point (Fig. 2.1) and the outlet plane located at 1.5 m downstream of the airfoil quarter-chord point, is meshed with 59,300 hexahedral grid cells. The grid is squeezed with an adequate grading towards the airfoil surface. The governing equations are integrated to the walls; the wall-adjacent computational node at the airfoil is situated deep within the viscous sublayer, ensuring the value of the dimensionless wall distance $y^+ \leq 1$. Such a fine grid resolution is necessary for applying the exact wall boundary conditions, formulated in relation to the physically correct behavior of the mean flow and turbulent quantities. The upper and lower bounding of the solution domain is realized by symmetry planes positioned equidistantly at 0.5 m from the airfoil chord line. Application of the symmetry conditions is justified, as they do not influence the flow around the airfoil. These computations were performed employing the baseline RSM. The credibility of performing two-dimensional computations is based on the experience gained by computing the flow in the empty plenum (the second configuration). These results, obtained for both two-dimensional and three-dimensional computations, exhibit no noticeable difference (see Fig. 2.2 and associated discussion).

The second configuration deals with the entire plenum (accounting also for the plenum walls) without the NACA 0006 airfoil, but including the active grid consisting of nine symmetric airfoil-like vanes, (Fig. 2.3).

The corresponding inflow conditions are realized by the oscillatory motion of the vanes using a dynamic meshing utility. This utility is based on the so-called ‘space conservation law’, implying the conservation of the grid cell number during the oscillatory vane motion. Accordingly, an additional equation describing the conservation of space is solved simultaneously with the continuity and momentum equations as well as with equations governing the turbulence quantities. The length of the solution domain accommodating the nine vanes is 2.8 m (see Fig. 2.3), where the zero-gradient outflow boundary conditions were applied. The spanwise extent of the solution domain amounts to 50 % of the NACA 0006 airfoil chord. The fully hexahedral grid consisted of 112,736 cells in the central vertical plane. The three-dimensional computational domain was meshed by ten grid cells covering the spanwise extent leading to the total number of cells corresponding to 1,127,360.

Whereas the grid resolution at the plenum walls enables the use of exact boundary conditions, the grid resolution at the vane surface is somewhat coarser. Depending on the value of the wall-shear stress, the dimensionless wall

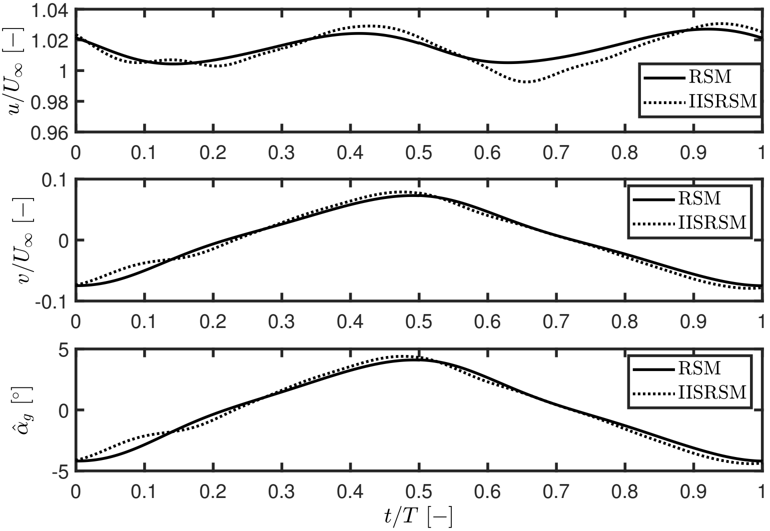

Figure 2.2: Computationally obtained time variation of the streamwise and normal component of the mean velocity field and gust angle amplitude by using baseline and eddy-resolving Reynolds stress models. (Reprinted from Wei et al. (2019a), with permission of Cambridge University Press. © 2019 Cambridge University Press.)

distance y^+ of the next-to-wall grid node can cover the entire boundary layer span from viscous sublayer and buffer transition zone up to the logarithmic region. Here, the so-called hybrid wall functions proposed originally by Popovac & Hanjalic (2007) are adopted and used in conjunction with a differential Reynolds stress model. This wall boundary condition, depending on the value of y^+, utilizes a functional blending between the exact boundary conditions corresponding to a fully-resolved boundary layer and the logarithmic law.

Both two-dimensional and three-dimensional computations were performed using the baseline RSM and its eddy-resolving counterpart. The flow conditions corresponding to wake regions generated by the active grid are characterized by intensive bulk flow unsteadiness indicating high turbulent activity. The results obtained by both turbulence models, illustrating the time variation of

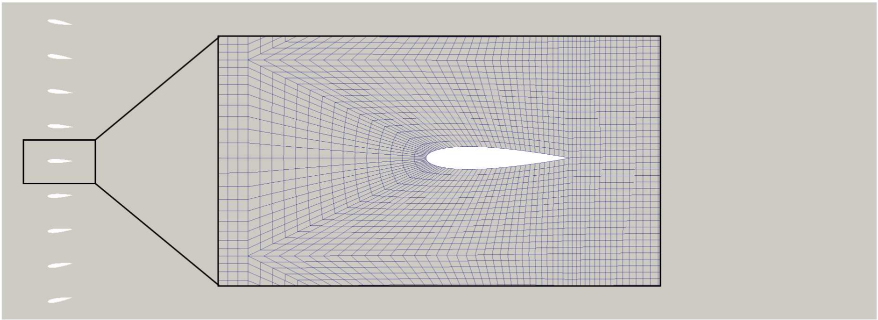

Figure 2.3: Computational domain accommodating the active grid and a blow-up of the numerical grid meshing the region immediately surrounding a vane. (Reprinted from Wei et al. (2019a), with permission of Cambridge University Press. © 2019 Cambridge University Press.)

the streamwise and vertical mean velocity components as well as the gust angle amplitude, are displayed in Fig. 2.2. The results show no significant difference between two-dimensional and three-dimensional computations. Accordingly, all consequent computations are performed two-dimensionally.

2.2 Periodic Gust Generation Setup

Facilities and methods used for the optimization of periodic gust generation with a single airfoil, discussed in section 3.2, will be introduced in this section.

Investigations of unsteady aerodynamic scenarios in this thesis focus on low *Re*, which require low wind speeds if the chord length of the airfoil cannot be reduced further. Corresponding adaptions of the open return wind tunnel at TU Darmstadt will be addressed below. To produce periodic gusts, a single NACA 0008 airfoil is pitched and plunged in the wind tunnel. The motion apparatus used to move the airfoil and corresponding operational procedures will be introduced in this section. Lastly, two PIV measurement setups for gust characterization are presented along with further data processing and analysis strategies. The entire setup used for gust generation is depicted in Fig. 2.4 in side and rear view. The side view in Fig. 2.4a shows the test section of the wind tunnel with the gust generation airfoil attached to two linear actuators. These allow arbitrary pitching and plunging kinematics of

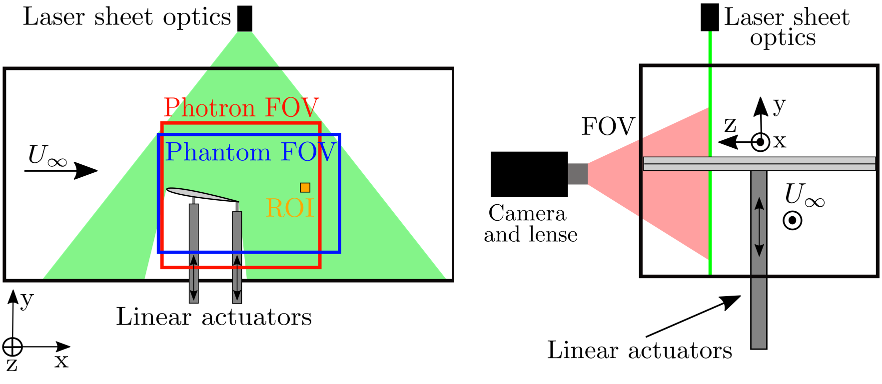

(a) (b)

Figure 2.4: Schematic of the experimental setup used to optimize gust generation: (a) side view, and (b) rear view. Fields of view of the two cameras are shown in (a). The region of interest (ROI) used to measure velocity and vorticity profiles is shown as an orange square in (a). (Reprinted from Wei et al. (2019b), with permission of Springer Nature. © 2019 Springer Nature.)

the airfoil. A laser light sheet illuminates the seeded flow field from the top for PIV measurements. The fields of view (FOVs) in which velocity information are acquired during two consecutive rounds of PIV measurements are also indicated.

The wind tunnel, airfoil motion apparatus and PIV setup for current experiments are also used to investigate the second transient aerodynamic scenario considered in this thesis, which is concerned with LEV characteristics and its manipulation.

2.2.1 Eiffel Wind Tunnel

Experiments for gust generation optimization were carried out in an open-return, Eiffel type wind tunnel at TU Darmstadt. This tunnel has a square test section with a side length of 0.45 m. Optical access from the side is provided by a removable glass plate that spans the length of the test section, as well as a window on the top of the test section through which the laser sheet for the PIV system is passed.

Since the air is sucked into the wind tunnel from outside, the flow velocity in the test section is susceptible to wind gusts. Additional environmental parameters like the air temperature and humidity, which affect the viscosity of the air, cannot be controlled and have to be considered when targeting flow field investigations at a certain chord based Reynolds number. With the aid of humidity and temperature sensors in the settling chamber of the wind tunnel the kinematic viscosity of the air is computed online and the wind speed corrected accordingly. The effect of temperature on dynamic viscosity is taken into account by implementation of the Sutherland (2009) formulation. The density of air, needed to compute the kinematic viscosity from the dynamic viscosity, is derived from the ideal gas law and partial pressures of air and vapour, where the latter is determined from the saturation vapour pressure and the current relative humidity.

The free stream velocity in the tunnel is controlled using a PID controller and an impeller anemometer of type *TS16/15GE-mc40A/125/p0/ZG1* from *Höntzsch GmbH* installed near the inlet of the test section. Its head axis is located at a depth of 50 mm from the wind tunnel wall. The impeller anemometer has an accuracy better than ± 0.5 % for the free stream velocity range investigated in this study (U_∞ = 2 - 6 m/s). To maintain the desired chord based Reynolds number during experiments, the free stream velocity is adapted by the PID controller, which accounts for viscosity changes of the air due to temperature and humidity changes and for gusts. The motion profile of the airfoil is adapted accordingly to maintain the desired k and St. In addition to the prescribed control measures, most experiments in the Eiffel wind tunnel were conducted during night time or at least after sunset and before sunrise to avoid significant temperature drift and accompanying thermals caused by sunlight.

The turbulence intensity in the test section is measured to be less than 2 % for all investigated free stream velocities (cf. Widmann & Tropea, 2015). More details on the wind tunnel and flow quality can be found in Rival et al. (2009a) and a detailed investigation of the flow quality at very low velocities in Widmann (2015).

2.2.2 Airfoil and Motion Apparatus

Airfoil

The test airfoil utilized for gust generation optimization is a symmetric NACA 0008 profile with a chord length of $c = 120\,\mathrm{mm}$ and a thickness of $\delta_a = 9.6\,\mathrm{mm}$. The airfoil is 3D-printed and reinforced in the spanwise direction with two carbon-fiber struts to inhibit elastic deformations. Two halves are printed, laminated in black foil to reduce reflections from the PIV laser light sheet, and attached to an aluminum mount, which is also laminated in black foil. The mount is located at half-span of the airfoil on its lower side.

Motion Apparatus

Pitch and plunge kinematics of the airfoil inside the wind tunnel are realised by two *LinMot PS01-48x240F-C* linear actuators. These are attached to the airfoil mount at two different chordwise locations. The downstream actuator is centered on the airfoil trailing edge and the upstream actuator at a distance of 6.3 mm. A schematic illustration of the actuators and the test airfoil is given in Fig. 2.4.

By execution of the same motion profiles on both linear actuators pure plunging motion is realised, while different motion profiles of the actuators allow combined pitching and plunging kinematics. Further details of the motion apparatus design can be found in Rival et al. (2009a) and Widmann & Tropea (2015).

The two linear actuators, which have a dynamic position accuracy of ± 0.1 mm, are controlled from a computer using the *LinMot-Talk* program and *E1100-GP-HC* controllers for drive communication. An external magnetic position sensor of type *MS01-1/D* is used to increase the dynamic accuracy of airfoil motion via a position feedback loop. Actuators are pre-loaded with sinusoidal motion profiles for each experiment according to the required pitch and plunge kinematics. Combined kinematics at frequencies of up to 10 Hz can be executed dependent on the plunge height. This increase of the dynamic motion range compared to previous studies (cf. Widmann, 2015) is achieved by implementation of an air cooling unit on each actuator. Careful cleaning of the actuator rods, maintenance of the position feedback system and regular lubrication increase the maximum frequency further.

Prior to each measurement campaign, all motion profiles are tested on the linear actuators without any airfoil. During this procedure, acceleration measurements are conducted to validate that actuators follow the desired motion profile accurately and without jitter. The procedure aims to exclude acceleration fluctuations from influencing the flow around the investigated airfoil. Details on the maintenance of actuators, acceleration measurements and position or acceleration deviations for different motion dynamics can be found in Triess (2018).

2.2.3 PIV Flow Field Measurements

To characterize produced gusts, two-dimensional flow fields in the wake of the gust generating airfoil are acquired using 2D2C time-resolved particle image velocimetry (PIV). The basic 2D2C PIV setup for gust optimization is also used to investigate the flow field and LEV on pitching and plunging airfoils in Chapters 4 and 5.

General PIV Setup and Image Correlation

Di-Ethyl-Hexyl-Sebacat (DEHS) seeding particles with a mean diameter of 0.5 - 1 μm were introduced into the settling chamber of the wind tunnel. Their response time τ_s was computed to be 2.7 μs according to Raffel et al. (2007). Compared to the minimum time scale of the flow, estimated by the convective time of the Kolmogorov length scale $\eta_K = c \times Re^{-3/4} \approx 60\,\mu$m with c as the macro-scale reference, $\tau_F = \eta_K / U_\infty = 20\,\mu$s, the response time is considered to be adequate.

The seeded flow field was illuminated using a dual cavity *Litron* DY-303 Nd:YLF laser with a nominal single pulse energy of 21 mJ (18 mJ available). The laser light sheet used for illumination was generated by cylindrical lenses mounted high above the test section, as depicted in Fig. 2.4, in order to provide as large a field of view as possible. It was positioned at the edge of the optical access window at the top of the test section, corresponding to a location of 20 % of the airfoil span from the midpoint. The location of the laser sheet is also shown in Fig. 2.4. Due to the high power of the laser, an additional strip of fluorescent foil was wrapped around the airfoil at the location of the laser sheet, to further reduce reflections in the images and to prevent the laser sheet from burning into the airfoil itself. A larger field of view was not possible, as the laser had to be operated at full power in the given configuration in order to sufficiently illuminate seeding particles in the flow.

Images were captured at a double-exposure repetition rate of 1 kHz using a high-speed camera. In the first round of experiments, a *Phantom* v 12.1 camera was used. Repairs on the lab *Photron* SA 1.1 camera were complete for the second round of experiments. A band-pass filter was applied with the *Photron* camera to further protect the camera sensor from reflections and to mitigate glare from reflections on the airfoil's surface. For both cameras, a *Zeiss* 50 mm lens was used. The approximate fields of view for both cameras are shown in Fig. 2.4b. The cameras were mounted on a traverse, and the scale was computed using a target placed in the laser sheet. The camera, laser cavities, and actuators were all controlled with an in-house *LabVIEW* script using a *National Instruments* PCI-6220 data-acquisition card. This allowed the measurements and data collection to be centrally synchronized using digital pulses. Further details on synchronization and timing aspects

Table 2.1: Camera and PIV processing parameters for gust generation experiments.

Property	Round 1	Round 2
Camera	Phantom v12.1	Photron SA1.1
Resolution (px)	1280 × 800	1024 × 1024
Scale (px/mm)	3.630	2.833
Frame-straddling interval Δt (μs)	400	450
Framerate (Hz)	2000	2000
Final interrogation window size (px)	32 × 32	16 × 16
Peak-finding algorithm	3 × 3 Gaussian fit	Whittaker reconstruction

of the cameras and laser cavities, which were operated in frame straddling mode, will be given below. Additional details regarding differences in the setup between the two rounds of experiments are given in table 2.1.

Image correlations were perfomed with *PIVview* 2C software from *PIVTEC GmbH* utilizing a multi-grid, multi-pass interrogation scheme including a sub-pixel routine. The interrogation window overlap was 50 %. Window sizes were selected so that, on average, about 10 particles could be found in each interrogation area (Tropea et al., 2007). Outliers were identified by a median test (cf. Westerweel & Scarano, 2005) in a 3×3 neighbourhood with a threshold of twice the velocity magnitude and found to be always less than 1.6 % of all computed vectors for all acquired image pairs.

Control, Timing and Synchronization

To allow flow fields from time-resolved PIV measurements to be related to the airfoil motion phase, multiple subsystems of the setup have to be controlled and synchronized precisely. All subsystems, computers (PCs) and corresponding components used for timing and synchronization in current investigations are depicted in Fig. 2.5. The wind tunnel speed is controlled using a PID controller. Both linear actuator drives are invoked via a NI-DAQ card.

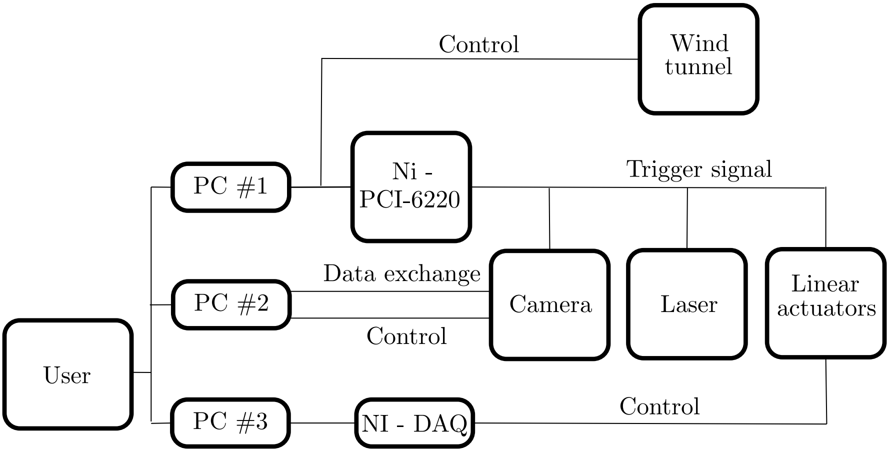

Figure 2.5: Wiring diagram of the synchronization, timing and control logic for modules used in the gust generation Setup, which includes a time-resolved PIV measurement setup.

To synchronize and trigger the motion of the gust generating airfoil with time resolved PIV measurements an in-house *LabVIEW* script is used. A *National Instruments* PCI-6220 digital I/O-card generates digital 5V TTL output signals from the script, which trigger the recording period and exposures of the camera, laser pulses of both cavities and the motion of linear actuators. This methodology is chosen since it allows internal clocks of each output channel of the I/O card to run synchronously on the same master clock. In this manner jitter effects and temporal lags between signals are reduced to a minimum. The trigger scheme is also illustrated in Fig. 2.5.

PIV measurements require a precise timing of the camera with the two laser cavities to ensure a distinct frame straddling interval Δt between laser pulses. Uncertainties in Δt directly increase the uncertainty of velocity measurements due to an imprecise temporal reference of the displacement obtained by cross-correlations. The camera receives an additional synchronization signal from the PCI-6220 I/O card for exposure synchronization according to a frame straddling approach. This frame straddling scheme is illustrated schematically in Fig. 2.6. The camera exposure is set as long as possible under the constraint of the framerate and an additional minimum shutter downtime of the camera.

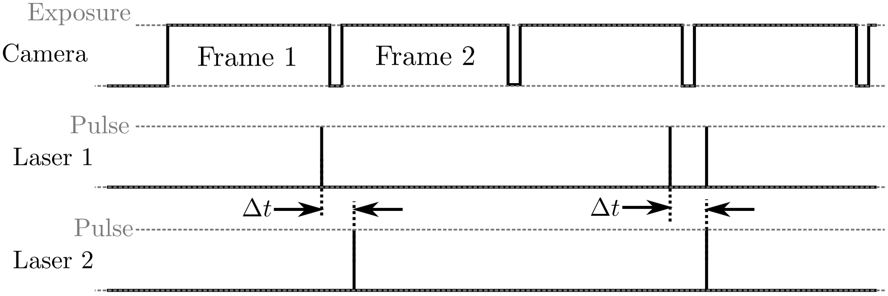

Figure 2.6: Frame straddling timing scheme used to synchronize and trigger the camera and lasers for time resolved PIV measurements.

Laser 1 is activated in the first frame of the camera (frame 1 in Fig. 2.6), shortly before the shutter closes and the frame ends. In the next frame (frame 2 in Fig. 2.6), laser 2 is activated shortly after exposure started. Note that laser 1 and 2 are set to the same frequency with a phase offset. So the seeded flow field is recorded in frame 1 and 2 with an inter-image frame straddling interval Δt.

Measurements of the maximum jitter and delay of all signals in the PIV setup yield a maximum deviation of signals below 9.6 ns.

2.2.4 Data Processing and Analysis

The location of interest within the flow field for gust generation experiments is a point one full chord length downstream of the trailing edge of the airfoil. This is selected with an eye towards future experiments: the experimental setup had been originally designed to study two oscillating airfoils in a tandem configuration (Rival et al., 2011), and the location of the leading edge of the downstream airfoil is 120 mm downstream of the trailing edge of the forward airfoil. Additionally, one chord length into the wake represents an intermediate distance at which the influences of neither transient effects nor viscous dissipation are significant. In future studies, it may be useful to investigate whether the results presented here also hold in the far-wake region. For most of the results in this thesis, a square box of length 15 mm within the measurement plane is isolated at $x = 1.0\,c$ behind the test airfoil for the purpose of characterization of the gust signal, through averaging all velocity vectors within the region. This region of interest (ROI) is located at the same height as the midpoint of the plunge amplitude of the airfoil, defined as $y = 0$, and is represented schematically as an orange box in Fig. 2.4a. In section 3.2.2 an ROI located at $x = 1.5\,c$ behind the test airfoil is used to evaluate the evolution of the gusts as they convect downstream.

In order to determine the number of test periods required to achieve statistical significance, the vertical velocity v at one instance of time within a test period is averaged over 60 periods at the point described above. A protocol with a large plunge amplitude ($h_0/c = 0.5$) and zero pitch is used to ensure that dynamic effects would be present and would be incorporated into the analysis. The averaged values for each period are randomly sampled in order to determine the convergence of the standard deviation $\sigma(n)$ with the number of periods n included in the phase-average. One thousand bootstrap samples are taken for each value of n, and an estimate for the population standard deviation is computed from these samples (cf. Efron, 1992). The results from this analysis, shown in Fig. 2.7, reveal that $n = 30$ test periods yield reasonable convergence in the standard deviation (within ±5% of the final value, $\sigma(n = 60)$). Thus, all data presented in this work are phase-averaged over at least 30 test periods. Furthermore, at the start of every experiment, the airfoil is oscillated through a few unrecorded motion periods to ensure that startup effects do not influence the phase-averaged data.

Using this number of phase-averaged test periods, the choice of the dimension of the ROI is tested. Using the bootstrap method with one thousand random samples, the standard deviation of the velocity vectors located within the ROI is computed for several ROI box sizes. The results of this analysis, shown in Fig. 2.8, confirm that a dimension of 15 mm produce a standard deviation in v below 1% of the free-stream velocity. Thus, this dimension is selected to maintain a high degree of statistical convergence while keeping the ROI small enough to represent a point measurement.

Finally, in order to quantify the two main parameters of interest for the gust-generation problem, two methods for analysis are developed. In order to quantify the character of the waveforms of the velocity fluctuations, the

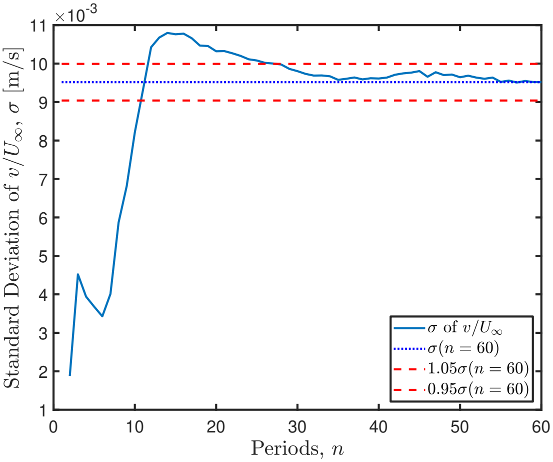

Figure 2.7: Standard deviation of the vertical velocity at $\frac{t}{T_0} = 0.8$ for $St = 0.096$ and $k = 0.603$, as a function of the number of test periods. Acceptable convergence is achieved by 30 periods. (Reprinted from Wei et al. (2019b), with permission of Springer Nature. © 2019 Springer Nature.)

average acceleration at the theoretical peaks of the signal is measured using linear fits about $\frac{t}{T_0} \approx 0.25$ and $\frac{t}{T_0} \approx 0.75$. The dimensionless time $\frac{t}{T_0}$ is given by the total period T_0 and is phase-referenced to the sinusoidal function. The fits encompassed 10 % of T_0 on either side of the instant of interest. After correcting for sign, the slopes of these two linear fits are averaged. For an ideal profile, this metric would yield a mean acceleration of $\frac{dv}{dt} = 0$ m/s^2, indicating symmetry in the velocity profiles. The idea is illustrated in Fig. 3.21 in section 3.2.2.

In order to quantify the influence of shed vortices in the wake of the airfoil on the region downstream of the gust generator, the vertical extent of the wake vorticity is measured at the location of interest, $x = 1.0\,c$. For every time instant in the phase-averaged period, vectors of vorticity at $x = 1.0\,c$ and y spanning the height of the domain are taken. These vectors are compiled into a 2D field in y and t to show the evolution of the thickness of the wake region over one period. The vorticity fields are smoothed using a 3×3 filter, to compensate for the effects of numerical differentiation. An automatically

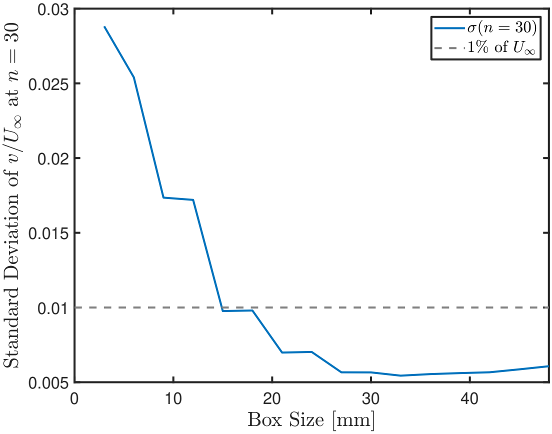

Figure 2.8: Standard deviation of 30 phase-averaged vertical-velocity measurements within the region of interest (ROI) at $\frac{t}{T_0} = 0.8$ for $St = 0.096$ and $k = 0.603$, as a function of the side length of the ROI. Statistical convergence is maintained if an ROI dimension of 15 mm is selected. (Reprinted from Wei et al. (2019b), with permission of Springer Nature. © 2019 Springer Nature.)

adaptive threshold based on the standard deviation across the entire y-t field to binarize the field, followed by a 2D 7×7 median filter and hole-filling method, is employed to identify and isolate areas of relatively high vorticity. The result of this procedure is an automatically generated mask that isolated the wake of the airfoil from the rest of the measurement domain. The width of the wake vorticity profile that is left after the mask has been applied is measured at every time instant across the phase-averaged cycle, and these values are then averaged to represent the mean width of the wake. Examples of vorticity profiles after application of the mask will be shown later in Fig. 3.23. In the ideal case, this metric would be minimized, indicating minimally low interference of the gust generator itself on the flow downstream of the wake.

2.3 Pitching and Plunging Airfoil Setup

To study characteristics of the leading edge vortex growth and detachment on a pitching and plunging flat plate airfoil in Chapter 4, different setups with a water tunnel at the Beihang University (BUAA) and a wind tunnel at the TU Darmstadt (TUDA) have been used. The difference in viscosity between water and air allows the attainable dimensionless parameter space to be significantly extended. Both setups will be introduced in this section along relevant preliminary investigations and data processing strategies.

Details on the Eiffel wind tunnel and motion apparatus used at TU Darmstadt for current investigations can be found in section 2.2.1 and section 2.2.2. The design of the flat plate airfoil on which the leading edge vortex growth and detachment is studied will be introduced below. To validate two dimensionality of the flow field, preliminary smoke-wire investigations were conducted, which will be discussed in this section. Additional parameter studies of different data processing strategies, which are used to quantify the flow field and LEV, will be introduced along with a statistical assessment of uncertainty estimates of vortex characteristics. Finally, the water tunnel, motion apparatus, flat plate airfoil and PIV measurement system used at the Beihang university will be briefly described.

Flat Plate Airfoil

Motion dynamics of the flat plate airfoil used for LEV investigations are determined by dimensionless parameters. These are chosen to be representative for biological flight and hovering, which are characterized by high St and k. For a larger stroke height and a short motion period, resulting from the desired St and k range, the airfoil has to be accelerated and decelerated very fast.

Highly dynamic kinematics require the airfoil to be stable enough to withstand large normal forces without significant deformations, which would distort the flow field on the airfoil. The natural frequency of the airfoil, when mounted on the linear actuators, has to be high enough compared to the motion frequency to avoid resonance effects. The lighter the airfoil, the higher the motion frequencies can be, since the force of the linear actuators used to accelerate the airfoil is limited. To allow for the manipulation of the LEV with a plasma actuator in subsequent studies, high voltage power lines to drive the plasma actuator have to be installed inside the airfoil. Due to the electromagnetic field induced by the power lines and the plasma itself, all parts of the airfoil have to be non-conductive to avoid interference and induction effects.

During optimization of the design with the aid of finite element method (FEM) simulations it was found that a sandwich design made of a 3D printed core and an outer cover of glass-fibre reinforced plastics provided the optimal trade-off between stability, weight and design freedom. All components are glued together using a two-component epoxy mixture. A representation of the flat plate airfoil design is shown in Fig. 2.9. The connecting mount at mid-span of the airfoil is fabricated from Torlon©, which is a non-conducting polyamide-imide that can resist high mechanical strain.

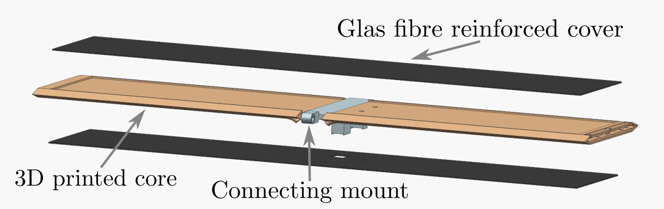

Figure 2.9: Flat plate airfoil design which uses a sandwich structure to reduce weight and enhance the dynamic stability.

Motion tests of the flat plate, which made use of a high-speed camera and image post-processing, showed that the natural frequency is about 77 Hz. Compared to the natural frequency of a flat plate airfoil of the same shape but without a glass-fibre reinforced sandwich core, which is at 35 Hz, the frequency is more than twice as high. The maximum wing tip displacement was found to be below 2% of the stroke height for maximum motion dynamics, which indicates that flow field disturbances caused by geometric deformation of the airfoil can be neglected. Further details on FEM optimization of the flat plate airfoil, the design process and its dynamic characterization can be found in Beck et al. (2018).

With the aid of the sandwich core design approach, different airfoil shapes were design and manufactured. These are shown in Fig. 2.10. The leading

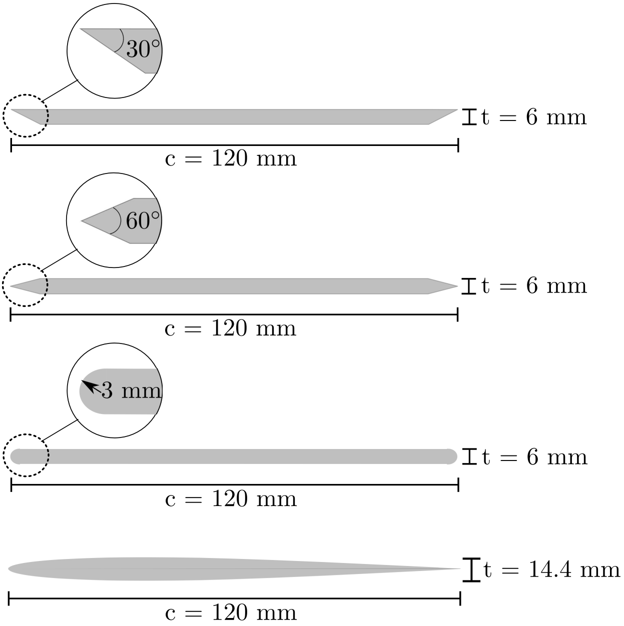

Figure 2.10: Airfoil types investigated in this thesis. The leading and trailing edges of the flat plate airfoil are interchangeable to realize investigations of an asymmetric sharp leading edge, a symmetric sharp edge and a round edge. A NACA 0012 is deemed to represent a more realistic airfoil.

and trailing edges of the flat plate airfoil are interchangeable to allow different edge curvatures to be investigated. The feature has been designed since the leading edge curvature has been found to affect the vorticity in the separated shear layer, the mass transport rate and thus the growth of the LEV (cf. Rival et al., 2014). A NACA 0012 airfoil was designed and manufactured to investigate the phenomena on a more realistic airfoil. All airfoils have a chord length of $c = 120\,\mathrm{mm}$. The relative thickness of the flat plate airfoil is less than $5\,\%$. To enable comparability of current results with previous studies of Widmann (2015), an asymmetric leading edge with $30\,^{\circ}$ will be used to study LEV growth and detachment.

2.3.1 Two-Dimensionality of the Flow Field

On finite wings which undergo pitching and plunging motion, three-dimensional effects in terms of tip vortices and spanwise stretching of the leading edge vortex occur (cf. Jardin et al., 2012). These effects have been found to dominate the flow field up to one chord inbound from the wing tip.

However, the present study focuses on LEV growth and detachment from a two-dimensional perspective, without the three-dimensional effects encountered on finite wings. Preliminary investigations of the flow field around the pitching and plunging airfoil with the aid of smoke wire experiments serve to validate the assumption of a two-dimensional flow field for the current investigations.

Smoke-Wire Investigations

To visualize three-dimensional effects of the flow over the airfoils in the Eiffel wind tunnel at TU Darmstadt, vertical smoke sheets are produced upstream of the test airfoils by dripping oil down a vertically mounted heated tungsten wire. The tungsten wire has knots every 20 mm to produce clear smoke lines and is heated by application of 22 VDC. Further details on the smoke-wire apparatus can be found in Hofmann (2015). One of the smoke sheets is located at 15 % span from the midspan position of the airfoil and the other at 40 % span, close to the wind tunnel side wall. The flow field is recorded from the side with a *Photron Fastcam SA 1.1* high-speed camera. Additionally, a *Photron Fastcam MC 2.1* camera system with an external camera head records the flow field from downstream of the test airfoil to enable evaluation of spanwise distortions of the smoke sheet. A high power LED array illuminates the flow field from the top through a glass window.

In Fig. 2.11 the flow field around a NACA 0012 airfoil is shown for dimensionless parameters representative for the ID 3 case, introduced in section 4. Fig. 2.11a and Fig. 2.11c show the flow field around the NACA airfoil from downstream of the test airfoil facing in direction of the inflow. Here, the midspan of the airfoil is at the left image border and the wind tunnel wall at the right border. For orientation, corresponding side views are depicted in Fig. 2.11b and Fig. 2.11d, where the inflow is from the right and the airfoil moves down.

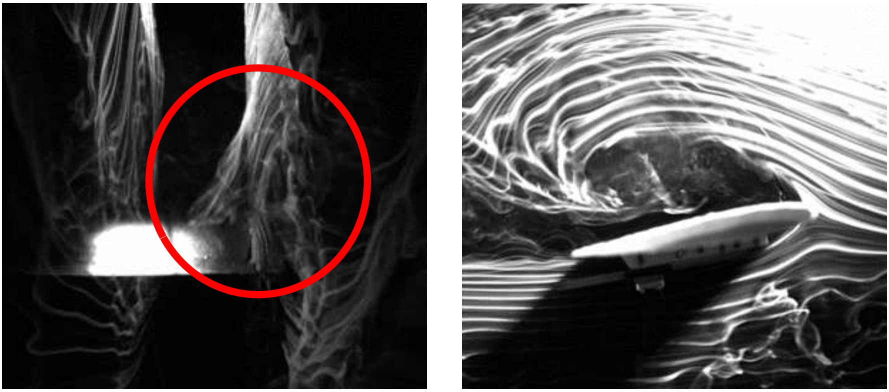

(a) $t/T = 0.322$; Rear view; No sealing **(b)** $t/T = 0.322$; Side view; No sealing

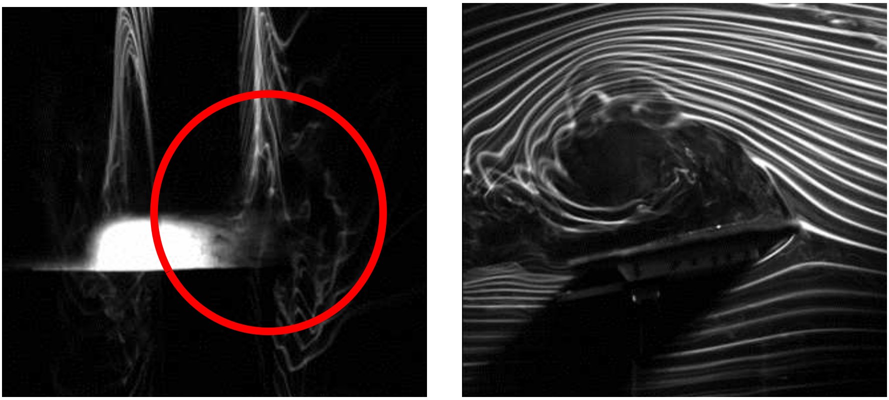

(c) $t/T = 0.322$; Rear view; Sealing **(d)** $t/T = 0.322$; Side view; Sealing

Figure 2.11: Smoke visualization of the flow field around a pitching and plunging NACA 0012 airfoil in rear (a and c) and side view (b and d) for the dimensionless time instant $t/T = 0.322$, normalized by the motion period T of the cycle. Between the wing tips and wind tunnel walls a gap of 2 mm exists in (a) and (b), which has been closed by a brush sealing in (c) and (d). Red circles highlight the smoke sheet close to the wind tunnel wall in the region where the LEV grows over the airfoil.

Initially, the airfoil spans the wind tunnel width with 2 mm gaps between the airfoil tips and wind tunnel side walls to avoid stick slip effects and collisions during highly dynamic pitch and plunge kinematics. The right smoke sheet in Fig. 2.11a is distorted significantly in midspan direction (to the left), which is highlighted by a red circle. This indicates the existence of three-dimensional effects at the wing tip, close to the wind tunnel wall. By studying the corresponding side view in Fig. 2.11b it is found that the LEV shape differs between both smoke sheets. The outer LEV, which is closer to the wing tip and wind tunnel wall, is larger and located more downstream compared to the inbound LEV. This indicates spanwise variations of the LEV shape. Such three-dimensional effects are found to occur very early in the downstroke at about $t/T = 0.2$ and increase towards the bottom end position.

To reduce three-dimensional effects, a brush sealing is installed at the wing tips to close the gap between them and the wind tunnel walls. An applied brush sealing is shown exemplary in Fig. 2.12. The sealing, which is made of velor to reduce friction on the wind tunnel wall and avoid scratches on the wind tunnel glass window, is glued on the wing tip.

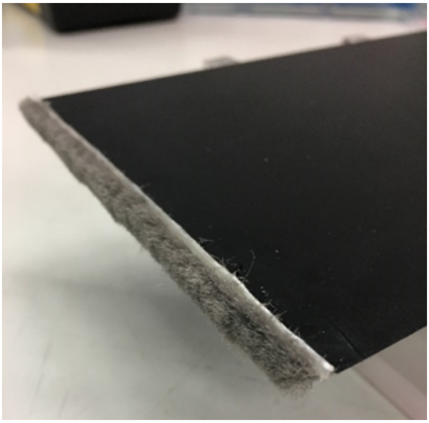

Figure 2.12: Brush sealing on the wing tip of a flat plate airfoil to inhibit airflow around the wing tip trough the gap between tip and wind tunnel wall.

Smoke sheet flow visualizations with installed brush sealing on the NACA 0012 airfoil are shown in Fig. 2.11c and Fig. 2.11d. From the rear view it can be seen, that there is no inbound distortion of the right smoke sheet anymore, which indicates that spanwise flow is eliminated. From the side view in Fig. 2.11d it can be seen that the LEV has the same shape and is located similar in both smoke sheets.

With the aid of the brush sealing, spanwise flow and wing tip effects are eliminated for the entire downstroke of the airfoil. For lower motion dynamics, different effective angles of attack and all flat plate airfoils, the installation of brush sealing is found to eliminate three-dimensional flow effects as well. Since no three-dimensional effects could be observed in any case after installation of the brush sealing, the flow field is assumed to be two-dimensional.

2.3.2 PIV Flow Field Measurements

Time-resolved 2D2C PIV flow field measurements of the leading edge vortex on a pitching and plunging flat plate are performed with the same equipment used for flow field measurements in the gust generation scenario, introduced in section 2.2.3. Differences of the current setup in respect to the gust generation setup are briefly addressed below.

A *Photron SA1.1* High-Speed Camera and a *Carl Zeiss* lens of 50 mm focal distance with an aperture of $f = 2.2$ captured images of the seeded flow around the flat plate with a resolution of $1024 \times 1024\,\text{px}$. The field of view spanned by a light sheet plane of 3 mm thickness, located at 28% span from the wind tunnel wall, was $1.9\,c \times 1.9\,c$, resulting in a spatial resolution of 4.556 px/mm. The inter-framing time $\triangle t$ is set to $150\,\mu\text{s}$ to ensure a particle displacement of the seeding between 2 and 8 pixels within image pairs. Image correlations are performed with the same software used in gust generation investigations but at an initial interrogation area (IA) size of $64\,\text{px} \times 64\,\text{px}$ and a final of $12\,\text{px} \times 12\,\text{px}$ at 50 % overlap, yielding 92 IA's over airfoil chord. Outlier identification and interpolation was treated in accordance with the methodology introduced in section 2.2.3.

2.3.3 Data Processing

To quantify characteristics of the leading edge vortex and key features of the flow field, different data processing methodologies are used. These include vortex identification methodology and the analysis of Lagrangian Coherent

Structures (LCS) based on the finite time Lyapunov exponent (FTLE) fields. To determine physically relevant processing parameters and improve the reliability of results, preliminary parameter studies have been conducted. These will be discussed below.

Vortex Identification Methodology

The circulation and position of the LEV are characteristic key parameters, which are essential to investigate the vortex growth and detachment. They are also used to compare its characteristics between different setups and for different motion kinematics. To investigate influences of the evaluation method used to obtain LEV circulation and position, different approaches have been tested on the same set of raw images. Considered methodologies to obtain LEV circulation are based on the identification of regions belonging to the vortex prior to a first order spatial integration of vorticity according to Stokes's theorem. In this thesis, vortex characteristics are extracted from single runs before they are ensemble averaged over multiple runs.

LEV boundaries computed using the λ_{ci} method, introduced by Zhou et al. (1999), are found to be strongly dependent on the threshold used to identify the vortex, whereas the Q criterion by Hunt et al. (1988) identifies only an inner vortex core while excluding outer vortex regions. Additionally, both methods are found to intermittently attribute the leading edge shear layer to the main vortex, leading to strong fluctuations of the subsequently determined circulation. The LEV boundary computed by thresholding the Γ_2 scalar field, introduced by Graftieaux et al. (2001), which considers regions of pure shear as the vortex area, is found to identify the vortex boundary most consistently using the default threshold of $\Gamma_2 = 2/\pi$. Therefore, it is used to quantify the circulation evolution of the LEV from velocity fields. This is done by integration of vorticity within the detected LEV boundary according to Stokes's theorem. The detection of the LEV center from maxima of the Γ_1 scalar function, also introduced by Graftieaux et al. (2001), as well as from the Q criterion, were found to be reliable, at least with respect to visual inspection of instantaneous vector fields. Although the Γ_1 function is not Galilean invariant by definition, deviations from the Galilean invariant Q criterion were found to be less than 2 %, which in turn provides evidence that the chosen plate-fixed frame of reference allows reasonable interpretation of the extracted topology.

For each location the Γ_1 and Γ_2 scalar fields are computed from velocity information within a square domain of size S, which is centered around the location of interest. The size of S is measured in velocity information locations. To enhance the statistical validity of vortex boundary detection, and thus the area considered to obtain LEV circulation by integration of vorticity, the effect of domain size S on the identified vortex boundary is investigated. Fig. 2.13 shows various vortex boundaries, as identified by different domain sizes S superimposed on the vorticity field of a single run. The single run is taken from the baseline case ensemble, discussed in Chapter 5 as ID 14, where a flat plate airfoil is considered. Additionally, Fig. 2.14 depicts the corresponding

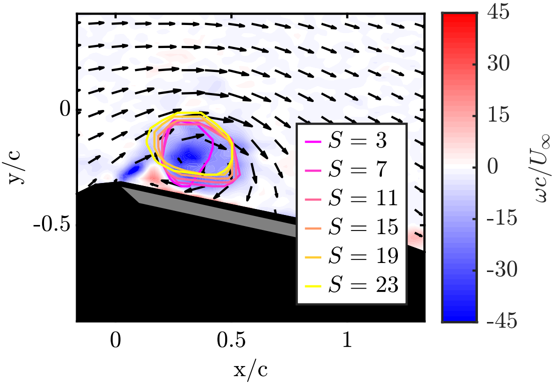

Figure 2.13: Effect of different domain sizes S used to compute the vortex boundary from the Γ_2 scalar field. $|\Gamma_2| = 2/\pi$ vortex contours for different S in velocity information distance superimposed on the normalized vorticity $\omega c/U_\infty$ field around a pitching and plunging flat plate at the dimensionless time instant $t/T = 0.26$. The onflow is from the left and the airfoil, which moves downward, is masked out in grey. The shadow of the airfoil in the laser light sheet is masked out in black. (Reprinted from Kissing et al. (2020c). © 2020 by American Physical Society.)

evolution of the LEV area A_{LEV} over dimensionless time t/T of the motion period. For small S only an inner core of the vortex is identified, which is

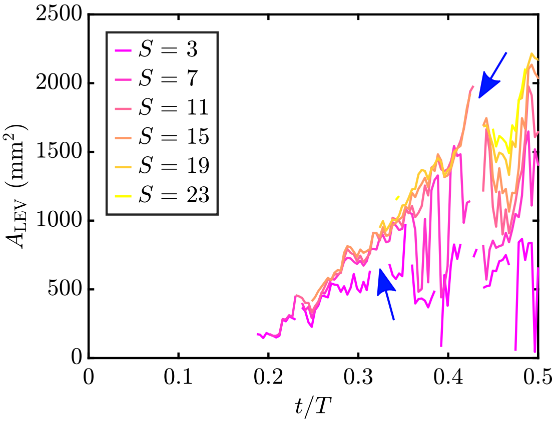

Figure 2.14: Effect of different domain sizes S used to compute the vortex boundary from Γ_2 scalar field. Evolution of the LEV area A_{LEV} for different domain sizes S over dimensionless time t/T of the airfoil motion. Exemplary gaps in area evolution caused by vortex center detection outside of its identified boundary are marked with a blue arrows. (Reprinted from Kissing et al. (2020c). © 2020 by American Physical Society.)

reflected by small values of A_{LEV} over the entire dimensionless period. On the other hand, for large values of S the area of the identified vortex increases while it is also shifted upwards and towards the leading edge. This shift can be classified as non-physical considering the vorticity field for vortex demarcation. For an underestimated LEV boundary and for large non-physical shifts the identified vortex center is even outside the vortex boundary, leading to a rejection of the identified vortex by validation procedures. This is indicated by large gaps in area evolutions caused by center positions lying outside the identified boundary, highlighted for exemplary instants in Fig. 2.14 with the aid of blue arrows. It should be noted that - in contrast to the boundary detection - the center detection methodology itself is not influenced by the size of the computation domain. The best trade-off between an underestimation of the vortex boundary and the observed non-physical upward shift is found to be $S = 11$, equivalent to $\approx 12\,\%$ of the airfoil chord. Consequently all presented vortex identification results are obtained using a domain size of $S = 11$.

During inspection of vortex identification results from single runs, short-term fluctuations of the identified vortex boundary occurred. In comparison to vortex identification results from ensemble averaged vector fields these fluctuations lead to an increased standard deviation of the LEV area A_{LEV} and thus, the LEV circulation Γ_{LEV}. To reduce the influence of fluctuations on the standard deviation, each velocity component of each information location is filtered temporally using a second order Savitzky-Golay filter, as introduced by Rival et al. (2014). In order to preserve physical validity of velocity information in terms of peak values, the influence of different filter lengths is investigated. The aim is to identify the shortest filter length that provides velocity signals without small scale fluctuations under the constraint of maintained peak values. For a filter length of $\Delta t = 11\,\text{ms}$ peak values are maintained at least up to 97 % while small scale fluctuations are reduced significantly. Therefore, all single run velocity information used for vortex identification are filtered accordingly.

Lagrangian Coherent Structure Saddle

With Eulerian vortex identification methods the LEV detachment, related to changes of the flow topology, can only be investigated implicitly by observation of effects on vortex characteristics. In contrast, Lagrangian methods in terms of coherent structures allow direct identification of topological changes of the flow field initiating vortex detachment. In this thesis, coherent structures are identified with the aid of finite-time Lyapunov exponent (FTLE) ridges, following the concept and methods introduced by Haller (2002) and Shadden et al. (2006). Ridges of repelling and attracting fluid regions are obtained by thresholding forward-time and backward-time FTLE scalar fields. Topological changes of the flow field can be identified directly by tracking Lagrangian saddle points of the flow field, which are intersection points of forward-time and backward-time FTLE ridges, as shown by Huang & Green (2015). In this study the FTLE computation package developed by Peng & Dabiri (2009) is used to obtain FTLE fields. In advance of the FTLE evaluations, the impact of different parameters governing the results of FTLE computations, including spatial and temporal resolution of the velocity information as well as the integration time τ were investigated.

Computation of physically relevant FTLE ridges requires a sufficient spatial and temporal resolution of the velocity information used for calculations. Both resolutions were tested for current FTLE computations by a reduction of the temporal and spatial resolution by a factor of 2. In both cases no significant changes were observed in FTLE fields, so both resolutions are assumed to be sufficient.

FTLE scalar fields are obtained over a specified time frame, which is referred to as the integration time τ. For further processing, raw FTLE scalar fields are thresholded using a percentage of maximum FTLE values in each frame to evaluate distinct ridges (80 % in this thesis). As mentioned by Peng & Dabiri (2009), τ does not have an impact on the FTLE ridge topology in terms of their location, but on the strength of ridges via their resolution. The effect of different τ is exemplary illustrated for FTLE raw fields and ridges, computed from ensemble averaged velocity fields, in Fig. 2.15. Velocity information are taken from the ID 3 case, discussed in Chapter 4. Fig. 2.15a and Fig. 2.15c show raw FTLE scalar fields for backward and forward computations in red and green, while Fig. 2.15b and Fig. 2.15d show thresholded ridges, used for further processing.

For lower τ of $0.06\,T$, shown in Fig. 2.15a and Fig. 2.15b, the raw FTLE scalar field is characterized by lower intensities for both scalar fields. After thresholding, only fragments of raw FTLE ridges are retrieved. For $\tau = 0.11\,T$, shown in Fig. 2.15c and Fig. 2.15d, FTLE values are higher leading to clear ridges after thresholding. The efforts of the present FTLE calculation center around the formation of secondary structures, which have a lifetime of approximately $0.25\,T$. A final integration time of $\tau = 0.11\,T$ was chosen accordingly, where the extracted FTLE ridges comprise all significant features of raw secondary structure contours at an acceptable computational effort. Note however that the conclusions from above only hold beyond a minimum τ that allows sufficient temporal development of LCS instead of quasi-streamline-based LCS determination of separatrices for $\tau \to 0$ (see e.g. Perry & Chong, 1987). Due to the robustness of FTLE calculations against interpolation errors (cf. Haller, 2002), velocity vector fields can be interpolated to obtain highly resolved FTLE fields. In this thesis the spatial interpolation is chosen based on the trade-off between resolution and computational costs. In final

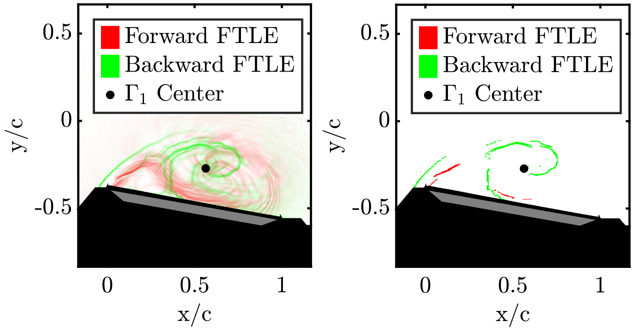

(a) FTLE fields; $\tau = 0.06\,T$ **(b)** FTLE ridges; $\tau = 0.06\,T$

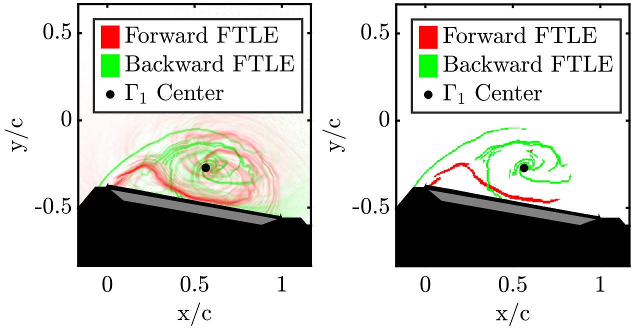

(c) FTLE fields; $\tau = 0.11\,T$ **(d)** FTLE ridges; $\tau = 0.11\,T$

Figure 2.15: Effects of different integration times τ on FTLE fields and thresholded ridges. Velocity information are taken from ensemble averaged velocity fields at $t/T = 0.21$ in the ID 3 case from Chapter 4. (a) and (c) show the flow field in terms of attracting and repelling FTLE scalar fields obtained from forward and backward FTLE computations. (b) and (d) show final ridges obtained by using a 80 % threshold of the respective maximum FTLE value in each frame. The airfoil is masked out in grey and the laser light shadow in black. The vortex center from Γ_1 criterion is marked as a black circle for orientation.

evaluations the spatial resolution of FTLE fields was twice as high as the resolution of the velocity vector fields, since ridges were clearly represented and computational costs were acceptable.

2.3.4 Uncertainty Assessment

To determine the number of repetitions necessary to achieve statistical significance of vortex characteristics and reduce operational efforts, the standard deviation evolution between single runs is considered in the following. The LEV circulation and position are key indicators for the vortex detachment, which is why considerations will concentrate on these quantities. To determine the required number of repetitions, the case with the highest mean standard deviation of LEV circulation and position of all investigated cases in Chapter 4 and Chapter 5 is chosen from a conservative point of view. This case is denoted as ID 14 in Chapter 5 and is characterized by the highest motion dynamics and largest α_{eff}.

Fig. 2.16 shows the evolution of the ensemble averaged, normalized leading edge vortex circulation $\Gamma_{\text{LEV}}/U_\infty c$ over dimensionless time t/T for the ID 14 case with the standard deviation between single runs indicated by a grey shadow. To obtain the ensemble average, 30 repetitions were taken into

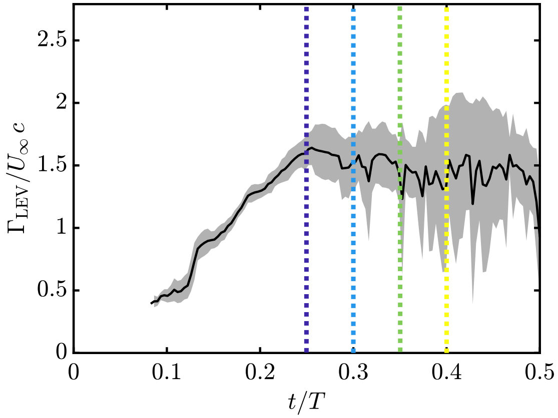

Figure 2.16: Ensemble averaged, normalized LEV circulation $\Gamma_{\text{LEV}}/U_\infty c$ evolution over dimensionless time t/T for the ID 14 case from Chapter 5. 30 repetitions are used for ensemble averaging. The standard deviation, depicted as a grey shadow, represents the deviation between repetitions. Instants at which the standard deviation evolution will be investigated as a function of the number of repetitions in Fig. 2.17, are marked by vertical dashed lines.

account from which the circulation was extracted separately with vortex identification prior to averaging. The standard deviation indicates the deviation between repetitions.

The LEV accumulates circulation up to $t/T \approx 0.25$, thereafter the circulation remains almost constant. The standard deviation is low during the phase of circulation accumulation and increases when the plateau is reached. The higher standard deviation towards later instants during constant circulation is attributed to the viscous decay and the detachment of the LEV. The viscous decay is indicated by rapidly decaying vorticity values inside the LEV, observed in vorticity fields. To allow for a differentiated assessment of the standard deviation evolution with respect to the LEV growth and detachment phases, it is investigated at four instants of the downstroke of the airfoil at $t/T = 0.25$, 0.3, 0.35 and 0.4. These instants are indicated by dashed vertical lines in Fig. 2.16.

Standard Deviation Evolution from Bootstrap Testing

Circulation standard deviation values for each number of repetitions (1 to 30) are randomly sampled to determine the convergence of the standard deviation with the number of repetitions n for each investigated instant. A total number of 1000 bootstrap samples are taken for each value of n to estimate the population standard deviation (cf. Efron, 1992). The results from bootstrap sampling are shown in Fig. 2.17 in terms of the relative standard deviations $\sigma_{\Gamma_{\mathrm{LEV}}}/\overline{\Gamma}_{\mathrm{LEV}}$ over the number of runs for each time instant. For the latest investigated instant at $t/T = 0.4$, the standard deviation is the highest, compared to the other instants. This is expected from observations with respect to Fig. 2.16, where a higher standard deviation was observed for later instants during downstroke of the airfoil due to the LEV decay and detachment.

Investigations in this thesis focus on the growth phase of the LEV and its detachment mechanism rather than its final decay. Therefore, time instants before $t/T = 0.4$ are considered relevant and will be further elaborated. For instants up to $t/T = 0.35$, the relative LEV circulation standard deviation

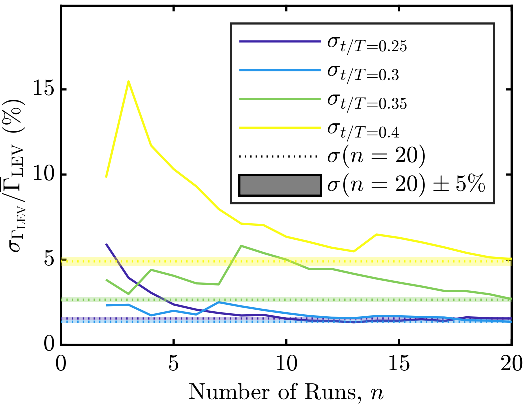

Figure 2.17: Relative standard deviation of circulation $\sigma_{\Gamma_{\mathrm{LEV}}}/\overline{\Gamma}_{\mathrm{LEV}}$ for different number of runs n at different dimensionless time instants t/T from 1000 bootstrap tests. Asymptotic values for each time instant are indicated as dashed lines and a 5 % range in respect to each asymptotic value as coloured shadow.

reaches values lower than 5 % already for $n = 10$. Therefore, 15 runs are considered as sufficient to ensure a standard deviation of the circulation below 5 % for all investigated cases in this thesis.

Similar conclusions can be drawn from bootstrap investigations of the LEV position, where a standard deviation below 5 % is reached for all investigated instants for 7 runs. The maximum standard deviation of all velocity information locations of flow fields was found to converge below 5 % after 8 repetitions for the current case. This confirms that 15 repetitions give reasonable convergence of LEV characteristics and flow fields, even from a conservative point of view. Consequently, 15 repetitions were recorded and used for ensemble averaging of vortex characteristics and flow fields in this thesis.

2.3.5 Beihang University Setup

To enlarge the attainable dimensionless parameter space for LEV investigations, a second setup with a water tunnel at the Beihang University (BUAA) was established. Due to the difference in viscosity between water and air, which is in the order of one order of magnitude, higher reduced frequencies and Strouhal numbers can be investigated in comparison to the wind tunnel at TUDA. Below, the water tunnel and motion apparatus used at BUAA will be presented along the PIV setup and respective correlation scheme effects on velocity field results.

Water Tunnel and Motion Apparatus
At BUAA a water tunnel with a test section of 1 m × 1.2 m in spanwise and vertical orientation was used in which the RMS turbulence level was found to be less than 1.3 % for $U_\infty = 0.2\,\mathrm{m/s}$.

A customized experimental platform, including a rotation stage and a linear translation stage, was designed to enable the combined pitching and plunging motion of the flat plate. The linear translation of the investigated airfoil to produce plunging motion was realized with a servomotor of type *YASKAWA* SGM7J-100 and a ball screw rod (LC-EA-030A). Rotational motion of the airfoil was realized with a servomotor of type *YASKAWA* SGM7J-400 and a decelerator (*KAMO* JFR90), which are both directly connected to the airfoil. A programmable multi-axis controller (*Delta Tau* Clipper) was used to synchronize all servomotors.

PIV Flow Field Measurements
In the BUAA PIV setup, a high-speed CMOS camera of type *Photron Fastcam* SA2/86K-M3 fitted with a Nikon lens of 50 mm focal length was used to acquire time-resolved PIV raw images. Image pairs were acquired at a frequency of 200 Hz with a resolution of 2048 px × 2048 px. The seeded flow field was illuminated by a continuous Nd-YAG laser with 8 W nominal power at midspan position with a laser light sheet of 3 mm thickness. Hollow glass beads with a median diameter of 20 μm and a density of 1.05 g/cm^3 were used as seeding particles in water. For final evaluations, the same correlation

algorithm from TUDA was used, where the final IA size was 16 px × 16 px with 50 % overlap resulting in about 82 velocity data points over the airfoil chord.

PIV Correlation Scheme Effects

Even when using the same vortex boundary identification and circulation computation method, as well as spatial vorticity derivation schemes, the LEV circulation evaluation was found to be dependent on the cross-correlation parameters used to obtain velocity data from the same raw images in PIV correlations. The LEV circulation obtained with identical post-processing routines but different correlation algorithms, a gradient-based cross-correlation optimization based on the Lucas-Kanade method (cf. Champagnat et al., 2011) and a standard FFT correlation algorithm, differs up to 9 %. The maximum circulation divergence occurs when the LEV starts to decay, which is accompanied by a blurred outer boundary leading to different areas identified as a vortex. This highlights that PIV correlation schemes influence the circulation computation within the vortex domain significantly, even when using the same vortex identification method for boundary detection, vorticity derivation and subsequent spatial integration procedures. When aiming to compare vortex characteristics between different facilities, these deviations can hinder comparability of characteristics obtained from flow fields. Consequently all evaluations have been performed using the same correlation software and parameters according to the TUDA setup described in section 2.3.2 and section 2.3.3.

2.4 Leading Edge Vortex Manipulation Setup

In this section, methods and facilities used to investigate leading edge vortex manipulation on pitching and plunging airfoils with a DBD plasma actuator, discussed in Chapter 5, will be introduced.

Details on the Eiffel wind tunnel and motion apparatus used at TU Darmstadt for manipulation studies can be found in section 2.2.1 and section 2.2.2. The basic design concepts of the considered flat plate and NACA 0012 airfoils which undergo pitching and plunging motion follows the design introduced in section 2.3. A brief recap of the working principle of DBD plasma actuators and their design will be given in section 2.4.1 along with a discussion of modifications of the actuator for current investigations. The PIV flow field measurement setup used to characterize flow control effects on the LEV will be introduced in section 2.4.2.

2.4.1 Dielectric Barrier Discharge Plasma Actuator

The structure of DBD plasma actuators for flow control applications will be introduced in this section along operating electric and fluid mechanic characteristics of the actuator. Adaptions of the actuator to allow for its application on pitching and plunging airfoils will be introduced as well. For a detailed description of the plasma actuator structure and its modifications the reader is referred to Stumpf (2019).

Structure and Operating Conditions of a DBD Plasma Actuator
Dielectric barrier discharge (DBD) plasma actuators have been used previously in various flow control applications (e.g. Duchmann, 2012; Kriegseis et al., 2016; Simon, 2017). Its electric and fluid mechanic properties have been investigated extensively in Kriegseis (2012), Kriegseis et al. (2013) and Kuhnhenn et al. (2016).

The plasma actuator design in present flow control experiments follows the design described in Simon (2017) and is schematically shown in Fig. 2.18. The lower grounded copper electrode, illustrated as a blue rectangle in Fig. 2.18, is 10 mm wide, 35 μm thick and insulated from the upper electrode, depicted

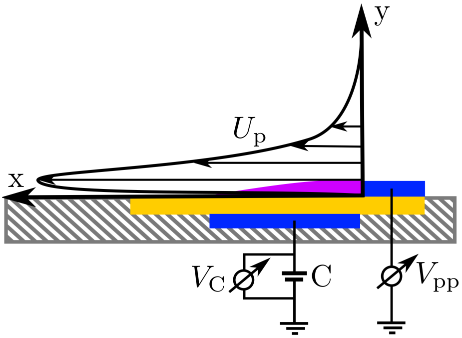

Figure 2.18: Schematic design of a DBD plasma actuator and the electric circuit to operate it. The wall jet induced by the plasma actuator is depicted in terms of the induced velocity profile U_p. Adopted from Corke et al. (2010).

as the upper blue rectangle, by a package consisting of five layers of Kapton© tape, shown as a yellow rectangle. Each layer of the Kapton© package consists of 25 μm Kapton and 35 μm adhesive, resulting in an overall thickness of the dielectric package of 300 μm. The upper electrode is also made of 35 μm thick copper tape with a width of 5 mm.

By application of a sinusoidal voltage with a frequency φ_PA of about 10 kHz and a peak-to-peak voltage V_pp of 10.8 kV, a cold plasma discharge is generated downstream of the upper electrode. The plasma is indicated in Fig. 2.18 in magenta. Ionized air molecules inside the plasma are accelerated in the electric field. Due to the collision of the ionized and accelerated molecules with surrounding molecules, a body force f_PA is produced above the plasma actuator. During positive half-cycle of the voltage, the body force direction is towards the upper electrode, while it is directed towards the lower electrode in positive x-direction for negative voltage. The body force produced during negative voltage is slightly higher, resulting in a mean force in the positive x-direction over the entire cycle. This mean force produces a wall jet towards the lower electrode, which is used for flow control and indicated in Fig. 2.18 by the velocity profile U_p.

Kriegseis et al. (2013) and Kriegseis et al. (2015) characterized the electric and fluid mechanic characteristics of a DBD plasma actuator with the aid of time-resolved PIV measurements. The investigated plasma actuator has the same design used in the present manipulation efforts. Key quantities from their investigations are reproduced in table 2.2 for different operating parameters. The peak-to-peak voltage V_{pp}, the plasma power per actuator length P_{PA}/L and the effective capacitance per actuator length C_{eff}/L were matched in current investigations to allow fluid mechanic effects in terms of the maximum induced velocity $U_{\max}$ and the body force per length F/L to be transferred. Key electric characteristics in terms of V_{pp}, the cold and effective capacitance C_{cold} and C_{eff}, as well as the plasma power P_{PA} were compared to nominal values given by Kriegseis et al. (2013) prior to each test to ensure constant fluid mechanic effects. If any of the mentioned key electric indicators changed more than 4 %, the actuator was replaced. To ensure comparability with the nominal values, the same measurement and data processing strategies for electric characteristics were chosen, as have been earlier described in Kriegseis et al. (2013).

Table 2.2: Electric and fluid mechanic characteristics of a DBD plasma actuator investigated by Kriegseis et al. (2013) and Kriegseis et al. (2015) with $C_0 = 83.3\,\mathrm{pF/m}$.

Configuration	9 kV	10 kV	11 kV
V_{pp} (kV)	8.82	9.83	10.81
P_{PA}/L (W/m)	30.35	45.71	67.97
C_{eff}/L (pF/m)	260.0	306.7	346.6
$U_{\max}$	3.04	4.04	5.43
f_{PA}/L (mN/m)	6.75	12.06	22.07

At $\varphi_{\mathrm{PA}} = 10\,\mathrm{kHz}$ the oscillating body force can be perceived as being quasi-steady by the LEV and secondary structures, which are in the far field of the actuator, where viscous effects dampen high frequency oscillations. For all presented flow manipulation efforts, V_{pp} was set according to the 11 kV configuration introduced in table 2.2. The maximum induced velocity by the plasma body force at the above mentioned operating parameters is about

5.43 m/s according to Kriegseis et al. (2013), which is in the order of the velocity induced by the LEV on the airfoil surface. The body force of the plasma actuator relative to the dynamic pressure and airfoil area is 0.01365, based on a plasma body force of 12.06 mN/m, which has also been obtained in Kriegseis et al. (2013) for current parameters of the actuator.

The AC high voltage input to the plasma actuator is generated using a *GBS Electronics GmbH Minipuls 2.1* high voltage generator.

DBD Plasma Actuator Application on a Pitching and Plunging Airfoil

To reduce reflections of the laser light used for PIV measurements from the actuator surface, which moves with the pitching and plunging flat plate, it was painted black. The painting methodology is depicted schematically in Fig. 2.19. The original plasma actuator design with the electrodes in blue and the dielectric layer in yellow is shown in Fig. 2.19a. During preliminary tests it was found that electric characteristics of the plasma actuator changed significantly if the entire surface of the actuator was covered by a layer of paint. When leaving the side of the upper electrode unpainted, all electric key characteristics listed in table 2.2 could be maintained. The painting methodology with an uncovered side of the upper electrode is schematically shown in Fig. 2.19b. The design was achieved by painting the actuator without

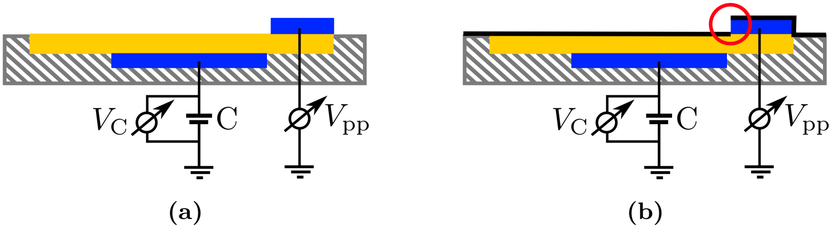

Figure 2.19: Reduction of laser light reflections from a plasma actuator with the aid of a layer of black paint. (a) Plasma actuator without black paint. (Reprinted from Kissing et al. (2020c). © 2020 by American Physical Society.) (b) Plasma actuator with a layer of black paint, where the side of the upper electrode is not painted to preserve electric key characteristics (red circle).

the upper electrode and the electrode separately. By cutting off the side of the painted upper electrode and its application onto the actuator, the desired design was established.

For further details on reflection reduction efforts, paint characteristics and corresponding effects on electric plasma actuator characteristics, the reader is referred to Stumpf (2019).

2.4.2 PIV Flow Field Measurements and Data Processing Strategies

Flow control effects of plasma actuation on the LEV are quantified using time-resolved 2D2C particle image velocimetry. The PIV setup is based on the setup for LEV investigations, introduced in section 2.3.2. Adaptions and extensions of the setup will be introduced in the following. Post processing strategies of raw PIV data, which use Savitzky Golay smoothing, a vortex identification method and Lagrangian coherent structures analysis, follow strategies introduced in section 2.3.3 closely.

The seeded flow field is recorded with a *Phantom V12.1* high-speed camera, with a resolution of 1280 px × 720 px. A narrow band-pass filter (530 nm±10 nm) in front of the camera lens is used to eliminate any discharge light emitted by the plasma (<430 nm). Image pairs are recorded at 1 kHz with a pulse delay of Δt =150 μs. Commercial software (*PIVview2C*) is used for standard FFT cross-correlation with a Gaussian sub-pixel peak detection. A multi-grid, multi-pass interrogation scheme of 64 px initial and 16 px final square IA size at 50 % overlap is used for correlations. The spatial resolution of 251 μm/px leads to 59 velocity information per chord. At maximum 2.3 % velocity outliers have been identified in a single frame by a normalized median test of threshold two (cf. Westerweel & Scarano, 2005), which have been replaced by a 3x3 neighborhood interpolation. The field of view for PIV measurements spans about 3 chords in mean free stream direction with one chord between the airfoil's trailing edge and the downstream FOV border. The LEV does not intersect with the downstream FOV border up to the end of the downstroke in any investigated case.

Effects of flow control on LEV circulation and center position are evaluated by means of a vortex identification methodology as proposed by Graftieaux et al. (2001). To reduce the influence of fluctuations on the standard deviation of the circulation, each velocity component is temporally filtered using a second order Savitzky-Golay filter of $\Delta t = 11\,\mathrm{ms}$ length (11 velocity information instants), as introduced by Rival et al. (2014).

Ensemble averaged LEV circulation and vortex center position were investigated with bootstrap sampling (cf. Efron, 1992) to determine the minimum number of repetitions necessary. Fifteen repetitions yield reasonable convergence of the standard deviation within ± 5 % of the asymptotic value. Thus, all cases are recorded 15 times.

Timing, Synchronization and Plasma Actuator Operation

Timing and synchronization of the PIV measurement setup with the airfoil motion and wind tunnel control follows the approach introduced in section 2.3.2. For LEV manipulation experiments, the active phase of the DBD plasma actuator has to be timed precisely to allow for a distinct manipulation of the flow field topology. The high voltage generator which drives the plasma actuator has to be controlled to produce the desired fluid mechanic effects. This is accomplished by monitoring of key electric characteristics during operation.

Fig. 2.20 illustrates required extensions of the existent experimental setup to synchronize and control the plasma actuator operation with the other experimental subsystems. Extensions from the previous setup, used for LEV characterization, are highlighted by red dashed border.

The high voltage generator that powers the plasma actuator is controlled using an in-house *LabVIEW* code, which is executed on PC #4. In this code, control parameters for the high voltage generator in terms of its phase and frequency can be set to match V_{pp} and φ_{PA} to the desired values. A *Picoscope* USB oscilloscope is used to provide online voltage and charge measurements to the code, which are used to derive electric key characteristics of the actuator (cf. table 2.2). Output from the *Labview* code to the high voltage generator is provided by a *NI-DAQ USB 6022* AD converter. The inhibitor of the high

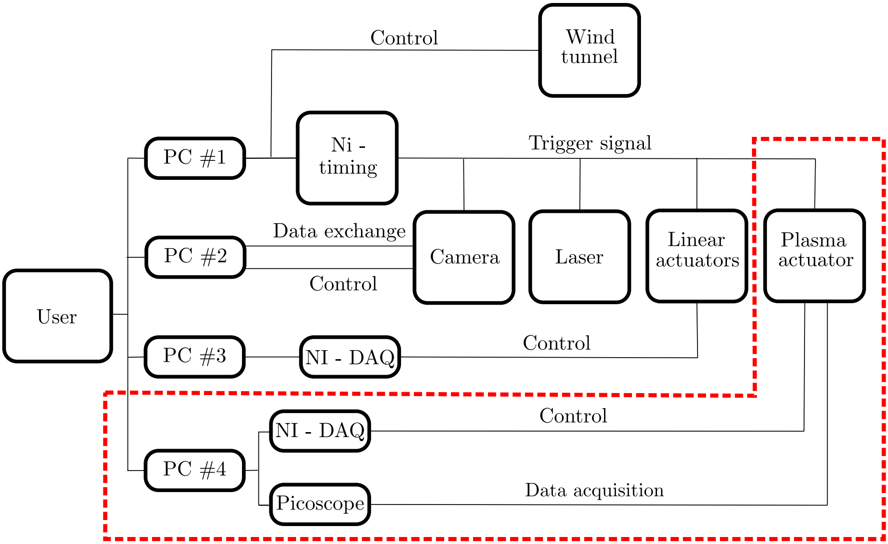

Figure 2.20: Wiring diagram of the synchronization, timing and control logic for modules used in the LEV manipulation setup. Extensions in terms of additional components for plasma actuator operation in respect to the wiring in Fig. 2.5 are highlighted by a red dashed border.

voltage generator is invoked from the Ni - timing script via the corresponding breakout box to ensure synchronicity with the PIV measurements and airfoil motion.

All signal lines were arranged around the wind tunnel test section to reduce induced voltages by the electro-magnetic field from the plasma, which was capable of triggering the laser and the camera unintentionally. On critical trigger lines to the laser and camera, in-house optocoupler were integrated and intensive pretesting conducted to ensure minimum jitter times of less than 9 ns. For further details on electro-magnetic compatibility efforts the reader is referred to Stumpf (2019)

3 Periodic Gust Encounter: Gust Response of Airfoils and Gust Generation

This chapter addresses periodic gust encounter scenarios on airfoils from two perspectives. First, differences of the Sears and Atassi transfer functions, which predict lift response of airfoils under periodic inflow conditions, are theoretically elaborated and experimentally validated in section 3.1. Second, a simplified method to generate periodic inflow conditions with a single airfoil, using the Theodorsen transfer function for optimization, will be introduced in section 3.2. An introduction into both scenarios and corresponding literature reviews are provided in section 1.2.1. Parts of this chapter have been published in Wei et al. (2019b) and Wei et al. (2019a).

3.1 Periodic Gust Response of Airfoils

In light of discrepancies encountered in literature (cf. section 1.2.1), assessment of the validity and differences of the Sears and Atassi transfer functions requires careful consideration of inflow assumptions of each theory. These details will be discussed in 3.1.1. Derived inflow constraints will be used to generate tailored periodic gusts for each transfer function with an active grid, which is discussed in section 3.1.2. In this section the determination of lift response of airfoils from raw force measurements is also addressed. Experimental results of lift response measurements for both investigated transfer functions will be presented and compared to predictions in sections 3.1.3 and 3.1.4. Respective considerations also address a normalization approach to enable comparability of lift response under different inflow constraints and potential reasons for encountered deviations from theories. Facilities, measurement systems and processing methods used for the investigations presented below are discussed in section 2.1.

3.1.1 Theoretical Considerations

Sears and Atassi Formulations

Both investigated transfer functions relate the unsteady lift L_{dyn} from the gust-airfoil interaction to the quasi-steady lift L_{qs}, or the lift amplitude that would result from the same range of gust angles of attack in steady flow. They take the form

$$h_L = \frac{L_{dyn}}{L_{qs}} = \frac{\hat{L}_{dyn}}{\hat{L}_{qs}} e^{i\phi}, \tag{3.1}$$

where hats denote amplitudes and ϕ represents the phase shift between the dynamic and quasi-steady lift-force signals. The time phase of the gust is taken to be positive, in accordance with Atassi (1984). The dynamic lift in the Sears function is computed as a combination of quasi-steady, apparent-mass, and wake-circulation lift components. The Atassi function adds contributions from distortions of the flow field due to camber and mean angle of attack to the dynamic lift from the Sears function. Thus, the two theories are quite similar; the Atassi function is simply an extension of the Sears function.

Influence of the Streamwise Reduced Frequency $\mathbf{k_2}$

The most obvious difference between the theories of Sears and Atassi lies in the setup of the problem to be modeled. The Sears function involves only periodic velocity fluctuations in the component normal to the airfoil (v), as shown in Fig. 1.4. The theory of Atassi, in contrast, also includes periodic velocity fluctuations in the streamwise velocity component u. These fluctuations, shown in Fig. 1.5, are characterized according to Atassi's notation by the reduced frequency k_2, and the oscillations of the vertical velocity component, corresponding to those of the theory of Sears using the reduced frequency k_1. The waveform of these streamwise fluctuations runs normal to the airfoil at a velocity of $u = \pi \frac{fc}{k_2}$ (m/s), so that the streamwise velocity at any height in the flow fluctuates about the free-stream velocity with an amplitude of $\hat{u}$. When k_2 is zero, the streamwise velocity fluctuations are not present and the Atassi problem reduces to that of Sears. This is stated explicitly in the mathematical definition of the Atassi function. If the Sears function is denoted as $S(k_1)$, the Atassi function can be written as

$$h_L(k_1, k_2) = \frac{k_1}{|k|} S(k_1) + \alpha_\beta h_\beta(k_1, k_2) + \alpha_m h_m(k_1, k_2), \tag{3.2}$$

where $|k| = \sqrt{{k_1}^2 + {k_2}^2}$, α_β is the mean angle of attack of the airfoil, and α_m is the airfoil camber, representing the deviation of the camber line from the symmetric case. h_β and h_m are both relatively complicated functions of k_1 and k_2 and are defined in Atassi (1984). Both functions become zero when k_2 is zero. Additionally, for the purposes of this work, only unloaded airfoils, i.e. at zero mean angle of attack ($\alpha_\beta = 0$) and with zero camber ($\alpha_m = 0$) are considered, so that these terms do not contribute to the Atassi function h_L. From this definition, it is evident that the Atassi function is distinct from the Sears function if and only if $k_2 \neq 0$. Furthermore, for a symmetric airfoil at zero mean angle of attack, the Atassi function is directly related to the Sears function:

$$A(k_1, k_2) = \frac{k_1}{|k|} S(k_1). \tag{3.3}$$

Thus, the factor $\frac{k_1}{|k|}$ allows the Atassi and Sears functions to be directly compared. The profiles of these two functions are shown in Fig. 3.1. Without this adjustment factor, the Atassi function starts from zero at $k_1 = 0$ and increases monotonically. When $A(k_1, k_2)$ is multiplied by the adjustment factor, the Sears function is retrieved. Neither the camber correction term h_m nor the angle-of-attack correction term h_β factors into this comparison. This emphasizes the point that the fundamental difference between the theories of Sears and Atassi lies not in the corrections for flow-field distortion in the presence of the airfoil, as Cordes et al. (2017) hypothesized, but rather in the additional gust parameter k_2.

The influence of k_2 is clearly visible in the magnitudes of the resulting transfer functions, shown in Fig. 3.1. When k_2 takes on a constant nonzero value, the Atassi function displays an inverted trend with regard to the Sears function: rather than starting from unity and decreasing monotonically, the function starts from the origin and increases monotonically. At high reduced frequencies, both functions converge asymptotically onto the same trajectory. The addition of the camber correction term h_m serves only to shift the curve along the reduced-frequency axis. Similarly, the angle-of-attack correction term h_β causes the curve to rise more sharply at low reduced frequencies before falling asymptotically to match the Sears curve. For the purposes of this study, the importance of these correction terms is that neither is responsible for producing the inverted trend of the Atassi curve in relation to the Sears curve.

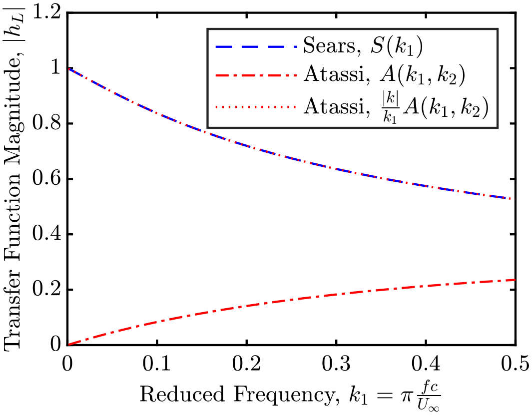

Figure 3.1: Profiles of the Sears and Atassi functions. The Atassi curve is given for $k_2 = 1$. When k_2 is zero, or when $A(k_1, k_2)$ is multiplied by $\frac{|k|}{k_1}$, the Atassi function collapses onto the Sears function. The phase remains the same, irrespective of the value of k_2. (Reprinted from Wei et al. (2019a), with permission of Cambridge University Press. © 2019 Cambridge University Press.)

Normalization of the Transfer Function

The importance of the k_2 parameter becomes more evident when the normalization of the two transfer functions is scrutinized. These factors are not used to compute the transfer functions themselves, but rather to normalize the unsteady lift force data obtained from gust response experiments ($\hat{L}_{dyn}$). They are therefore measures of the quasi-steady lift ($\hat{L}_{qs}$), which by definition must include a parameter to represent the strength of the unsteady gust fluctuations. For the Sears function, the factor is given by the relation

$$\hat{L}_{qs} = \pi \rho c U_\infty \hat{v} \approx \pi \rho c {U_\infty}^2 \hat{\alpha}_\mathrm{g}, \tag{3.4}$$

where $\hat{v}$ is the amplitude of the velocity fluctuations normal to the airfoil. Since $\hat{v} << U_\infty$, $\hat{v}$ can be approximated as being directly proportional to $\hat{\alpha}_{\mathrm{g}}$, the amplitude of the inflow angles of attack created by the gust. From this normalization, it is clear that the Sears function should be independent of the gust strength $\hat{v}$ and thus also independent of the gust angle amplitude $\hat{\alpha}_{\mathrm{g}}$.

Defining a gust strength is more difficult when the streamwise gust defined by k_2 is introduced. In Atassi's theory, a single parameter ϵ represents simultaneously the gust strength of the normal and streamwise velocity fluctuations. The amplitudes of the gusts in the streamwise and normal velocity components are given respectively as $\hat{u} = U_\infty \epsilon k_2 / |k|$ and $\hat{v} = U_\infty \epsilon k_1 / |k|$ (cf. Fig. 1.5). The gust strength is defined such that $\epsilon << 1$, implying that $\hat{u} << U_\infty$ and $\hat{v} << U_\infty$. This allows the gust strengths from the theories of Sears and Atassi to be compared via the physical quantity $\hat{\alpha}_{\mathrm{g}}$. The gust angle amplitude can thus be represented as

$$\hat{\alpha}_{\mathrm{g}} = \arctan\left(\frac{\hat{v}}{U_\infty + \hat{u}}\right) \approx \arctan\left(\frac{\hat{v}}{U_\infty}\right) \approx \epsilon \frac{k_1}{|k|}. \tag{3.5}$$

When k_2 is zero, the gust strength ϵ is simply $\hat{\alpha}_{\mathrm{g}}$, as for the Sears function. When k_2 takes a nonzero value, a constant value of ϵ means that $\hat{\alpha}_{\mathrm{g}}$ becomes a monotonically increasing function of k_1. Thus, the gust strength in the Atassi problem is not strictly tied to the physical quantity $\hat{\alpha}_{\mathrm{g}}$. This is important for the normalization of the Atassi function, given by

$$\hat{L}_{qs} = \pi \rho c {U_\infty}^2 \epsilon. \tag{3.6}$$

Since the factor $\frac{|k|}{k_1}$ appears in equation 3.5, exchanging ϵ for $\hat{\alpha}_{\mathrm{g}}$ in this normalization is mathematically equivalent to applying the adjustment factor from equation 3.3. This confirms that the Sears and Atassi functions are related by a factor of $\frac{|k|}{k_1}$, which is already evident from equation 3.2. In this work, both normalizations for the Atassi function are considered, in order to demonstrate that they are both valid.

The normalization of the transfer functions thus allows a wide range of experimental conditions to be captured by a single curve defined only by k_2, provided that the parameters k_2, $\hat{\alpha}_{\mathrm{g}}$, and by extension ϵ, can be controlled and accurately measured.

Significance for Experiments

The mathematical details outlined above are important considerations for the setup of experiments investigating the Sears and Atassi problems. They show that control over the fluctuations in the streamwise velocity is required for the comparison of the transfer functions. Thus, to reproduce the conditions of the Sears problem, $\hat{u}$ must be kept as small as possible so that k_2 can be set to zero. If this condition is not taken into account, then the resulting conditions will be those of the Atassi problem and not strictly those of Sears. No previous study has considered systematically controlling the oscillations in u while performing Sears measurements, and therefore a central goal of this study is to demonstrate the importance of this distinction in an experimental context.

In addition, in order to compute experimental transfer function values from unsteady lift force data, the parameter $\hat{\alpha}_{\mathrm{g}}$ must be accurately determined, and the correct normalizations for the transfer functions in question must be employed. In previous studies (e.g. Cordes et al., 2017), the proper normalization for the transfer functions had not been clarified, and $\hat{\alpha}_{\mathrm{g}}$ was not characterized over the entire range of experimental gust conditions. If data are to be compared directly with the Atassi function, values for the parameters k_2 and ϵ must also be known. These can be difficult to quantify accurately in experiments. All of these considerations must be accounted for in experiments seeking to compare the two transfer functions.

The transfer function phase profiles for the Sears and Atassi functions are identical when camber and mean angle of attack are both zero, irrespective of the values of k_2, ϵ, and $\hat{\alpha}_{\mathrm{g}}$. Therefore, the phase is not considered in detail here.

3.1.2 Experimental Considerations

Active Grid Setup

Because the parameters k_2 and $\hat{\alpha}_\mathrm{g}$ are important for the experimental validation of and comparison between the Sears and Atassi functions, careful attention must be paid to the construction of an apparatus to produce and control gusts with the required character. The flows produced should be as two-dimensional as possible to avoid the influence of three-dimensional unsteady effects on the experimental data. To this end, nine two-dimensional vanes, shown in Fig. 2.1, replaced the arrays of diamond shaped paddles used in the experiments of Cordes et al. (2017). In addition, relations had to be defined so that the gust angle amplitude $\hat{\alpha}_\mathrm{g}$ could be controlled for any given combination of a grid motion frequency and free-stream velocity.

The Sears formulation of the gust response problem requires gusts composed purely of sinusoidal fluctuations in v, normal to the airfoil. This implies that in the area above and below the airfoil, fluctuations in u need to be minimized across the height of the wind tunnel. Formulated in the terminology of Atassi's theory, this means that k_2 effectively has to be zero.

The Atassi formulation of the problem, on the other hand, is distinguished from the Sears function by the presence of these u-fluctuations. For these experiments, the theory of Atassi was interpreted such that the u- and v-velocities fluctuate with the same frequency, so that both could be controlled by the active grid while keeping k_1 and k_2 independent from each other.

Active Grid Protocols

In order to achieve these two gust scenarios using the new active grid setup, two different grid motion protocols and two different grid configurations were developed. The two motion protocols were defined for the full set of nine vanes. The first protocol, called the focused protocol, involved setting the nine vanes so that their chord lines were all focused to a single point on the test airfoil. As the vanes oscillated, the focal point of the vanes moved across the height of the wind tunnel. This moving focal point directed the flow in a sweep across the height of the tunnel, producing significant fluctuations in u around the test airfoil. This also allowed relatively high gust amplitudes to be maintained for lower grid frequencies and higher free-stream velocities. The second protocol, termed the limited protocol, was simpler, involving basic sinusoidal motions for all vanes. The top and bottom two vanes, however, were limited in their motions so that they would not direct flow into the tunnel walls and create unwanted fluctuations. The full range of the vane motions (i.e. twice the amplitude) is defined as $\hat{\theta}$.

In addition to these two grid protocols, the central three vanes of the active grid could be removed, leaving the grid in a six-vane configuration. This construction removed the influence of the wakes of the grid vanes on the test airfoil, which were in part responsible for the fluctuations in u in the nine-vane grid configuration. Similar configurations have been used by Ham et al. (1974) and Lancelot et al. (2015) to produce pure sinusoidal fluctuations in v without disturbing the regularity of u. This helped to minimize fluctuations in u, in accordance with the assumptions of the Sears function; thus it was only used with the limited protocol. Because of this, in combination with the lack of influence from the central three vanes, the gust amplitudes achievable in this configuration were smaller than those from the nine-vane configuration. Conversely, the nine-vane grid configuration was only used with the focused protocol, so that the fluctuations in u could be maximized, according to the prescriptions of the Atassi function.

Therefore, when the six-vane grid configuration is referenced in this work, it will be assumed that limited protocols were utilized. Similarly, the nine-vane grid configuration will imply that focused protocols were employed.

Lift Response Determination

To compute transfer functions from experimental data, the force data were first shifted from the airfoil frame of reference to that of the wind tunnel. The first two seconds of each data set were discarded in order to remove start-up effects. A Fourier transform of the signal yielded the magnitude of the lift force fluctuations, corresponding to $\hat{L}_{dyn}$ from equation 3.1. For the Sears function, the quasi-steady lift amplitude $\hat{L}_{qs}$ was interpolated from steady lift curves L_{U_∞} using the relation

$$\hat{L}_{qs} = f(U_\infty, \hat{\alpha}_g, \alpha_m) = \frac{1}{2}\big(L_{U_\infty}(\alpha_m + \hat{\alpha}_g) - L_{U_\infty}(\alpha_m - \hat{\alpha}_g)\big). \tag{3.7}$$

Because α_m in these experiments was always zero, this was approximately equivalent to

$$\hat{L}_{qs} = \frac{\partial L_{U_\infty}}{\partial \alpha} \hat{\alpha}_g, \tag{3.8}$$

where $\frac{\partial L_{U_\infty}}{\partial \alpha}$ represents the lift slope of the airfoil as computed from a fit of the linear portion of the steady lift curve. This is the experimental equivalent of the ideal quasi-steady lift factor given in equation 3.4, since a value for the lift slope that reflected the test airfoil used in experiments was preferable to the theoretical lift slope $\pi \rho c {U_\infty}^2$. This modified form was used to compute $\hat{L}_{qs}$ for the Atassi function, with ϵ substituted for $\hat{\alpha}_g$. ϵ was computed from equation 3.5. To compare the Atassi function directly with the Sears function, the quasi-steady lift expression given in equation 3.8 was used instead of relying on values of ϵ and k_2, which were not measured directly.

The data points were validated using both force balance data and, for the six cases in which stereo PIV was employed, phase averaged velocity vector fields. Error bars were computed from the standard deviation of the phase averaged lift force signal and the standard deviation of the gust angle amplitudes from hot-wire data. For data taken at $U_\infty = 10$ m/s, no hot-wire data was available, and therefore gust angle amplitudes were extracted from the stereo PIV vector fields and errors were estimated.

3.1.3 Measurement Results and Discussion

Inflow characterization for the Atassi problem

In order to verify that distinct inflow conditions for the Sears and Atassi problems could be produced with the active grid configurations detailed above, the flow in the wind tunnel was characterized using hot-wire anemometers and stereo PIV, and additionally with numerical simulations of the wind tunnel.

For each combination of reduced frequencies k_1 and grid amplitude $\hat{\theta}$, a gust angle amplitude $\hat{\alpha}_\mathrm{g}$ was computed from the phase averaged velocity data. An example data set for $\hat{\theta} = 10°$ with the nine-vane grid configuration is shown in Fig. 3.2.

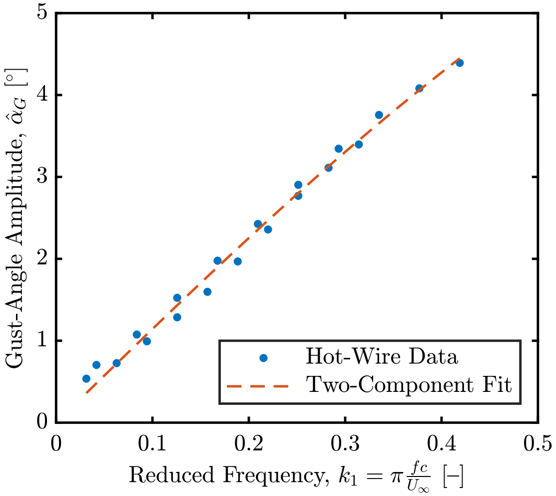

Figure 3.2: Two-parameter fit (based on equation 3.5) of hot-wire data taken behind the nine-vane active grid configuration at the location of the leading edge of the test airfoil, for ten grid frequencies and three free-stream velocities. The grid vanes oscillated through $\hat{\theta} = 10°$. (Reprinted from Wei et al. (2019a), with permission of Cambridge University Press. © 2019 Cambridge University Press.)

For every combination of frequency and free-stream velocity, $\hat{\alpha}_g$ was plotted against $\hat{\theta}$, and a power-law fit was applied to the data. The standard deviation of $\hat{\alpha}_g$ was used to demarcate the region of the parameter space where the grid produces gusts with the quality required by the stringent constraints of the Sears and Atassi theories. Using these fits and limits, given desired values for $\hat{\alpha}_g$ and k_1, a corresponding grid amplitude could be selected so that gusts with the right character would be produced.

Additionally, for the data sets taken behind the nine-vane grid configuration, a two-parameter, nonlinear-regression fit based on equation 3.5 was employed to model the data. Through this type of fit, estimates for ϵ and k_2 were computed. As shown in Figs. 3.3a and 3.3b, between $\hat{\theta} = 10°$ and $\hat{\theta} = 25°$, ϵ increased linearly with $\hat{\theta}$, and k_2 remained approximately constant within confidence intervals.

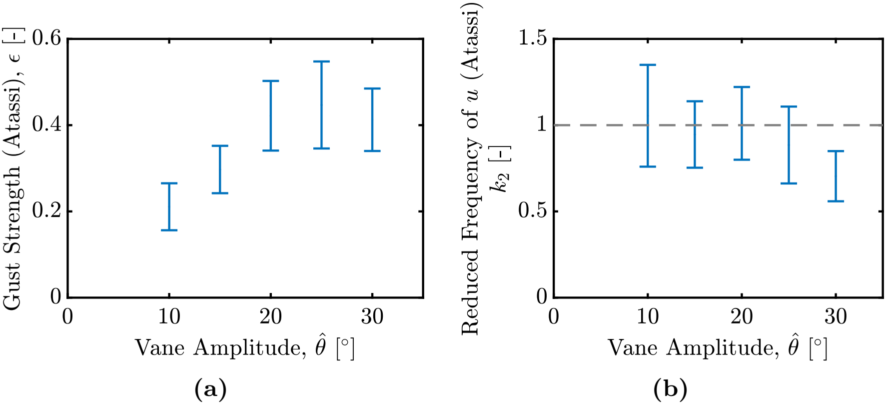

Figure 3.3: Estimated values for the parameters k_2 and ϵ for various vane amplitudes in the grid nine-vane configuration, computed using the type of fit shown in Fig. 3.2. At most vane amplitudes, ϵ increased monotonically and k_2 remained relatively constant. The value of k_2 used in these experiments is represented as a dashed line. (Reprinted from Wei et al. (2019a), with permission of Cambridge University Press. © 2019 Cambridge University Press.)

From $\hat{\theta} = 25°$ on, the effects of full stall on the grid vanes caused these trends to break down. For the nine-vane grid configuration, the grid amplitude could be correlated to the Atassi definition of gust strength as long as stall effects were not considerable. More importantly, the data provided an estimate for k_2 – the distinguishing factor between the Sears and Atassi theories – that remained at a constant nonzero value across the range of grid amplitudes employed in the experiments. The average of the estimates below $\hat{\theta} = 25°$, $k_2 = 1.0$, was used to compute Atassi function values for all experiments using the nine-vane grid configuration, since most of the amplitudes used in this study were within the range $5° < \hat{\theta} < 25°$.

These results were confirmed in experiments and simulations of the active grid without the test airfoil installed. The u component of the flow velocity is shown to fluctuate significantly in time and across the height of the wind tunnel in Fig. 3.4, which compares PIV data taken in experiments with data from corresponding numerical simulations.

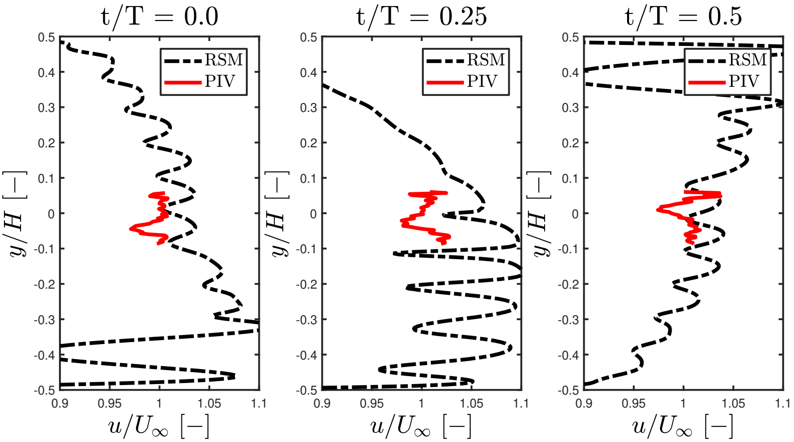

Figure 3.4: Variation of the normalized velocity fluctuations in u across the height of the wind tunnel with the active grid running a focused protocol in its nine-vane configuration, from simulations and experiments. The plots represent different dimensionless time instants t/T within one gust period, and $y/H = 0$ represents the location of the leading edge of the airfoil. It is clear that u varies significantly in space and time, implying that k_2 is nonzero. (Reprinted from Wei et al. (2019a), with permission of Cambridge University Press. © 2019 Cambridge University Press.)

The experimental data were limited in scope by the width of the laser sheet, whereas the simulations resolved the entire cross-section of the wind tunnel. The numerical results suggest further that the likely cause of these fluctuations lies in the combination of the wake profiles of the vanes in the center region of the tunnel and the use of focused protocols, which are responsible for the large-scale undulations in velocity across the height of the tunnel. These results confirmed that the value of k_2 for the Atassi function is significantly greater than zero for the nine-vane configuration.

Inflow characterization for the Sears problem

The hot-wire data were also used to determine relationships between $\hat{\alpha}_{\mathrm{g}}$ and $\hat{\theta}$ for the six-vane grid configuration. Since the goal of using this grid configuration was to achieve $k_2 \approx 0$, it was not necessary to estimate k_2 and ϵ using the two-parameter fits discussed above. Thus, the fluctuations in the

u-component of the flow velocity were observed as an indicator of the presence of a significant k_2-fluctuation in the same manner as described in the section above. To this end, results from both stereo PIV experiments in the empty tunnel and numerical simulations of the setup were compared. Figs. 3.5 and 3.6 show the experimental and simulated properties of the flow field from grid motions at $f = 10\,\text{Hz}$, $U_\infty = 15$ m/s and $\hat{\theta} = 11.73\,°$.

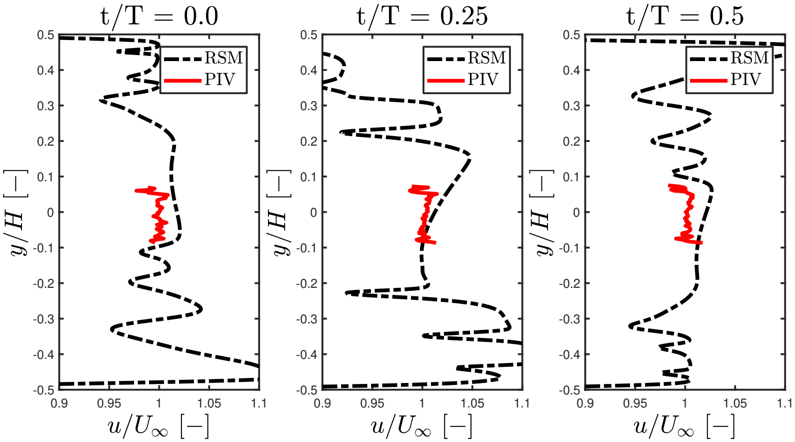

Figure 3.5: Variation of the normalized velocity fluctuations in u across the height of the wind tunnel with the active grid running a limited protocol in its six-vane configuration, from simulations and experiments. Three dimensionless time instants t/T within one gust period are given. Here, u remains effectively constant in the region of the test airfoil, implying $k_2 = 0$. (Reprinted from Wei et al. (2019a), with permission of Cambridge University Press. © 2019 Cambridge University Press.)

The u-profile across the height of the tunnel, shown in Fig. 3.5, remained relatively uniform across the central region of the tunnel in both simulations and experiments, with no evidence of the temporal and spatial fluctuations present in Fig. 3.4 that signified a nonzero k_2. Additionally, the fluctuations of u in time were very small (on the order of 1 % of U_∞), further suggesting that k_2 for the six-vane grid configuration was effectively zero. The fact that the PIV data and data from the numerical simulations exhibited such strong agreement suggests that the simulations can be used reliably to characterize the inflow conditions in the tunnel in the region of the test airfoil.

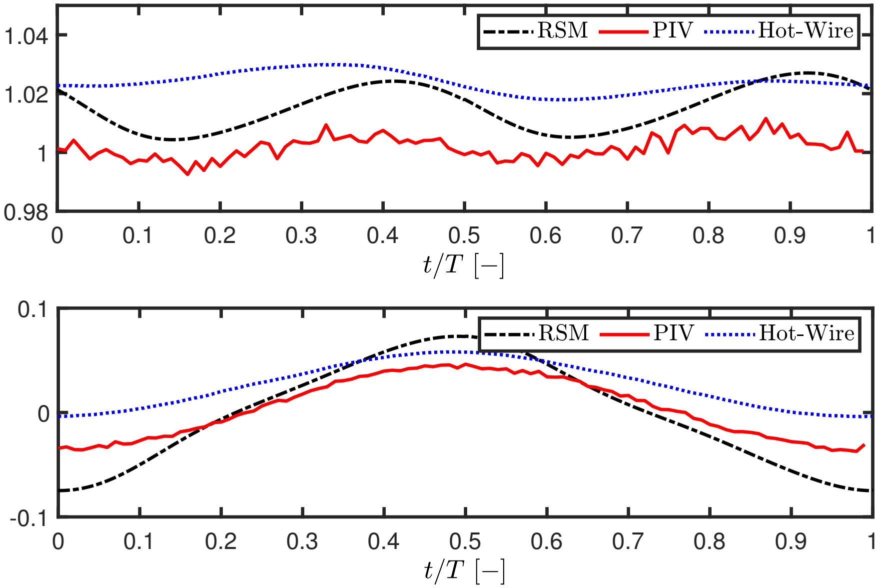

Figure 3.6: Evolution of the normalized velocity fluctuations in u and v over a single gust period with the six-vane configuration and limited protocols, from simulations and experiments (PIV and hot-wire probe data). The data agree remarkably well in magnitude and trend, showing that the variations in u are small and thus that $k_2 \approx 0$. (Reprinted from Wei et al. (2019a), with permission of Cambridge University Press. © 2019 Cambridge University Press.)

Measurements of the Sears Problem

After the flows produced by the active grid had been characterised, the two grid configurations were used to investigate the Sears and Atassi functions in their respective flow situations. The Sears function was tested using the six-vane grid configuration and limited grid protocols. Tests were conducted using two free-stream velocities of $U_\infty = 15$ and $20\,\mathrm{m/s}$ (corresponding to Reynolds numbers of $200,000$ and $260,000$) over a range of gust frequencies, with vane amplitudes tuned to produce gusts with $\hat{\alpha}_\mathrm{g} = 2°$. This amplitude was chosen to avoid dynamic effects and flow separation on the thin airfoil while maintaining a high enough signal-to-noise ratio from the force balances. The experimental data from this investigation are shown in Fig. 3.7.

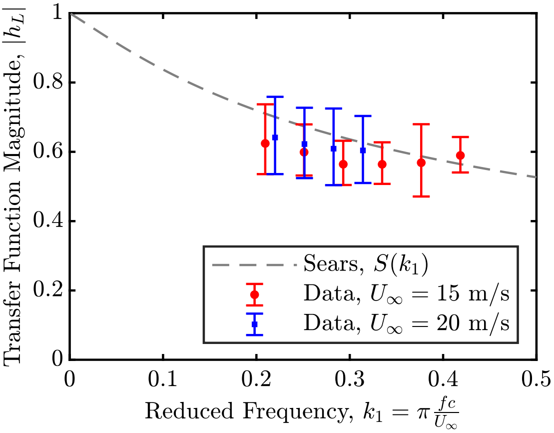

Figure 3.7: Gust response of a NACA 0006 airfoil under Sears inflow conditions for a variation of the reduced frequency k_1 and a gust-angle amplitude of $\hat{\alpha}_g = 2°$. Aside from the single outlier, the data follow the general trend of the Sears function. (Reprinted from Wei et al. (2019a), with permission of Cambridge University Press. © 2019 Cambridge University Press.)

These data follow the trend of the Sears function reasonably well within one standard deviation.

To verify that $\hat{\alpha}_g$ does not affect experimental correspondence with the Sears function, a series of gusts with $\hat{\alpha}_g = 3°$ was also tested. These data, shown in Fig. 3.8, lie slightly above the $\hat{\alpha}_g = 2°$ data, likely because of the dynamic effects that would have enhanced the amplitude of the lift fluctuations at this relatively high angle of attack. However, the data still follow the Sears trend within one standard deviation, thus confirming that the shape of the Sears function holds irrespective of gust strength, as long as flow separation does not occur. Values of $\hat{\alpha}_g$ smaller than 2° were also tested, but these did not exhibit a clear trend due to the influence of noise.

In order to improve the convergence of the experimental data onto the Sears function, further measures were taken to ensure that the experimental flow conditions conformed to the stipulations of the Sears problem. Because of the thin profile of the NACA 0006 airfoil, flow separation was predicted by XFOIL to occur on the airfoil even at low angles of attack. To hinder

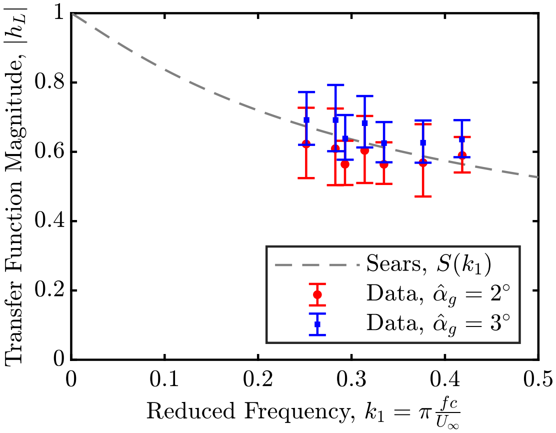

Figure 3.8: Gust response of a NACA 0006 airfoil under Sears inflow conditions for a variation of the reduced frequency k_1. Two gust angle amplitudes ($\hat{\alpha}_\mathrm{g} = 2°$ and $\hat{\alpha}_\mathrm{g} = 3°$) are shown. As predicted by the theory, there is little difference between the two cases. The slight offset in the 3° case could be due to the onset of dynamic stall effects on the thin airfoil. (Reprinted from Wei et al. (2019a), with permission of Cambridge University Press. © 2019 Cambridge University Press.)

these deviations from the theory, thin strips of tape were applied to the airfoil in order to trip transition to turbulence in the boundary layer. The strips of tripping tape used were 3.5 mm wide and 0.1 mm thick, and were placed symmetrically on both sides of the airfoil. Three separate locations along the chord of the airfoil were tested: $x = 0.05c$, $0.10c$, and $0.40c$. Static lift-drag measurements at zero angle of attack showed an increase in the total drag over the case of the airfoil without tape for free-stream velocities between 10 and 25 m/s, implying higher skin friction on the airfoil surfaces due to turbulence in the boundary layer. Additionally, the linear regime of the lift slope was extended when tape was present, especially at higher free-stream velocities. These observations strongly suggested that the tripping tape was effective in inducing transition to turbulence in the boundary layers on the airfoil. Each of the three tape locations was tested over the set of reduced

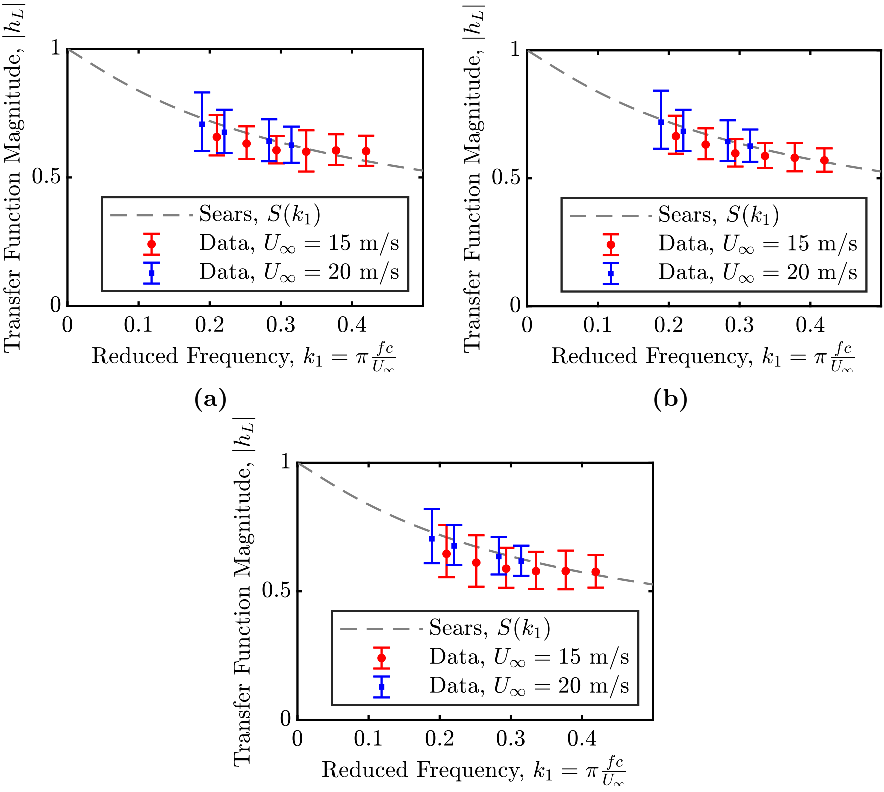

(a) **(b)**

(c)

Figure 3.9: Gust response of a NACA 0006 airfoil under Sears inflow conditions for a variation of the reduced frequency k_1 at $\hat{\alpha}_g = 2°$, with the addition of tripping tape at (a) 5 %, (b) 10 %, and (c) 40 % of the chord length behind the leading edge. The convergence to the Sears function was significantly improved from the clean airfoil configuration, with the best agreement observed in case (b). (Reprinted from Wei et al. (2019a), with permission of Cambridge University Press. © 2019 Cambridge University Press.)

frequencies and free-stream velocities from the original Sears function series. The data from these series of experiments are shown in Figs. 3.9a, 3.9b, and 3.9c.

In all three cases, the correspondence with the Sears function is significantly improved compared to the case without tape given in Fig. 3.7. This result itself confirms in retrospect that the tripping tape did indeed affect the character of the boundary layer, as all other experimental parameters remained the same between the series. The degree of correspondence can be quantified by comparing the mean square error between each data set and the Sears function: for the tape locations of $x = 0.05c$, $0.10c$, and $0.40c$, the mean square errors were 8.79×10^{-4}, 6.62×10^{-4}, and 1.36×10^{-3}. These values are significantly lower than the case without tripping tape, which had a mean square error of 3.04×10^{-3}. The best convergence was observed in the case where the tripping tape was located nearest to the point of greatest curvature on the airfoil.

Jancauskas and Melbourne speculated that the physical cause of the improved convergence with increasing turbulence intensity lay in the fact that turbulent flows generally follow the shapes of profiles better than laminar flows. According to this line of reasoning, flows with high levels of background turbulence would reduce separation and boundary-layer thickness effects, thereby making the overall flow field fit the assumptions of Sears more closely. The ambiguity with their experiments, however, was that the incoming gusts themselves were turbulent, and therefore the root cause of the effect could not be localized to the surface of the test profile itself. In this study, the gusts produced had very low levels of background turbulence, and therefore the cause of the improved convergence could be isolated to the surface of the airfoil. The character of the boundary layer on the airfoil is thus a critical parameter for determining how well the Sears function matches experimental data. The mechanism by which this occurs remains unclear. The hypothesis of Jancauskas and Melbourne is still a feasible explanation; another explanation could stem from the argument that the transport of momentum from the gust to the airfoil is more effective in turbulent rather than laminar boundary layers. The latter hypothesis would explain why no clear trend was found when gusts with $\hat{\alpha}_\mathrm{g} = 1°$ were used. In either case, the results presented here demonstrate that the presence of turbulent boundary layers on an airfoil leads to better correspondence with the Sears function. This finding is rather counterintuitive in light of the potential flow assumptions of the Sears theory, and suggests that the Sears function may be far more applicable in real-world flow situations than its first-order origins would let it appear. This particular hypothesis will be addressed in future studies.

Measurements of the Atassi Problem

In order to validate the Atassi function in experiments, the nine-vane grid configuration was employed. As for the Sears function, an initial range of reduced frequencies was tested with a constant gust-angle amplitude of $\hat{\alpha}_\mathrm{g} = 2°$. It has been shown that though the Atassi function is normalized by the gust-strength parameter ϵ, multiplying the function by the adjustment factor $\frac{|k|}{k_1}$ is equivalent to normalizing the function by $\hat{\alpha}_\mathrm{g}$. To demonstrate this fact experimentally, the same set of data is shown in Figs. 3.10a and 3.10b, normalized by ϵ and $\hat{\alpha}_\mathrm{g}$ and compared against $A(k_1, k_2)$ and $\frac{|k|}{k_1} A(k_1, k_2)$ respectively.

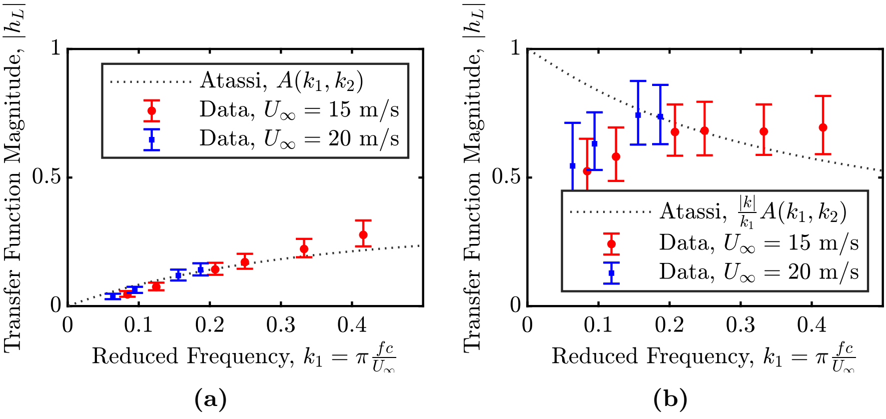

Figure 3.10: Gust response of a NACA 0006 airfoil under Atassi inflow conditions for a variation of the reduced frequency k_1 with $k_2 = 1$ and $\hat{\alpha}_\mathrm{g} = 2°$, with the data normalized by the gust strengths ϵ (a) and $\hat{\alpha}_\mathrm{g}$ (b). Reasonable agreement with theory is observed for $k_1 \gtrsim 0.15$. (Reprinted from Wei et al. (2019a), with permission of Cambridge University Press. © 2019 Cambridge University Press.)

For the former case, the value of k_2 was fixed at $k_2 = 1$, taken from the analysis of the hot-wire probe data detailed previously. Under both normalizations, the data generally follow the theoretical predictions within the measurement uncertainty for $k_1 > 0.15$. The difference in the sizes of the error bars is due to the differences in the magnitudes of the values of the transfer function. The error bounds are significantly larger than those observed in equivalent Sears function experiments. Furthermore, what appear to be slight deviations from $A(k_1, k_2)$ for $k_1 < 0.15$ are shown to be significant departures from the adjusted function $\frac{|k|}{k_1} A(k_1, k_2)$. The reason for these departures will be discussed below. For the purposes of comparison with the Sears function, the data presented in all subsequent plots will be normalized by $\hat{\alpha}_\mathrm{g}$ and plotted with the adjusted Atassi function.

Since the Atassi function, like the Sears function, does not depend on the gust strength, changes in the gust strength parameters ϵ and $\hat{\alpha}_\mathrm{g}$ should not affect the trends observed in the properly normalized experimental data. Since these parameters are related through equation 3.5, either one can be held constant over a given range of reduced frequencies by setting the vane amplitude $\hat{\theta}$ of the active grid accordingly. As outlined for the six-vane grid configuration used to validate the Sears function, changing $\hat{\theta}$ allows $\hat{\alpha}_\mathrm{g}$ to be controlled for a given value of k_1. ϵ, on the other hand, scales proportionally with $\hat{\theta}$ without depending on k_1 (cf. Fig. 3.3a), thus implying that a constant $\hat{\theta}$ yields a constant value of ϵ irrespective of k_1 and $\hat{\alpha}_\mathrm{g}$. The latter variant was employed by Cordes et al. (2017) using the older, three-dimensional configuration of the Oldenburg active grid.

A range of grid amplitudes and gust angle amplitudes was therefore tested in order to demonstrate that the Atassi function is independent of both $\hat{\alpha}_\mathrm{g}$ and ϵ. The results for $10° \leq \hat{\theta} \leq 20°$ and $1° \leq \hat{\alpha}_\mathrm{g} \leq 3°$ are shown in Figs. 3.11a and 3.11b, respectively. As expected, the trend of the data remained unchanged, including the deviation of the data from theoretical predictions for $k_1 < 0.15$. This confirmed that both definitions of gust strength worked in practice to collapse the data, further supporting the idea that the Atassi function is simply an extension of the Sears function.

Numerical simulations of a similar problem confirmed these results. These simulations were carried out to model the experiment of Cordes et al. (2017), which had obtained a general Atassi trend despite the use of an incorrect normalization. A Clark-Y profile (11.7 % thickness) with a chord length of $c = 0.18\,\mathrm{m}$ and at zero angle of attack was used as the test airfoil, and 2D RSM

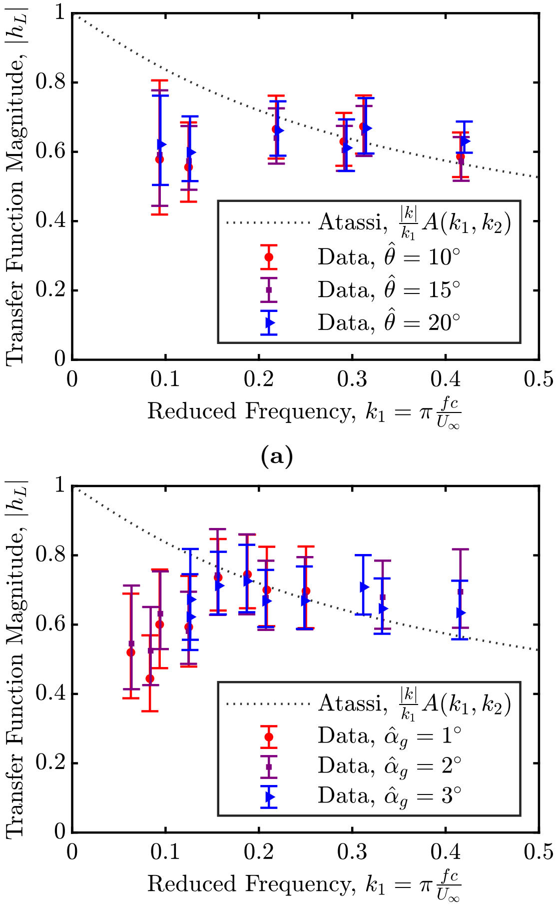

(a)

(b)

Figure 3.11: Gust response of a NACA 0006 airfoil under Atassi inflow conditions for a variation of the reduced frequency k_1, across variations in (a) the vane amplitude $\hat{\theta}$ and (b) the gust-angle amplitude $\hat{\alpha}_g$. In both cases, the data follow the trend of the Atassi function for $k_1 \gtrsim 0.15$. (Reprinted from Wei et al. (2019a), with permission of Cambridge University Press. © 2019 Cambridge University Press.)

simulations were carried out at three free-stream velocities and a range of grid frequencies. The grid was modeled with focused protocols and amplitudes of $\hat{\theta} = 30°$, thus producing gusts with non-negligible fluctuations in u. The forces on the airfoil were computed from the flow field. More information regarding the setup of these simulations is given in Wegt (2017), and the resulting transfer-function values are shown in Fig. 3.12.

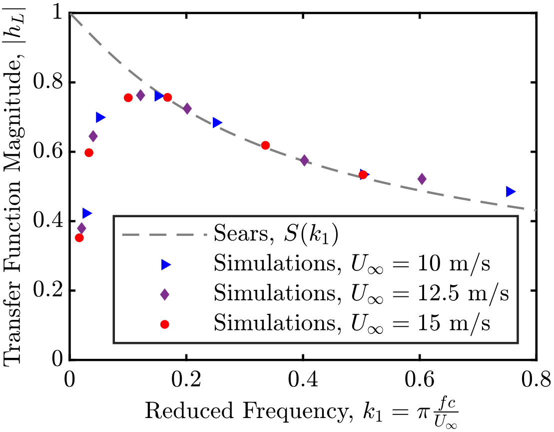

Figure 3.12: 2D RSM simulations of the setup of Cordes et al. (2017) with a Clark-Y airfoil and using a nine-vane active-grid configuration. Despite the use of a different type of airfoil, there is very good agreement between these simulations and the experiments shown in Figs. 3.11a and 3.11b. (Reprinted from Wei et al. (2019a), with permission of Cambridge University Press. © 2019 Cambridge University Press.)

In spite of the use of different airfoil profiles, the same trend as that observed in the experiments detailed above was retrieved in the numerical data. Most strikingly, the deviation from the Sears and adjusted Atassi functions occurred in the simulations at around the same reduced frequency of $k_1 \approx 0.15$.

All of the data presented thus far align well with the Atassi function for $k_1 > 0.15$, but deviate from theoretical predictions for $k_1 < 0.15$. This deviation is systematic across the range of free-stream velocities, grid frequencies, and gust strengths $\hat{\alpha}_g$ and ϵ tested in these experiments, and will be shown in the next section to be a consequence of the experimental apparatus and not of any failings of the theory of Atassi. The data for $k_1 > 0.15$ for both the Sears and Atassi functions demonstrate quite clearly that the adjusted Atassi function is identical to the Sears function irrespective of the value of k_2. This confirms the analysis of the two models presented in section 2, and suggests that the Sears function can be used to model the behavior of a thin symmetric airfoil subjected to streamwise and normal gusts at zero mean angle of attack. Mathematically, this is not a novel result. The experiments presented here, however, provide a helpful framework for past and future experimental investigations. For example, these observations offer an explanation for the trends seen in previous experiments involving gusts generated by a turbulence grid (e.g. Larose, 1999; Hatanaka & Tanaka, 2002; Lysak et al., 2016). The gusts in these studies would have had significant k_2 gust components, and therefore would have been better represented by the Atassi function. However, since all of these data were normalized by the Sears gust strength $\hat{\alpha}_\mathrm{g}$ instead of the Atassi gust strength ϵ, each was able to retrieve a clear Sears trend.

Influence of Inflow Turbulence Level

It has been noted that the convergence of the data around the Atassi function appears to be worse than that observed in the Sears function experiments, and that the data fail to follow the Atassi function for $k_1 < 0.15$. These idiosyncrasies are effects of the turbulent wakes of the central vanes in the nine-vane grid configuration.

Jancauskas & Melbourne (1983) showed that increasing the background turbulence intensity in gusty flows on bridge-deck sections leads to better correspondence with the Sears function. In the nine-vane grid configuration, the wakes of the central vanes were responsible for higher turbulence intensities in the flows impinging on the airfoil than in the six-vane grid configuration where the middle section of the tunnel was free from disturbances. This was determined using the hot-wire probe data from the tunnel characterisation experiments. A centered moving average over 200 data samples was applied to each velocity component in order to extract the turbulent velocity fluctuations from the generally sinusoidal velocity profile of the gust. A turbulence intensity was then computed from these two velocity fluctuation components for every combination of k_1 and $\hat{\theta}$ tested. The distribution of these turbulence intensity values is represented in Fig. 3.13.

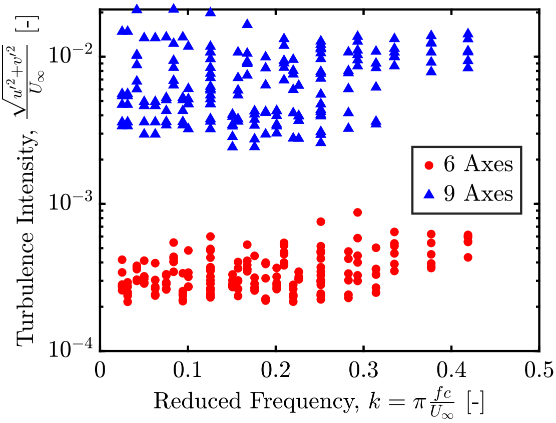

Figure 3.13: Turbulence intensities of the fluctuation velocities from the six- and nine-vane grid configurations, computed from hot-wire measurements at the position of the leading edge of the test airfoil. The turbulence intensities behind the nine-vane grid were consistently higher than those behind the six-vane grid. (Reprinted from Wei et al. (2019a), with permission of Cambridge University Press. © 2019 Cambridge University Press.)

From these data, it is clear that the central three axes in the nine-vane grid configuration generated uniformly higher background turbulence levels than were observed in the six-vane grid configuration.

One would expect, then, that the Atassi data would converge to the theoretical predictions more cleanly than the Sears data. This, however, was not the case. Here, it is necessary to distinguish between background turbulence and turbulent fluctuations within the gust itself. The experimental apparatus of Jancauskas and Melbourne used a turbulence-generating screen to produce nominally homogeneous turbulence, on top of which a fluctuating velocity signal was overlaid by their gust generation apparatus. In the present study, by contrast, the source of the turbulence intensity was the wakes of the central vanes of the active grid. The test airfoil would pass in and out of these turbulent wakes, leading to alternating smooth and turbulent flow conditions within a single gust period. This intermittent turbulent effect was not captured by the values of $\hat{\alpha}_g$ used to normalize the experimental data, since these were computed from phase averaged velocity signals. To quantify the extent of this effect, in addition to computing the gust-angle amplitude from the phase-averaged velocity signals, the peak velocity values within each gust period were isolated, and an average amplitude and corresponding angle of attack, $\hat{\alpha}_{peak}$, was computed from these local maxima. The ratio of $\hat{\alpha}_{peak}$ to $\hat{\alpha}_{\mathrm{g}}$ for a range of grid protocols with $10° \leq \hat{\theta} \leq 30°$ is plotted in Fig. 3.14.

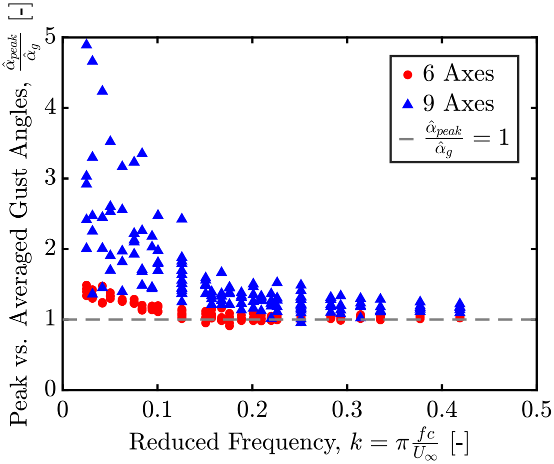

Figure 3.14: The ratio of peak gust angle amplitude $\hat{\alpha}_{peak}$ to phase-averaged gust-angle amplitude $\hat{\alpha}_{\mathrm{g}}$ from the six- and nine-vane grid configurations, computed from hot-wire measurements. Values of $\frac{\hat{\alpha}_{peak}}{\hat{\alpha}_{\mathrm{g}}} \gtrsim 2$ represent a strong influence of the wakes of the central vanes on the character of the gust. (Reprinted from Wei et al. (2019a), with permission of Cambridge University Press. © 2019 Cambridge University Press.)

The plot shows that the peak velocity fluctuations were significantly larger than unity for $k_1 \lesssim 0.15$, and remained close to unity for $k_1 \gtrsim 0.15$. These results demonstrate that the intermittent turbulent fluctuations caused by the wakes of the central vanes had a significant effect on the quality of the gusts produced by the active grid precisely in the reduced frequency regime, in which a deviation from theory was observed in the data. The large instantaneous angles of attack from the turbulence in the gust, combined with the high frequencies of this forcing, contributed to a diminished gust response of the airfoil in this regime. These turbulent peaks were much less significant for $k_1 \gtrsim 0.15$, implying that the data for these higher reduced frequencies are free from the influence of the vane wakes. Preliminary simulations using oscillating inflow conditions instead of simulated vanes to produce gusts confirmed that data at low reduced frequencies follow the Sears and adjusted Atassi trend when the influence of the grid is removed (cf. Wegt, 2017).

The effect of turbulence on the gust response of airfoils thus depends heavily on the character of the turbulence in question. Jancauskas & Melbourne (1983) showed that homogeneous background turbulence can improve correspondence with the Sears function. The experiments with tripping tape presented in this work have demonstrated that inducing turbulence in the boundary layer of an airfoil can similarly improve convergence. This suggests that small-scale homogeneous turbulence enhances the ability of the flow to interact with the airfoil, by facilitating momentum transport through the boundary layer or by hindering separation on surfaces with an adverse pressure gradient. Large-scale intermittent turbulent fluctuations, on the other hand, have been shown to increase experimental uncertainty and cause significant deviations from theoretical predictions at low reduced frequencies. Because these turbulent fluctuations are large in magnitude and frequency content compared to the baseline sinusoidal gust signal, reconciling their effects with the predictions of the Sears and Atassi functions is a nontrivial problem that lies beyond the scope of this work. This problem, however, is similar to the interaction of an airfoil with a periodic vortical gust disturbance, and could be of interest to several applications in aerodynamics, such as formation flight in flocks.

3.1.4 Discussion and Conclusions

It has been demonstrated that no fundamental difference between the Sears and Atassi functions exists, outside of an adjustment factor of $\frac{|k|}{k_1}$. In practice, this implies that the Sears function can be applied even when significant fluctuations in u are present, as long as the data are normalized appropriately. These conclusions have been confirmed in experiments, where the gust conditions were generated using an active grid and were characterized and controlled to an unprecedented degree. Both transfer functions have been demonstrated to be robust across the range of parameters taken into account by the models.

Additionally, some effects of turbulence on the gust response of airfoils have been characterized. Small-scale fluctuations within a turbulent boundary layer can lead to improved correspondence with the predictions of the analytical models. Experiments investigating the effect of gusts on momentum transfer through laminar and turbulent boundary layers would shed light on the physical mechanism responsible for this phenomenon. Conversely, large-scale intermittent turbulent fluctuations, such as the wake of an oscillating upstream structure, can lead to significant deviations from model predictions. A thorough investigation of these more complex gust disturbances would yield valuable insights into the dynamics of schooling and flocking animals, as well as several other problems in unsteady aerodynamics.

The results also show that the correspondence with the Atassi function found by Cordes et al. (2017) stems not from the thickness and camber of the airfoil but rather from the character of the gusts themselves. The effects of thickness, camber, and mean angle of attack, modeled by the Atassi function but not the Sears function, must therefore be decoupled from the gust character in order to be fully analyzed in an experimental context. At higher angles of attack and gust amplitudes, dynamic-stall flow phenomena become significant and cause the unsteady loads to deviate from the predictions of the Sears and Atassi functions. Studying these flow structures and their resulting load profiles would extend the findings of this study into the realm of real-world applications such as wind turbines and rotorcraft. Experiments along these lines were conducted in the scope of this project, and the results will be presented in a future article.

An obvious consequence of these results is that inflow conditions in active grid wind tunnels should be carefully scrutinized for unintended aerodynamic effects, especially if gusts at low reduced frequencies are of interest. While the influence of fluctuations in u may not be a cause for concern if agreement with the Sears function is desired, even these gusts could have unforeseen consequences to more sensitive phenomena, such as the dynamics of leading-edge vortices in dynamic stall. The present results reveal the impact of various types of gusts on airfoil gust response; however, their effect in other flow situations, e.g. on a vehicle, have yet to be studied in detail. A further implication is that additional effort in characterizing and tuning active grid generators may be necessary to avoid unwanted effects.

3.2 Periodic Gust Generation

The unsteadiness of various aerodynamic scenarios encountered in realistic applications arises from gusty inflow conditions. Experimental investigations of such scenarios under controlled conditions requires the production of controlled gusts inside a wind tunnel, which has been objective to numerous studies in the past (cf. section 1.2.1). Optimization efforts of gust generation in this thesis aim to simplify gust generation by using a single airfoil. To reduce wake effects of the gust generating airfoil on gust characteristics, a theoretical approach for kinematic optimization based on the Theodorsen theory will be introduced.

The optimization approach for gust generation kinematics will be derived from the Theodorsen theory in section 3.2.1. Characteristics of uncontrolled gusts, produced by different kinematics will be discussed for various parameter variations in section 3.2.2. These results will be compared directly with optimized gust characteristics. Based on the evaluation of optimization effects in section 3.2.2, limits of gust generation with a single airfoil and optimized kinematics will be compared to other gust generation approaches from literature in section 3.2.3. Facilities, measurement systems and processing methods used for the investigations presented below are introduced and discussed in section 2.2.

3.2.1 Theoretical Considerations

In this section, several considerations from the literature regarding the wakes of oscillating airfoils are discussed. These ideas undergird the hypothesis that the generation and control of well-defined periodic gusts is possible with a single airfoil as a gust generator. A theory for the generation of these gusts is then developed from the Theodorsen model for unsteady aerodynamics. These theoretical considerations provide guidance for the experiments that follow.

Considerations from Literature

In order to generate smooth, symmetric, and periodic gusts with a single airfoil, inspiration is derived from studies regarding the aerodynamics of oscillating airfoils. Anderson et al. (1998) characterized the wake patterns behind a NACA 0012 airfoil actuated in pitch and plunge over a range of reduced frequencies and Strouhal numbers. Note, that the reduced frequency is defined by the frequency of oscillation in radians per second $\omega = 2\pi f$ for their investigations. For a range of combinations of pitch and plunge amplitudes, several distinct wake regimes were identified. Of particular interest to this study is the region defined by Strouhal numbers less than 0.2 and pitch amplitudes less than 50 °, in which a “wavy wake” without significant vortex shedding was observed. The implied periodicity of the wake fluctuations and the lack of strong unsteady flow phenomena highlight this regime as one that would be particularly well-suited for the purpose of generating and controlling smooth, periodic gust waveforms with a single airfoil. This result suggests that the formation of well-defined quasi-sinusoidal oscillations in the wake of an airfoil can be achieved systematically as a function of pitch and plunge kinematics.

Two subsequent studies analyzed the effects of airfoil kinematics on wake structures generated by a pitching and plunging airfoil. For pitching and plunging airfoils, these wake structures are predominantly formed in dynamic stall, where strong leading-edge vortices (LEVs) and trailing-edge vortices (TEVs) roll up on and behind the airfoil, and convect downstream into the wake (Carr, 1988). Rival et al. (2009b) studied the effects of non-sinusoidal actuation profiles on the propagation of these structures into the wake, demonstrating that the strength of the LEV on the airfoil and its persistence into the wake were affected by the shape of the motion waveforms followed by the airfoil. Extending this result, Prangemeier et al. (2010) demonstrated that the addition of a quick pitch-down motion in the downstroke of an oscillating airfoil served to decrease the circulation of the TEV by as much as 60 %. The additional pitch motion of the airfoil interfered with the formation of the TEV, so that the strength of the TEV was not significantly dependent on the characteristics of the LEV. Similar reductions in wake vorticity were demonstrated in numerical simulations by Gharali & Johnson (2013). Therefore, though the strengths of LEVs and TEVs are inherently connected, the addition of pitching motions for a plunging airfoil can inhibit the generation of large trailing-edge vorticity in spite of large accumulations of vorticity at the leading edge. This is instructive to current investigations, because the shedding of large, intermittent velocity fluctuations is antithetical to the generation of smooth, periodic velocity signals downstream.

In order to minimize vorticity effects in the flow downstream of the gust generator, the wake of the generator itself should be minimized along with the persistence of dynamic effects. To this end Hufstedler & McKeon (2019) developed a vortical gust generator using an impulsively plunging plate. The plunging motions of the plate meant that the wake vorticity from the plate had a limited effect on the gust region, since the wake vorticity would only cross through the measurement domain twice per cycle. This is in contrast to gust generators that employ purely pitching vanes, which are fixed in place and thus continually disturb the downstream flow conditions.

These considerations, taken together, imply that the generation of gusts with smooth, symmetric waveforms is possible with a single airfoil, provided the kinematics of that airfoil are carefully controlled. Relatively low Strouhal numbers and reduced frequencies are required to mitigate vortex shedding due to dynamic stall flow phenomena. Plunge oscillations can help reduce the effects of the airfoil wake on the downstream flow properties. Adding pitch motions can further attenuate trailing-edge vorticity, thereby reducing intermittency in the downstream velocity signals.

The remainder of this work is therefore concerned with the combination of these observations: specifically, which combinations of pitch and plunge produce satisfactorily smooth, approximately sinusoidal velocity fluctuations for a range of Strouhal numbers and reduced frequencies. In order to achieve these gust conditions, intermittent effects from vortices shed by the gust generator should be avoided, and the resulting velocity profiles should be as symmetric and regular as possible. These criteria will drive the development and characterization of a robust theory for gust generation with a single airfoil.

In this study, gust fluctuations in the direction normal to the flow are specifically investigated. Fluctuations in the streamwise velocity and in the flow vorticity were not central to the application of this work, and measurements of these quantities demonstrated that they were insensitive across the range of parameters tested in these experiments. Additionally, Wei et al. (2019a) have shown that, in the case of the Sears function, streamwise velocity fluctuations are not critical to obtaining experimental convergence with analytical predictions. Thus, gust fluctuations in the flow-normal direction are the main quantity of interest in this work.

Adaption of the Theodorsen Theory

Theodorsen (1934) developed a first-order theory for the forces and moments experienced by a pitching and plunging flat-plate airfoil. The theory combines added-mass forces from the pitch (θ) and plunge (h) motions of the airfoil with the influence of the circulation in the wake to predict the unsteady aerodynamic loads on the airfoil. Since the theory accounts for the effects of both kinematics and wake circulation, it can be used to build a relation for the kinematic parameters needed to generate smooth, periodic gusts. It has also been validated in the same experimental apparatus used in the present study (Cordes et al., 2017). The theory was used by Brion et al. (2015) to estimate the amplitude of gusts produced by a purely pitching airfoil in transonic flow. Apart from this, it has been absent from the gust-generation literature.

The pitching moment on the airfoil is of particular interest because it provides a connection between airfoil dynamics and downstream flow characteristics. While the Theodorsen theory does not model dynamic effects, the vortices associated with dynamic stall should not be present in the ideal gust-generation case, and thus the forces and moments on the airfoil should be captured well by the Theodorsen function. In this ideal case, the airfoil would simply redirect flow up and down, creating vertical fluctuations in velocity without introducing significant circulation into the downstream region. The leading edge of the airfoil would minimally disturb the incoming flow, so that the flow on the upper and lower surfaces of the airfoil follow the airfoil surface without significant differences between the upper and lower surface. The resulting lack of velocity gradients at the trailing edge of the airfoil would then minimize the circulation injected into the wake. In this sense, both the added-mass moments and moments due to wake circulation would be optimally small, and the total pitching moment on the airfoil would be minimized.

The kinematics required to achieve this ideal gust generation case can be calculated using Theodorsen's theory. For a given plunge amplitude h_0, inflow velocity U_∞, and gust frequency f, it is possible to find the pitch amplitude θ^* that will minimize the amplitude of the pitching moment on the airfoil. The plunge amplitude is defined in this case by the peak-to-peak excursion distance of the trailing edge of the airfoil, as in Anderson et al. (1998), so that the length scale within the Strouhal number approximately represents the width of the airfoil wake. The equation for the pitching moment is given in terms of these parameters as

$$\begin{aligned} M_\theta = -\rho b^2 &\left[\pi\left(\frac{1}{2}-a\right)U_\infty b\dot{\theta} + \pi b^2\left(\frac{1}{8}+a^2\right)\ddot{\theta} - a\pi b\ddot{h}\right] \\ &+ 2\rho U_\infty b^2 \pi\left(a+\frac{1}{2}\right)C(k)\left[U_\infty\theta + \dot{h} + b\left(\frac{1}{2}-a\right)\dot{\theta}\right], \end{aligned} \tag{3.9}$$

where b is the half-chord of the airfoil, $a \in [-1, 1]$ is the center of rotation of the airfoil (nondimensionalized by b), θ is the pitch angle of the airfoil, h is the plunge location of the airfoil (positive downward), U_∞ is the free-stream velocity, and ρ is the density of the working fluid. In this case, we define the pitching moment about the trailing edge, corresponding to $a = 1$, in order to quantify the cumulative influence of the airfoil on the flow from the leading edge up to the trailing edge. The Theodorsen function $C(k)$ is a function only of the reduced frequency $k = \omega b/U_\infty$, and has both real and imaginary components, i.e. $C(k) = F(k) + iG(k)$. These functions are defined in the original work by Theodorsen (1934). Since $C(k)$, and thereby $F(k)$ and $G(k)$, does not depend on θ, these functions do not factor into the optimization of the pitch amplitude, θ_0, undertaken here.

In order to calculate the optimal pitch amplitude for gust generation, θ^*, we define the kinematics of the airfoil and their time derivatives as sinusoidal waveforms in the complex plane (following McGowan et al., 2011):

$$\begin{aligned} &h = -\frac{h_0}{2}e^{i\omega t}, \quad \dot{h} = -i\omega\frac{h_0}{2}e^{i\omega t}, \quad \ddot{h} = \omega^2\frac{h_0}{2}e^{i\omega t}; \\ &\theta = \theta_0 e^{i\omega t}e^{i\phi}, \quad \dot{\theta} = i\omega\theta_0 e^{i\omega t}e^{i\phi}, \quad \ddot{\theta} = -\omega^2\theta_0 e^{i\omega t}e^{i\phi}. \end{aligned} \tag{3.10}$$

Here, ϕ is the phase offset of θ with respect to h. The time-dependent pitching moment can be written as $M_\theta = \hat{M}_\theta e^{i\omega t} e^{i\phi}$, so that the time-dependent portion of the waveforms can be removed. Additionally noting that $\omega = kU_\infty/b$, Eqn. 3.9 can be written as

$$\begin{aligned}\frac{\hat{M}_\theta e^{i\phi}}{\pi\rho b^2 U_\infty^2} &= \left(a - \frac{1}{2}\right) k\theta_0 e^{i\phi} i + \left(\frac{1}{8} + a^2\right) \theta_0 k^2 e^{i\phi} \\ &+ \frac{a}{2b} k^2 h_0 + 2\left(a + \frac{1}{2}\right)\Big(F(k) + iG(k)\Big) \\ &\cdot \left[\theta_0 e^{i\phi} - i\frac{kh_0}{2b} - \left(\frac{1}{2} - a\right) k\theta_0 e^{i\phi}\right].\end{aligned} \tag{3.11}$$

The square of the magnitude of this complex expression reduces to a quadratic function in θ_0, after a rather unpleasant amount of algebra:

$$\left(\frac{\hat{M}_\theta}{\pi\rho b^2 U_\infty^2}\right)^2 = \left(C_R^2 + C_I^2\right)\theta_0^2 + 2\left(C_R D_R + C_I D_I\right)\theta_0 + D_I^2, \tag{3.12}$$

where

$$\begin{aligned}C_R &= k\left[\left(a - \frac{1}{2}\right)\sin(\phi) + \left(\frac{1}{8} + a^2\right) k\cos(\phi)\right] \\ &+ F(k)\left[3\cos(\phi) - 2\left(\frac{1}{4} - a^2\right) k\sin(\phi)\right] \\ &- G(k)\left[3\sin(\phi) + 2\left(\frac{1}{4} - a^2\right) k\cos(\phi)\right], \\ C_I &= k\left[\left(\frac{1}{2} - a\right)\cos(\phi) + \left(\frac{1}{8} + a^2\right) k\sin(\phi)\right] \\ &+ F(k)\left[3\sin(\phi) + 2\left(\frac{1}{4} - a^2\right) k\cos(\phi)\right] \\ &+ G(k)\left[3\cos(\phi) - 2\left(\frac{1}{4} - a^2\right) k\sin(\phi)\right],\end{aligned} \tag{3.13}$$

$$
\begin{aligned}
D_R &= \frac{a}{2b}k^2 h_0 + \left(a + \frac{1}{2}\right)\frac{kh_0}{b}G(k), \text{ and} \\
D_I &= -\left(a + \frac{1}{2}\right)\frac{kh_0}{b}F(k).
\end{aligned}
\tag{3.14}
$$

D_R and D_I can be written in terms of k and St, so that the four coefficients given in Eqn. 3.14 are only functions of k, St, ϕ, and a:

$$
\begin{aligned}
D_R &= \pi a k St + 2\pi St\left(a + \frac{1}{2}\right)G(k), \\
D_I &= -2\pi St\left(a + \frac{1}{2}\right)F(k).
\end{aligned}
\tag{3.15}
$$

To minimize the pitching moment, we take the derivative of its magnitude with respect to the pitch amplitude and set this derivative equal to zero:

$$
\frac{\partial \hat{M}_\theta}{\partial \theta_0} = 0. \tag{3.16}
$$

The solution is easily found as

$$
(\theta_0)_{min} = \theta^* = -\left[\frac{C_R D_R + C_I D_I}{C_R^2 + C_I^2}\right]. \tag{3.17}
$$

θ^* is thus the pitch amplitude that produces the minimum pitching moment $\hat{M}_\theta^*$ for a given combination of k, St, a, and ϕ. For the reasons outlined previously, we have chosen $a = 1$ in this study, which means θ^* and the corresponding $\hat{M}_\theta^*$ are functions of k, St, and ϕ only. Selecting a set of plunge kinematics determines k and St, leaving ϕ as the remaining free parameter. Thus, for any given phase offset ϕ, the pitch amplitude θ^* that produces the minimum pitching moment $\hat{M}_\theta^*$ can be calculated using Eqn. 3.17. The variations of θ^* and $\hat{M}_\theta^*$ with ϕ are shown in Fig. 3.15 for a given set of dynamic parameters ($k = 0.603$, $St = 0.096$). Here, it is clear that while each selection of ϕ has a corresponding minimized pitching moment $\hat{M}_\theta^*$, there exists a value of ϕ that has a lower associated optimal pitching moment than all others. In the case shown in Fig. 3.15, this phase offset is $\phi^\dagger = 113.7°$, with

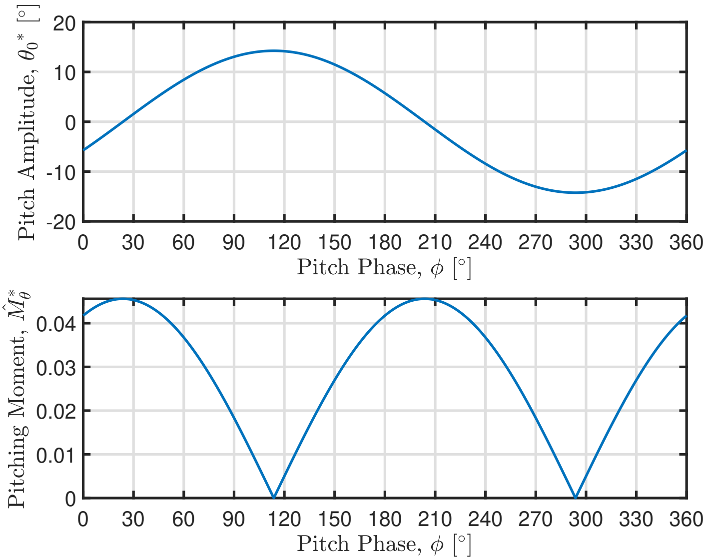

Figure 3.15: Variations of the optimal pitch amplitude θ^* and resulting minimized pitching moment $\hat{M}_\theta^*$ with pitch phase ϕ, for $St = 0.096$ and $k = 0.603$. The global minimum pitching moment for this case occurs at $\phi^\dagger = 113.7°$. A phase ϕ_i with $\theta^*(\phi_i) < 0$ is equivalent to a phase of $\phi_i \pm 180°$ and amplitude of $|\theta^*|$. (Reprinted from Wei et al. (2019b), with permission of Springer Nature. © 2019 Springer Nature.)

a corresponding pitch amplitude of $\theta^* = 14.25°$ and precisely zero pitching moment about its trailing edge. This condition of zero pitching moment for a particular $\phi^\dagger$ exists for every combination of k and St, and according to the arguments put forth previously in this section, would be optimally conditioned to produce smooth, periodic gusts with minimal interference from the airfoil itself.

In practice, however, one may not be able to select any desired phase offset due to actuation constraints. In the experiments presented here, the airfoil was actuated with two separate linear actuators that were each controlled with sinusoidal waveforms. This setup restricted the accessible phase offsets to 0° and 180°. Though these values of ϕ do not result in zero pitching moment, the θ^* values from the theory still produce the lowest possible pitching moment given the constraints on ϕ; the experiments presented in this work aim to show that this moment-minimization scheme produces the most optimal gusts for any desired combination of k, St, and ϕ. Fig. 3.15 shows that at $\phi = 0°$ and $\phi = 180°$, the minimized pitching moment has the same value, but the sign of θ^* at $\phi = 0°$ is negative. Since the pitch waveform is sinusoidal, a negative amplitude is equivalent to a positive amplitude with a 180° phase shift. The $\phi = 0°$ case with $\theta^* < 0$ is thus equivalent to the $\phi = 180°$ case with $\theta^* > 0$: both describe a scenario in which the pitch waveform is out of phase with the plunge waveform. Therefore, there exists no positive pitch amplitude that will minimize the pitching moment for $\phi = 0°$, and moreover, employing pitch in phase with plunge should not be conducive to the production of smooth, controlled gusts. Given these constraints on the pitch phase, optimal pitch amplitudes for several sets of airfoil kinematics are given in tables 3.1 and 3.2 in Sec. 3.2.2.

In this section, an analytical method for establishing pitch kinematics for a given reduced frequency and Strouhal number that will produce regular, well-defined periodic gusts has been outlined. These results are notably only indirectly dependent on the Reynolds number, through the dependence of k and St on U_∞ and c. This series of assumptions and arguments for gust generation are theoretical in nature and require experimental investigation to verify whether they apply in practice. The character of the gusts produced by such a gust generator provides the validation criteria for the theory. In particular, the sinusoidal character of the velocity profiles and the extent of the wake of the airfoil downstream of the gust generator will serve as indicators for the quality of the gusts generated according to these principles.

3.2.2 Results

In this section, the arguments put forward in section 3.2.1 are examined experimentally. First, various experiments are performed to establish a baseline for effects of airfoil kinematics on the character of the gusts produced. Based on these baseline cases, a template for the kinematics of the gust generator is proposed, which arises from the conclusions of the theoretical analysis in section 3.2.1. The predictions of the Theodorsen theory as applied to gust generation are tested using the metrics outlined in section 2.2.4 in order to demonstrate that gusts with a satisfactorily smooth and symmetric character can be produced using a single pitching and plunging airfoil. Lastly, the effects of the gust generator on fluctuations of the streamwise velocity and spanwise vorticity are analyzed, and the effectiveness and limitations of the gust-generation scheme with regard to other measurement locations and conditions are evaluated. All investigations of gust characteristics consider a free stream velocity of $U_\infty = 2.5\,\mathrm{m/s}$, which corresponds to a chord-based Reynolds number of about 20,000 to reduce the complexity of relevant parameter combinations.

Baseline Case Gust Characteristics

To understand the effects of the various free parameters in the kinematics of a pitching and plunging airfoil on the vertical velocity signal in the wake, a series of concise parametric studies is conducted. First, the two dimensionless parameters governing the dynamics of the oscillating airfoil, St and k, are varied independently for an airfoil moving in pure plunge. For $k = 0.603$, the plunge amplitude of the airfoil is varied to produce Strouhal numbers between 0.032 and 0.112. The resulting velocity profiles, taken at the region of interest specified in section 2.2.4, are shown in Fig. 3.16. Conversely, for $St = 0.080$, the reduced frequency is varied between 0.302 and 0.905. These baseline conditions ($St = 0.080$, $k = 0.603$) represent moderate values of k and St for the range of parameters tested in this study, which allow the effects of each of these parameters to be observed independently. The velocity profiles for these experiments are shown in Fig. 3.17. These results show that the amplitude of the fluctuations in the vertical velocity ($\hat{v}$) is a strong linear function of Strouhal number and a weaker function of reduced frequency. These trends are shown explicitly in Fig. 3.32 for cases utilizing both pitch and plunge, and will be discussed in more detail in section 3.2.2. In addition, most of the curves shown are asymmetric, with peaks occurring relatively early within each half-cycle, or more geometrically conceived, leftward-leaning maxima. This “leaning" behavior should be avoided if symmetric signals are desired. Finally, in many cases, the waveform is interrupted by a deviation around $\frac{t}{T_0} = 0.95$ that is not present in the corresponding positive half of the signal. This is likely an artifact of flow around the actuator mounts interfering with the wake, an unavoidable asymmetry in the present experiment. Thus, though

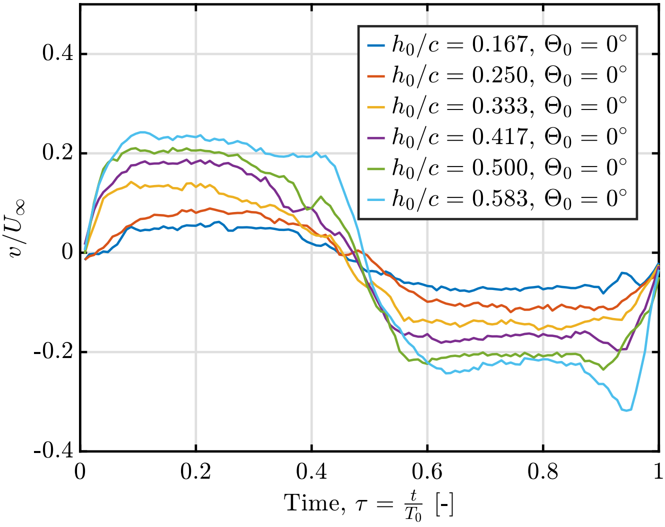

Figure 3.16: Baseline profiles of vertical velocity v for a purely plunging airfoil for a range of Strouhal numbers ($0.032 \leq St \leq 0.112$ and $k = 0.603$). Measurements are taken one chord behind the airfoil trailing edge, and are phase-averaged over 30 cycles. The peaks of the profiles tend to be biased toward earlier dimensionless times. (Reprinted from Wei et al. (2019b), with permission of Springer Nature. © 2019 Springer Nature.)

the negative portions of the waveforms show similar trends to the positive portions, the positive halves of the velocity profiles should be viewed as more reliable indicators of trends than the negative halves.

Next, the effect of pure pitch on wake character is studied. The airfoil is pitched through $5\,° \leq \theta_0 \leq 15\,°$, first about its leading edge and then about its trailing edge. The reduced frequency is again $k = 0.603$. The resulting profiles are shown in Fig. 3.18. Upon inspection, pitching about the leading edge appears to result in smoother, more regular profiles than pitching about the trailing edge. This is due to significant dynamic effects and resultant shedding of vortices instigated by large excursions of the leading edge of the airfoil that are observed in the velocity and vorticity fields when the airfoil was pitched about its trailing edge (cf. Widmann, 2015). Thus, it is concluded that excessive motions of the leading edge are counterproductive

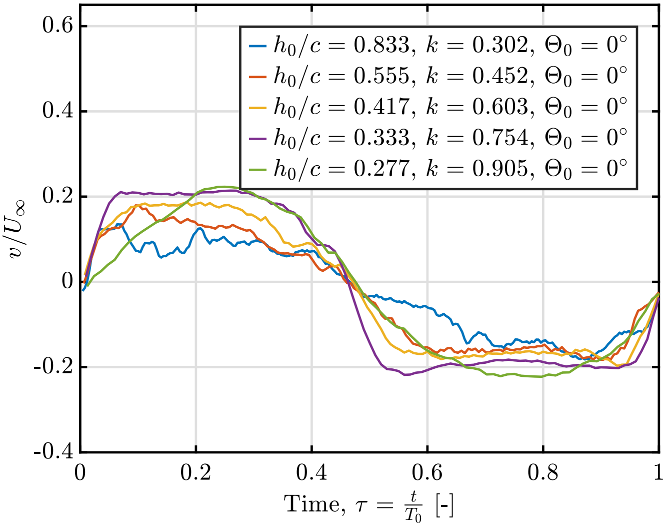

Figure 3.17: Baseline profiles of vertical velocity v for a purely plunging airfoil for a range of reduced frequencies ($0.302 \leq k \leq 0.905$ and $St = 0.080$). Measurements are taken one chord behind the airfoil trailing edge, and are phase-averaged over 30 cycles. The peaks of the profiles tend to be biased toward earlier dimensionless times. (Reprinted from Wei et al. (2019b), with permission of Springer Nature. © 2019 Springer Nature.)

to the generation of smooth, well-defined velocity signals. Additionally, the velocity profiles in the case of pitch about the leading edge peak later in each half-cycle. This suggests that the addition of pitch to plunge could potentially offset the leftward lean observed in Figs. 3.16 and 3.17.

A similar conclusion is drawn by combining pitch and plunge kinematics, and changing the phase offset between the two. At $k = 0.603$, a set of three increasing pitch amplitudes is combined with a proportionally increasing set of plunge amplitudes. This series is carried out with phases of $\phi = 0\,°$ and $180\,°$. Since the trailing-edge amplitude defines the plunge waveform, a phase of $0\,°$ produces larger excursions of the leading edge, and correspondingly less regular velocity profiles, as seen in Fig. 3.19a. Conversely, a phase of $180\,°$ results in smaller motions of the leading edge; the velocity profiles (shown in Fig. 3.19b) exhibited the same rightward-shifted maxima as in Fig. 3.18a.

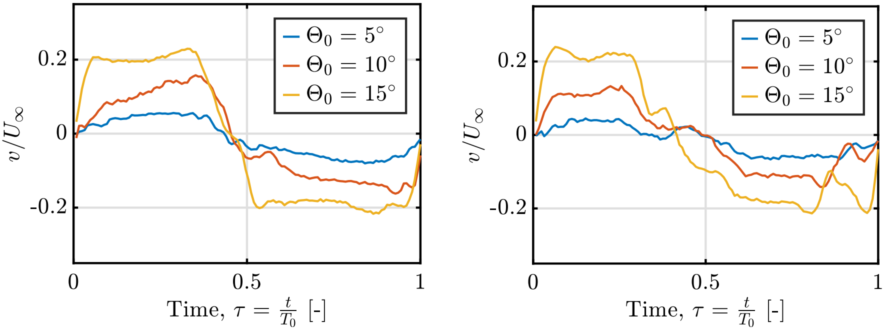

(a) Pure pitch about the leading edge **(b)** Pure pitch about the trailing edge

Figure 3.18: Baseline profiles of v for a purely pitching airfoil ($k = 0.603$), rotating about its (a) leading edge and (b) trailing edge. The profiles appear to be more regular when leading-edge motion is minimized – achieved by the kinematics of (a) in this case. (Reprinted from Wei et al. (2019b), with permission of Springer Nature. © 2019 Springer Nature.)

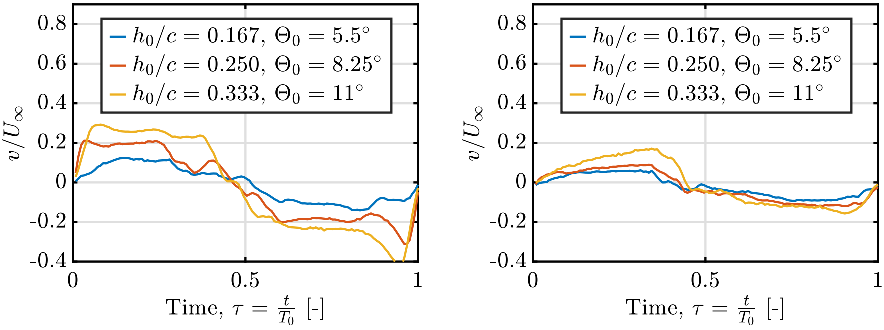

(a) $\phi = 0\,°$ **(b)** $\phi = 180\,°$

Figure 3.19: Baseline profiles of v for a pitching and plunging airfoil ($k = 0.603$, range of St), with pitch phase (a) $\phi = 0\,°$ and (b) $\phi = 180\,°$. A phase of $180\,°$ results in more regular profiles (due to the reduction in leading-edge motion) and biases the waveform peaks toward later dimensionless times. (Reprinted from Wei et al. (2019b), with permission of Springer Nature. © 2019 Springer Nature.)

The results observed in these small parametric studies suggest an ideal set of kinematics for the generation of smooth, symmetric gusts. Plunge motions allow for higher gust amplitudes to be created, but introduce asymmetry into the gust profiles. Pitch creates asymmetries in the opposite sense when significant leading-edge motion of the airfoil is avoided. A phase offset of 180 ° between pitch and plunge, so that the leading edge of the airfoil moves through a smaller amplitude than the trailing edge, combines these considerations. This was thus selected as the ideal set of kinematics for periodic-gust generation. A schematic of these kinematics is given in Fig. 3.20. These kinematics are identical to those identified in section 3.2.1 by means of physical and analytical arguments.

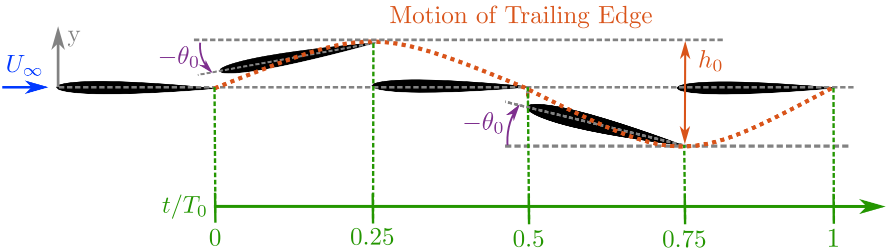

Figure 3.20: Schematic of the kinematics employed for gust generation, as determined by the Theodorsen theory outlined in section 3.2.1 and the set of test cases given in tables 3.1 and 3.2. The sinusoidal waveform shown as a dashed orange line represents the motion of the trailing edge of the airfoil. (Reprinted from Wei et al. (2019b), with permission of Springer Nature. © 2019 Springer Nature.)

Generation of Gusts with Controlled Character

With the concurrence of theory and experiments in defining a set of kinematics for gust generation, it was then possible to test the specific predictions of the analytical theory in relation to the gust generation problem.

First, a series of intermediate steps in the metrics described in section 2.2.4 are meant to demonstrate the effect of adding pitch out of phase with plunge. In Fig. 3.21, the positive half of the waveform for a case with $\theta_0 = 0°$ (Fig. 3.21a) is compared with the corresponding section for a case with $\theta_0 = 9.98\,°$ (Fig. 3.21b). The addition of pitch reverses the sign of the average acceleration around the midpoint of the profile, further suggesting that, with the right pitch amplitude, the acceleration at the midpoint could be controlled to be zero – in other words, the symmetry of the gust could

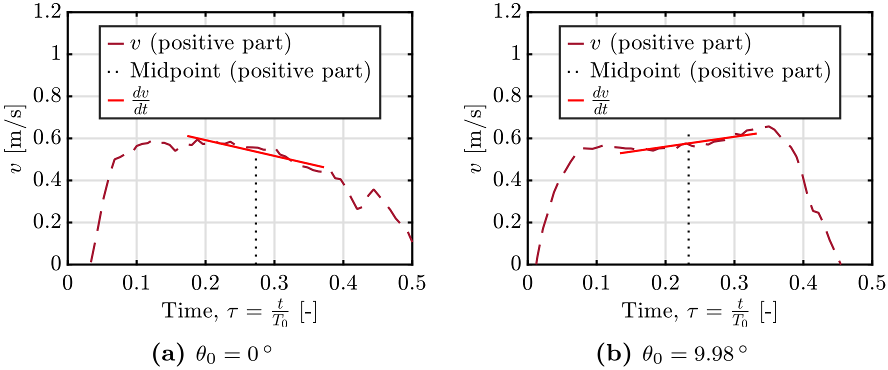

(a) $\theta_0 = 0\,°$

(b) $\theta_0 = 9.98\,°$

Figure 3.21: Mean acceleration $\frac{dv}{dt}$ of the flow for the positive half of two velocity profiles from experiments with identical parameters (i.e. f, h_0, and U_∞). The fit used to compute the mean acceleration is shown as a solid red line. The slope of the line quantifies the relative bias of the profiles, and thereby the deviation from the ideal, symmetric case. (Reprinted from Wei et al. (2019b), with permission of Springer Nature. © 2019 Springer Nature.)

be controlled. For the same cases, phase averaged vorticity fields (shown in Fig. 3.22) demonstrate that the structure of the wake shed off the oscillating airfoil is thinner and more organized when pitch is present. This is also reflected in the wake-width analysis, representations of which are shown in Fig. 3.23.

These figures demonstrate the capacity of the metrics to capture physical differences in gust character within the area of interest, and also highlight the ability of phase-offset pitch to reverse some of the trends seen in the purely plunging cases.

Quantitative values from these two metrics are obtained for four combinations of Strouhal number and reduced frequency over a range of pitch amplitudes, in order to test the predictions of the Theodorsen theory. For a reduced frequency of $k = 0.603$, Strouhal numbers of 0.032, 0.064, and 0.096 are tested. A case with $k = 0.754$ and $St = 0.080$ is added to ensure that the theory is valid across reduced frequencies as well. These cases will be

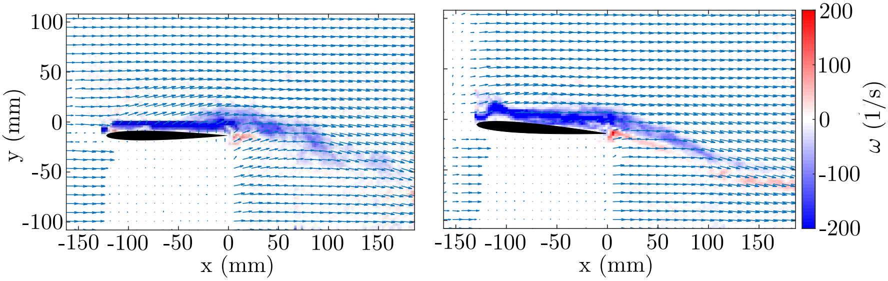

(a) Pure Plunge **(b)** Pitch and Plunge

Figure 3.22: Vorticity fields (taken from Round 1 of experiments) for the same cases as shown in Fig. 3.21, at $t/T_0 = 0.2$. Noise under the airfoil (due to the airfoil shadow) and on the left side of the frame (due to insufficient illumination by the laser sheet) has been masked for clarity. The regularizing effect of pitch on the vorticity shed by the airfoil is evident in this comparison. (Reprinted from Wei et al. (2019b), with permission of Springer Nature. © 2019 Springer Nature.)

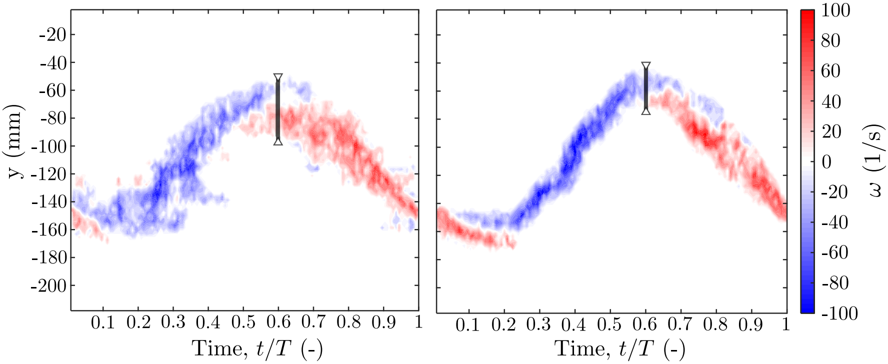

(a) Pure Plunge **(b)** Pitch and Plunge

Figure 3.23: Phase averaged wake profiles at $x = 1.0\,c$ behind the trailing edge of the airfoil, taken from the cases shown in Fig. 3.22. The wake widths δ_{wake} are shown qualitatively by a gray vertical line at a single time instant in these profiles; the values of the wake width given in Fig. 3.24 are averaged over the entire period. (Reprinted from Wei et al. (2019b), with permission of Springer Nature. © 2019 Springer Nature.)

denoted as (a), (b), (c), and (d), respectively. The airfoil kinematics for these cases and corresponding optimal pitch amplitudes according to theory (θ^*) are given in table 3.1.

Table 3.1: Kinematic parameters and corresponding optimal pitch amplitudes θ^* for the four cases shown in Figs. 3.24 and 3.25. For all cases, $U_\infty = 2.5$ m/s.

Case	f (Hz)	h_0 (mm)	k	St	θ^*
(a)	4	20	0.603	0.032	1.91°
(b)	4	40	0.603	0.064	3.82°
(c)	4	60	0.603	0.096	5.73°
(d)	5	40	0.754	0.080	5.30°

The average wake width δ_{wake} (normalized by the thickness of the airfoil, δ_{foil}) is shown over a range of pitch amplitudes for these four cases in Fig. 3.24. In each case, a relative minimum in wake width is observed very close to the optimal pitch amplitude predicted by the Theodorsen analysis, shown as a red vertical dashed line on each plot. The parabolic fits are only shown as guides for the eye, and are not intended to be prescriptive in any way. The effects of error in these data are more evident, stemming from the inherent noise associated with computing vorticity from velocity fields, the sensitivity of the thresholding procedure used to compute the wake width, and the fact that the field of view was so large (with respect to limits on laser power and seeding density) that achieving both sufficient illumination and sufficient resolution were difficult. Case (a), though still showing a minimum at the value of θ^* given by the Theodorsen theory, is less conclusive because of its low plunge amplitude. Inspection of the vorticity fields showed that the excursion of the airfoil, and thus the extent of the gust, is only marginally larger than the wake of the airfoil in the stationary case. As the flow in this regime is dominated by Kelvin-Helmholtz vortices from the surface of the airfoil rather than the unsteadiness of the airfoil, differences in the gust character are therefore much harder to measure. In spite of the influence of noise, every case investigated demonstrates general agreement with the Theodorsen theory in terms of a reduced influence of the airfoil in the downstream wake. Measurements of the metric for gust symmetry similarly validated the predictions of the analytical

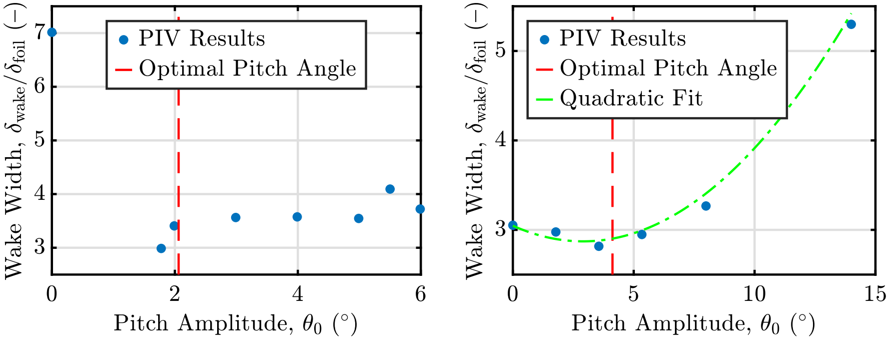

(a) $St = 0.032$, $k = 0.603$ **(b)** $St = 0.064$, $k = 0.603$

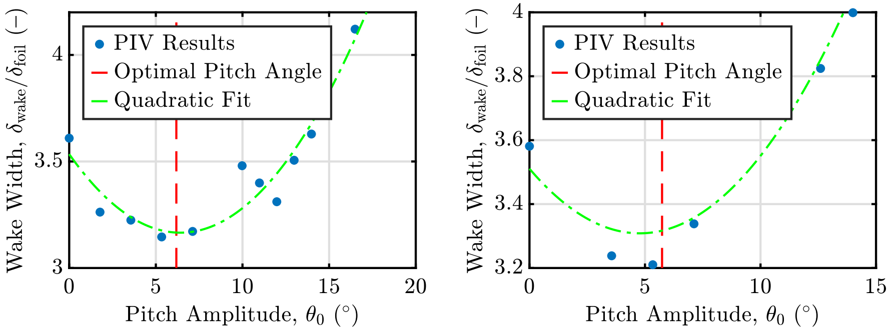

(c) $St = 0.096$, $k = 0.603$ **(d)** $St = 0.080$, $k = 0.754$

Figure 3.24: Time averaged wake width δ_{wake}, normalized by airfoil thickness δ_{foil}, of the flow at $x = 1.0\,c$ for four combinations of Strouhal number and reduced frequency. In each case, the airfoil is actuated in plunge with given f and h_0, and the pitch amplitude is varied. Parabolic fits are given as dashed curves to show the trends, except for case (a). The influence of the wake of the gust generator is minimized in all cases near the pitch amplitude θ^* prescribed by the Theodorsen theory. (Reprinted from Wei et al. (2019b), with permission of Springer Nature. © 2019 Springer Nature.)

theory. Fig. 3.25 shows the mean acceleration data for each of the four cases over a range of pitch amplitudes. The prediction of the Theodorsen theory, again shown as a red vertical dashed line on each plot, coincides very well with the point where the trend of the data crosses the $\frac{dv}{dt}$ axis in each case, in spite of minor scatter in the data due to experimental error stemming

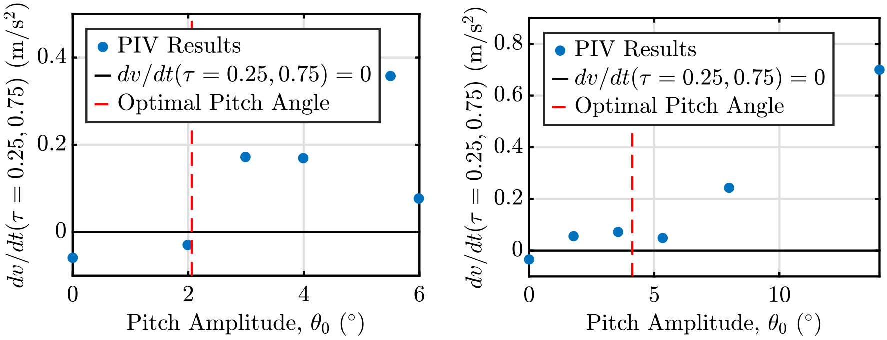

(a) $St = 0.032$, $k = 0.603$ **(b)** $St = 0.064$, $k = 0.603$

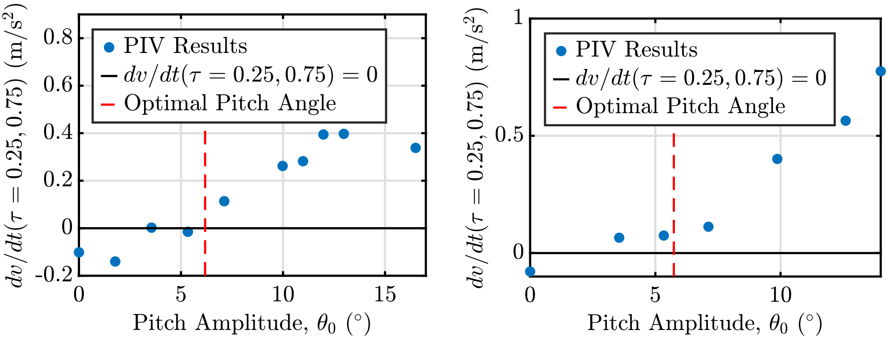

(c) $St = 0.096$, $k = 0.603$ **(d)** $St = 0.080$, $k = 0.754$

Figure 3.25: Mean acceleration $\frac{dv}{dt}$ of the flow at $\frac{t}{T_0} = 0.25$ and $\frac{t}{T_0} = 0.75$ for four combinations of Strouhal number and reduced frequency. In each case, the airfoil is actuated in plunge with given f and h_0, and the pitch amplitude is varied. As shown by the intersection of the data trends with $\frac{dv}{dt} = 0$ at the red vertical dashed lines (denoting θ^*), the theory satisfactorily predicts the generation of optimally symmetric gust profiles. (Reprinted from Wei et al. (2019b), with permission of Springer Nature. © 2019 Springer Nature.)

from the limits of the apparatus and the sensitivity of the mean-acceleration metric. These results demonstrate that the gusts produced according to the Theodorsen theory are more symmetric than those produced at other pitch amplitudes.

Finally, in order to more clearly demonstrate the effectiveness of the Theodorsen theory for gust generation, a range of Strouhal numbers and reduced frequencies are tested with the addition of pitch according to the theory. The values of these optimal pitch amplitudes are given in table 3.2.

Table 3.2: Kinematic parameters and corresponding optimal pitch amplitudes θ^* for the baseline cases shown in Figs. 3.26 (variation in St) and 3.27 (variation in k). The actual pitch amplitudes used in the experiments are given under θ_0 (exp.).

Var.	f (Hz)	h_0 (mm)	k	St	θ^*	θ_0 (exp.)
St	4	20	0.603	0.032	1.91°	1.99°
St	4	30	0.603	0.048	2.86°	2.67°
St	4	40	0.603	0.064	3.82°	3.56°
St	4	50	0.603	0.080	4.77°	4.45°
St	4	60	0.603	0.096	5.73°	5.34°
St	4	70	0.603	0.112	6.68°	6.23°
k	2	100	0.302	0.080	2.84°	2.67°
k	3	66.7	0.452	0.080	3.96°	3.56°
k	4	50	0.603	0.080	4.77°	4.45°
k	5	40	0.754	0.080	5.30°	5.34°
k	6	33.3	0.905	0.080	5.59°	5.34°

These results are compared directly with the baseline cases shown in Figs. 3.16 and 3.17. Due to the process of selecting test cases for the experiments, the pitch amplitudes tested in the experiments are not precisely equivalent to those supplied by the theory, differing at most by 0.45 ° (less than 7 % of the optimal pitch amplitude). These differences, recorded in table 3.2, are not large enough to significantly affect the experimental results. The optimized gust profiles – shown in Figs. 3.26 and 3.27 – showed significant improvement in control over the waveform shape, in comparison to the baseline cases. The leftward shift of the maxima visible in Fig. 3.16 for the cases of pure plunge is essentially removed for all cases in Fig. 3.26.

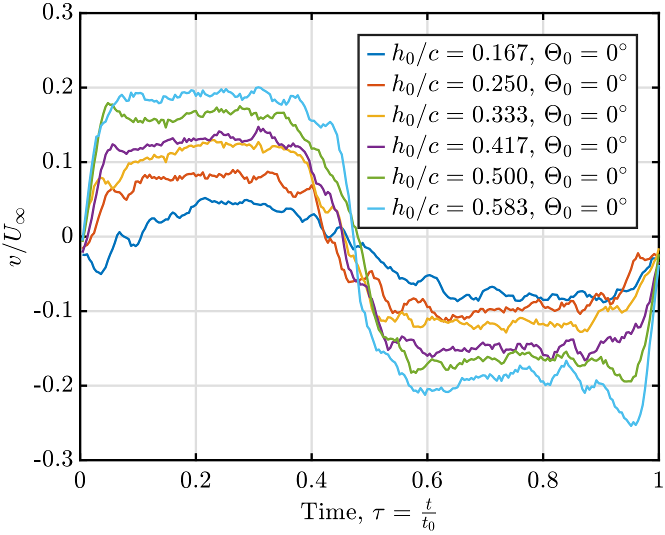

Figure 3.26: Profiles of v behind a pitching and plunging airfoil for a range of Strouhal numbers ($0.032 \leq St \leq 0.112$ and $k = 0.603$). Despite the actual pitch amplitudes being slightly lower than those prescribed by the theory (by no more than 0.45°), these curves still compare favorably in terms of symmetry and smoothness to those in Fig. 3.16. (Reprinted from Wei et al. (2019b), with permission of Springer Nature. © 2019 Springer Nature.)

At higher reduced frequencies, shown in Fig. 3.27, a slight rightward bias becomes evident, likely an effect of an earlier roll-up of shear-driven instabilities due to the more dramatic motions of the airfoil, which are not taken into account by the theoretical predictions. These limiting effects will be discussed further in section 3.2.2. Overall, the addition of pitch according to theory regularizes the vertical-velocity profiles over a range of Strouhal numbers and reduced frequencies, making the resultant gusts more uniform in shape and less affected by the wake of the airfoil generating the gust.

Evaluation of Optimization Effects

To highlight the differences between the baseline cases and the final gust-generation cases, two direct comparisons are shown in Figs. 3.28 and 3.29, in addition to fits of sine waveforms to the gust-generation cases. These

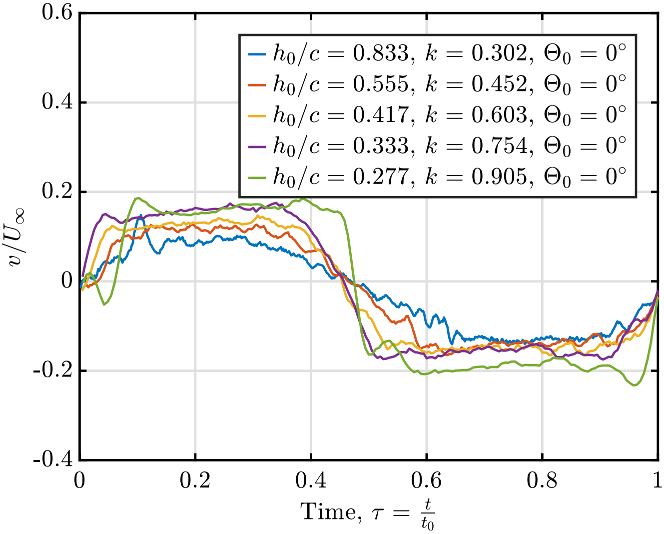

Figure 3.27: Profiles of v behind a pitching and plunging airfoil for a range of reduced frequencies ($0.302 \leq k \leq 0.905$ and $St = 0.080$). Despite the actual pitch amplitudes being slightly lower than those prescribed by the theory (by no more than 0.45°), these curves still compare favorably in terms of symmetry and smoothness to those in Fig. 3.17. (Reprinted from Wei et al. (2019b), with permission of Springer Nature. © 2019 Springer Nature.)

comparisons highlight the influence of pitch in making the gust profiles more symmetric about their peaks. In these cases as well, the presence of pitch seems to reduce the influence of velocity spikes in the profiles, which are likely artifacts of vortex shedding from the airfoil. This aligns with the wake mitigation shown previously in Fig. 3.24. For moderate combinations of St and k, such as that shown in Fig. 3.28, the gust profiles are very close to sinusoidal. Most notably, the regularizing effect of pitch according to the prescriptions of theory, in terms of gust symmetry and smoothness, is still significant for the highest-amplitude gusts produced in this study (shown in Fig. 3.29).

Thus, the gust generation protocol presented in this work is able to produce high amplitude gusts without losing control over the character of their waveforms. The generated gusts are also significantly higher in amplitude

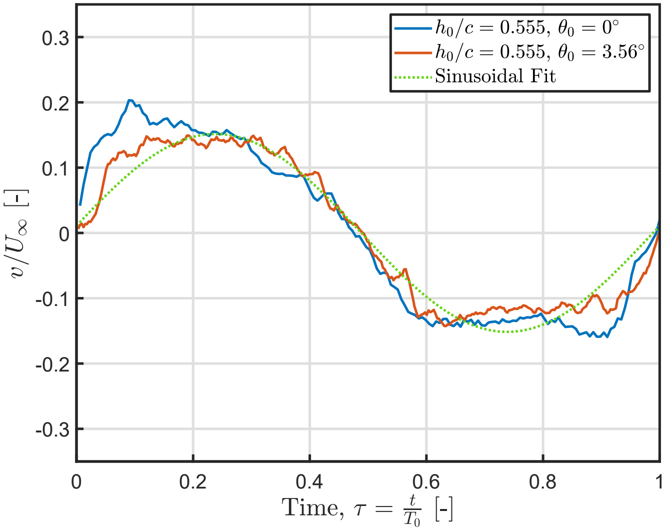

Figure 3.28: Comparison of gust with a moderate-amplitude generated by a plunging airfoil with and without pitching kinematics according to the Theodorsen theory for comparison case 1: $St = 0.080$ and $k = 0.452$. A sinusoidal fit of the case with pitch is shown as a dashed green line in both figures. The addition of pitch yields a curve that is more symmetric about its peak, thus more closely representing the ideal sinusoidal gust profile. Deviations in the negative halve of the gust profile are due to aerodynamic interference from the airfoil actuators. (Reprinted from Wei et al. (2019b), with permission of Springer Nature. © 2019 Springer Nature.)

(up to 13.8°) and reduced frequency (up to $k = 0.905$) than those produced by generators with the same number of actuators (e.g. Lancelot et al., 2015; Wood et al., 2017), as well as more complex systems with multiple vanes (e.g. Saddington et al., 2015; Wei et al., 2019a). A more detailed comparison of the performance of the gust generator with those found in the literature is presented in table 3.3.

This gust-generation scheme is thus well-suited for experiments involving highly dynamic inflow conditions. Since the derivation for θ^* shows that the optimal pitch amplitude was not a function of Reynolds number, it is also

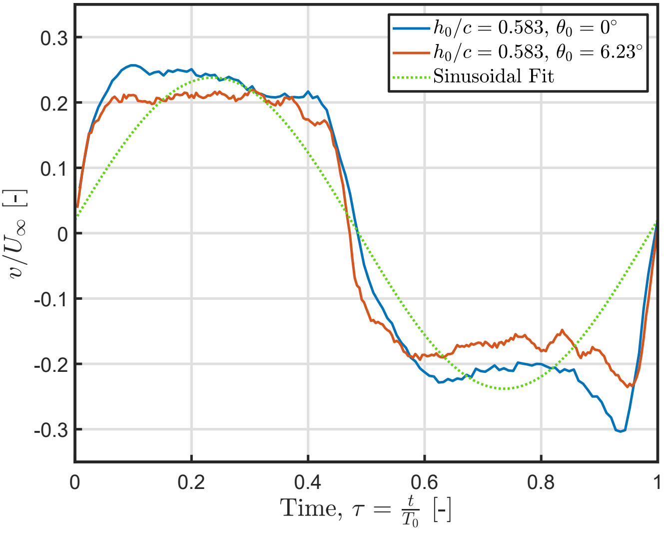

Figure 3.29: Comparison of gust with the highest-amplitude generated by a plunging airfoil with and without pitching kinematics according to the Theodorsen theory for comparison case 2: $St = 0.112$ and $k = 0.603$. A sinusoidal fit of the case with pitch is shown as a dashed green line in both figures. The addition of pitch yields a curve that is more symmetric about its peak, thus more closely representing the ideal sinusoidal gust profile. Deviations in the negative halve of the gust profile are due to aerodynamic interference from the airfoil actuators. (Reprinted from Wei et al. (2019b), with permission of Springer Nature. © 2019 Springer Nature.)

expected that the gust generator will perform well across a wide range of Reynolds numbers, especially since high Reynolds numbers generally imply significantly lower values of k and St.

To complete the characterization of the gust-generation apparatus, it is instructive to examine briefly the effects of the gust generator on the streamwise-velocity and vorticity fluctuations in the region of interest. The streamwise-velocity profiles and vorticity profiles corresponding to the cases shown in Fig. 3.26 are presented in Figs. 3.30 and 3.31, respectively.

The streamwise velocity fluctuations also increase linearly in amplitude ($\hat{u}$) with the plunge amplitude h_0, as shown in Fig. 3.32.

Table 3.3: Comparison of the reduced frequency ranges and maximum gust-angle amplitudes ($\hat{\alpha}_G$) of several gust-generation mechanisms in the literature with the one presented in this work. Here, k is defined by the length of the gust generator in each study, and not a downstream test profile.

Gust-generation study	k range	Max $\hat{\alpha}_G$
Hakkinen & Richardson (1957)	0.1 – 0.2	0.3°
Bennett & Gilman (1966)	0.08 – 0.34	1.4°
Jancauskas & Melbourne (1980)	0.08 – 2.5	11°
Saddington et al. (2015)	0.02 – 0.1	12°
Lancelot et al. (2015)	0.04 – 0.19	7°
Wood et al. (2017)	0.12 – 1.2	7°
Wei et al. (2019a)	0.09 – 0.42	12°
Present work	0.30 – 0.90	13.8°

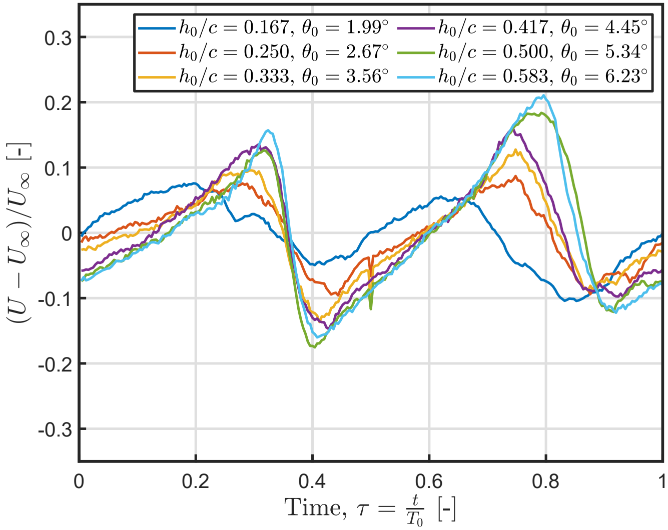

Figure 3.30: Phase averaged profiles of fluctuations in u for the cases shown in Fig. 3.26. The fluctuations in u remain small compared to U_∞. (Reprinted from Wei et al. (2019b), with permission of Springer Nature. © 2019 Springer Nature.)

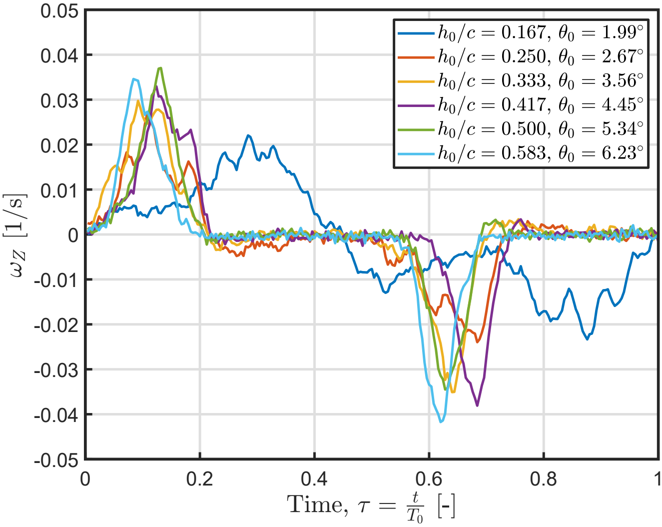

Figure 3.31: Phase averaged profiles of spanwise vorticity ω_z for the cases shown in Fig. 3.26. For all cases except the smallest plunge amplitude, the influence of vorticity is limited to brief periods where the wake of the gust generator passes through the region of interest. (Reprinted from Wei et al. (2019b), with permission of Springer Nature. © 2019 Springer Nature.)

In each case, the amplitude of these fluctuations is about one third of the amplitude of the vertical velocity fluctuations ($\hat{v}$). This is expected from the operating principle of the gust generator, which ideally would redirect the incoming flow in a sinusoidal fashion with minimal disturbance of the flow properties themselves. This kind of flow redirection necessitates fluctuations of $\hat{u}$ that scale with $\hat{v}$ and the gust-angle amplitude $\hat{\alpha}_G$, a relationship that is captured well in the experimental data presented in Fig. 3.32. These data imply that the gust generator is able to produce disturbances in a similar fashion to the ideal gust generator outlined in section 3.2.1. Overall, the fluctuations in u comprised only a small fraction of the free-stream velocity, and thus did not significantly influence the character of the angle-of-attack variations, which were dominated by v.

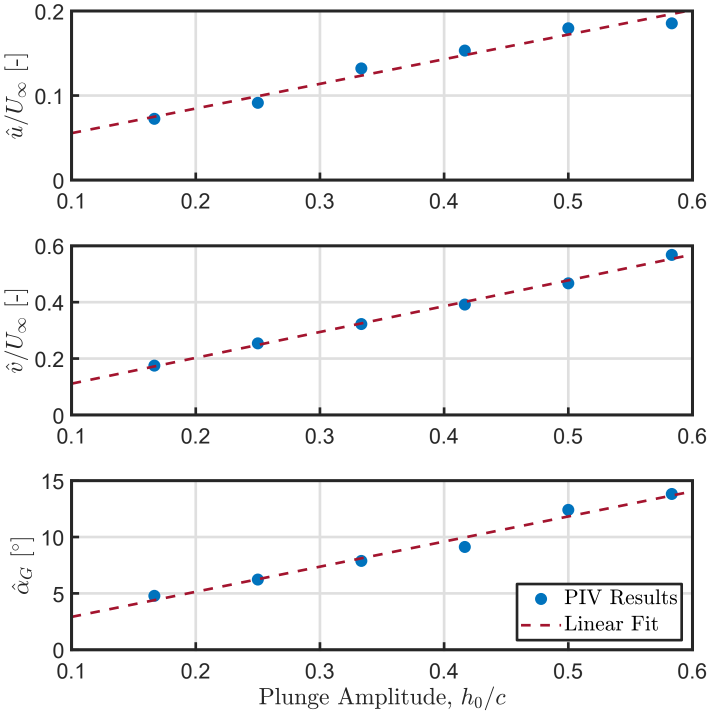

Figure 3.32: Amplitudes of the fluctuations in u, v, and α_G from the cases presented in Fig. 3.26, which all increase linearly with h_0. These linear trends are expected from the behavior of the idealized gust generator outlined in section 3.2.1, and imply that the apparatus operates sufficiently close to the ideal gust-generation scenario. (Reprinted from Wei et al. (2019b), with permission of Springer Nature. © 2019 Springer Nature.)

The vorticity profiles shown in Fig. 3.31 are also well-conditioned for the gust-generation problem. In all cases except that involving the lowest tested plunge amplitude ($h_0/c = 0.167$), the vorticity remained zero for most of the period. This means that the influence of the wake of the gust generator is minimized not only in its spatial extent, as shown previously in Fig. 3.24, but also in its temporal significance. At the lowest plunge amplitude, the motion of the airfoil is not large enough for the airfoil wake to clear the region of interest at any time, since h_0/c in this case is around twice δ_{foil}/c, and thus

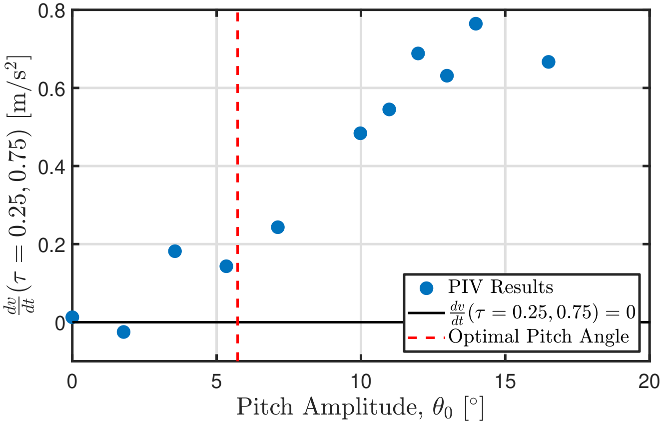

Figure 3.33: Mean acceleration $\frac{dv}{dt}$ of the flow at $\frac{t}{T_0} = 0.25$ and $\frac{t}{T_0} = 0.75$ for $St = 0.096$ and $k = 0.603$ (from Fig. 3.25c), measured at $x = 1.5\,c$ downstream of the airfoil trailing edge. The data are uniformly shifted up by approximately 0.1 m/s^2, compared to the measurements at $x = 1.0\,c$. (Reprinted from Wei et al. (2019b), with permission of Springer Nature. © 2019 Springer Nature.)

the Kelvin-Helmholtz instabilities shed by the airfoil always passes through the ROI. These observations validate the argument from above, based on the work of Hufstedler & McKeon (2019), that employing plunge kinematics can mitigate the influence of the wake of the airfoil on the gusts it produces. The complete removal of the influence of the airfoil wake is impossible for airfoils of finite thickness, but these results demonstrate that it is possible to limit these effects to short intervals within the gust period.

Until now, all analyses has been carried out at a point one chord length behind the gust generating airfoil. In order to project how the gust properties would change further downstream, the point furthest downstream from the airfoil in the measurement domain (at $x = 1.5\,c$ behind the trailing edge) is considered. Admittedly, this is not much farther downstream than the original test case, but restrictions on optical access for the laser sheet in the wind tunnel prohibits the acquisition of PIV measurements at larger downstream distances. For the sake of brevity, only the case of $St = 0.096$ and $k = 0.603$ from Fig. 3.25c is presented here. The corresponding data generated from the $x = 1.5c$ location for the mean accelerations are shown in Fig. 3.33.

These data retain their shape but are shifted up in value by approximately $0.1\,\mathrm{m/s^2}$ compared to the corresponding data from $x = 1.0\,c$. This would suggest that the value of θ_0 needs to produce symmetric gusts at this downstream location would need to be slightly lower than that predicted by theory. Other than this slight asymmetry, the gust profiles measured at this location do not appear any less smooth or less regular than their upstream counterparts. The reason for this small deviation from the predictions of the theory most likely lies in the influence of viscous effects in the wake. The Theodorsen theory only accounts for the wake circulation of the airfoil, and is not concerned with the properties of the global flow field further downstream of the airfoil. It is thus not surprising that instabilities, such as shear-layer roll-up due to velocity gradients in the gust, would lead to more complex dynamics as the flow develops further downstream. These roll-up effects were observed in smoke-wire visualizations, but could not be quantified using PIV because of the aforementioned limitations of the experimental setup. This “drift" of the gust profiles toward asymmetry with increased downstream distance from the gust generator would require additional analytical and experimental work to quantify and correct against. With regard to the present study, however, it is sufficient to note that this deviation is relatively small and does not affect the smoothness or controllability of the gust profiles. Furthermore, the viscous dynamics responsible for these effects will be attenuated in influence at higher Reynolds numbers. Therefore, the deviation from the predictions of the theory, while interesting from a fluid-mechanics standpoint, should not greatly affect the efficacy of the gust-generation scheme presented here.

3.2.3 Conclusions

In this work, considerations have been outlined for the generation of gusts with carefully controlled character using a single airfoil actuated in plunge and pitch. The Theodorsen theory for unsteady aerodynamics is used in order to predict the pitch amplitude necessary to produce smooth, symmetric gusts at a given Strouhal number and reduced frequency. The validity of the theory is supported both by physical arguments and by experimental investigations.

The quantitative predictions given by the theory are then confirmed in experiments that measured the symmetry of the vertical-velocity profiles produced in the wake of the airfoil, and the extent of the wake of the airfoil itself within the gust region. The gust signals produced are reasonably smooth, and reached significantly higher amplitudes and reduced frequencies than those attained by other gust-generation methods. For low to moderate Strouhal numbers and reduced frequencies, the gusts produced are very close to sinusoidal; the gusts remained smooth and symmetric even at the highest values of St and k examined in this work. In addition to the vertical-velocity fluctuations, the effects of the gust generator on the streamwise velocity and spanwise vorticity are also quantified, and the evolution of the gust profiles at measurement locations further downstream from the airfoil is evaluated. The results of this work suggest that the physics of the gust-generation problem do not require high degrees of mechanical complexity to solve, but rather can be manipulated as needed with just a single airfoil and potential flow theory.

Additional steps could be taken to improve the quality of the gust flows produced in the wake of the airfoil. Employing airfoil actuators that do not protrude into the center of the test section would greatly regularize the quality of the gust in the negative portion of the profile. A thinner airfoil, built from a less flexible material, would produce an even thinner wake, and could also be actuated more reliably over a wider range of kinematics. Measurement of the forces and moments on the airfoil would also be of interest, to see more quantitatively how unsteady loads may be reduced by these kinds of kinematics. Force measurements would also allow the effect of pitch phase, which was not thoroughly explored in this work, to be more rigorously determined. Specifically, changing the pitch phase using non-sinusoidal actuation waveforms (or, perhaps more easily, with independent pitch and plunge actuators) would allow the true minimum for the pitching moment ($\hat{M}_\theta^* = 0$) to be realized and validated. Lastly, tests at higher Reynolds numbers would allow the gust generator to be used in larger-scale experiments.

These findings have significant implications not only for the generation of well-defined gusts in aerodynamics experiments, but also for the aerodynamic behavior of tandem-wing configurations, for example in dragonfly wings, or on a larger scale, within flocks of birds or schools of fish. The control of wake structures purely by kinematics could also apply to gust-load alleviation in rotorcraft and biologically inspired unmanned aerial vehicles (UAVs). It is important to note, however, that the trends shown in this study will break down at higher Strouhal numbers and reduced frequencies, where dynamic effects become unavoidable. Nevertheless, a foray into this sector of the parameter space would allow the results of this work to be generalized to a much wider range of applications in aerodynamics, flow control, biological propulsion, and other related fields.

4 Leading Edge Vortex Characteristics on a Pitching and Plunging Flat Plate

A major objective of this chapter is to establish a basis for future flow control attempts on LEVs by studying LEV characteristics on a pitching and plunging flat plate. Flow control attempts will focus on the manipulation of secondary structures ahead of the main LEV, which can initiate vortex detachment and thereby prolong the LEV growth phase and attain higher net lift, as outlined in section 1.2.2. Therefore, secondary structure occurrence and effects on the LEV detachment are a central objective of investigations in this chapter.

To enlarge the attainable dimensionless parameter space, experiments presented in this chapter are carried out both in water and air under geometric, kinematic and dynamic similarity. At first, a common baseline case is defined and evaluated in section 4.1 to enable comparability of the flow field and vortex characteristics between results from the two facilities. Second, with the intention to better understand the formation of secondary structures during LEV growth as well as their consequences regarding the LEV detachment process, the topology of the flow field for different dimensionless parameters and effective angle of attack amplitudes is investigated in section 4.2. Additionally, the emergence of secondary structures is modelled to allow for precise timing of flow control approaches targeting secondary structure manipulation.

Facilities, measurement systems and processing methods used for the investigations presented below are discussed in section 2.3. Data sets in terms of correlated velocity fields of the baseline cases from TUDa and BUAA are available online as reference cases (http://dx.doi.org/10.25534/tudatalib-168). For additional insights into the LEV detachment process, the reader is referred to Li et al. (2020). Parts of this chapter have been published in Kissing et al. (2020a,b,c). Furthermore, parts of the experimental setup have been described in the theses of Berchtenbreiter (2018) and Bergner (2018). A complementary numerical and experimental consideration of the baseline case and an assessment of the lift force on the airfoil can be found in Kissing et al. (2020d).

Motion kinematics
Studies of the LEV detachment process from literature consider various dimensionless and geometric parameters (cf. section 1.2.2). A parameter that has not been considered in existing LEV detachment models is the history of the effective angle of attack $\alpha_{\text{eff}}(t)$. It affects the shear layer and LEV characteristics most directly through the vertical velocity component at the leading edge. The magnitude of $\alpha_{\text{eff}}(t)$, $\hat{\alpha}_{\text{eff}}$, is determined by the addition of the inflow angle induced by the plunging motion $\alpha_{\text{plunge}}(t) = \dot{h}(t)/U_\infty$ and the geometric angle of the airfoil due to the pitching motion $\alpha_{\text{geo}}(t)$, as shown in Fig. 4.1 for the common baseline case with $\hat{\alpha}_{\text{eff}} = 30\,^\circ$. By adapting $\alpha_{\text{geo}}(t)$ for different dimensionless parameter values, $\hat{\alpha}_{\text{eff}}$ can be kept constant.

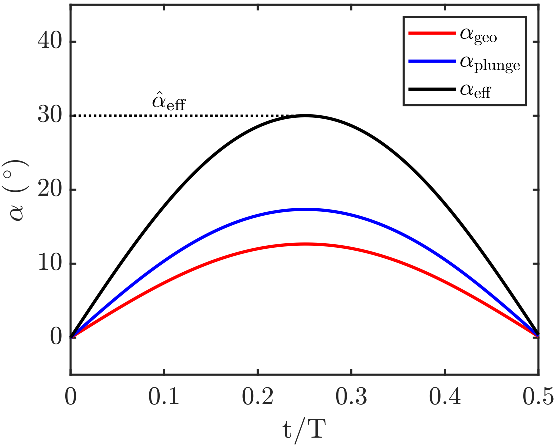

Figure 4.1: Evolution of the effective angle of attack $\alpha_{\text{eff}}(t)$ during the airfoil downstroke as a result of the superposition of the induced angle of attack due to the plunging motion $\alpha_{\text{plunge}}(t)$ and the geometric angle of attack $\alpha_{\text{geo}}(t)$ as a function of dimensionless time (t/T) for the common baseline case. The effective angle of attack amplitude $\hat{\alpha}_{\text{eff}}$ is additionally indicated. (Reprinted from Kissing et al. (2020c), with permission of Springer Nature. © 2019 Springer Nature.)

Additionally, different $\hat{\alpha}_{\text{eff}}$ can be produced independent of the dimensionless parameters. All kinematics investigated in this study are designed with a quasi-sinusoidal evolution of $\alpha_{\text{eff}}(t)$. As an extract from cyclic motion, only the downstroke of the airfoil is investigated. The phase offset between the pitching and plunging motion was set to zero to allow results to be compared with previous studies of the LEV detachment.

4.1 Establishment of Flow Similarity in Different Working Media

To extend the dimensionless parameter space in which secondary structure and LEV characteristics can be investigated, two facilities with different working media will be used. A water tunnel at the Beihang University (BUAA) and wind tunnel at TU Darmstadt (TUDA). The difference in viscosity, which is in the order of one magnitude, allows to attain higher Strouhal numbers and reduced frequencies in water due to lower dynamics of airfoil motion. To allow complementary investigations from both facilities, a common baseline case with identical parameters serves for validation of flow and LEV characteristics similarity. This common baseline case is defined from a comparison of attainable parameter spaces at each facility in section 4.1.1, where the extended parameter space used for consecutive investigations will also be introduced. Flow fields, LEV characteristics and its detachment mechanism will be compared between both facilities for the common baseline case in section 4.1.2 to validate comparability of results.

4.1.1 Parameter Space

Common Baseline Case Definition

The definition of a common baseline case, which enables comparability of results from both facilities, requires *a priori* consideration of the overlap of parameter spaces. Limiting factors for the maximum reduced frequency and Strouhal number are the maximum available actuator force to move the airfoil and maximum allowable plunge height, considering the airfoil mass and chord length. The *Re* range is determined by the lowest and highest free-stream velocity attainable in the respective tunnels, in relation to the chord length, while U_∞ also influences the k and St ranges. Fig. 4.2 illustrates the attainable parameter ranges in the respective facilities and their overlap for $St = 0.1$ and $\hat{\alpha}_{\text{eff}} = 30\,^\circ$ with $c = 120\,\text{mm}$. Here, the attainable parameter ranges are compared for different k and Re. St and the effective angle of attack amplitude $\hat{\alpha}_{\text{eff}}$ were additionally considered for the definition of the common baseline case.

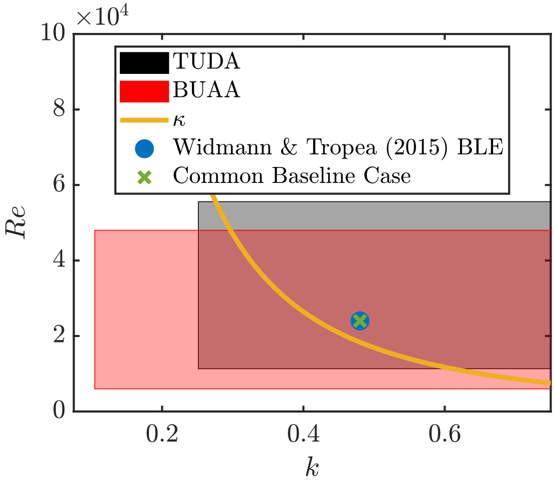

Figure 4.2: Dimensionless parameter ranges of facilities at BUAA and TUDa for $St = 0.1$, $\hat{\alpha}_{\text{eff}} = 30\,^\circ$ and $c = 120\,\text{mm}$. The covering ratio κ introduced by Widmann & Tropea (2015), differentiating between detachment mechanisms, is indicated with a curve in addition to their condition where boundary-layer eruption detachment (BLE) was observed. Finally, the chosen common baseline case for this study is shown. (Reprinted from Kissing et al. (2020c), with permission of Springer Nature. © 2019 Springer Nature.)

The dimensionless and geometric parameters of the common baseline case have been chosen such that a boundary-layer eruption detachment mechanism of the LEV can be expected, as discussed in section 1.2.2. Widmann & Tropea (2015) developed an analytical parameter, which enables the identification of dimensionless parameters that lead to boundary-layer eruption detachment, termed the dimensionless covering ratio κ. This parameter is based on the assumption that if the LEV is large enough to cover the entire airfoil chord, recirculation around the trailing edge is initiated. The coverage of the LEV is determined by an approximation of the mass flux into the LEV, which is in turn dependent on the shear layer thickness. The shear layer thickness is approximated using the Falkner-Skan solution, which takes the leading edge curvature into account. Through a series of parameter variations they find a threshold value of κ at which transition between detachment mechanisms occurs. This threshold is illustrated in Fig. 4.2 as an orange line. For cases with parameters located above this line, the LEV should detach due to boundary-layer eruption. One case where a boundary-layer eruption was identified at $k = 0.48$, $Re = 24{,}000$, $St = 0.1$ and $\hat{\alpha}_{\mathrm{eff}} = 30\,^{\circ}$ for $c = 120\,\mathrm{mm}$ is depicted with a blue dot. This is chosen as the common baseline case for both facilities in the current study.

Extended Parameter Space

After establishing good agreement between results from both facilities for the baseline case, a larger parameter range was tested at both facilities to characterise secondary structure emergence and their dynamics during vortex detachment. Although the dimensionless parameter range covered in current investigations is within the range of MAVs, it is also assumed to be transferable to biological propulsion as discussed and quantified in section 1.2.2. The Reynolds number was fixed at 24,000 for all experiments while the reduced frequency was varied between 0.3 and 0.48 and the Strouhal number between 0.04 and 0.16. Table 4.1 lists all cases investigated at TUDa including the common baseline case (ID 3) with their dimensionless parameters and the geometric parameters $\hat{\alpha}_{\mathrm{eff}}$ and $\hat{\alpha}_{\mathrm{geo}}$. Additionally, the motion period of the entire cycle T and the full plunge height H are listed. The ID assigned to each case will be used for identification in subsequent evaluations. The color, shape and fill of markers is chosen to allow for a differentiation of parameter variations: The color represents the Strouhal number and is coded from blue to red to yellow to green for increasing Strouhal numbers. The shape of markers marks the reduced frequencies, where round symbols represent $k = 0.48$ and rectangles $k = 0.3$. Cases with $\hat{\alpha}_{\mathrm{eff}} = 30\,^{\circ}$ can be identified by filled markers and cases with $20\,^{\circ}$ by open symbols.

The St-range at TUDa was limited to below 0.1 due to high inertial forces of fast motion kinematics in air. The difference in dynamic motions between facilities becomes evident by considering the motion period T for the common

Table 4.1: Dimensionless and geometric parameter range investigated at TUDa for $Re = 24,000$, including the common baseline case (ID 3).

ID	Sym.	k	T	St	H	$\hat{\alpha}_{\text{eff}}$	$\hat{\alpha}_{\text{geo}}$
1	●	0.48	236	0.04	0.016	30	22.69
2	●	0.48	236	0.08	0.031	30	16.07
3	●	0.48	236	0.1	0.039	30	12.67
4	○	0.48	236	0.1	0.039	20	2.67
5	○	0.48	236	0.08	0.031	20	6.07
6	○	0.48	236	0.04	0.016	20	12.7
7	■	0.3	377	0.08	0.05	30	15.95
8	■	0.3	377	0.04	0.025	30	22.86
9	□	0.3	377	0.08	0.05	20	5.95
10	□	0.3	377	0.04	0.025	20	12.86

baseline case listed in tables 1 and 2, which differ by an order of magnitude. By including a set of cases with $\hat{\alpha}_{\text{eff}} = 20\,^\circ$ (ID 4 to 6 and 9 to 10) and variations of St (ID 1 to 3) and k (ID 7 and 8) with respect to the baseline case, effective inflow angles close to pure plunging motion, indicated by their low $\hat{\alpha}_{\text{geo}}$, can also be investigated. The parameter space investigated at BUAA is depicted in table 4.2, again including the common baseline case referred to ID 3 (TUDA) and ID 11 (BUAA). With the higher attainable Strouhal number the dimensionless parameter range at BUAA could be extended towards the regime of efficient forward flight, characterized by higher St. It is notable that ID 10 and 13 match in all key parameters even though they will not be examined in detail below.

Table 4.2: Dimensionless and geometric parameter range investigated at BUAA for $Re = 24,000$, including the common baseline case (ID 11).

ID	Sym.	k	T	St	H	$\hat{\alpha}_{\text{eff}}$	$\hat{\alpha}_{\text{geo}}$
11	♦	0.48	3927	0.1	0.039	30	12.67
12	✳	0.48	3927	0.16	0.063	30	3.31
13	△	0.3	6285	0.04	0.025	20	12.86

4.1.2 Baseline Case Comparison

With the aim of comparing results from the two different facilities at BUAA and TUDa in water and air, this section focuses on the evaluation of the common baseline case.

Kinematic Comparison

To allow flow fields to be compared between both facilities, the vertical leading edge position of the airfoil $h(t)$ was extracted from masked raw PIV images via image processing. In Fig. 4.3, $h(t)$ of both facilities and the intended curve are shown for the common baseline case, normalized with the respective full stroke height H.

Deviations between the measured and intended leading edge positions were found to be smaller than 0.6 % of the full stroke height for all investigated cases, which is within the accuracy of the actuators used to pitch and plunge the flat plates. These deviations are small enough to allow velocity fields and vortex characteristics from both setups to be directly compared to one another.

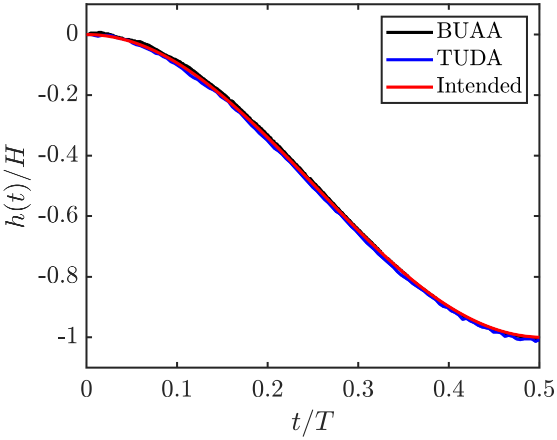

Figure 4.3: Comparison of the intended and experimentally realised vertical leading edge positions h, normalized by the plunge height H as a function of dimensionless time (t/T) for the common baseline case. (Reprinted from Kissing et al. (2020c), with permission of Springer Nature. © 2019 Springer Nature.)

Flow Fields

A qualitative aspect of comparability is the evolution of the flow field and its topology, which is depicted in terms of ensemble averaged vorticity fields in Fig. 4.4. While the first three rows depict the entire field with only every 6th vector for clarity, figures in the last row show the leading edge region with every 3rd vector as highlighted in the third row by a red square. In the first row the rear confining stagnation point behind the LEV is marked with an orange diamond. The coordinate system is fixed at the initial top position of the airfoil leading edge and both axes are normalized by the flat plate chord. At $t/T = 0.25$ the LEV containing concentrated negative (blue color coded) vorticity grows on the airfoil by accumulating circulation from the leading edge shear-layer (first row in Fig. 4.4). A thin layer of counterclockwise rotational fluid, indicated by the positively signed (red color coded) vorticity, can be observed below the vortex in addition to a distinct region comprising positively signed vorticity ahead of the main vortex. This counterclockwise rotational fluid forms a secondary vortex rotating in the opposite direction of the clockwise rotating LEV. A third clockwise rotating vortex between the leading edge shear layer and the secondary vortex completes the secondary vortex structures. This is identifiable from the indicated velocity vectors at the latest dimensional time instant in Fig. 4.4. At this early stage the flow fields from both setups are in very good agreement with respect to the observed topology and vorticity intensity within the vortices.

Furthermore, towards the end of the downstroke, the LEV continues growing, although at $t/T = 0.35$ the connection between vortex and leading edge shear layer appears to be interrupted in the vorticity fields from BUAA, while it is unimpaired in the TUDa fields. An inspection of the entire time series of the flow fields revealed that the LEV and shear layer are frequently interrupted for TUDa results, while for BUAA flow fields their connection appears to be generally weaker, indicated by lower vorticity values of the connecting region.

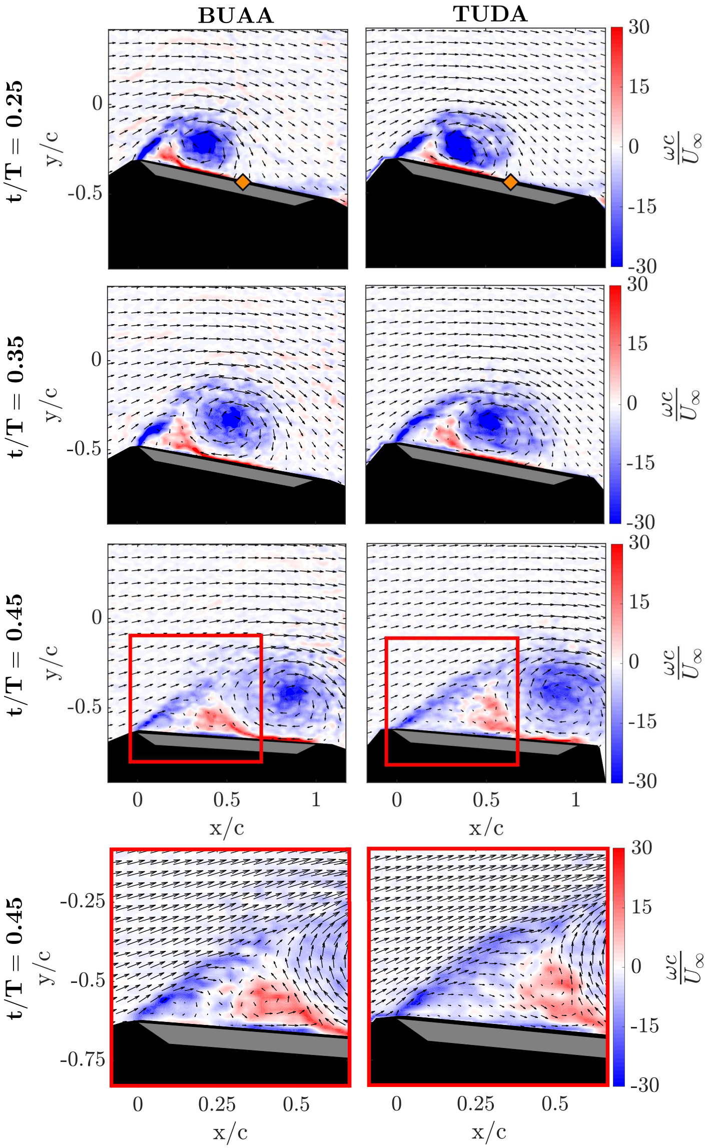

Figure 4.4: Flow field in terms of normalized vorticity $\omega c/U_\infty$ for different dimensionless time instants t/T from ensemble averaged PIV measurements at BUAA (left column) and TUDa (right column) for the common baseline case. The inflow is from the left, the airfoil is masked out in grey and the laser light shadow caused by the airfoil in black. (Reprinted from Kissing et al. (2020c), with permission of Springer Nature. © 2019 Springer Nature.)

Differences of single events in the instantaneous velocity fields are of minor relevance for the present study, aimed at highlighting the main features of the ensemble averaged velocity fields. Shortly before the end of the downstroke at $t/T = 0.45$, a slight deviation of the LEV center position can be observed comparing third row depictions in Fig. 4.4. At this late stage of the downstroke the LEV is only weakly connected to the leading edge shear layer for both evaluations, indicating the end of circulation accumulation. Overall, the topological evolution of the ensemble averaged flow fields and the qualitative vortex characteristics evolution are in very good agreement between the two facilities.

Vortex Characteristics

The LEV characteristics in terms of its position, size and circulation determine the lift that is induced on the pitching and plunging flat plate. Therefore, these quantities are of key interest in future flow control approaches. To allow comparability of these key quantities between both facilities, vortex characteristics of the common baseline case will now be compared quantitatively. Fig. 4.5 depicts the normalized LEV circulation $\Gamma_{\mathrm{LEV}}/U_{\infty}c$ determined by the integration of vorticity within its detected boundary of the Γ_2 scalar field. Raw images were correlated using the same algorithm implemented at TUDa and the same vortex identification method in addition to the same vorticity derivation and integration schemes. The circulation of the vortex was computed for each individual run prior to ensemble averaging of the extracted circulation for all 15 runs. In this manner the standard deviation can be computed for the final, ensemble averaged results, indicated as coloured shading in Fig. 4.5.

Early during vortex growth, the LEV circulation from both facilities increases with the same slope but with a somewhat higher vortex circulation magnitude of the TUDa results before $t/T \approx 0.22$. After this phase, stronger normalized circulation fluctuations are observed in the TUDa results compared to those from BUAA. These fluctuations and the initial offset originate from an intermittent inclusion of the leading edge shear layer into the computational vortex boundary, evident in single frame evaluations, which are only observed for TUDa experiments. This was confirmed by simultaneous fluctuations of the detected area of the vortex boundary. The LEV stops

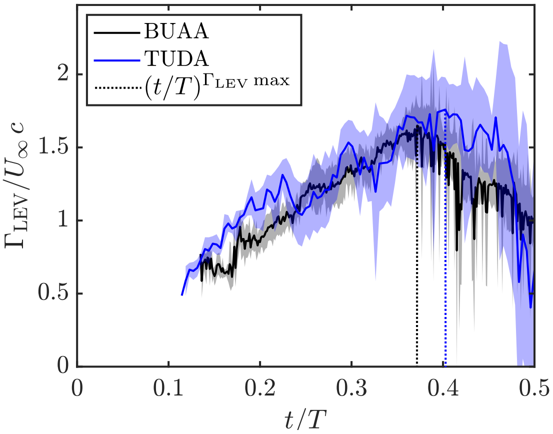

Figure 4.5: Evolution of the normalized leading edge vortex circulation $\Gamma_{\mathrm{LEV}}/U_\infty\, c$ for the common baseline case from both setups. The respective standard deviation is indicated as a coloured shadow and the peak circulation $(t/T)^{\Gamma_{\mathrm{LEV}}\,\max}$ as dashed line. Circulation is obtained by integration of vorticity over the vortex area identified from the Γ_2 scalar field. (Reprinted from Kissing et al. (2020c), with permission of Springer Nature. © 2019 Springer Nature.)

accumulating circulation between $0.38 \leq t/T \leq 0.41$ in BUAA and TUDa results, indicated by the peak circulation instants $(t/T)^{\Gamma_{\mathrm{LEV}}\,\max}$ (dashed lines in Fig. 4.5).

To verify that intermittent inclusion of the leading edge shear layer into the calculation of the circulation is an error source for deviations of the circulation evolution during the early LEV growth phase, the circulation was also computed using the entire field of view as an integration domain. A comparison of the normalized circulation from the entire field of view for both setups is shown in Fig. 4.6. Despite very small deviations of the circulation, the overall quantitative agreement of the evolution is very good. In both experiments (at BUAA and TUDA), the maximum circulation is reached between $0.4151 \leq t/T \leq 0.4195$ with 3% amplitude difference. Deviations in circulation remain below 5.3% at any instant throughout the downstroke. Based on this good quantitative agreement it can be concluded that the observed deviations of circulation evolution in Fig. 4.5 are caused by an

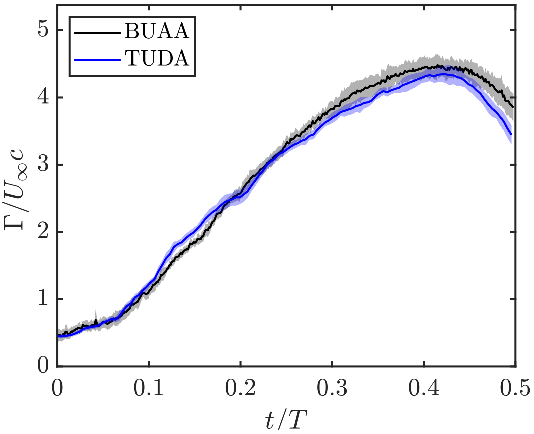

Figure 4.6: Evolution of the normalized circulation $\Gamma/U_\infty\, c$ for the common baseline case evaluated from the entire field of view to identify vortex boundary detection as the error source for circulation deviations. The standard deviation is indicated as coloured shadows. (Reprinted from Kissing et al. (2020c), with permission of Springer Nature. © 2019 Springer Nature.)

intermittent inclusion of the leading edge shear layer into the integration domain for TUDa results during vortex identification. Potential reasons for these deviations could be the different spatial resolution of velocity fields or different free-stream turbulence levels of the tunnels used.

Figure 4.7 shows a comparison of the normalized streamwise LEV center position x_{LEV}/c in a plate-fixed frame of reference. Again, the position is extracted from phase-locked velocity fields taken at each individual run prior to ensemble averaging. The evolution is in good agreement up to $t/T = 0.39$, whereupon small deviations of the position between BUAA and TUDa results occur. Since the accumulation of circulation in the vortex was found to stop at $t/T \approx 0.4$, these deviations are attributed to the final convection of the vortex downstream of the airfoil and thus are not of interest for current investigations. Note however, that the vortex center evolution in TUDa results might be considered as more parabolic. Overall, good agreement of vortex characteristics is achieved between ensemble averaged results derived from the experiments performed at BUAA and TUDA.

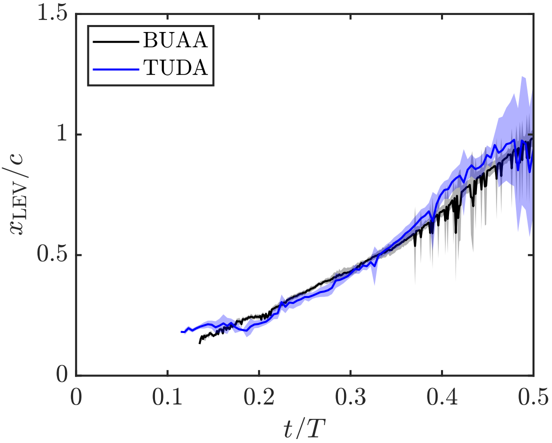

Figure 4.7: Evolution of the normalized streamwise LEV center position x_{LEV}/c in a plate-fixed frame of reference from the maximum of the Γ_1 scalar field for the common baseline case. The standard deviation is indicated as a coloured shadow. (Reprinted from Kissing et al. (2020c), with permission of Springer Nature. © 2019 Springer Nature.)

Detachment Mechanism

Two different mechanisms of LEV detachment are postulated in literature, as pointed out in section 1.2.2. One is related to fluid recirculation around the trailing edge of the airfoil, when the rear stagnation point of the flow behind the LEV on the airfoil convects beyond the trailing edge. This mechanism is investigated in the common baseline case discussed in this section. Fig. 4.8 shows the topological situation during LEV growth on a flat plate for orientation, where the rear stagnation point of the flow behind the LEV is marked as an orange diamond. As demonstrated by Rival et al. (2014), the extraction of the velocity immediately above and parallel to the airfoil surface allows the convection of the rear confining stagnation point of the LEV (denoted as H_1 and illustrated as orange diamond in Fig. 4.8 and Figs. 4.4 in the top row) to be tracked according to the change of velocity sign. The tangential velocity induced by vortices on the airfoil surface is schematically shown in Fig. 4.8 for an arbitrary point during airfoil motion. By identification of the rear stagnation point evolution, the temporal instant

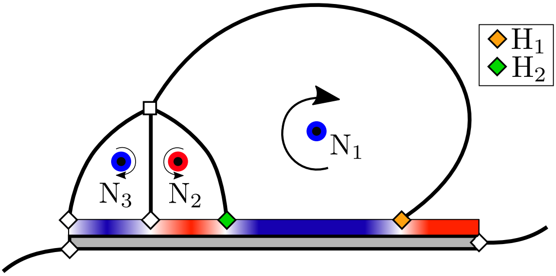

Figure 4.8: Sketch of the flow topology during leading edge vortex growth on an unsteady flat plate. Half-saddles are marked with diamonds and full-saddle with a circle. The main LEV (node N$_1$) and secondary vortices (nodes N$_2$ and N$_3$) are highlighted in addition to the tangential velocity on the airfoil surface u induced by them. Adapted from Rival et al. (2014). (Reprinted from Kissing et al. (2020c), with permission of Springer Nature. © 2019 Springer Nature.)

of maximum circulation can be compared to that of recirculation. Note, that the growth of secondary structures can also be traced by consideration of the H$_2$ half-saddle behind the structures.

Figure 4.9 shows tangential velocity distributions on the airfoil surface over dimensionless time. Velocities are extracted along three lines parallel to the surface and running tangential to the plate from the leading edge at $x/c = 0$ to the trailing edge at $x/c = 1$ for time steps of $\Delta(t/T) \approx 0.002$. Fig. 4.9 shows averaged values of these three lines that are located $y/c = 0.011$ apart from each other with $y/c = 0.011$ spacing to the surface.

Red colour coded areas indicate downstream velocities while blue colour coded areas velocity represents upstream fluid motion induced by the clockwise rotating LEV on the airfoil surface. So a LEV driven upstream velocity region can be clearly identified in Fig. 4.9 convecting downstream on the airfoil. Upstream velocities on the airfoil surface occur from about $t/T \approx 0.1$ for both evaluations. After emergence of the LEV a change of sign in velocity can be observed downstream of the vortex, which indicates the rear stagnation point of the flow at the rear of the LEV. For clarity it is marked with a orange dashed line in Fig. 4.9. During the growth of the LEV, the stagnation point travels downstream until it reaches the trailing edge at $x/c = 1$ (instant marked by an orange diamond). From this instant on, recirculation of fluid

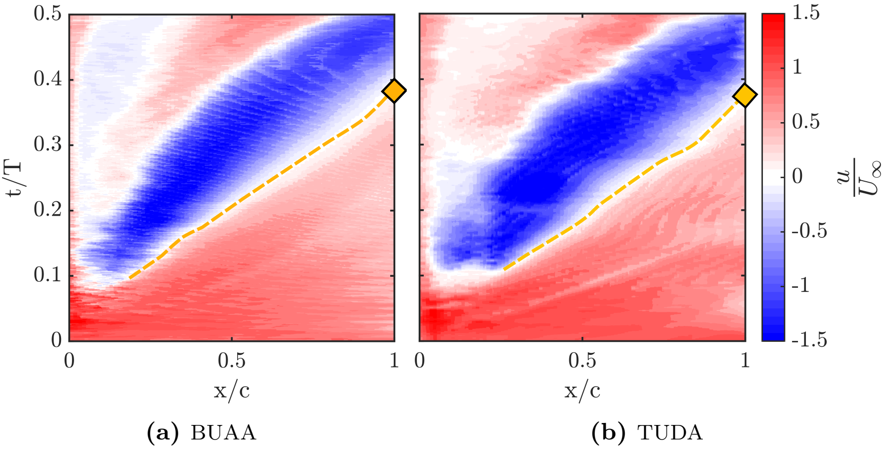

(a) BUAA **(b)** TUDA

Figure 4.9: Evolution of the velocity tangential to the airfoil surface u scaled by the free-stream velocity U_∞ over dimensionless chordwise position and time. The trace of the rear stagnation point of the flow behind the LEV is marked with a orange dashed line; (a) tangential velocity from measurements in water at BUAA; (b) tangential velocity from measurements in air at TUDA. (Reprinted from Kissing et al. (2020c), with permission of Springer Nature. © 2019 Springer Nature.)

from beneath the airfoil around the trailing edge is initiated. This instant agrees well between the two facilities: $t/T = 0.39$ for BUAA and $t/T = 0.38$ for TUDA. Reconsidering the instant at which circulation accumulation stops, identified from the LEV circulation evolution (at $t/T \approx 0.39$), the recirculation of fluid occurs slightly before peak circulation. This shows that for the investigated baseline case, the termination of circulation accumulation of the LEV correlates with recirculation of fluid around the trailing edge for both facilities. The correlation indicates that the LEV detaches in accordance with the process described by Rival et al. (2014) in the baseline case. Considering the covering ratio κ, a detachment in accordance with the boundary layer eruption detachment was expected. A potential reason for the encountered deviation of the detachment mechanism could be the leading edge curvature of the airfoil, which affects the shear layer properties and thus the circulation accumulation rate of the LEV. Nevertheless, it should be noted that distinct secondary structures upstream of the LEV can be observed at later instants for $t/T \geq 0.2$, indicated by additional changes of tangential velocity sign in horizontal direction in Fig. 4.9.

Since ID 10 and ID 13 cases are at the same dimensionless parameters, they were also compared using all measures from the baseline case examination. In accordance with the comparisons from above, the agreement of ID 10 and 13 cases is similarly good.

4.2 Secondary Structure Occurrence and Effect on the Leading Edge Vortex Detachment

Flow control attempts to prolong the LEV growth phase on pitching and plunging airfoils in this thesis focus on the delay of secondary structure initiated vortex detachment. The occurrence of secondary structures and their effect on the detachment process of the LEV is still not fully understood, as described in section 1.2.2; their emergence and effect on the instant when the LEV ceases to accumulate circulation will be investigated in detail below in section 4.2. Based on the observed comparability of results obtained at the two facilities, each evaluation will consider results from both facilities to extend the covered parameter range.

A combination of Lagrangian flow field analysis based on FTLE and Eulerian vortex characteristics is used for a detailed investigation of secondary structures and their effect on LEV characteristics, as discussed in section 2.3.3. Fig. 4.10 depicts FTLE flow fields in terms of attracting and repelling (backward and forward) FTLE ridges for different dimensionless time instants computed from velocity data obtained at the TUDa facility. All ridges that passed the 80% threshold are depicted at the same color level to allow topological structures to be identified more easily.

Early in the downstroke at $t/T = 0.15$, shown in Fig. 4.10a, the LEV is confined at the top and to the rear by a shell-shaped repelling ridge (highlighted in red). At $t/T = 0.175$ and for further time instants the confining ridge disappears, since its strength decreases. The leading edge shear layer feeding the LEV is demarcated in upstream direction by an attracting ridge

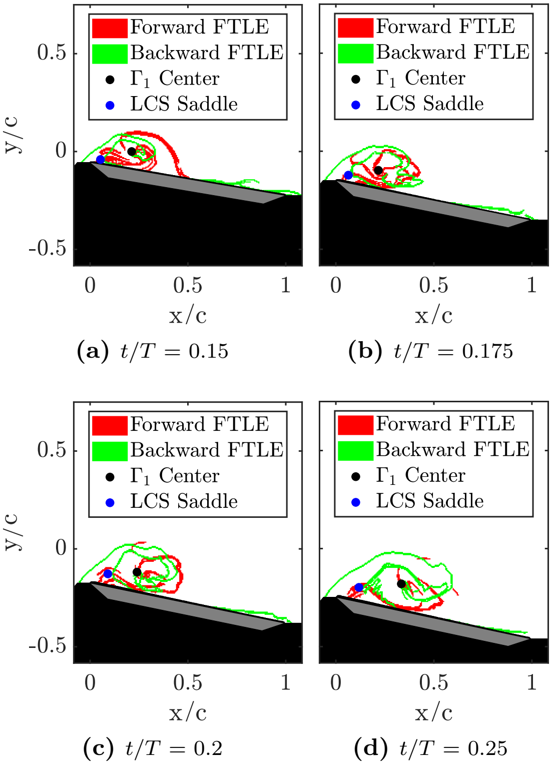

(a) $t/T = 0.15$ **(b)** $t/T = 0.175$

(c) $t/T = 0.2$ **(d)** $t/T = 0.25$

Figure 4.10: Flow field in terms of repelling and attracting ridges for different dimensionless time instants obtained from forward and backward FTLE computations for the common baseline case (ID 3 from TUDA). FTLE ridges are obtained using a 80 % threshold of the respective maximum FTLE value in each frame. The airfoil is masked out in grey and the laser light shadow in black. The vortex center from Γ_1 criterion and the LCS saddle are marked as well. (Reprinted from Kissing et al. (2020c), with permission of Springer Nature. © 2019 Springer Nature.)

(highlighted in green). In the downstream direction it is demarcated by an attracting ridge arising from the airfoil surface, forming a channel with the upstream demarcation line that curls up into the vortex. For $t/T = 0.15$ and 0.175 there are no distinct flow structures visible at the leading edge, immediately above the airfoil. However from $t/T = 0.175$ to 0.2 a region of fluid right above the airfoil surface at the leading edge emerges, which is isolated from the flow field by a repelling ridge. Fluid particles close to this ridge will depart from each other at future instances by becoming entrained into different topological structures, namely the main LEV and the secondary vortices, which are located close to the leading edge. The qualitative evolution of FTLE fields obtained from BUAA data was found to be in very good agreement regarding the observed topology.

4.2.1 Secondary Structure Occurrence (SSO)

In continuation of earlier efforts by Kissing et al. (2020c), the occurrence of secondary structures is quantified with the approach introduced by Huang & Green (2015). This method identifies Lagrangian Coherent Structure (LCS) saddle points in the flow field by intersections of repelling and attracting ridges. The flow saddle point is indicated in Fig. 4.10 as a blue point. As soon as secondary structures arise and grow, the LCS saddle point moves downstream as a result of the increased area covered by the structures. Therefore, the streamwise LCS saddle location in a plate-fixed frame of reference is extracted to evaluate secondary structure growth as depicted for ID 3 case from TUDa in Fig. 4.11. The LCS saddle location was extracted by an automated identification of the first intersection of attracting and repelling ridges downstream of the leading edge. Only intersections below the height of the vortex center were considered.

After an initial phase where the LCS saddle remains close to the leading edge at about $x/c = 0.05$, it starts to convect downstream shortly before $t/T = 0.2$, as shown in Fig. 4.11, indicating an increase of the area covered by secondary structures and thus their growth. This evolution is in agreement with the observed secondary structure onset from FTLE fields in Fig. 4.10. To determine the instant of convection increase and thus secondary structure occurrence, the LCS saddle location is approximated to first order separately from $t/T = 0.15$ to 0.18 and from 0.18 to 0.25. The dimensionless time instant of secondary structure occurrence (SSO), denoted as $(t/T)_{\mathrm{SSO}}^{\mathrm{Exp.}}$, can be determined by the intersection of both convection slopes. It is marked in Fig. 4.11 by a vertical dashed line. The convection of the LCS saddle evaluated from FTLE fields obtained from BUAA for baseline case data was found to

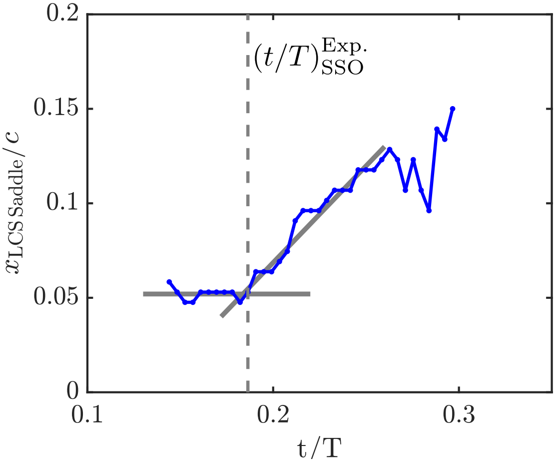

Figure 4.11: Normalized streamwise LCS saddle position $x_{\mathrm{LCS\,Saddle}}/c$ as a function of dimensionless time t/T. The position is extracted in a plate-fixed frame of reference. The convection of the LCS saddle at different phases is approximated linear and indicated by solid grey lines. The derived instant of secondary structure occurrence $(t/T)^{\mathrm{Exp.}}_{\mathrm{SSO}}$ is marked with a vertical dashed line. (Reprinted from Kissing et al. (2020c), with permission of Springer Nature. © 2019 Springer Nature.)

occur about 3 % earlier than from TUDa with respect to the downstroke period, which is considered to be very good agreement. Subsequently, $(t/T)^{\mathrm{Exp.}}_{\mathrm{SSO}}$ was evaluated for all investigated cases.

The circulation of the LEV from vortex identification evaluations, discussed in respect to Fig. 4.5, was additionally used to compute the vortex Reynolds number $Re_v = \Gamma_{\mathrm{LEV}}/\nu\pi$ proposed by Doligalski et al. (1994) at the determined secondary structure onset. The vortex Reynolds number represents the tendency of the boundary layer below the vortex on the airfoil surface to respond to the vortex induced pressure gradient. The viscous response of the boundary layer occurs concurrent with a high concentration of vorticity in the boundary layer and leads to an eruption of a fluid spire and subsequent formation of secondary structures. For low Re_v, the vortex circulation and thus the induced velocity and pressure gradient on the airfoil surface are lower and the boundary layer response is suppressed. For higher Re_v, the response is more likely triggered. For additional information on the phenomena, the reader is referred to Doligalski et al. (1994). Re_v is shown as a function of $(t/T)_{\mathrm{SSO}}^{\mathrm{Exp.}}$ in Fig. 4.12. Horizontal error bars indicate the error in identification

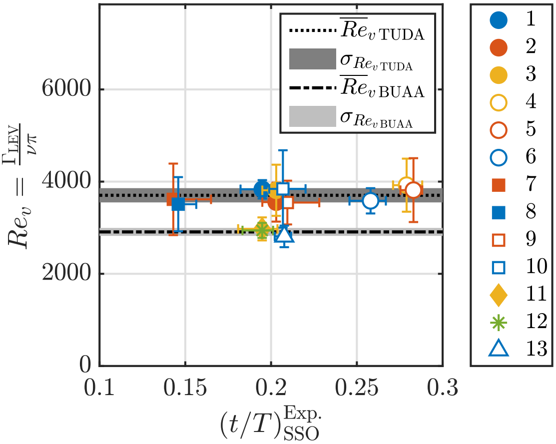

Figure 4.12: Vortex Reynolds number Re_v at secondary structure onset $(t/T)_{\mathrm{SSO}}^{\mathrm{Exp.}}$. Measurements at TUDa (ID 1 to 10) and measurements at BUAA (ID 11 to 13) are used to obtain separate mean vortex Reynolds numbers $\overline{Re}_v$ and their respective standard deviations σ_{Re_v}, indicated as dashed lines and grey patches; see Table 4.1 and 4.2 for the respective parameter combinations of ID 1-13 and marker style schemes. (Reprinted from Kissing et al. (2020c), with permission of Springer Nature. © 2019 Springer Nature.)

of secondary structure onset from the convection of the LCS saddle and vertical bars the standard deviation of Re_v caused by the standard deviation of circulation at the determined secondary structure onset. Considering the secondary structure onset for cases with $\hat{\alpha}_{\mathrm{eff}} = 30\,^\circ$ from TUDA, represented by the filled markers (ID 1; 2; 3; 7; 8), it can be observed that secondary structures arise at earlier dimensionless times for lower k (square markers) than for a higher ones (circle markers). The Strouhal number has a minor influence on the onset instant (different colours). Similar trends can be observed for $\hat{\alpha}_{\mathrm{eff}} = 20\,^\circ$ cases, indicated by the open markers (ID 4; 5; 6; 9; 10), with a general temporal lag. The instants of secondary structure onset from BUAA agree well with the TUDa results, considering cases of the same parameters (ID 3 and 11 as well as ID 10 and 13). The observation of a minor influence of the Strouhal number is additionally confirmed by the ID 12 case agreement with ID 3 and 11 cases, since it denotes a case with parameters identical to them but with a higher St of 0.16.

For parameters investigated in this thesis, secondary structures occur when the vortex Reynolds number reaches a threshold within a very narrow band for each setup, although the mean vortex Reynolds numbers $\overline{Re_v}$ differ between both. For TUDa results, secondary structures occur for Re_v between 3,500 and 3,900 with $\overline{Re_v} = 3{,}700$ and a standard deviation σ_{Re_v} of about 150. At BUAA they arise for $\overline{Re_v} = 2900$ with a smaller σ_{Re_v} of about 90. Reconsidering the comparison of circulation evolution for the common baseline case from Fig. 4.5, where an offset for earlier instants could be attributed to the inclusion of the leading edge shear layer for the TUDa evaluations, the higher Re_v from TUDa results can be expected and attributed to the vortex identification methodology.

Based on a known $\overline{Re_v}$ threshold at the onset of secondary structures, which is in turn dependent on the LEV circulation, their onset could be predicted if the accumulation of circulation of the LEV were known. The observed $\overline{Re_v}$ threshold indicates that secondary structures emerge at a certain circulation of the LEV. Their onset could be temporally determined via the instant where the LEV reaches a circulation threshold. This approach is considered a valuable prediction tool for future attempts to delay LEV detachment, which focus on secondary structure suppression. With the capability of predicting secondary structure emergence, their onset could be specifically delayed or suppressed. Wong & Rival (2015) derive an expression for the rate of circulation accumulation of the LEV, $\dot{\Gamma}_{\mathrm{LEV}}$, in which it is proportional to the square of the effective inflow velocity on the airfoil u_{eff}:

$$\dot{\Gamma}_{\mathrm{LEV}} \propto u_{\mathrm{eff}}^2(t). \tag{4.1}$$

Their model builds upon an analytical expression for the mass flux into the LEV, derived by Wong et al. (2013) based on the vorticity transport equation. With an approximation of the circulation flux per mass flux from a path integral around the shear layer, the circulation flux into the LEV is derived. Their model was found to capture Γ_{LEV}, experimentally obtained via vortex identification, precisely for cases where the LEV forms very early in the downstroke.

During the comparison of the circulation evolution predicted by the aforementioned model and measured evolution, significant deviations were encountered for several cases. In these cases the LEV was found to emerge delayed in respect with the motion start, caused by a delayed roll-up of the leading edge shear layer. This led to a temporal offset of the measured LEV circulation with respect to the predicted value, although the slope of circulation accumulation was still in very good agreement. To account for the observed delayed LEV formation, Mulleners & Raffel (2012) developed a scaling for the temporal LEV formation lag with respect to the motion start $t^{\mathrm{Exp.}}_{\mathrm{LEV\,onset}}$, which is tested as a potential solution to adapt the aforementioned circulation flux model. It is based on the assumption that the rate of change of the inflow angle on the airfoil during the period when the inflow angle exceeds the static stall angle is responsible for the temporal lag of LEV formation. Fig. 4.13a shows the correlation between the rate of change of the effective inflow angle during this period $\dot{\alpha}_{\mathrm{eff,SS}}$ and the LEV onset delay $t^{\mathrm{Exp.}}_{\mathrm{LEV\,onset}}$, determined by visual inspection of FTLE fields. By comparing the observed LEV emergence from TUDa and BUAA evaluations with a linear approximation according to

$$t^{\mathrm{Exp.}}_{\mathrm{LEV\,onset}} \cdot \frac{U_\infty}{c} = a \cdot \dot{\alpha}_{\mathrm{eff,SS}} \cdot \frac{c}{U_\infty} + b, \tag{4.2}$$

indicated by the dashed red line, good agreement in terms of a linear scaling by $\dot{\alpha}_{\mathrm{eff,SS}}$ can be observed. a and b are empirical parameters determined from reference measurements.

Accordingly, the circulation flux model by Wong & Rival (2015) is adapted to account for the delayed vortex formation. This is done by offsetting temporal information used to integrate $\dot{\Gamma}_{\mathrm{LEV}}$ from equation 4.1 according to the approximated $t^{\mathrm{Exp.}}_{\mathrm{LEV\,onset}}$:

$$\Gamma_{\mathrm{LEV}} = \int u^2_{\mathrm{eff}} \, \mathrm{d}(t - t^{\mathrm{Exp.}}_{\mathrm{LEV\,onset}}). \tag{4.3}$$

By using separate circulation threshold values, derived from $\overline{Re_v}$ thresholds for TUDa and BUAA, the dimensionless time instant of expected secondary structure onset $(t/T)^{\mathrm{Theor.}}_{\mathrm{SSO}}$ is obtained from the adapted circulation flux model. It is compared to the experimentally observed secondary structure occurrence $(t/T)^{\mathrm{Exp.}}_{\mathrm{SSO}}$ in Fig. 4.13b. The maximum deviation between the predicted and

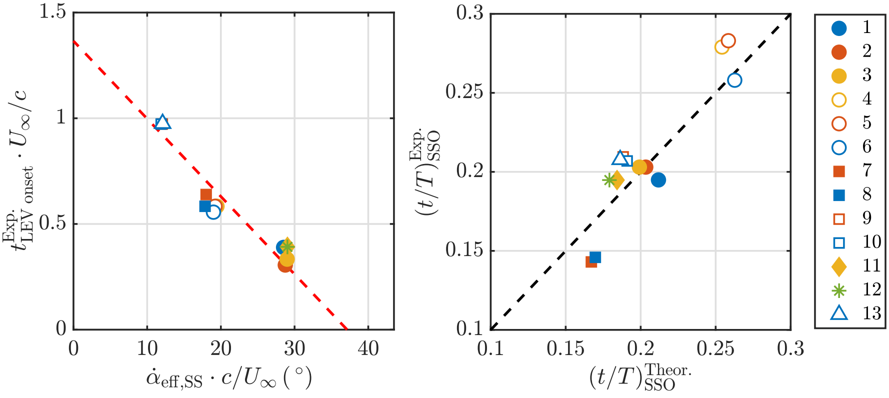

(a) LEV formation delay **(b)** Modelled secondary structure occurrence

Figure 4.13: Modelling secondary structure onset (a) LEV onset delay $t^{\mathrm{Exp.}}_{\mathrm{LEV\ onset}}$ as a function of the rate of change of the effective inflow angle on the airfoil during static stall angle $\dot{\alpha}_{\mathrm{eff,SS}}$. A linear approximation of the scaling is indicated as dashed red line. (b) Modelling secondary structure occurrence $(t/T)^{\mathrm{Theor.}}_{\mathrm{SSO}}$ based on a vortex Reynolds number threshold, taking the delay of LEV formation in circulation approximation into account; see Table 4.1 and 4.2 for the respective parameter combinations of ID 1-13 and marker style schemes. (Reprinted from Kissing et al. (2020c), with permission of Springer Nature. © 2019 Springer Nature.)

measured secondary structure occurrence $\Delta(t/T)$ is 0.0248 (equivalent to 4.9% of the downstroke period), which is considered as a reasonably accurate prediction.

With the introduced model for secondary structures, it is possible to compute their onset based on kinematic parameters. Therefore, the effective inflow velocity, determined by the inflow and plunging velocity, and the pitching rate evolution have to be known. The only necessary empirical input is the scaling parameter for the delay in LEV formation $t^{\mathrm{Exp.}}_{\mathrm{LEV\ onset}}$. This can be obtained using a limited number of reference measurements.

4.2.2 Secondary Structure Effect on Leading Edge Vortex Detachment

The role of the effective inflow angle amplitude on the airfoil in the LEV detachment process has not been considered in detachment mechanisms proposed in literature (cf. section 1.2.2). Therefore, the effect of secondary structures in the detachment process is discussed in the following by consideration of different effective angle of attack amplitudes. This discussion will focus on secondary structure effects on the termination of circulation accumulation of the LEV to clarify their role as a trigger of secondary topological structures. It should be noted that the LEV detachment can also be defined in terms of the lift force decrease, which however, has not been measured in this study.

To identify parameter sets where circulation accumulation of the LEV stops as a direct consequence of secondary structure emergence, the concurrency of both events is compared. This is done with the aid of the dimensionless time lag between secondary structure onset ($(t/T)_{\mathrm{SSO}}^{\mathrm{Exp.}}$) and maximum LEV circulation ($(t/T)^{\Gamma_{\mathrm{LEV}}\,\max}$), denoted as $\Delta(t/T)_{\mathrm{SSO}}^{\Gamma_{\mathrm{LEV}}\,\max}$. It is shown in Fig. 4.14 as a function of the effective inflow angle amplitude on the airfoil $\hat{\alpha}_{\mathrm{eff}}$. The instant of secondary structure onset is determined by topological FTLE field evaluations according to the methodology introduced along the discussion of Fig. 4.11 and the instant of LEV peak circulation from vortex identification results, indicated by the dashed lines in Fig. 4.5. For parameter sets with $\hat{\alpha}_{\mathrm{eff}} = 20\,^{\circ}$ a small time lag can be observed. On the other hand the time lag is larger for cases with $\hat{\alpha}_{\mathrm{eff}} = 30\,^{\circ}$.

Although $\hat{\alpha}_{\mathrm{eff}}$ seems to allow for a classification whether secondary structure occurrence causes circulation accumulation termination as a more direct consequence, it does not scale $\Delta(t/T)_{\mathrm{SSO}}^{\Gamma_{\mathrm{LEV}}\,\max}$ directly nor solely, as evident from different $\Delta(t/T)_{\mathrm{SSO}}^{\Gamma_{\mathrm{LEV}}\,\max}$ for the same $\hat{\alpha}_{\mathrm{eff}}$. Additional scalings have been tested on results presented in Fig. 4.14. A correlation of $\dot{\alpha}_{\mathrm{eff,\,SS}}$ with $\Delta(t/T)_{\mathrm{SSO}}^{\Gamma_{\mathrm{LEV}}\,\max}$ did not exhibit correlation of both quantities. Convective normalization of the time lag has also been considered, but did not exhibit clear correlations. Recall that such a convective scaling might allow modelling of secondary structure onset via circulation accumulation and the Re_v threshold, but does not directly determine effects of secondary structures on LEV detachment.

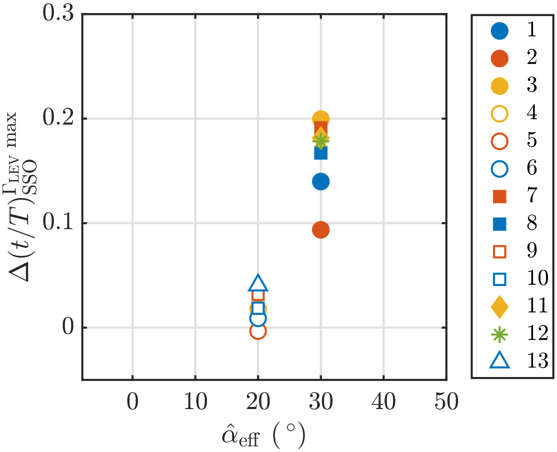

Figure 4.14: Dimensionless time lag between the onset of secondary structures and the instant of maximum LEV circulation $\Delta(t/T)_{\mathrm{SSO}}^{\Gamma_{\mathrm{LEV}}\,\max}$ to evaluate the concurrency of both events, shown over of the effective inflow angle amplitude on the airfoil $\hat{\alpha}_{\mathrm{eff}}$; see Table 4.1 and 4.2 for the respective parameter combinations of ID 1-13 and marker style schemes. (Reprinted from Kissing et al. (2020c), with permission of Springer Nature. © 2019 Springer Nature.)

These observations suggest that for lower effective angle of attack amplitudes of 20 °, the emergence of secondary structures causes the LEV to stop the accumulation of circulation independent of fluid recirculation around the trailing edge. This is in accordance with the detachment mechanism defined by Widmann & Tropea (2015). On the other hand, the termination of circulation accumulation of the LEV occurs coincident with fluid recirculation in the common baseline case with $\hat{\alpha}_{\mathrm{eff}} = 30\,°$, discussed in section 4.1.2. As it can be seen in Fig. 4.12, secondary structures occur already at $t/T = 0.2$, but do not cause the LEV to stop accumulating circulation as a direct consequence in this case. This suggests a detachment in accordance with Rival et al. (2014).

To validate if fluid recirculation around the trailing edge causes the LEV to stop accumulation of circulation for all cases with $\hat{\alpha}_{\mathrm{eff}} = 30\,°$, they were investigated by means of the tangential velocity plot discussed in respect to Fig. 4.9. The instant of fluid recirculation around the trailing edge and maximum LEV circulation coincide or recirculation occurs slightly before maximum circulation for all cases. This confirms that the LEV detaches in accordance with the mechanism described by Rival et al. (2014) in cases where $\hat{\alpha}_{\text{eff}}$ is 30 °. The change of the prevalent detachment mechanism for different $\hat{\alpha}_{\text{eff}}$ but the same dimensionless parameters highlights its role as an important parameter influencing vortex detachment. Additionally, the LEV stops accumulating circulation as a more direct consequence of secondary structure occurrence for cases with a lower $\hat{\alpha}_{\text{eff}}$. Both facts clearly indicate that $\hat{\alpha}_{\text{eff}}$ has to be taken into account in models that aim to distinguish between detachment mechanisms like the covering ratio κ. The mechanism, which causes the LEV to stop accumulating circulation after secondary structure occurrence will be investigated further below.

A potential scenario explaining how secondary structures cause the LEV to stop accumulating circulation is an interaction of the shear layer fluid from the leading edge of the airfoil with secondary structures, which takes place before the shear layer fluid reaches the LEV. An interaction of the negatively signed vortical fluid from the shear layer with the positively signed of secondary structures would presumably result in cross-annihilation of vorticity, as described by Wojcik & Buchholz (2014). Additionally, the shear layer of high velocity could push secondary structures and the main LEV downstream if a low shear layer angle directs fluid directly into those structures. Likewise, secondary structures could guide the shear layer curvature in an upward or downward direction such that it no longer reaches the main LEV.

The geometric factors determining whether an interaction of any kind is enabled are the evolution of position and size of secondary structures in combination with the shear layer angle. As soon as secondary structures arise, they will grow and consequently cover a larger area. If the shear layer angle does not increase further from the instant of secondary structure onset, an interaction of both due to growing secondary structures is a direct consequence. For lower peak inflow angles on the airfoil the shear layer angle is assumed to reach lower peak values and an interaction of secondary structures with the shear layer occurs earlier. This could explain the observed concurrency of secondary structure onset and the termination of circulation accumulation of the LEV for cases where $\hat{\alpha}_{\text{eff}}$ is 20 ° as shown in Fig. 4.14.

To test this hypothesis, the influence of the shear layer angle after separation from the leading edge α_{SL} will be investigated as a potential factor causing the simultaneous cessation of circulation accumulation and onset of secondary structures for $\hat{\alpha}_{\mathrm{eff}} = 20\,^\circ$. The methodology used to extract α_{SL} from vorticity fields is based on the fact that the leading edge shear layer is characterized by very high vorticity values. This methodology is illustrated exemplary for the ID 8 Case at $t/T = 0.26$ in Fig. 4.15a. Maximum vorticity values, denoted as $\omega_{\max}$ and indicated as orange dots in Fig. 4.15a, are extracted in a square, plate-fixed region of interest (ROI) that spans from the leading edge downstream up to the region of secondary structures. The final α_{SL} evolution is obtained from the angle between a first order fitted line (O^1) of the extracted

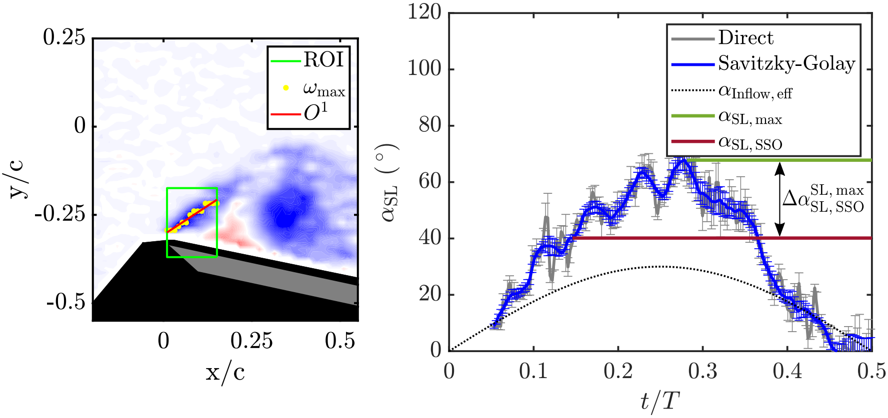

(a) Extraction of α_{SL} **(b)** Evolution of α_{SL} over dimensionless time t/T.

Figure 4.15: Characterisation of the shear layer angle after separation from the leading edge with respect to the airfoil surface α_{SL}. (a) Extraction methodology: the normalized vorticity field around the leading edge region is depicted at $t/T = 0.26$ from ID 8 case. (b) Ensemble averaged evolution of the extracted shear layer angle after separation from the leading edge α_{SL} over dimensionless time t/T for the ID 8 case from TUDA. Error bars represent the standard deviation of single run ensemble averaging. The shear layer angle during secondary structure onset $\alpha_{\mathrm{SL,\,SSO}}$ and the overall maximum angle $\alpha_{\mathrm{SL,\,max}}$ in addition to their difference $\Delta\alpha_{\mathrm{SL,\,SSO}}^{\mathrm{SL,\,max}}$ are also indicated. see Table 4.1 and 4.2 for the respective parameter combinations of ID 1-13 and marker style schemes. (Reprinted from Kissing et al. (2020c), with permission of Springer Nature. © 2019 Springer Nature.)

maximum value locations, indicated by a red line in Fig. 4.15a, and the airfoil surface. To exclude large fluctuations of the shear layer angle, its evolution is smoothed using a second order Savitzky-Golay filter of 15 frames width (corresponding to $\Delta(t/T) = 0.1$). After extraction of the angle from single runs, it is ensemble averaged for each parameter set. An exemplary evolution of α_{SL} for the ID 8 case from TUDa is depicted in Fig. 4.15b, where the direct ensemble averaged angle evolution is shown in grey and the smoothed in blue with error bars, indicating the standard deviation between single runs.

Two geometric factors determine where an interaction between secondary structures and the leading edge shear layer is initiated. The first factor is the size of secondary structures and the second is the shear layer angle evolution after secondary structure emergence. Secondary structures will grow after their emergence and if the shear layer angle does not increase further during this period, an interaction is initiated. So the difference between the shear layer angle at secondary structure onset $\alpha_{\mathrm{SL,\,SSO}}$ and the maximum shear layer angle $\alpha_{\mathrm{SL,\,max}}$ is considered as a measure where interaction likely occurs. This difference is denoted as $\Delta\alpha_{\mathrm{SL,\,SSO}}^{\mathrm{SL,\,max}}$ and highlighted in Fig. 4.15b by a double-sided arrow. For larger values of $\Delta\alpha_{\mathrm{SL,\,SSO}}^{\mathrm{SL,\,max}}$ the shear layer angle increases more after secondary structure onset and an interaction is unlikely to take place immediately, while it is likely to occur directly if the angle does not increase further. Fig. 4.16 shows the concurrency of the emergence of secondary structures and the peak circulation of the LEV as a function of $\Delta\alpha_{\mathrm{SL,\,SSO}}^{\mathrm{SL,\,max}}$. In cases with $\hat{\alpha}_{\mathrm{eff}} = 20\,^{\circ}$, indicated by open symbols, $\Delta\alpha_{\mathrm{SL,\,SSO}}^{\mathrm{SL,\,max}}$ is generally lower, so the shear layer angle at the leading edge increases less from the instant of secondary structure onset before reaching its maximum. This trend occurs concurrent with lower $\Delta(t/T)_{\mathrm{SSO}}^{\Gamma_{\mathrm{LEV}}\,\mathrm{max}}$ values, indicating a circulation accumulation stop of the vortex as a more direct consequence of secondary structure emergence. In contrast, the shear layer angle increases significantly after secondary structure emergence before reaching its maximum for $\hat{\alpha}_{\mathrm{eff}} = 30\,^{\circ}$ (filled markers). As discussed above, an interaction of secondary structures and the shear layer is assumed to be delayed for cases where the shear layer continues to increase after secondary structure emergence. For these conditions, secondary structures have sufficient space to grow without an interaction with the shear layer. The observations indicate that the interaction of the leading edge shear layer with secondary structures causes the LEV to

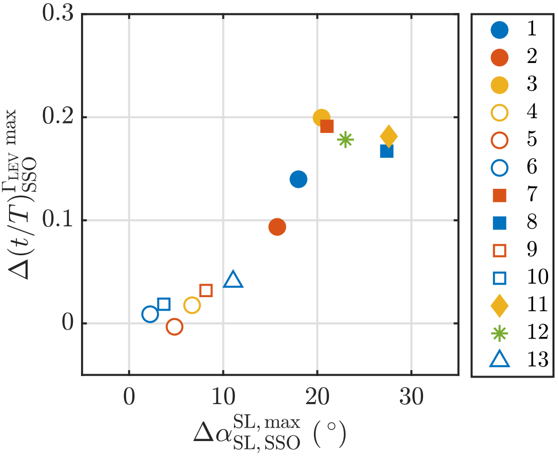

Figure 4.16: Correlation of the temporal concurrency between circulation accumulation stop of the LEV and secondary structure occurrence $\Delta(t/T)_{\mathrm{SSO}}^{\Gamma_{\mathrm{LEV}}\,\max}$ with the shear layer angle difference at secondary structure onset and the maximum angle $\Delta\alpha_{\mathrm{SL,\,SSO}}^{\mathrm{SL,\,max}}$; see Table 4.1 and 4.2 for the respective parameter combinations of ID 1-13. (Reprinted from Kissing et al. (2020c), with permission of Springer Nature. © 2019 Springer Nature.)

stop accumulation of circulation as a direct consequence in cases with $\hat{\alpha}_{\mathrm{eff}} = 20\,°$. It also highlights the interaction as the main cause for the change of the prevalent detachment mechanism observed in respect to Fig. 4.14 for cases with different $\hat{\alpha}_{\mathrm{eff}}$ but the same key parameters.

For either case in Fig. 4.16, $\Delta(t/T)_{\mathrm{SSO}}^{\Gamma_{\mathrm{LEV}}\,\max}$ and $\Delta\alpha_{\mathrm{SL,\,SSO}}^{\mathrm{SL,\,max}}$ correlate. Under the assumption, that the onset of interaction is determined by the shear layer angle increase after secondary structure occurrence, this shows that an interaction leads to the termination of circulation accumulation of the LEV, independent of recirculation.

4.3 Conclusions

In this chapter an approach to establish comparability of flow fields and LEV characteristics on a pitching and plunging flat plate obtained from facilities working with air and water as media is developed and validated. An order of magnitude difference in viscosity of the media extends the attainable parameter space in terms of dimensionless parameters.

The definition of a common baseline case was found to require careful consideration of the viable parameter range due to inherently different time scales of the airfoil motion caused by the difference in viscosity. Flow fields and topological evolution agreed well in air and water, but the LEV circulation differed. An intermittent inclusion of the leading edge shear layer into the LEV domain was identified as the source for deviations of the computed circulation. This highlights that small deviations in velocity information can affect circulation evaluations via the identified vortex domain used for circulation computation, even when using the same correlation algorithm. Data sets of baseline cases from TUDa and BUAA are also available online as reference cases (http://dx.doi.org/10.25534/tudatalib-168).

An investigation of secondary structures ahead of the LEV with the aid of a Lagrangian flow field analysis by FTLE ridges allowed a precise identification of their onset and effect on the LEV detachment process. The combination of both facilities enabled investigations of secondary structures over an extended parameter range, including variations of the reduced frequency, the Strouhal number and the effective angle of attack amplitude.

Secondary structures were found to emerge at similar vortex Reynolds numbers, computed from LEV circulation, at each setup and for all investigated parameters. Secondary structure occurrence, which is triggered by a viscous response of the boundary layer below the airfoil, is thus governed by the vortex circulation.

With the aid of existing circulation flux models from literature and their adaptation to account for a delayed LEV formation, a model to predict the temporal occurrence of secondary structures was developed and found to be in agreement with the observed onset.

For cases with a lower effective angle of attack amplitude, the LEV was found to cease accumulate circulation in close temporal correlation with secondary structure emergence and prior to fluid recirculation around the trailing edge. For cases with the same dimensionless parameters but a higher effective angle of attack amplitude, the vortex stopped accumulating circulation concurrent with fluid recirculation around the trailing edge. This highlights the effective angle of attack as an important parameter determining the prevalent LEV detachment mechanism, which should be considered for future LEV detachment investigations.

The temporal concurrence of secondary structure onset and the circulation accumulation stop was found to closely correlate with the leading edge shear layer angle increase after secondary structure onset. It is hypothesized that the interaction of secondary structures with the shear layer from the leading edge causes the observed correlation. This interaction occurs sooner after secondary structure occurrence for lower effective angles of attack, since the shear layer angle increases less after secondary structure occurrence. An in-depth study of the effect of secondary structure growth on the shear layer angle evolution by means of pressure field analysis is foreseen to provide sufficient information on their exact cause-effect relationship. Nevertheless, the observed correlation allows to infer, that the interaction of secondary structures with the shear layer causes the observed difference in LEV detachment for different effective angle of attack amplitudes.

Cessation of circulation accumulation of the LEV due to the occurrence of secondary structures implies that a suppression of their onset or growth is a promising approach for future flow control strategies targeting a prolonged LEV growth phase. The timing of secondary structure suppression can be optimized using the developed model for secondary structure onset. Alternatively, the interaction of the shear layer with secondary structures could be prevented/delayed by directing the shear layer upward. Both approaches are assumed to be more effective for cases with a lower effective angle of attack amplitude due the direct stop of circulation accumulation of the LEV as a consequence of interaction in those cases.

5 Leading Edge Vortex Manipulation with a Plasma Actuator

In this chapter, a flow control approach to exploit the LEV induced lift on pitching and plunging airfoils is introduced and experimentally validated. This approach adapts the biological principle of enhancing the LEV induced lift instead of suppressing the vortex by separation control and was first proposed by Kütemeier et al. (2019). More specifically, higher lift is assumed to be achieved by a prolongation of the LEV growth phase, which in turn is achieved by delaying the vortex detachment process. Based on findings from Chapter 4, the growth of secondary structures will be delayed to manipulate the LEV detachment.

Considerations in this study focus on the proof of concept for the manipulation approach in terms of its effectiveness regarding the prolongation of the vortex growth phase, assessed by means of the LEV circulation accumulation and its center convection. This is intended to serve as a first step towards the validation of the manipulation approach in terms of quantitative lift gain and efficiency considerations. During the prolonged LEV growth phase, a positive circulation accumulation rate in combination with a reduced center convection rate contribute to an increased overall lift, considering findings of other studies, discussed in section 1.2.2. Although direct lift measurements are not considered in this study, these findings provide evidence that an observation of the LEV circulation and center position evolution allow for a qualitative assessment of manipulation effects on overall lift. The body force induced by a plasma actuator applied at topologically critical locations will be utilized to achieve the prolonged LEV growth phase.

After an introduction of the manipulation hypothesis by means of topological arguments in section 5.1, its implementation on a pitching and plunging flat plate will be demonstrated. Flow fields and vortex characteristics, obtained from time-resolved particle image velocimetry (PIV) measurements, are used to investigate control effects in sections 5.2.1 and 5.2.2. The robustness of the proposed flow control concept is tested with different motion kinematics of the flat plate and complementary tests on a NACA 0012 airfoil in section 5.3. Finally, the control authority of the plasma actuator is evaluated in section 5.4 to provide the basis for efficiency enhancements in terms of the minimum effective actuation period.

Facilities and methods used for LEV manipulation and the characterization of manipulation effects on the LEV are introduced in section 2.4. Velocity fields from PIV correlations, vortex identification results and movies of the manipulated flow field are available online at: `http://dx.doi.org/10.25534/tudatalib-175`. Parts of this chapter have been published in Kissing et al. (2020c). Furthermore, parts of the experimental setup and results have been described in the theses of Stumpf (2019) and Büchel (2020).

Airfoils, Motion Kinematics and Parameter Space

LEV manipulation with a DBD plasma actuator will be investigated in the following on a flat plate airfoil with sharp, asymmetric leading and trailing edges and a NACA 0012 airfoil, which are described in detail in section 2.3.

Combined motion kinematics of the airfoils follow the kinematics presented at the beginning of Chapter 4. All investigated kinematics in this chapter consider a quasi-sinusoidal effective inflow angle evolution, and only the downstroke of the airfoil. In Table 5.1, relevant experimental parameters of test cases considered in this chapter are listed. Dimensionless parameters have been chosen to allow current results to be compared to previous studies of the LEV detachment (cf. Widmann, 2015; Rival et al., 2014). The free stream velocity U_∞ is set such that Re yields 22,000. Note that the investigated Re is higher than typical Reynolds numbers, for which flapping flight propulsion is more efficient than rotary wing concepts. However, based on findings of Widmann & Tropea (2017), the detachment mechanism of the LEV and thus the proposed control strategy is assumed to be transferable to lower Re. IDs of the respective cases will be used for identification in the following discussion. The location of the plasma actuator $(x/c)_{\mathrm{PA}}$ is provided in a plate-fixed frame

Table 5.1: Experimental parameters of test cases considered to evaluate effectiveness of flow control of the LEV with a DBD plasma actuator. All cases are investigated at $Re = 22000$. For kinematic details in terms of dimensional numbers of the respective cases, the reader is referred to Table 4.1.

ID	Sym.	Airfoil	k	St	α_{eff} in $^\circ$	α_{geo} in $^\circ$	$(x/c)_{\mathrm{PA}}$	$\Delta(t/T)_{\mathrm{PA}}$
14	●	Flat Plate	0.48	0.1	30	12.76	0.25	0.15 - 0.5
15	🔵	Flat Plate	0.48	0.1	20	2.67	0.25	0.15 - 0.5
16	🟢	Flat Plate	0.3	0.04	20	22.86	0.25	0.15 - 0.5
17	🔴	NACA 0012	0.48	0.1	30	12.67	0.285	0.25 - 0.5

of reference, which is located at the leading edge, and normalized by the airfoil chord c. The period where the plasma actuator is activated $\Delta(t/T)_{\mathrm{PA}}$ is normalized by the full motion period T.

A detailed investigation of flow control effects on flow fields, their topology and vortex characteristics will be conducted for the ID 14 case. This case considers a flat plate airfoil with sharp, asymmetric leading and trailing edges and is characterized by the highest investigated dynamics in terms of dimensionless parameters and effective inflow angle amplitude. To test whether the proposed manipulation hypothesis is effective for different kinematics, the concept is transferred to lower α_{eff} in the ID 15 case, which results in quasi-plunging motion evident from the low pitching angle of $\alpha_{\mathrm{geo}} = 2.67\,^\circ$. Lower motion dynamics in terms of St and k are tested in the ID 16 case. Finally, the manipulation hypothesis is also tested on a NACA 0012 airfoil in the ID 17 case, which allows direct comparison with flow control effects on the flat plate airfoil, due to the same dimensionless and geometric parameters of airfoil motion.

5.1 Manipulation Hypothesis

Manipulation efforts in this study aim at a prolonged LEV growth phase to attain higher overall lift. This increased lift is accompanied by higher drag and an increased nose-down pitching moment during final LEV detachment. In applications where nose-down pitching moments are to be avoided, suppression of the LEV would be a superior strategy. This applies also for applications where low drag is the main control aim. Regarding manipulation efforts towards higher dynamic lift, it was found that the highest lift on a pitching NACA 0015 airfoil could not be achieved by suppression of the LEV formation, but rather with a combination of LEV formation and fast flow reattachment after LEV shedding with the aid of a plasma actuator at the leading edge of the airfoil (cf. Post & Corke, 2006). This demonstrates that for manipulation approaches targeting a dynamic lift increase, irrespective of the nose-down pitching moment and additional drag, exploitation of the LEV induced lift is a promising strategy.

The proposed manipulation hypothesis, which targets a prolonged LEV growth phase to attain higher net lift, is based on the suppression of the LEV detachment process and follows the approach introduced in Kütemeier et al. (2019). For nominally two-dimensional airfoils in flapping flight, two vortex detachment mechanisms are known, as discussed in section 1.2.2: A detachment triggered by viscous effects and denoted as boundary-layer eruption (cf. Doligalski et al., 1994; Widmann & Tropea, 2015) and the so-called bluff body detachment introduced by Rival et al. (2014), with the chord of the airfoil as a characteristic length scale. Both mechanisms can be explained with a topological flow field analysis as introduced in Foss (2004) and adapted to the dynamic stall phenomenon by Rival et al. (2014).

For a boundary layer type LEV detachment, the growth of secondary vortices, which arise from a viscous response of the boundary layer on the airfoil upstream of the main vortex, initiates the detachment. This can be illustrated by considering the flow topology during LEV growth, depicted in Fig. 5.1a.

Secondary vortices, termed secondary structures, are denoted here as nodes N_2 and N_3. Once they grow, their rear confining half-saddle (highlighted as a green diamond and denoted as H_2 in Fig. 5.1a) moves towards the trailing edge. When secondary vortices N_2 and N_3 grow, vorticity carrying fluid from the leading edge shear layer is redirected into N_3 and does no reach the main LEV N_1 anymore. This causes the main LEV to detach. To compress the secondary structures – thus delaying LEV detachment – plasma actuators are

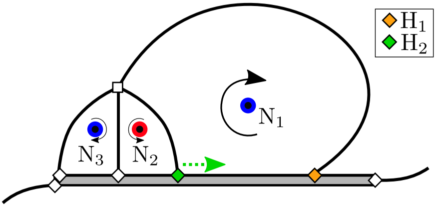

(a) LEV detachment caused by growing secondary vortices (also termed secondary structures and shown as nodes N$_2$ and N$_3$), in accordance with the boundary layer eruption mechanism.

(b) Manipulation hypothesis to delay LEV detachment by compression of secondary vortices with the plasma induced body force f$_{PA}$

Figure 5.1: Topological sketch of the flow field around a pitching and plunging flat plate with a leading edge vortex (LEV), denoted as node N$_1$, growing on the airfoil. Nodes are indicated by circles, a full-saddle by a square and half-saddles by diamonds. (Reprinted from Kissing et al. (2020c). © 2020 by American Physical Society.)

applied and operated in upstream direction on the plate so as to counteract the H$_2$-advection towards the trailing edge. The compression is realized with the aid of the plasma induced body force f$_{PA}$, as depicted in Fig. 5.1b. Note that vorticity produced by the plasma actuator is negatively signed, which is identical to the vorticity sign of the LEV. Therefore, cross-annihilation of plasma actuator vorticity with LEV vorticity should not diminish the control effect.

Determination of actuation location and timing requires an identification of topologically key characteristics in terms of half-saddles on the airfoil surface. As outlined by Rival et al. (2014), the tangential velocity immediately above the airfoil is a good indicator of half-saddles, through its change of velocity sign. An exemplary evolution of the tangential velocity on the flat plate airfoil in the uncontrolled baseline case is shown in Fig. 5.2a. The extraction and interpretation of the tangential velocity follows the discussion with respect to Fig. 4.9 closely. Nevertheless, a brief review for the interpretation is given below.

At $t/T = 0$ the airfoil is at the initial top position and at 0.5 at its final bottom end position. The diagonal blue trace in Fig. 5.2a indicates the upstream orientated (negative) tangential velocity induced by the LEV while

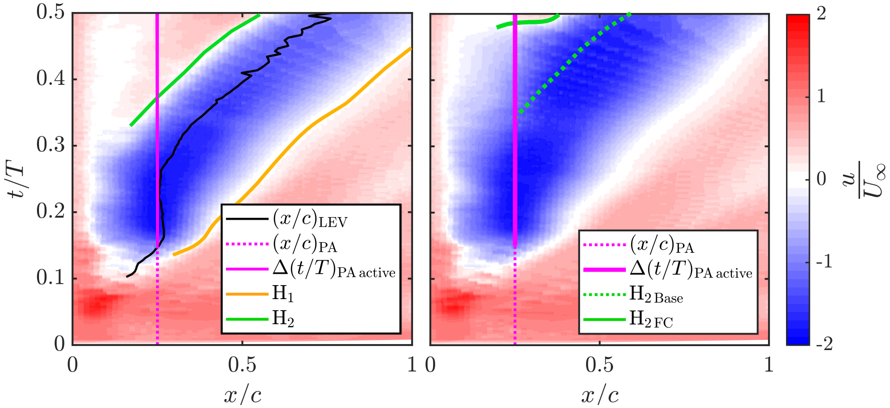

(a) Evolution without flow control. The leading edge vortex center position $(x/c)_{\mathrm{LEV}}$ and LEV confining half-saddles (H_1 and H_2) are indicated.

(b) Evolution with flow control applied. The secondary structure confining half-saddle in the uncontrolled ($\mathrm{H}_{2\,\mathrm{Base}}$) and the controlled case ($\mathrm{H}_{2\,\mathrm{FC}}$) are compared, to evaluate flow control effects.

Figure 5.2: Tangential velocity u on the airfoil surface over dimensionless time t/T, shown in a plate fixed frame of reference over the dimensionless chord position x/c with the origin at the leading edge ($x/c = 0$). The location of the plasma actuator $(x/c)_{\mathrm{PA}}$ and the actuation period $\Delta(t/T)_{\mathrm{PA\,active}}$ are also indicated. (Reprinted from Kissing et al. (2020c). © 2020 by American Physical Society.)

it convects over the airfoil. The rear confining half-saddle of the LEV (H_1 in Fig. 5.1a) can be identified by the change of velocity sign downstream of the LEV, as indicated by the orange line in Fig. 5.2a. In the upstream direction the LEV is separated from secondary structures by another half-saddle (H_2 in Fig. 5.1a) and thus another change of velocity sign, marked in Fig. 5.2a with a green line. In the uncontrolled case in Fig. 5.2a, H_2 can be identified from about $t/T = 0.325$ by the change of velocity sign upstream of the LEV.

From a topological point of view, successful compression of secondary structures would result in a half-saddle located further upstream of H_2 (green line in Fig. 5.2a to the top left). To test whether secondary structures can be compressed using the plasma induced body force f_{PA}, the plasma actuator is placed at $x/c = 0.25$ and switched on from $t/T = 0.15$ to 0.5 for motion parameters of the ID 14 case. The plasma actuator location is chosen under consideration of the trade-off between an upstream orientated location for an early actuation and a downstream orientation for a longer effective compression of secondary structures before they grow beyond the plasma actuator. Compared to the instant when H_2 can be identified in the uncontrolled case ($t/T = 0.325$), the plasma body force is deployed very early to make sure that secondary structures are compressed, even before they are visible in the tangential velocity plot.

5.2 Manipulation Effects

5.2.1 Manipulation Effects on Flow Fields

To investigate flow control effects qualitatively, flow fields for the ID 14 without flow control (Base) and with flow control (FC) are contrasted in Fig. 5.3. Videos of flow fields in direct comparison are available online (`http://dx.doi.org/10.25534/tudatalib-175`).

The vortex center is marked by a black circle. The LEV can be identified as the clockwise rotating region of negatively signed (blue color-coded) vortical fluid. It grows by accumulation of vorticity from the leading edge shear layer. For both cases, a small region of positively signed (red color-coded) vorticity upstream of the LEV is evident already in the first depicted dimensionless time instant $t/T = 0.25$ in Fig. 5.3. This region is indicative of the secondary vortex N_2. For subsequent time instants in the uncontrolled case, secondary structures grow and the connection between the LEV and the leading edge shear layer becomes weaker (e.g. at $t/T = 0.35$). This process is accompanied by large secondary structures, which are topologically identified in the zoomed leading edge flow field in the last row in Fig. 5.3. The LEV finally detaches from the leading edge shear layer at about $t/T = 0.45$.

In contrast, secondary structures are hardly identifiable in the controlled case at $t/T = 0.35$, shown in the right column in Fig. 5.3. This is also topologically evaluated in the last row of Fig. 5.3, where very small secondary structures can be observed in comparison to the case without flow control.

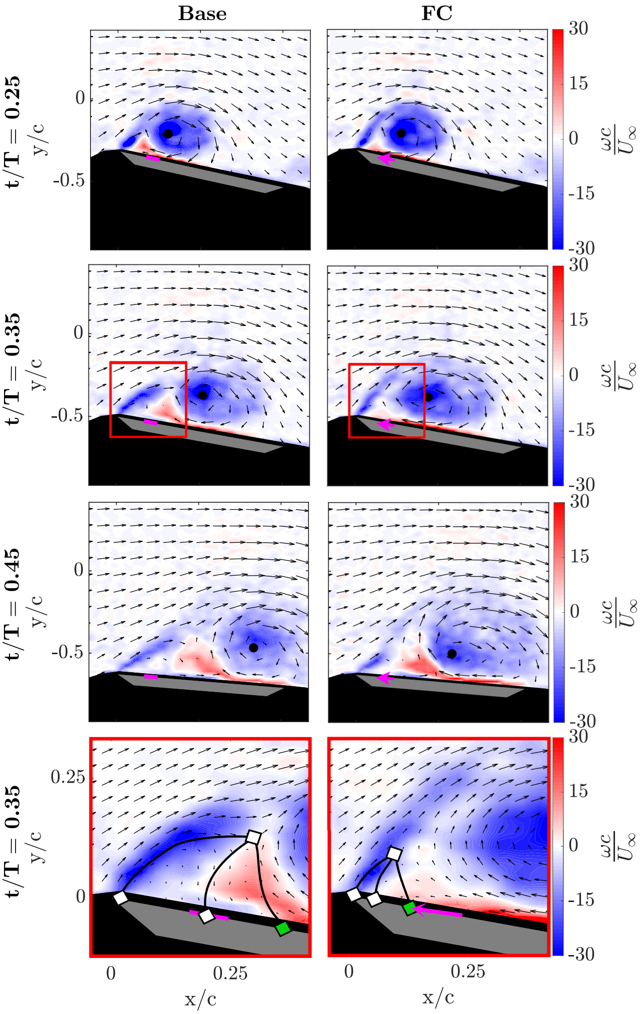

Figure 5.3: Velocity field and normalized vorticity $\omega c/U_\infty$ for different dimensionless time instants t/T. Left column without flow control (Base); right column controlled case (FC). An inactive plasma actuator is indicate by a magenta line and an active one by a magenta arrow. The first three instants in the three top rows depict the flow field with only every sixth velocity vector for clarity, the last two instants show the leading edge region with every second vector. The inflow is from the left, the airfoil is masked out in grey and the laser light shadow caused by the airfoil in black. (Reprinted from Kissing et al. (2020c). © 2020 by American Physical Society.)

The LEV center is located farther upstream in the controlled case when the plasma actuator is deployed. These observations indicate successful compression of secondary structures ahead of the main LEV by the plasma actuator and a reduced vortex center convection. In the controlled case, the LEV remains directly connected to the leading edge shear layer for a longer period and grows larger, as evident from the last depicted dimensionless time instant $t/T = 0.45$, which additionally indicates a prolonged growth phase.

To confirm secondary structure suppression, the footprint of the topological structures is shown in Fig. 5.2b for immediate comparison with the baseline case (Fig. 5.2a). To evaluate flow control effects, the rear confining half-saddle of secondary structures, H_2, is compared with and without flow manipulation. To enable comparability, the trajectory of H_2 in the uncontrolled case is projected into Fig. 5.2b, where it is marked by a dashed green line. In comparison to the case without flow manipulation, where H_2 was identifiable from $t/T = 0.325$ onward, it arises delayed at about $t/T = 0.47$ in the case when flow control is deployed. For later instants during the downstroke, where both half-saddles can be compared directly, $H_{2\ \mathrm{FC}}$ is located closer to the leading edge, indicated by lower x/c values.

The delayed emergence of the rear confining half-saddle of secondary structures, and its position closer to the leading edge of the airfoil, confirm a successful compression of secondary structures, as intended in the manipulation hypothesis.

5.2.2 Manipulation Effect on Vortex Characteristics

To study the effect of secondary structure compression on the LEV detachment process, the LEV circulation and position is characterized. A successful prolongation of the LEV growth phase, and thus higher induced lift, would be indicated by a prolonged circulation accumulation and a reduced convection velocity of the center of the vortex.

The vortex circulation, obtained according to Stokes theorem by integration of vorticity within the detected vortex boundary, is shown as a function of dimensionless time t/T in Fig. 5.4. Details on the vortex identification methodology and an evaluation of its reliability can be found in section 2.3.3.

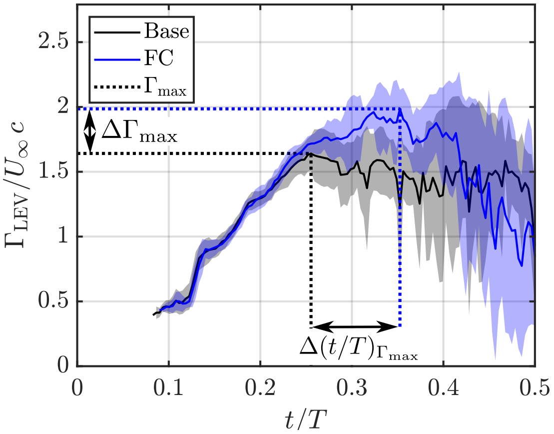

Figure 5.4: Normalized leading edge vortex circulation $\Gamma_{LEV}/U_\infty c$ evolution over dimensionless time t/T. The case without flow manipulation (Base) is shown in black and the controlled case (FC) in blue. The standard deviation between single runs is indicated by shaded areas of the respective color. The peak circulation $\Gamma_{\max}$ of the uncontrolled and controlled case is highlighted by dashed lines of the respective color in addition to the derived peak circulation increase $\Delta\Gamma_{\max}$ and temporal delay of peak circulation $\Delta(t/T)_{\Gamma_{\max}}$. (Reprinted from Kissing et al. (2020c). © 2020 by American Physical Society.)

Vortex identification results for all investigated cases are also available as raw data online (`http://dx.doi.org/10.25534/tudatalib-175`). In the uncontrolled case (black curve), the LEV accumulates circulation up to $t/T \approx 0.25$ and reaches a normalized peak circulation of about 1.6. In contrast, the controlled case (blue curve) leads to a LEV normalized peak circulation of about 2. This is equivalent to a relative peak circulation increase $\Delta\Gamma_{\max}$ of 21 % with respect to the case without flow control. The peak circulation in the controlled case is reached at about $t/T \approx 0.35$. So the delay of peak circulation in the controlled case $\Delta(t/T)_{\Gamma_{\max}}$ is about 20 % with respect to the downstroke. Note that both circulation histories collapse well, beyond the start of the plasma actuator at $t/T = 0.15$ up to 0.25. In addition to good repeatability of the flow scenario, this result also demonstrates that secondary structures, which are compressed in the controlled case, affect the vortex circulation significantly from $t/T = 0.25$ onward. A higher peak circulation of the LEV, which occurs later during the downstroke, indicates a prolonged LEV growth phase and thus, higher induced lift.

Another indicator for a prolonged growth phase of the LEV on the airfoil is its center convection. A reduced center convection indicates a delayed detachment of the vortex from the airfoil and thus, a longer phase of vortex induced lift. The normalized LEV center position x_{LEV}/c with and without flow control is compared in a plate-fixed frame of reference over t/T in Fig. 5.5.

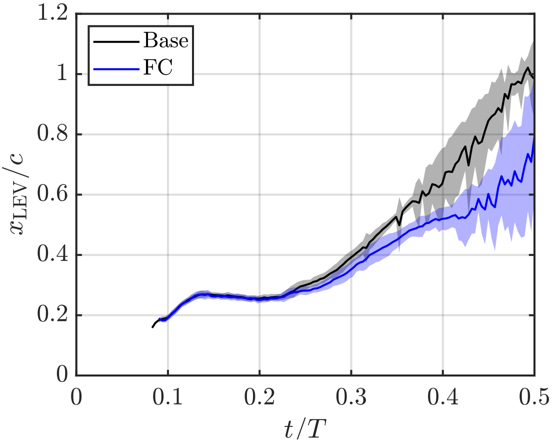

Figure 5.5: Normalized LEV center position x_{LEV}/c evolution over dimensionless time t/T. The case without flow manipulation (Base) is shown in black and the controlled case (FC) in blue. The standard deviation between single runs is indicated by shaded areas of the respective color. (Reprinted from Kissing et al. (2020c). © 2020 by American Physical Society.)

For the case where flow control is deployed (blue curve), the LEV center is located closer to the leading edge compared to the case without flow manipulation (black curve) from about $t/T = 0.25$ onward. At the end of the downstroke, the LEV center of the controlled case is located 20 % more upstream compared to the uncontrolled case. In accordance with findings regarding the LEV circulation, its center convection is reduced by flow control and infers a prolonged growth phase of the vortex.

5.3 Transferability of the Manipulation Hypothesis

To test whether the introduced manipulation approach can also be used to prolong the LEV growth phase for other motion kinematics and on other airfoils, additional flow control cases were tested, as listed in Table 5.1.

Exemplary flow fields with and without flow control for the ID 15 and ID 17 cases at different dimensionless time instants t/T are compared in Fig. 5.6 (a)-(d). Videos of all investigated cases are also available online (`http://dx.doi.org/10.25534/tudatalib-175`). In the ID 15 case, secondary structures can be identified by the positive (red) vorticity upstream of the main leading edge vortex in Fig. 5.6a. For the equivalent time instant in the controlled case, depicted in Fig. 5.6b, no secondary structures can be identified. This trend is even more pronounced for the ID 17 case of the NACA 0012 airfoil (see Fig. 5.6c and 5.6b), which already indicates that the proposed manipulation hypothesis holds across a range of parameter combinations. In both discussed cases and in all other considered cases, the LEV is connected to the leading edge shear layer longer, grows larger and is located farther upstream when flow control is deployed.

The relative LEV peak circulation increase $\Delta\Gamma_{\max}$ and the temporal delay of peak circulation $\Delta(t/T)_{\Gamma_{\max}}$ with and without flow control are considered to evaluate the effectiveness of flow manipulation with respect to vortex characteristics. Both measures indicate the termination of circulation accumulation of the LEV and thus allow the effectiveness of flow control in prolonging the growth phase of the vortex to be determined. Examples for peak LEV circulation increase and delay are given in the ID 14 case in Fig. 5.4 and shown for all cases in Fig. 5.7.

The peak circulation of the LEV increases between 19 % and 26 % with a maximum relative standard deviation of 4.5 % when flow control is deployed. The peak circulation instant is delayed by about 20 % for ID 14 - ID 15 and ID 17 cases with respect to the downstroke, indicated by $\Delta(t/T)_{\Gamma_{\max}}$ values around 0.1. For the ID 16 case, the delay of peak circulation is smaller compared to the others. For this case, the circulation evolution without flow control reaches a plateau at about $t/T \approx 0.2$, before it drops after $t/T = 0.3$,

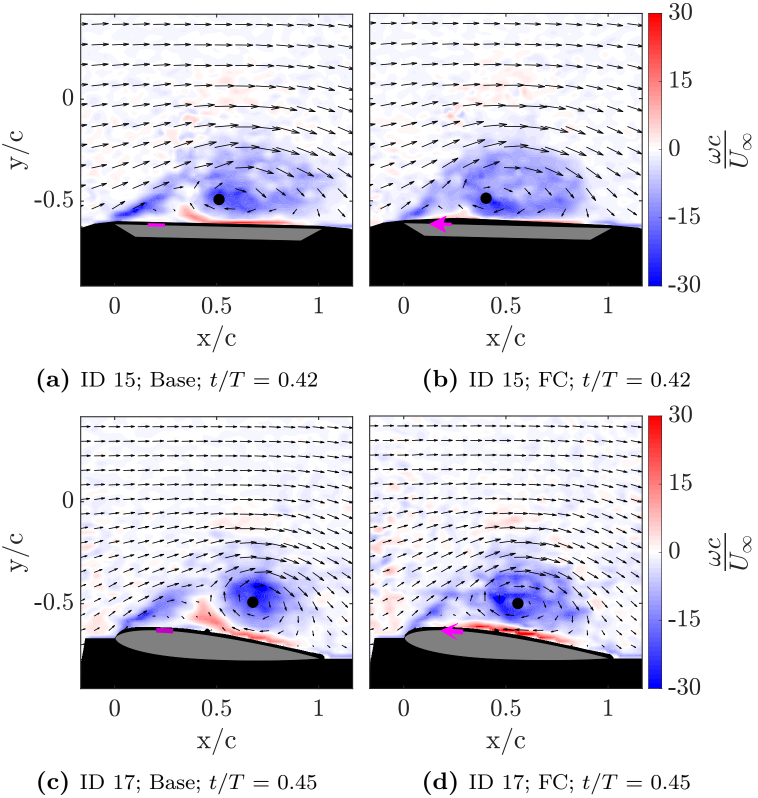

(a) ID 15; Base; $t/T = 0.42$ **(b)** ID 15; FC; $t/T = 0.42$

(c) ID 17; Base; $t/T = 0.45$ **(d)** ID 17; FC; $t/T = 0.45$

Figure 5.6: Unactuated (Base) and actuated (FC) flow field in terms of normalized vorticity $\omega c/U_\infty$ for ID 15 ((a) and (b)) and ID 17 ((c) and (d)) cases at different dimensionless time instants t/T. (Reprinted from Kissing et al. (2020c). © 2020 by American Physical Society.)

similar to the circulation evolution for the ID 14 case, shown in Fig. 5.4. The peak circulation in the uncontrolled case occurs at the end of the plateau, and leads to a smaller temporal delay between the uncontrolled and controlled case $\Delta(t/T)_{\Gamma_{\max}}$. However, Fig. 5.7 saliently demonstrates that the tested flow manipulation leads to significantly prolonged LEV growth and increased peak circulation for all investigated parameter combinations.

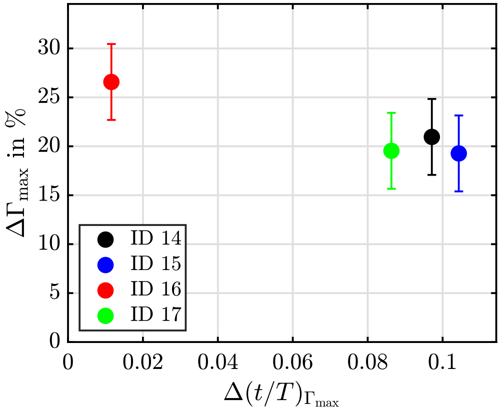

Figure 5.7: Relative peak circulation increase $\Delta\Gamma_{\mathrm{max}}$ between controlled and uncontrolled cases and the temporal delay of peak circulation $\Delta(t/T)_{\Gamma_{\mathrm{max}}}$. Error bars indicate the standard deviation of circulation increase. (Reprinted from Kissing et al. (2020c). © 2020 by American Physical Society.)

In all cases listed in Table 5.1, the LEV center is located significantly upstream in the controlled case, which indicates a reduced center convection rate. Considering the LEV center convection rate as an alternative indicator for vortex detachment, this also confirms a delayed detachment of the LEV in all cases. It highlights that the introduced manipulation hypothesis is also effective for very different motion kinematics and can be used to prolong the LEV growth phase on more practical airfoils, like a NACA 0012 airfoil. Additionally, due to the prolonged phase of vortex induced lift on the airfoil, the overall lift is assumed to be increased by flow control.

5.4 Flow Control Authority

Efficiency enhancements of the proposed manipulation approach can be achieved by consideration of the minimum actuation period of the plasma actuator, which still allows for an effective prolongation of the LEV growth phase. A reduction of the actuation period and thus the power input to the plasma actuator will be addressed in the following by consideration of the control authority of flow manipulation over the LEV growth phase. As shown above, an effective prolongation of the vortex growth phase is directly determined by a successful compression of secondary structures. An inactivation of the plasma actuator during phases where control authority over secondary structures cannot be established, so their growth is inevitable, remains without consequences on the prolongation of the vortex growth phase, but allows for power input savings.

To evaluate control authority of the plasma actuator in its current application, the instant where flow control is deployed and the instant where it is switched off are varied in the following manner. The ignition instant of the plasma actuator is varied to determine the latest possible ignition instant of flow control with respect to the occurrence of secondary structures, which still allows their compression. Different switch-off instants are tested to investigate when the control authority of the plasma actuator diminishes so that it can be switched off. The circulation accumulation phase and the center convection of the vortex are used as indicators for the LEV growth phase, following considerations from above.

In addition to efficiency considerations, knowledge about the limits of flow control can serve to design future adaptions and extensions of the control concept more effectively. This aspect will be addressed at the end of the section.

5.4.1 Ignition Instant Variation

The proposed manipulation hypothesis is based on the compression of secondary structures as the key objective to achieve a prolonged LEV growth phase and attain higher lift. A variation of the flow control ignition instant around the instant of secondary structure occurrence is intended to determine the most latest possible control deployment, which still allows for an effective compression of these structures. A detailed investigation of the design and results of the ignition instant variation is first presented for the ID 14 case. Variations of the actuation period for the ID 15, ID 16 and ID 17 cases will be addressed at the end of this section.

To identify the onset of secondary structures in the uncontrolled ID 14 case and to design the variation of the ignition instant of plasma flow control accordingly, flow fields in terms of FTLE ridges are considered. Corresponding data processing strategies and interpretation follow the methodologies introduced in sections 2.3.3 and 4.2.1. Fig. 5.8 shows the flow field in terms of repelling and attracting FTLE ridges, computed from forward and backward FTLE fields in the uncontrolled ID 14 case for different dimensionless time instants t/T.

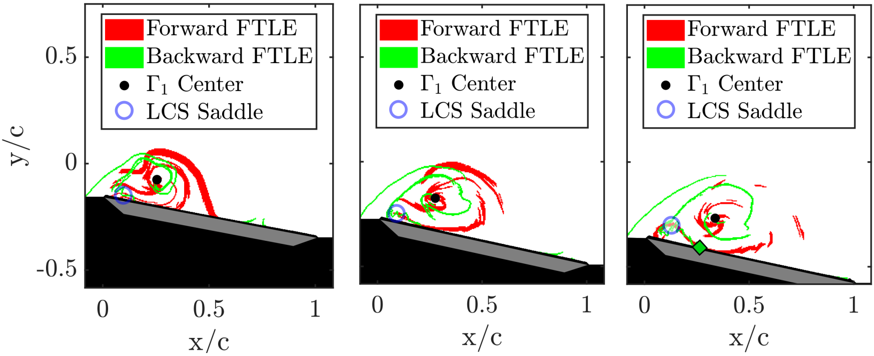

(a) Base; $t/T = 0.17$ **(b)** Base; $t/T = 0.23$ **(c)** Base; $t/T = 0.28$

Figure 5.8: Characterization of secondary structures with the aid of FTLE ridges for the ID 14 case. Repelling and attracting FTLE ridges are obtained from forward and backward FTLE computations using a 80 % threshold of the respective maximum FTLE value in each frame. The airfoil is masked out in grey and the laser light shadow in black. The vortex center from Γ_1 criterion and the LCS saddle are marked as well. The rear confining half-saddle of secondary structures H_2 is marked as green diamond in the last depicted instant.

The vortex center, determined from Γ_1 scalar fields, is marked by a black circle for orientation. The top of the secondary structures represents a Lagrangian saddle point (LCS saddle) in the flow field, as introduced by Huang & Green (2015) and examined in section 4.2.1, which can be tracked by the intersection of repelling and attracting ridges. The LCS saddle is highlighted by a blue, open circle in Fig. 5.8. A growth of secondary structures inevitably causes convection of the saddle, which allows their evolution to be tracked via the saddle motion.

For the first depicted dimensionless instant in Fig. 5.8a, a repelling ridge from forward FTLE computations is located parallel to the airfoil surface at its leading edge. At this instant, no intersection of FTLE ridges right above the airfoil - and thus no LCS saddle - can be clearly identified. This shows that secondary structures did not occur up to this phase. At about $t/T = 0.23$, a cavity between the lowest repelling ridge and the airfoil surface starts to form in the leading edge region, on top of which an LCS saddle (blue circle) can be identified by the intersection of repelling and attracting ridges. This indicates the onset of secondary structure growth. The origin of the secondary structure confining repelling ridge on the airfoil surface marks the origin of fluid that becomes entrained in secondary structures. From a topological perspective, this is the H_2 half-saddle, discussed with respect to Fig. 5.1, which is marked for orientation in Fig. 5.8c by a green diamond. At the period of secondary structure emergence, H_2 is found to be located at about $x/c = 0.13$. For the last depicted instant in Fig. 5.8c, the LCS saddle has moved upward and downstream compared to previous instants, which indicates further growth of secondary structures.

The ignition instant of plasma flow control is varied around the instant of secondary structures occurrence with four different instants of plasma activation. Two variations consider flow control deployment prior to secondary structure occurrence and two variations consider an actuation start after secondary structure occurrence. These variations are illustrated with respect to the topological situation on the airfoil surface where the flow field is manipulated with the aid of the normalized tangential velocity u/U_∞ evolution for the uncontrolled ID 14 case in Fig. 5.9.

The extraction and interpretation methodology is in accordance with the discussion regarding Fig. 5.2. The vortex center evolution $(x/c)_{\mathrm{LEV}}$ is indicated by a black line in Fig. 5.9 for orientation. The temporal onset of secondary structures $(t/T)_{\mathrm{SS\,Onset}}$ is marked by a horizontal, dashed green line. A vertical, dashed and magenta coloured line highlights the location of the plasma actuator $(x/c)_{\mathrm{PA}}$, which produces a wall jet in upstream direction. Its position at $(x/c)_{\mathrm{PA}} = 0.25$ ensures that secondary structures arise ahead of the actuator in the uncontrolled case to allow them to be compressed.

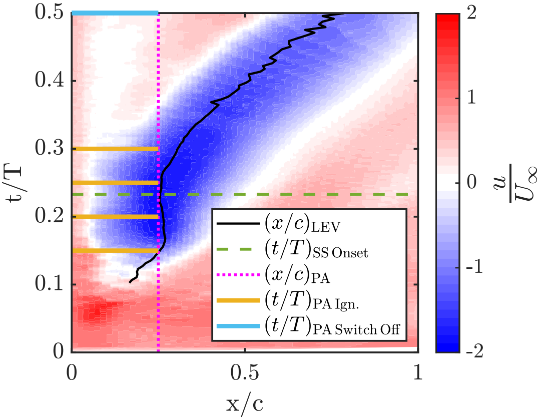

Figure 5.9: Design of the ignition instant variation of the plasma actuator $(t/T)_{\mathrm{PA\,Ign.}}$, illustrated with the aid of the tangential velocity on the airfoil surface u/U_∞ in the uncontrolled ID 14 case. The extraction and interpretation of u/U_∞ follows the discussion with respect to Fig. 5.2.

The four different instants at which the actuator is ignited $(t/T)_{\mathrm{PA\,Ign.}} = [0.15;\ 0.2;\ 0.25;\ 0.3]$ are marked by horizontal, orange lines. For the first two ignition instants, secondary structures did not occur previously, while they are already growing for the last two ignition instants. Interestingly, the onset of secondary structures can be identified from the tangential velocity evaluation significantly later at $t/T = 0.32$ by the occurrence of the H_2 saddle compared to the identification from LCS considerations $(t/T = 0.23)$. In all cases, the plasma actuator is switched off at the end of the downstroke at $(t/T)_{\mathrm{PA\,Switch\,Off}} = 0.5$, marked by a blue line in Fig. 5.9, which allows effects of the ignition instant variation to be investigated independent of actuation termination.

An increased lift on the airfoil, which is the aim of current flow control efforts, is assumed to be achieved by a prolonged growth phase of the LEV on the airfoil. The duration of the LEV growth phase is assessed qualitatively by means of the LEV circulation Γ_{LEV} and its center position x_{LEV}, following the discussion of these vortex characteristics as indicator for its growth phase from above. Fig. 5.10 contrasts the evolution of the normalized LEV circulation and center evolution in the uncontrolled ID 14 case against the evolution for different ignition instants of the plasma actuator. In the uncontrolled baseline case, depicted as a black lines in Fig. 5.10, the LEV accumulates circulation up to $t/T = 0.25$, where it also reaches its peak circulation. From this instant on, $\Gamma_{\mathrm{LEV}}/U_\infty c$ decreases in the baseline case. In both variations where flow control is deployed prior to secondary structure occurrence ($\Delta(t/T)_{\mathrm{PA}} = 0.15$-0.5 and 0.2-0.5, depicted as blue and red lines in Fig. 5.10), the circulation accumulation phase of the LEV is prolonged beyond $t/T = 0.32$. Additionally, higher peak circulation of at least 16 % above the uncontrolled baseline case is reached for both variations. With respect to efficiency considerations, it is interesting to notice that there are no beneficial effects on the circulation evolution when flow control is deployed very early before secondary structure occurrence at $(t/T)_{\mathrm{PA\,Ign.}} = 0.15$ compared to 0.2. In contrast, flow control deployment after secondary structure occurrence ($\Delta(t/T)_{\mathrm{PA}} = 0.25$-0.5 and 0.3-0.5, depicted as green and yellow lines in Fig. 5.10) causes the LEV circulation to follow the evolution in the uncontrolled baseline case closely.

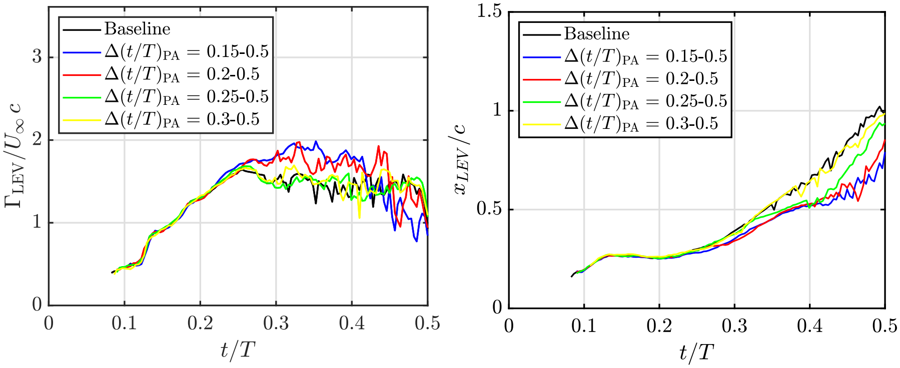

(a) LEV circulation $\Gamma_{\mathrm{LEV}}/U_\infty c$ **(b)** LEV center position x_{LEV}/c

Figure 5.10: Evolution of LEV characteristics over dimensionless time t/T for a variation of the ignition instant in the ID 14 case. The period of plasma flow control $\Delta(t/T)_{\mathrm{PA}}$ is chosen to investigate the ignition instant with respect to secondary structure occurrence at $(t/T)_{\mathrm{SS\,Onset}} = 0.23$. The plasma actuator is located at $(x/c)_{\mathrm{PA}} = 0.25$ for all cases. The standard deviation is not indicated for clarity but evolve similar to the deviation in Fig. 5.4.

In these cases, secondary structure evolution is in close temporal and spatial agreement with the baseline case evolution, considering flow fields in terms of FTLE ridges and the LCS convection.

Towards the end of the downstroke, from $t/T = 0.42$ onward, the circulation evolution for both cases with an ignition instant prior to secondary structure occurrence fall below the baseline case circulation. By consideration of the standard deviation for these cases, which evolves in a qualitatively similar manner to the standard deviation discussed with respect to Fig. 5.4, it is found that the observed effect cannot be classified as significant, due to the decay of the LEV.

Findings related to the prolongation of the LEV growth phase from circulation evolution are validated by consideration of the LEV center position, depicted in Fig.5.10b. Vortex center evolution for the two latest ignition instants follows the center evolution in the baseline case or approaches this evolution towards the end of the downstroke. The center position is farther upstream than in the baseline case, when plasma flow control is deployed before secondary structure occurrence, which indicates a prolonged LEV growth phase and confirms findings from above. An actuation of flow control long before secondary structure occurrence at $t/T = 0.15$ does not cause the LEV center to be located farther upstream compared to $t/T = 0.2$.

The evolution of LEV characteristics demonstrate that flow control has to be deployed prior to secondary structure occurrence to prolong the vortex growth phase successfully. However, there is no additional gain from flow control deployment very early before secondary structure occurrence.

To investigate the transferability of findings from above to other motion kinematics and airfoil types, variations of the ignition instant were also conducted and evaluated in the ID 15, ID 16 and ID 17 cases. For these cases, plasma flow control had to be deployed prior to secondary structure occurrence to prolong the LEV growth phase successfully as well. Again, an early actuation long before secondary structure occurrence yielded no additional benefit. This shows that findings from above also hold true for different motion kinematics of the flat plate airfoil and for airfoils with a round leading edge, that are thick and deemed more realistic.

5.4.2 Variation of Switch-Off Instant

The LEV detaches from the airfoil also in cases where flow control is capable of suppressing secondary structures and successfully prolongs the LEV growth phase, which indicates that control authority of the plasma actuator vanishes at a certain time. To evaluate the earliest possible instant where flow control can be switched off without losing control benefits, an investigation of the period where control authority of the plasma actuator diminishes is undertaken in this section. The corresponding variation of the switch-off instant of flow control aims at a reduction of the duration of flow manipulation to achieve the minimum effective actuation period and enhance flow control efficiency. Additionally, insights gained with respect to the control authority are intended to serve as a basis for future extensions and adaptions of the manipulation approach. In accordance with the variation of the ignition instant, the controlled ID 14 case will be considered first and the ID 15, ID 16 and ID 17 cases will be addressed at the end of this section.

Variations of the switch-off instant of flow control center around the instant where secondary structures occur in the controlled ID 14 case. This instant is chosen because the occurrence of secondary structures indicates that the plasma actuator loses its control authority over the compression of secondary structures. Their occurrence also indicates that the LEV detachment process is initiated despite activated flow control.

To determine the instant of secondary structure occurrence in the controlled ID 14 case, flow fields in terms FTLE ridges are again considered. Similar to the evaluation of secondary structure growth in the previous section and in Chapter 4, the convection of the LCS saddle will be used to determine the instant of secondary structure growth. The flow field in the controlled ID 14 case is shown in terms of repelling and attracting FTLE ridges from forward and backward FTLE computations in Fig. 5.11 for different t/T. The vortex center, evaluated from the Γ_1 scalar field, is highlighted in Fig. 5.11 as a black circle for orientation. The LCS saddle is denoted as a blue, open circle and the location and direction of the plasma actuator as a magenta arrow.

At the earliest depicted instant, $t/T = 0.34$ in Fig. 5.11a, the LCS saddle remains on the airfoil surface, because no intersection of repelling and attracting FTLE ridges above the airfoil surface occurs. A repelling ridge

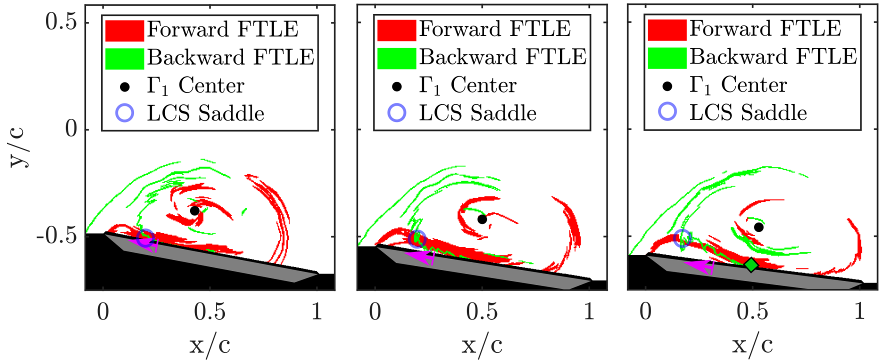

(a) FC; $t/T = 0.34$ **(b)** FC; $t/T = 0.38$ **(c)** FC; $t/T = 0.41$

Figure 5.11: Determination of secondary structure occurrence with the aid of FTLE ridges for the controlled ID 14 case. Repelling and attracting FTLE ridges are obtained from forward and backward FTLE computations using a 80 % threshold of the respective maximum FTLE value in each frame. The airfoil is masked out in grey, the laser light shadow in black. The location and direction of the plasma induced body force is indicated by a magenta arrow. The vortex center from Γ_1 criterion and the LCS saddle are marked as well. The rear confining half-saddle of secondary structures H_2 is marked as green diamond in (c).

(color-coded in red) is located directly above and parallel to the airfoil surface from mid-chord to the leading edge. This confirms that there are no secondary structures present that would result in a cavity of the repelling ridge above the airfoil surface. At $t/T = 0.38$, the repelling ridge has lifted up from the airfoil surface in the leading edge region, which causes the LCS saddle to also lift up. Between the airfoil surface and the repelling ridge a cavity can be identified, which represents the area of secondary structures. These aspects indicate the growth of secondary structures from $t/T = 0.38$ onward. For $t/T = 0.41$, the cavity at the leading edge has grown further and the LCS saddle is located high above the airfoil surface, which shows further growth of secondary structures. The origin of fluid that is entrained into secondary structures, which represents the rear confining half-saddle of the structures H_2 from a topological point of view, is indicated by the intersection of the repelling ridge with the airfoil surface. It is highlighted by a green diamond in Fig. 5.11c.

Based on the identification of secondary structure growth from $t/T = 0.38$ onward, the variation of the plasma actuator switch-off instant centers around $t/T = 0.38$. Two variations consider switching off flow control prior to the occurrence of secondary structures behind the plasma actuator at $(t/T)_{\mathrm{PA\,Switch\,Off}} = 0.2$ and 0.3 and two after their occurrence at $(t/T)_{\mathrm{PA\,Switch\,Off}} = 0.4$ and 0.5. To investigate effects of the switch-off instant independent of the ignition instant of flow control, the plasma actuator is switched on at $(t/T)_{\mathrm{PA\,Ign.}} = 0.15$ for all variations. This results in actuation periods $\Delta(t/T)_{\mathrm{PA}}$ of [0.15-0.2; 0.15-0.3; 0.15-0.4; 0.15-0.5].

To evaluate control effects on LEV characteristics, which finally also determine the unsteady lift on the airfoil, the normalized LEV circulation $\Gamma_{\mathrm{LEV}}/U_\infty c$ and center position x_{LEV}/c in a plate-fixed frame of reference are considered again. The evolution of both quantities as a function of dimensionless time t/T is shown in Fig. 5.12.

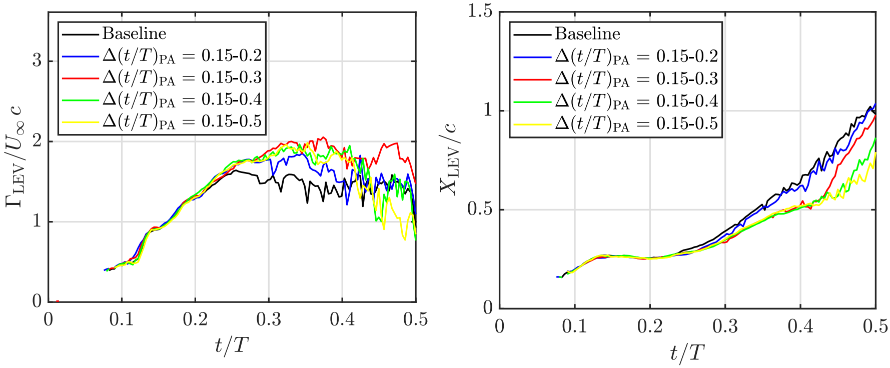

(a) LEV circulation $\Gamma_{\mathrm{LEV}}/U_\infty c$

(b) LEV center position x_{LEV}/c

Figure 5.12: Evolution of LEV characteristics over dimensionless time t/T for a variation of the actuation switch-off instant in the controlled ID 14 case. The period of plasma flow control $\Delta(t/T)_{\mathrm{PA}}$ is chosen to investigate effects of actuation termination with respect to secondary structure occurrence at $t/T = 0.38$ behind the actuator. The plasma actuator is located at $(x/c)_{\mathrm{PA}} = 0.25$ for all cases.

With respect to the LEV circulation evolution, shown in Fig. 5.12a, it can be observed that for very early termination of plasma flow control at $t/T = 0.2$ (blue curve), the peak circulation increase with respect to the baseline case (black curve) is not as high compared to other cases. During inspection of single flow fields, it is found that secondary structures grow shortly after termination of flow control. Additionally, the LEV center evolution follows closely the evolution in the uncontrolled baseline case, as evident from Fig. 5.12b. These aspects clearly indicate that a short flow control period up to $t/T = 0.2$ allows early growth of secondary structures and thus a reduced prolongation of the LEV growth phase compared to longer actuation periods.

For flow control termination between $t/T = 0.3$ and 0.5, $\Gamma_{\text{LEV}}/U_\infty c$ evolves very similar up to $t/T = 0.4$. Small deviations of the vortex circulation in these cases and the evolution after $t/T = 0.4$ are not significant due to the increased standard deviation at these periods. Therefore, the LEV center evolution, shown in Fig. 5.12b, is considered to quantify the control effects on the LEV growth phase for these cases. For $\Delta(t/T)_{\text{PA}} = 0.15$-0.3 (red curve), the LEV center is located upstream compared to the baseline case only up to $t/T = 0.4$. Thereafter the center evolution approaches the evolution in the uncontrolled baseline case, which indicates a reduced effectiveness of flow control with respect to the LEV growth phase. Additionally, secondary structures occur immediately after termination of flow control. Overall, control effectiveness over the downstroke is reduced for $\Delta(t/T)_{\text{PA}} = 0.15$-0.3 compared to longer actuation periods.

For cases where the flow control period is set to $\Delta(t/T)_{\text{PA}} = 0.15$-0.4 and 0.15-0.5, shown in green and yellow in Fig. 5.12b, the center convection of the LEV is reduced significantly compared to the baseline case. The evolution of x_{LEV}/c is similar in both cases with minor deviations towards the end of the downstroke. In both cases, secondary structures are found to arise at $t/T \approx 0.38$. This similarity of flow control effects on secondary structures and the LEV characteristics for $\Delta(t/T)_{\text{PA}} = 0.15$-0.4 and 0.15-0.5 demonstrates that the plasma actuator can be switched off already at $t/T = 0.4$ without loss of control authority over the LEV growth phase. The reduction of the actuation period represents an improvement of the actuator efficiency via a reduced period of power input to the plasma actuator. With respect to control authority considerations, it demonstrates that flow control in its current application is only successful as long as no secondary structures grow behind the plasma actuator.

For the ID 15, ID 16 and ID 17 cases the shortest actuation period, which allows a successful compression of secondary structures and a prolongation of the LEV growth phase, was also determined by the occurrence of secondary structures behind the actuator.

The optimal ignition instant of flow control in the ID 14 case of $(t/T)_{\mathrm{PA,\,Ign.}} = 0.2$ and the instant where plasma manipulation of the flow can no longer affect the LEV at $t/T = 0.4$ give an optimal actuation period of $\Delta(t/T)_{\mathrm{PA}} = 0.2\text{-}0.4$. This actuation period is tested in the ID 14 case and contrasted to vortex characteristics of the initial actuation period of $\Delta(t/T)_{\mathrm{PA}} = 0.15\text{-}0.5$ and the uncontrolled baseline case in Fig. 5.13. The comparison is intended to test whether the minimum actuation period allows to prolong the LEV growth phase as effective as the longest investigated actuation period. The LEV circulation evolution and its center evolution for the minimum actuation period, shown in red in Fig. 5.13a and 5.13b, are in very close agreement with the longest investigated actuation period, shown in blue. Both cases allow a prolongation of the LEV growth phase, indicated by higher peak circulation, which occurs later, and a reduced center convection. This suggests that the LEV growth phase can be prolonged equally effectively for the minimum

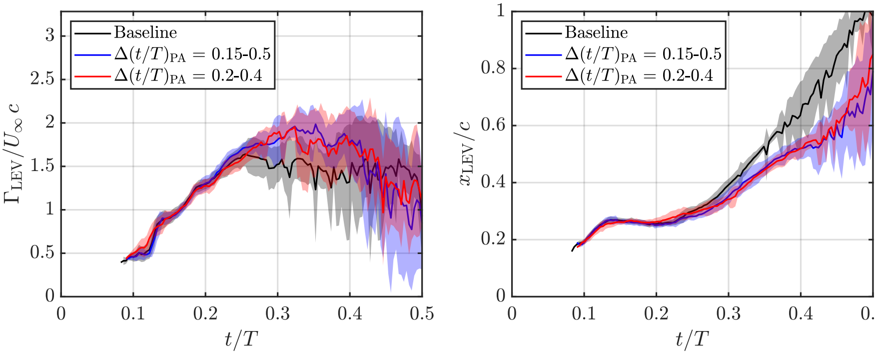

(a) LEV circulation $\Gamma_{\mathrm{LEV}}/U_\infty c$ **(b)** LEV center position x_{LEV}/c

Figure 5.13: Evolution of LEV characteristics over dimensionless time t/T for a variation of the actuation period, which aims to achieve the minimum effective actuation period in the ID 14 case. The plasma actuator is located at $(x/c)_{\mathrm{PA}} = 0.25$ for all cases. Respective standard deviations are indicated as colored shadows.

flow control period. Additionally, it allows the period of power input to the plasma actuator to be reduced by more than 40 % with respect to the longest investigated actuation period.

The occurrence of secondary structures behind the plasma actuator motivated a temporal and spatial investigation of their occurrence in these cases. Flow fields in terms of FTLE ridges were considered to extract the location and instant of secondary structure occurrence behind the plasma actuator. The extraction methodology and results are shown in Fig. 5.14 for the ID 14 case with different actuation periods. Only cases with an effective prolongation of the LEV growth phase and the uncontrolled baseline case are considered.

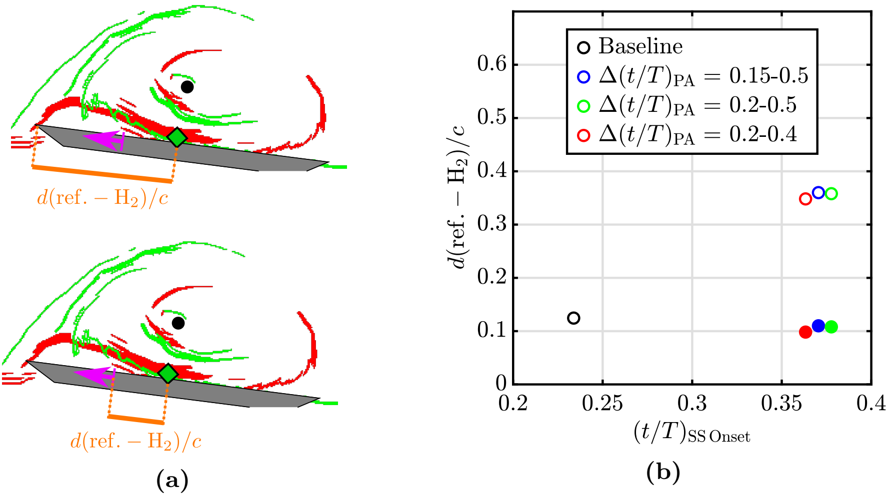

Figure 5.14: Distance between the origin of secondary structures and different reference locations $d(\mathrm{ref.} - \mathrm{H}_2)/c$ for the uncontrolled ID 14 case and effective actuation periods in the ID 14 case. (a) Extraction methodology of $d(\mathrm{ref.} - \mathrm{H}_2)/c$ by identification of the H_2 saddle from FTLE fields, marked as a green diamond. Different reference locations in terms of the leading edge (ref.: $x/c = 0$) and the downstream end of the plasma actuator (ref.: $x/c = 0.25$) are considered. The location and direction of the plasma actuator is highlighted by a magenta arrow and the vortex center from Γ_1 evaluation by a black circle. (b) $d(\mathrm{ref.} - \mathrm{H}_2)/c$ as a function of the instant of secondary structure occurrence $(t/T)_{\mathrm{SS\,Onset}}$. For open marker results, the leading edge is considered as reference and for filled markers the downstream end of the plasma actuator is used as a reference.

To determine the location of secondary structure emergence precisely, flow fields in terms of repelling and attracting FTLE ridges are considered. From these fields, the intersection of the secondary structure confining repelling ridge (red ridge above the airfoil surface in Fig. 5.14a) with the airfoil surface is extracted. The intersection is marked by a green diamond in Fig. 5.14a. This intersection represents the H_2 half-saddle from a topological point of view, which is further discussed with respect to Fig. 5.1. The location of H_2 is determined in a plate-fixed frame of reference with its origin at the leading edge and related to a reference location to extract the distance of secondary structure emergence $d(\text{ref.} - \text{H}_2)/c$. As illustrated in Fig. 5.14a, both the leading edge and the downstream end of the plasma actuator are considered as reference locations.

The distance of secondary structure emergence location, represented by the H_2 half-saddle, from the refernbce location $d(\text{ref.} - \text{H}_2)/c$ is shown over the dimensionless instant of secondary structure occurrence $(t/T)_{\text{SS Onset}}$ in Fig. 5.14b. Open symbols represent distances for which the leading edge is referenced and filled markers distances where the downstream end of the plasma actuator is considered as reference. These locations are tested to evaluate whether the leading edge represents a barrier for the occurrence of secondary structures in the baseline case and the plasma actuator for controlled cases. Irrespective of the choice of reference location, secondary structures occur significantly later for all cases where flow control is deployed with respect to the uncontrolled baseline case, indicated by larger $(t/T)_{\text{SS Onset}}$ values. This comes as no surprise considering findings from above, where secondary structures were found to be compressed successfully for some time when flow control is deployed. For cases where the location of secondary structure occurrence is related to the leading edge, indicated by open circles in Fig. 5.14, $d(\text{ref.} - \text{H}_2)/c$ is generally higher for cases with flow control. This trend is expected considering findings from above related to secondary structure growth behind the plasma actuator for the controlled cases.

When the plasma actuator downstream end is used as a reference location for all controlled cases (filled circles in Fig. 5.14), $d(\text{ref.} - \text{H}_2)/c$ for all cases is in close agreement with the distance for the baseline case, where the leading edge is used as reference. From a topological perspective, these results suggest that for the controlled cases the plasma actuator represents a barrier for secondary structures, similar to the leading edge in the uncontrolled case. Behind these barriers, secondary structures grow with very similar distances. Conversely, the control authority of the plasma actuator diminishes at a certain distance from the actuators downstream end in downstream direction for controlled cases. For future extensions of the proposed manipulation concept, a second plasma actuator could be placed at a certain distance from the first actuator to allow the LEV growth phase to be prolonged further.

5.5 Conclusions

This chapter addresses flow control of the leading edge vortex on pitching and plunging airfoils by dielectric barrier discharge plasma actuators. The overall goal is to prolong the vortex growth phase and thereby increase the vortex induced lift on the airfoil. A manipulation hypothesis is introduced based on flow manipulation at topologically critical locations and which aims to delay the vortex detachment process. The hypothesis is experimentally validated on a flat plate airfoil in deep dynamic stall and is extended to different motion kinematics and more realistic airfoils.

The compression of secondary structures upstream of the LEV leads to a prolongation of the circulation accumulation phase and a reduced center convection of the LEV. Both are indicators for a prolonged growth phase and thus higher net lift. Similar trends, with a peak circulation increase between 19 % and 26 %, are also observed for pure plunging motion, lower motion dynamics of the flat plate airfoil and on a NACA 0012 airfoil, which demonstrates applicability of the manipulation approach for various motion kinematics and more realistic airfoils. A careful consideration of the actuation location and timing, in light of topological flow field developments identified by appropriate measures, is found to be crucial for flow control success.

An investigation into the control authority of the plasma actuator in its current application shows that the LEV growth phase can only be prolonged if flow control is deployed prior to the occurrence of secondary structures. The ignition of plasma flow control can be timed precisely with respect to the occurrence of secondary structures with the aid of the model for secondary structure onset, introduced in Chapter 4. In cases where secondary structures are initially compressed, they emerge at later periods and behind the plasma actuator. From an actuation of the flow field beyond the late occurrence of secondary strucures, no additional prolongation of the LEV growth phase is gained. The location where secondary structures occur behind the plasma actuator is found to be consistent over different actuation periods, which can serve as a basis for future extensions of the control concept in terms of actuator arrays. With the aid of the lessons learned from control authority considerations, the minimum effective actuation period is tested and found to allow the power input to the actuator to be reduced more than 40 % compared to the longest actuation period. These aspects demonstrate the potential for future efficiency enhancements of flow control of the LEV with a DBD plasma actuator under consideration of further actuation parameters, like burst modes and their duty cycle or reduced voltage inputs.

The manipulation of the LEV detachment by a zero net mass flux device at topologically critical locations offers the potential for an increased flow control efficiency with a minimum power input, based on a maximized lift enhancement. To allow for an assessment of the efficiency of the proposed manipulation approach, future investigations could focus on the determination of flow control effects on the overall lift and address the cost of control versus gain.

Finally, higher efficiency of MAVs in cruise flight and hovering as well as an increased maneuverability may be possible by using the proposed manipulation approach, which exploits beneficial lift effects of the LEV.

6 Summary of Conclusions and Outlook

In this thesis, two unsteady aerodynamic scenarios are considered. One is concerned with periodic gust encounter of airfoils and the other with characteristics and manipulation of the leading edge vortex on pitching and plunging airfoils. The overall scope of corresponding efforts is to develop and validate potential approaches for future efficiency enhancements for unsteady aerodynamic scenarios.

Based on the conclusions derived at the end of each chapter, a summary of conclusions is given in this chapter along a critical assessment of respective insights and potential future research efforts. These aspects are discussed separately for each considered scenario before final remarks are given for both scenarios.

6.1 Periodic Gust Encounter

Gust Response of Airfoils

Transient inflow conditions encountered by blades of wind turbines, bridge decks or aircraft wings due to gusts or misalignment can cause significant fluctuations of aerodynamic loads. Corresponding safety margins, which have to be recognised during design to ensure structural integrity, increase their relative weight. Precise knowledge of transient loads allows to reduce the required safety margins and consequently the weight of aerodynamically loaded structures and an enhancement of their efficiency. In this thesis, the Sears and the Atassi transfer functions were investigated, which allow a prediction of transient loads for periodic inflow situations on a stationary airfoil.

Previous studies found the gust response of an airfoil to be in correspondence with the Atassi function instead of the Sears function (cf. Cordes et al., 2017). In light of this deviation, differences in formulations and inflow assumptions of both transfer functions have been theoretically elaborated and experimentally validated. These theoretical and experimental efforts demonstrate that no fundamental difference between the Sears and Atassi functions exists if inflow assumptions are reproduced precisely and if they are normalized appropriately. The validity of both transfer functions over a broad range of parameters allows their applicability in future aerodynamic design procedures to be inferred. However, this only holds true under particular inflow conditions and in light stall, where no flow separation occurs.

The agreement of both theories with experimental results is moderated significantly by several factors. A turbulent boundary layer on the airfoil is found to cause an improved correspondence with theoretical predictions while intermittent turbulent large scale fluctuations of the inflow lead to significant deviations. Additionally, at higher angles of attack and gust amplitudes, the dynamic stall flow phenomenon causes the unsteady loads to deviate from theoretical predictions. A thorough investigation of these more complex gust encounter scenarios would not just widen the applicability of transfer functions, but yield valuable insights into the dynamics of several other problems in unsteady aerodynamics concerned with wake scenarios or turbulent inflows.

Realistic inflow scenarios encountered by wind turbine blades, aircraft wings or bridge decks are often more complex than the periodic and isolated fluctuations of inflow components considered in this thesis. Research efforts into combined scenarios, where a moving airfoil experiences periodic inflow conditions equivalent to the combination of the Sears/Atassi and Theodorsen transfer functions, would allow for a more realistic prediction of loads. Since the respective transfer functions depend linearly on inflow variations, a superposition of them is deemed mathematically possible.

Gust Generation

Experimental investigation of unsteady aerodynamic scenarios with transient inflow conditions necessitate the generation of controlled gusts in a wind tunnel. A multitude of gust generation approaches have been proposed in literature, which utilize single airfoils or arrays of multiple airfoils. Single airfoils in pure plunging motion have been found to produce irregular gusts due to vortex shedding while large gust generation arrays with multiple airfoils are complex and cost intensive.

The gust generation approach proposed in this thesis considers a single airfoil and optimized combined pitching and plunging kinematics. This approach is found to allow for the production of controlled gusts of very high frequency and amplitude compared to other approaches. The optimization of gust generation kinematics is based on the minimization of the pitching moment around the trailing edge of the airfoil, derived from the Theodorsen theory. Due to the fact that only a single airfoil is involved, the simplicity of the proposed gust generator is superior, although combined kinematics require a more complex apparatus. Efficiency enhancement approaches for aerodynamic scenarios, which consider unsteady inflow conditions, can be investigated with reduced experimental efforts with the proposed gust generation approach.

Hardware restrictions in current investigations allowed only certain phase lags between pitching and plunging motion to be investigated, which do not provide optimal gust characteristics according to the developed theory. To further improve gust quality, experimental efforts should focus on kinematics with an optimal phase lag between pitch and plunge.

The formulation of the minimal pitching moment, which is used for optimization, has been found to be independent of the free stream velocity. Therefore, challenging the hypothesis that the same gust generation kinematics can be used for different Reynolds numbers would be valuable to widen the applicability of the approach. An optimization of the airfoil shape is assumed to improve the quality of gusts further.

6.2 Leading Edge Vortex Characteristics and Control

Leading Edge Vortex Characteristics on a Pitching and Plunging Flat Plate

Flapping wing based propulsion concepts for aerial vehicles adapt principles of biological flight to achieve unrivaled manoeuvrability and lift at low flight speeds. These advantages are attributed to the leading edge vortex growing on unsteady wings in deep dynamic stall. Flow control of the LEV is a promising approach to exploit beneficial effects of the vortex for improved flight characteristics and higher efficiency of MAVs. Manipulation approaches, which aim at a prolonged growth phase of the LEV to attain higher net lift, require precise knowledge of its detachment process. In this thesis, the LEV detachment is studied and modelled to provide the basis for consecutive manipulation efforts.

The dimensionless parameter space for corresponding investigations is extended significantly by using two facilities; a water tunnel at the Beihang University and a wind tunnel at TU Darmstadt. To allow results from both facilities to be interpreted complementary, an approach to establish comparability of flow fields and LEV characteristics is developed and validated. In order to provide the basis for flow control design, the occurrence of secondary structures is studied with the aid of a combination of Eulerian and Lagrangian evaluation methods. The emergence of these structures is found to be governed by a vortex Reynolds number threshold Re_v, which was consecutively used to derive a model that predicts the temporal occurrence of secondary structures precisely. This model allows for a precise timing of flow control approaches targeting the suppression of secondary structures.

For cases with a lower effective angle of attack amplitude, the LEV was found to cease accumulate circulation in close temporal correlation with secondary structure emergence, which indicates that their compression is a promising flow control approach.

An interaction of secondary structures with the leading edge shear layer is identified as the trigger of LEV detachment at lower angle of attack amplitudes. However, the exact mechanism of interaction between secondary structures and the leading edge shear layer remains unknown. Considerations of the pressure field could shed light on the cause effect relation between both structures.

Incorporation of the effective angle of attack amplitude into models for the LEV detachment would allow prediction of the vortex detachment for various combined pitching and plunging kinematics. Such adapted models would not just provide insights into the vortex detachment process but could also be used to derive flow control approaches for combined kinematics more precise.

Leading Edge Vortex Manipulation with a Plasma Actuator
Various studies considered manipulation of the LEV with different aims, corresponding manipulation strategies and actuators. In this thesis, the overall lift on a pitching and plunging airfoil is intended to be enhanced by a prolongation of the LEV growth phase. Therefore, a DBD plasma actuator is utilized to manipulate the flow field at a topologically critical location to delay the LEV detachment.

A manipulation hypothesis based on topological arguments has been designed and validated for a flat plate airfoil and a NACA 0012 airfoil undergoing different motion kinematics. Successful compression of secondary structures ahead of the main LEV is found to allow for peak circulation increases of at least 19 % and a significantly reduced center convection rate. Both vortex characteristics govern transient lift on unsteady airfoils in deep dynamic stall, which allows to conclude on a qualitative lift increase for current flow control efforts. A variation of flow control initiation and termination showed that the impact of manipulation with respect to the LEV growth phase is limited by the occurrence of secondary structures. Considerations of the minimum effective actuation period indicate, that without a careful assessment of control authority of flow manipulation, significant reduction of the control efficiency are caused by ineffective actuation periods.

The reduction of power input demonstrates the potential for efficiency enhancements of the proposed flow control approach by consideration of further plasma operation modes and parameters. Burst mode operation of the actuator or lower voltage inputs could be considered to attain higher efficiency. The spatial control authority of the plasma actuator is found to be limited by a late occurrence of secondary structures behind the actuator. This insight could be used to extend the manipulation approach in terms of plasma actuator arrays to prolong the LEV growth phase further. To allow for an assessment of the efficiency of the proposed manipulation approach, future investigations should focus on the determination of flow control effects on the overall lift and address the cost of control versus gain.

6.3 Final Remarks

Finally, it is worth to briefly comment on the achievements of the present work from a broader view point, which in turn attempts to outline possible future efforts in continuation of the uncovered insights into the elaborated efficiency enhancement approaches for unsteady aerodynamic scenarios.

The prediction of unsteady aerodynamic loads caused by periodic inflow situations is found to be possible with aerodynamic transfer functions. Precise knowledge of transient loads allows safety margins of aerodynamically loaded structures to be reduced, which allows a lighter design and an increased efficiency. The incorporation of aerodynamic transfer functions into the design process of wind turbine blades or bridge decks will require further investigations of more complex inflow scenarios to enable load prediction for realistic operational scenarios.

Flow manipulation efforts, targeted at higher lift on unsteady airfoils, indicate that an effective manipulation of the leading edge vortex detachment is feasible at topologically critical locations of the flow field. At these locations, significant effects can be realized with minimum manipulation efforts. This implicates high potential for increased efficiency and maneuverability of MAVs using the proposed manipulation approach. Optimization efforts of flow manipulation efficiency, as successfully tested in the present work, clearly outline avenues for further flow control optimization and extension studies, which might serve as motivation for future investigations.

Bibliography

Akkala, J. M. & Buchholz, J. H. (2017). Vorticity transport mechanisms governing the developement of leading-edge vortices. *J. Fluid Mech.*, 829:512–537.

Anderson, J. M., Streitlien, K., Barrett, D. S., & Triantafyllou, M. S. (1998). Oscillating foils of high propulsive efficiency. *J. Fluid Mech.*, 360:41–72.

Atassi, H. M. (1984). The sears problem for a lifting airfoil revisited - new results. *J. Fluid Mech.*, 141:109–122.

Baik, Y. S., Bernal, L. P., Granlund, K., & Ol, M. V. (2012). Unsteady force generation and vortex dynamics of pitching and plunging aerofoils. *J. Fluid Mech.*, 709:37–68.

Beck, L., Hofmann, J., Kiefer, A., & Stumpp, M. (2018). *Design, implementation and validation of airfoils for active flow control of leading-edge vortices for unsteady airfoils by plasma actuators*. Advanced design project (adp), Technische Universität Darmstadt.

Ben-Harav, A. & Greenblatt, D. (2016). Plasma-based feed-forward dynamic stall control on a vertical axis wind turbine. *Wind Energ.*, 19(1):3–16.

Bennett, R. M. & Gilman, J. (1966). A wind-tunnel technique for measuring frequency-response functions for gust load analyses. *J. Aircr.*, 3(6):535–540.

Berchtenbreiter, V. (2018). *Investigation of the effect of the reduced frequency on the flow field around an unsteady flat plate using Particle Image Velocimetry*. Bachelor thesis, Technische Universität Darmstadt.

Bergner, J. (2018). *Investigation of the effect of the Strouhal-number on the flow field around an unsteady flat plate using Particle Image Velocimetry*. Bachelor thesis, Technische Universität Darmstadt.

Billah, K. Y. & Scanlan, R. H. (1991). Resonance, Tacoma Narrows bridge failure, and undergraduate physics textbooks. *Am. J. Phys.*, 59(2):118–124.

Brion, V., Lepage, A., Amosse, Y., Soulevant, D., Senecat, P., Abart, J. C., & Paillart, P. (2015). Generation of vertical gusts in a transonic wind tunnel. *Exp. Fluids*, 56(7):145.

Büchel, M. K. (2020). *Optimization study of the manipulation of the leading edge vortex on a pitching and plunging flat plate using a plasma actuator.* Bachelor thesis, Technische Universität Darmstadt.

Carr, L. W. (1988). Progress in analysis and prediction of dynamic stall. *J. Aircr.*, 25(1):6–17.

Cattafesta, L. N. & Sheplak, M. (2011). Actuators for active flow control. *Annu. Rev. Fluid Mech.*, 43(1):247–272.

Cebeci, T., Platzer, M., Chen, H., Chang, K.-C., & Shao, J. P. (2005). *Analysis of Low-Speed Unsteady Airfoil Flows.* Springer, Berlin, Heidelberg.

Cekli, H. E. & van de Water, W. (2010). Tailoring turbulence with an active grid. *Exp. Fluids*, 49(2):409–416.

Champagnat, F., Plyer, A., Le Besnerais, G., Leclaire, B., Davoust, S., & Le Sant, Y. (2011). Fast and accurate piv computation using highly parallel iterative correlation maximization. *Exp. Fluids*, 50(4):1169.

Commerford, G. L. & Carta, F. O. (1974). Unsteady aerodynamic response of a two-dimensional airfoil at high reduced frequency. *AIAA J.*, 12(1):43–48.

Cordes, U., Kampers, G., Meißner, T., Tropea, C., Peinke, J., & Hölling, M. (2017). Note on the limitations of the Theodorsen and Sears functions. *J. Fluid Mech.*, 811.

Corke, T. C., Enloe, C. L., & Wilkinson, S. P. (2010). Dielectric barrier discharge plasma actuators for flow control. *Annu. Rev. Fluid Mech.*, 42(1):505–529.

de Croon, G., Perçin, M., Remes, B., Ruijsink, R., & de Wagter, C. (2015). *The DelFly: Design, Aerodynamics, and Artificial Intelligence of a Flapping Wing Robot.* Springer Netherlands, Dordrecht, first edition.

Dickinson, M. H., Lehmann, F. O., & Sane, S. P. (1999). Wing rotation and the aerodynamic basis of insect flight. *Science*, 284(5422):1954–1960.

Doligalski, T. L., Smith, C. R., & Walker, J. D. A. (1994). Vortex interactions with walls. *Annu. Rev. Fluid Mech.*, 26(1):573–616.

Drela, M. (1989). Xfoil: An analysis and design system for low reynolds number airfoils. In *Low Reynolds Number Aerodynamics*, Lecture Notes in Engineering. Springer, Berlin, Heidelberg.

Duchmann, A. (2012). *Boundary-layer stabilization with dielectric barrier discharge plasmas for free-flight application.* PhD thesis, Technische Universität Darmstadt.

Efron, B. (1992). Bootstrap methods: Another look at the jackknife. In *Breakthroughs in Statistics*, pages 569–593. Springer, NY.

Ekaterinaris, J. A. & Platzer, M. F. (1998). Computational prediction of airfoil dynamic stall. *Prog. Aerosp. Sci.*, 33(11):759–846.

Eldredge, J. D. & Jones, A. R. (2019). Leading-edge vortices: Mechanics and modeling. *Annu. Rev. Fluid Mech.*, 51(1):75–104.

Ellington, C. P. (1984). The aerodynamics of hovering insect flight. vi. lift and power requirements. *Philos. Trans. R. Soc. B*, 305(1122):145–181.

Ellington, C. P., van den Berg, C., Willmott, A. P., & Thomas, A. L. R. (1996). Leading-edge vortices in insect flight. *Nature*, 384(6610):626–630.

Foss, J. F. (2004). Surface selections and topological constraint evaluations for flow field analyses. *Exp. Fluids*, 37(6):883–898.

Gharali, K. & Johnson, D. A. (2013). Dynamic stall simulation of a pitching airfoil under unsteady freestream velocity. *J Fluids Struct.*, 42:228–244.

Goldstein, M. E. & Atassi, H. (1976). A complete second-order theory for the unsteady flow about an airfoil due to a periodic gust. *J. Fluid Mech.*, 74(4):741–765.

Graftieaux, L., Michard, M., & Grosjean, N. (2001). Combining piv, pod and vortex identification algorithms for the study of unsteady turbulent swirling flows. *Meas. Sci. Technol.*, 12(9):1422–1429.

Greenberg, J. M. (1947). Airfoil in sinusoidal motion in a pulsating stream. Technical note 1326, National Advisory Committee for Aeronautics.

Greenblatt, D., Ben-Harav, A., & Mueller-Vahl, H. (2014). Dynamic stall control on a vertical-axis wind turbine using plasma actuators. *AIAA J.*, 52(2):456–462.

Greenblatt, D., Nishri, B., Darabi, A., & Wygnanski, I. (2001). Dynamic stall control by periodic excitation, part 2: Mechanisms. *J. Aircr.*, 38(3):439–447.

Greenblatt, D. & Wygnanski, I. (2001). Dynamic stall control by periodic excitation, part 1: NACA 0015 parametric study. *J. Aircr.*, 38(3):430–438.

Griffin, K. P., Wei, N. J., Bodenschatz, E., & Bewley, G. P. (2019). Control of long-range correlations in turbulence. *Exp. Fluids*, 60(4):55.

Gursul, I., Wang, Z., & Vardaki, E. (2007). Review of flow control mechanisms of leading-edge vortices. *Prog. Aerosp. Sci.*, 43(7-8):246–270.

Hakkinen, R. J. & Richardson, A. S. (1957). Theoretical and experimental investigation of random gust loads part I: Aerodynamic transfer function of a simple wing configuration in incompressible flow. Technical note 3878, National Advisory Committee for Aeronautics.

Haller, G. (2002). Lagrangian coherent structures from approximate velocity data. *Phys Fluids*, 14(6):1851–1861.

Ham, N. D., Bauer, P. H., & Lawrence, T. L. (1974). Wind tunnel generation of sinusoidal lateral and longitudinal gusts by circulation of twin parallel airfoils. Technical report 137547, National Advisory Committee for Aeronautics.

Hatanaka, A. & Tanaka, H. (2002). New estimation method of aerodynamic admittance function. *J. Wind. Eng. Ind. Aerodyn.*, 90(12):2073–2086.

Ho, S., Nassef, H., Pornsinsirirak, N., Tai, Y.-C., & Ho, C.-M. (2003). Unsteady aerodynamics and flow control for flapping wing flyers. *Prog. Aerosp. Sci.*, 39(8):635–681.

Hofmann, J. (2015). *Rauchvisualisierung zur Abschätzung der Wandeffekte an instationären Profilen.* Bachelor thesis, Technische Universität Darmstadt.

Huang, Y. & Green, M. A. (2015). Detection and tracking of vortex phenomena using Lagrangian coherent structures. *Exp. Fluids*, 56(7):41.

Hufstedler, E. A. L. & McKeon, B. J. (2019). Vortical gusts: Experimental generation and interaction with wing. *AIAA J.*, 57(3):921–931.

Hunt, C. R. J., Wray, A., & Moin, P. (1988). Eddies, streams, and convergence zones in turbulent flows. In *Proceeding of the Summer Program in Center for Turbulence Research*, Stanford, California, USA.

Jakirlic, S. & Hanjalic, K. (2002). A new approach to modelling near-wall turbulence energy and stress dissipation. *J. Fluid Mech.*, 459:139–166.

Jakirlić, S. & Maduta, R. (2015). Extending the bounds of 'steady' RANS closures: Toward an instability-sensitive Reynolds stress model. *Int J Heat Fluid Flow*, 51:175–194.

Jancauskas, E. D. & Melbourne, W. H. (1980). The measurement of aerodynamic admittance using discrete frequency gust generation. In *Proceedings of the 7th Australasian Hydraulics and Fluid Mechanics Conference*, Brisbane, Australia.

Jancauskas, E. D. & Melbourne, W. H. (1983). The aerodynamic admittance of a slender box girder bridge section. In *Proceedings of the 8th Australasian Fluid Mechanics Conference*, Newcastle, Australia.

Jancauskas, E. D. & Melbourne, W. H. (1986). The aerodynamic admittance of two-dimensional rectangular section cylinders in smooth flow. *J. Wind. Eng. Ind. Aerodyn.*, 23:395–408.

Jardin, T., Farcy, A., & David, L. (2012). Three-dimensional effects in hovering flapping flight. *J. Fluid Mech.*, 702:102–125.

Johnson, S. J., Baker, J. P., van Dam, C. P., & Berg, D. (2010). An overview of active load control techniques for wind turbines with an emphasis on microtabs. *Wind Energ.*, 13(2-3):239–253.

Jones, A. R. & Babinsky, H. (2010). Unsteady lift generation on rotating wings at low Reynolds numbers. *J. Aircr.*, 47(3):1013–1021.

Jones, K. & Platzer, M. (2001). Flapping-wing propulsion for a micro air vehicle. In *38th Aerospace Sciences Meeting and Exhibit*. Reno, Nevada, USA.

Kissing, J., Kriegseis, J., Li, Z., Feng, L.-H., Hussong, J., & Tropea, C. (2020a). Insights into leading edge vortex formation and detachment on a pitching and plunging flat plate. *Exp. Fluids*, 61(9):512.

Kissing, J., Kriegseis, J., & Tropea, C. (2020b). On the role of secondary structures during leading edge vortex lift off and detachment on a pitching and plunging flat plate. In Dillmann, A., Heller, G., Krämer, E., Wagner, C., Tropea, C., & Jakirlić, S., editors, *New Results in Numerical and Experimental Fluid Mechanics XII*, pages 204–213, Cham. Springer International Publishing.

Kissing, J., Stumpf, B., Kriegseis, J., Hussong, J., & Tropea, C. (2020c). Delaying leading edge vortex detachment by plasma flow control at topologically critical locations. *Phys. Rev. Fluids*, (Under review).

Kissing, J., Wegt, S., Jakirlic, S., Kriegseis, J., Hussong, J., & Tropea, C. (2020d). Leading edge vortex formation and detachment on a flat plate undergoing simultaneous pitching and plunging motion: Experimental and computational study. *Int J Heat Fluid Flow*, 86:108726.

Klein, S., Hoppmann, D., Scholz, P., & Radespiel, R. (2014). High-lift airfoil interacting with a vortical disturbance: Wind-tunnel measurements. *AIAA J.*, 53(6):1681–1692.

Klein, S., Scholz, P., & Radespiel, R. (2017). A two-element high-lift airfoil in disturbed flow conditions. *CEAS Aeronaut. J.*, 8(1):79–91.

Knebel, P., Kittel, A., & Peinke, J. (2011). Atmospheric wind field conditions generated by active grids. *Exp. Fluids*, 51(2):471–481.

Kramer, V. M. (1932). Die zunahme des maximalauftriebes von tragfluegeln bei ploetzlicher anstellwinkelvergroesserung (boeneffekt). *Z. Flugtech. Motorluftschiff*, 23:185–189.

Kriegseis, J. (2012). *Performance characterization and quantification of dielectric barrier discharge plasma actuators: Zugl.: Darmstadt, Techn. Univ., Diss., 2011*, volume 26 of *Forschungsberichte Strömungslehre und Aerodynamik*. Shaker, Aachen.

Kriegseis, J., Maden, I., Schwarz, C., Tropea, C., & Grundmann, S. (2015). Addendum to 'velocity-information based force-term estimation of dielectric barrier discharge plasma actuators'. *J. Phys. D: Appl. Phys.*, 48(32):329401.

Kriegseis, J. & Rival, D. E. (2014). Vortex force decomposition in the tip region of impulsively-started flat plates. *J. Fluid Mech.*, 756:758–770.

Kriegseis, J., Schwarz, C., Tropea, C., & Grundmann, S. (2013). Velocity-information-based force-term estimation of dielectric-barrier discharge plasma actuators. *J. Phys. D: Appl. Phys.*, 46(5):055202.

Kriegseis, J., Simon, B., & Grundmann, S. (2016). Towards in-flight applications? A review on dielectric barrier discharge-based boundary-layer control. *Appl. Mech. Rev.*, 68(2):020802.

Kuhnhenn, M., Simon, B., Maden, I., & Kriegseis, J. (2016). Interrelation of phase-averaged volume force and capacitance of dielectric barrier discharge plasma actuators. *J. Fluid Mech.*, (809):R1.

Kütemeier, D., Wegt, S., Maden, I., Kissing, J., Maduta, R., Kriegseis, J., Jakirlic, S., & Tropea, C. (2019). Plasma-actuated lift enhancement of a plunging airfoil: A computational study. In *AIAA Scitech 2019 Forum*, Reston, Virginia.

Lancelot, P. M. G. J., Sodja, J., Werter, N. P. M., & de Breuker, R. (2015). Design and testing of a low subsonic wind tunnel gust generator. In *Proceedings of the 16th international forum on aeroelasticity and structural dynamics, IFASD*, St. Petersburg, Russia.

Larose, G. L. (1999). Experimental determination of the aerodynamic admittance of a bridge deck segment. *J Fluids Struct.*, 13(7):1029–1040.

Leishman, J. G. (2017). *Principles of Helicopter Aerodynamics*. Cambridge aerospace series. Cambridge University Press, Cambridge, United Kingdom, second edition.

Li, Z., Feng, L.-H., Kissing, J., Tropea, C., & Wang, J.-J. (2020). Experimental investigation on the leading-edge vortex formation and detachment mechanism of a pitching and plunging plate. *J. Fluid Mech.*, 901:A17.

Lombardi, A. J., Bowles, P. O., & Corke, T. C. (2013). Closed-loop dynamic stall control using a plasma actuator. *AIAA J.*, 51(5):1130–1141.

Lysak, P. D., Capone, D. E., & Jonson, M. L. (2013). Prediction of high frequency gust response with airfoil thickness effects. *J Fluids Struct.*, 39:258–274.

Lysak, P. D., Capone, D. E., & Jonson, M. L. (2016). Measurement of the unsteady lift of thick airfoils in incompressible turbulent flow. *J Fluids Struct.*, 66:315–330.

Maduta, R., Ullrich, M., & Jakirlic, S. (2017). Reynolds stress modelling of wake interference of two cylinders in tandem: Conventional vs. eddy-resolving closure. *Int. J. Heat Fluid Flow*, 67:139–148.

Makita, H. (1991). Realization of a large-scale turbulence field in a small wind tunnel. *Fluid Dyn.*, 8:53.

Manar, F. & Jones, A. R. (2019). Evaluation of potential flow models for unsteady separated flow with respect to experimental data. *Phys. Rev. Fluids*, 4(3):034702.

Massaro, M. & Graham, J. (2015). The effect of three-dimensionality on the aerodynamic admittance of thin sections in free stream turbulence. *J Fluids Struct.*, 57:81–90.

McCroskey, W. J. (1982). Unsteady airfoils. *Annu. Rev. Fluid Mech.*, 14(1):285–311.

McCroskey, W. J., Carr, L. W., & McAlister, K. W. (1976). Dynamic stall experiments on oscillating airfoils. *AIAA J.*, 14(1):57–63.

McGowan, G. Z., Granlund, K., Ol, M. V., Gopalarathnam, A., & Edwards, J. R. (2011). Investigations of lift-based pitch-plunge equivalence for airfoils at low Reynolds numbers. *AIAA J.*, 49(7):1511–1524.

Menter, F. R. & Egorov, Y. (2010). The scale-adaptive simulation method for unsteady turbulent flow predictions. Part 1: Theory and model description. *Flow Turbul. Combust.*, 85(1):113–138.

Moreau, E. (2007). Airflow control by non-thermal plasma actuators. *J. Phys. D: Appl. Phys.*, 40(3):605–636.

Mulleners, K. & Raffel, M. (2012). The onset of dynamic stall revisited. *Exp. Fluids*, 52(3):779–793.

Nudds, R. L., Taylor, G. K., & Thomas, A. L. R. (2004). Tuning of strouhal number for high propulsive efficiency accurately predicts how wingbeat frequency and stroke amplitude relate and scale with size and flight speed in birds. *Proc. Royal Soc. B*, 271(1552):2071–2076.

Ol, M. V., Bernal, L., Kang, C.-K., & Shyy, W. (2009). Shallow and deep dynamic stall for flapping low Reynolds number airfoils. *Exp. Fluids*, 46(5):883–901.

Peng, J. & Dabiri, J. O. (2009). Transport of inertial particles by Lagrangian coherent structures: Application to predator–prey interaction in jellyfish feeding. *J. Fluid Mech.*, 623:75–84.

Perry, A. E. & Chong, M. S. (1987). A description of eddying motions and flow patterns using critical-point concepts. *Annu. Rev. Fluid Mech.*, 19(1):125–155.

Popovac, M. & Hanjalic, K. (2007). Compound wall treatment for RANS computation of complex turbulent flows and heat transfer. *Flow Turbul. Combust.*, 78(2):177.

Post, M. L. & Corke, T. C. (2006). Separation control using plasma actuators: Dynamic stall vortex control on oscillating airfoil. *AIAA J.*, 44(12):3125–3135.

Prangemeier, T., Rival, D., & Tropea, C. (2010). The manipulation of trailing-edge vortices for an airfoil in plunging motion. *J Fluids Struct.*, 26(2):193–204.

Raffel, M., Willert, C. E., Wereley, S., & Kompenhans, J. (2007). *Particle Image Velocimetry: A Practical Guide.* Springer-Verlag, Berlin Heidelberg, second edition.

Riddle, T. W., Wadcock, A. J., Tso, J., & Cummings, R. M. (1999). An experimental analysis of vortex trapping techniques. *J. Fluids Eng.*, 121(3):555.

Ristroph, L., Bergou, A. J., Ristroph, G., Coumes, K., Berman, G. J., Guckenheimer, J., Wang, Z. J., & Cohen, I. (2010). Discovering the flight autostabilizer of fruit flies by inducing aerial stumbles. *Proc. Natl. Acad. Sci. U.S.A.*, 107(11):4820–4824.

Rival, D., Prangemeier, T., & Tropea, C. (2009a). The influence of airfoil kinematics on the formation of leading-edge vortices in bio-inspired flight. *Exp. Fluids*, 46(5):823–833.

Rival, D., Schönweitz, D., & Tropea, C. (2011). Vortex interaction of tandem pitching and plunging plates: A two-dimensional model of hovering dragonfly-like flight. *Bioinspir. Biomim.*, 6(1):016008.

Rival, D. E., Kriegseis, J., Schaub, P., Widmann, A., & Tropea, C. (2014). Characteristic length scales for vortex detachment on plunging profiles with varying leading-edge geometry. *Exp. Fluids*, (55):1660 ff.

Rival, D. E., Prangemeister, T., & Tropea, C. (2009b). The influence of aerofoil kinematics on the formation of leading-edge vortices in bio-inspired flight. *Exp. Fluids*, (46):823–833.

Rossow, V. J. (1978). Lift enhancement by an externally trapped vortex. *J. Aircr.*, 15(9):618–625.

Saddington, A. J., Finnis, M. V., & Knowles, K. (2015). The characterisation of a gust generator for aerodynamic testing. *Proc. Inst. Mech. Eng. G*, 229(7):1214–1225.

Sankaran, R. & Jancauskas, E. D. (1992). Direct measurement of the aerodynamic admittance of two-dimensional rectangular cylinders in smooth and turbulent flows. *J. Wind. Eng. Ind. Aerodyn.*, 41(1):601–611.

Sattari, P., Rival, D. E., Martinuzzi, R. J., & Tropea, C. (2012). Growth and separation of a start-up vortex from a two-dimensional shear layer. *Phys Fluids*, 24(10):107102.

Sears, W. R. (1938). *A systematic presentation of the theory of thin airfoils in non-uniform motion.* PhD thesis, California Institute of Technology.

Sears, W. R. (1941). Some aspects of non-stationary airfoil theory and its practical application. *Aeronaut. J.*, 8(3):104–108.

Shadden, S. C., Dabiri, J. O., & Marsden, J. E. (2006). Lagrangian analysis of fluid transport in empirical vortex ring flows. *Phys Fluids*, 18(4):047105.

Siala, F. F. & Liburdy, J. A. (2019). Leading-edge vortex dynamics and impulse-based lift force analysis of oscillating airfoils. *Exp. Fluids*, 60(10):37.

Simon, B. J. (2017). *Active cancellation of Tollmien-Schlichting waves under varying inflow conditions for in-flight application.* PhD thesis, Technische Universität Darmstadt.

Spinato, F., Tavner, P. J., van Bussel, G. J., & Koutoulakos, E. (2009). Reliability of wind turbine subassemblies. *IET Renew. Power Gener.*, 3(4):387–401.

Stumpf, B. (2019). *Manipulation of the leading edge vortex detachment on a pitching and plunging flat plate using a DBD plasma actuator.* Master thesis, Technische Universität Darmstadt.

Sutherland, W. (2009). LII. the viscosity of gases and molecular force. *Philos. Mag.*, 36(223):507–531.

Tang, D. M., Cizmas, P. G. A., & Dowell, E. H. (1996). Experiments and analysis for a gust generator in a wind tunnel. *J. Aircr.*, 33(1):139–148.

Taylor, K. & Amitay, M. (2015). Dynamic stall process on a finite span model and its control via synthetic jet actuators. *Phys Fluids*, 27(7):077104.

Theodorsen, T. (1934). General theory of aerodynamic instability and the mechanism of flutter. Technical report NACA-TR-496, National Advisory Committee for Aeronautics.

Traphan, D., Wester, T. T. B., Peinke, J., & Gülker, G. (2018). On the aerodynamic behavior of an airfoil under tailored turbulent inflow conditions. In *Proceedings of the 5th International Conference on Experimental Fluid Mechanics*, Munich, Germany.

Triantafyllou, G. S., Triantafyllou, M. S., & Grosenbaugh, M. A. (1993). Optimal thrust development in oscillating foils with application to fish propulsion. *J Fluids Struct.*, 7(2):205–224.

Triess, S. (2018). *Development, implementation and validation of an apparatus for the characterization of the boundary layer on a moving airfoils.* Bachelor thesis, Technische Universität Darmstadt.

Tropea, C., Yarin, A., & Foss, J. F., editors (2007). *Springer Handbook of Experimental Fluid Mechanics.* Springer Handbooks. Springer-Verlag, Berlin Heidelberg.

Veers, P. & Butterfield, S. (2001). Extreme load estimation for wind turbines - issues and opportunities for improved practice. In *20th 2001 ASME Wind Energ. Symposium*, Aerospace Sciences Meetings.

Visbal, M. (1991). On the formation and control of the dynamic stall vortex on a pitching airfoil. In *29th Aerospace Sciences Meeting*, Aerospace Sciences Meetings.

Visbal, M. R. (2011). Numerical investigation of deep dynamic stall of a plunging airfoil. *AIAA J.*, 49(10):2152–2170.

von Karman, T. (1938). Airfoil theory for non-uniform motion. *Aeronaut. J.*, 5(10):379–390.

Wang, S., Zhang, X., He, G., & Liu, T. (2013). A lift formula applied to low-Reynolds-number unsteady flows. *Phys Fluids*, 25(9):093605.

Wang, Z. & Gursul, I. (2017). Lift enhancement of a flat-plate airfoil by steady suction. *AIAA J.*, 55(4):1355–1372.

Wegt, S. (2017). *Numerische Modellierung der Tragflügelaerodynamik unter Bedingungen böiger Anströmung.* Master thesis, Technische Universität Darmstadt.

Wei, N. J., Kissing, J., & Tropea, C. (2019a). Generation of periodic gusts with a pitching and plunging airfoil. *Exp. Fluids*, 60(11):41.

Wei, N. J., Kissing, J., Wester, T. T. B., Wegt, S., Schiffmann, K., Jakirlic, S., Hölling, M., Peinke, J., & Tropea, C. (2019b). Insights into the periodic gust response of airfoils. *J. Fluid Mech.*, 876:237–263.

Westerweel, J. & Scarano, F. (2005). Universal outlier detection for PIV data. *Exp. Fluids*, 39(6):1096–1100.

Widmann, A. (2015). *Formation and detachment of leading edge vortices on unsteady airfoils*. Phd thesis, Technische Universität Darmstadt, Darmstadt.

Widmann, A. & Tropea, C. (2015). Parameters influencing vortex growth and detachment on unsteady aerodynamic profiles. *J. Fluid Mech.*, 773:432–459.

Widmann, A. & Tropea, C. (2017). Reynolds number influence on the formation of vortical structures on a pitching flat plate. *Interface focus*, 7(1):20160079.

Wojcik, C. J. & Buchholz, J. H. J. (2014). Vorticity transport in the leading-edge vortex on a rotating blade. *J. Fluid Mech.*, 743:249–261.

Wong, J. G., Kriegseis, J., & Rival, D. E. (2013). An investigation into vortex growth and stabilization for two-dimensional plunging and flapping plates with varying sweep. *J Fluids Struct.*, 43:231–243.

Wong, J. G. & Rival, D. E. (2015). Determining the relative stability of leading-edge vortices on nominally two-dimensional flapping profiles. *J. Fluid Mech.*, 766:611–625.

Woo, G. T. K. & Glezer, A. (2010). Transitory control of dynamic stall on a pitching airfoil. In *Active Flow Control II*, volume 108 of *Notes on Numerical and Fluid Dynamics*, pages 3–18. Springer-Verlag.

Wood, K. T., Cheung, R. C., Richardson, T. S., Cooper, J. E., Darbyshire, O., & Warsop, C. (2017). A new gust generator for a low speed wind tunnel: Design and commissioning. In *55th AIAA Aerospace Sciences Meeting*, AIAA SciTech Forum.

Zhao, X., Gouder, K., Graham, J. M. R., & Limebeer, D. J. N. (2016). Buffet loading, dynamic response and aerodynamic control of a suspension bridge in a turbulent wind. *J Fluids Struct.*, 62:384–412.

Zhou, J., Adrian, R. J., Balachandar, S., & Kendall, T. M. (1999). Mechanisms for generating coherent packets of hairpin vortices in channel flow. *J. Fluid Mech.*, 387:353–396.

Nomenclature

Capital Roman letters

A	m^2	area
$A(k_1,\, k_2)$	–	Atassi function
C	F	capacitance
$C(k)$	–	Theodorsen function
$F(k)$	–	real part of the Theodorsen function
F_x	$\mathrm{N{=}kg\ m/s^2}$	force in x direction
$G(k)$	–	imaginary part of the Theodorsen function
H	m	plunge height
H_1	–	secondary structure confining half-saddle
H_2	–	LEV confining half-saddle
L_x	$\mathrm{N{=}kg\ m/s^2}$	aerodynamic lift
M_θ	$\mathrm{Nm{=}kg\ m^2/s^2}$	aerodynamic pitching moment
$\hat{M}_\theta^*$	$\mathrm{Nm{=}kg\ m^2/s^2}$	minimum pitching moment amplitude
N_x	–	node x
N_1	–	leading edge vortex node
N_2	–	secondary vortex node
N_3	–	tertiary vortex node
P	$\mathrm{W{=}kg\ m^2/s^3}$	power
R_x	$\mathrm{m^2/s^2\ K}$	specific gas constant of gas x
$S(k_1)$	–	Sears function
T	s	motion period
U_x	m/s	flow velocity in x direction
V	$\mathrm{V{=}kg\ m^2/s^2A}$	voltage

Lowercase Roman letters

a	m	center of rotation of airfoil
a_0	–	leading edge curvature coefficient
b	m	half-chord of airfoil

c_d	–	drag coefficient
c	m	chord length
f	1/s	frequency
f_{PA}	N=kg m/s^2	plasma induced body force
g	m/s^2	gravitational acceleration
h	m	plunge location of airfoil
h_0	m	plunge amplitude
$h_L(k_1, k_2)$	–	universal Atassi function
k_1	–	reduced frequency of mean inflow fluctuation
k_2	–	reduced frequency of normal inflow fluctuation
l	m	length
n	–	number of runs or periods
p	Pa	pressure
r	m	radius
t	s	time
u	m/s	inflow velocity parallel to mean flow
v	m/s	inflow velocity normal to mean flow
w	m	width
x	m	horizontal coordinate
y	m	vertical coordinate
y^+	–	dimensionless wall distance

Capital Greek letters

Γ	m^2/s	circulation
Γ_1	–	scalar to determine vortex center position
Γ_2	–	scalar to determine vortex boundary
Θ	deg	pitch angle of gust generation vane
Θ^*	deg	optimal pitch amplitude for gust generation
Θ_0	deg	pitch amplitude for gust generation

Lowercase Greek letters

α	deg	geometric angle
α_β	deg	mean angle of attack
α_m	–	deviation of airfoil camber from symmetry
β	–	inflow perturbation wavelength to chord ratio
δ_a	m	airfoil thickness

ϵ	–	normalization parameter in $A(k_1,\, k_2)$
η	Pa s	dynamic viscosity
λ	m	wavelength
ν	$\mathrm{m^2/s}$	kinematic viscosity
ω	1/s	angular frequency
ϕ	deg	phase offset
$\phi^\dagger$	deg	phase offset for minimum pitching moment
φ_{PA}	1/s	AC voltage frequency
ρ	$\mathrm{kg/m^3}$	density
σ	–	standard deviation
τ_s	s	response time of seeding particles

Indices

dyn	dynamic
eff	effective
Exp.	experimental
g	gust
geo	geometric
LEV	leading edge vortex
max	maximum
N	normal
p	perturbation
plunge	plunging
PA	plasma actuator
pp	peak to peak
qs	quasi-steady
SL	shear layer at the leading edge
ss	static stall
SSO	secondary structure occurrence
Theor.	theoretical
∞	free stream
U_∞	steady inflow

Symbols

$\overline{x}$	–	mean value of x
$\hat{x}$	–	amplitude of x

$\dot{x}$	1/s	time derivative of x
$\ddot{x}$	1/s^2	second time derivative of x
Δx	s	inter image pair delay of x

Dimensionless numbers

k	$\pi f c/U_\infty$ $\omega c/2U_\infty$	reduced frequency, ratio of the time for a fluid element to convect across the airfoil to the period of oscillation/perturbation
κ	–	covering ratio, introduced by Widmann (2015), used to distinguish between leading edge vortex detachment mechanisms
Re	$U_\infty c/\nu$	Reynolds number, ratio of inertial forces to viscous forces
Re_v	$\Gamma_{\mathrm{LEV}}/\nu\pi$	vortex Reynolds number which determines viscous response of the boundary layer on a wall below a vortex
St	$2\hat{h}f/U_\infty$	Strouhal number, ratio of the convectively covered distance by the incoming flow during one stroke period and the airfoil plunging height

Abbreviations

AC	alternating current
DBD-PA	dielectric barrier discharge plasma actuator
DEHS	Di-Ethyl-Hexyl-Sebacat
DSV	dynamic stall vortex
FTLE	finite time Lyapunov exponent
IISRSM	improved instability-sensitive Reynolds stress model
LCS	Lagrangian coherent structures
LEV	leading edge vortex
LES	large-eddy simulation
MAV	micro air vehicle
NACA	*National Advisory Committee for Aeronautics*
Nd:YLF	neodymium doped yttrium lithium fluoride crystal

PID	control loop with proportional, integral and differential component
PIV	particle image velocimetry
px	picture element (pixel)
RAM	random-access memory
RANS	Reynolds averaged Navier Stokes
ROI	region of interest
RSM	Reynolds stress model
SAS	scale-adaptive simulation
SLA	Institute for Fluid Mechanics and Aerodynamics at TU Darmstadt
SSO	secondary structure occurence
SST	Menter's shear stress transport
TEV	trailing edge vortex
TUDa	Technische Universität Darmstadt
USB	universal serial bus

List of Figures

List of Tables